Exploring Pain Neurobiology: Molecular Investigation of Genetic Sensory Disorders

Nivedita Sarveswaran

Wolfson College
University of Cambridge

A thesis submitted
for the degree of Doctor of Philosophy

October 2021

Declaration of Originality

This thesis is the result of my own work; any data produced in collaboration is acknowledged in the preface and main text. It is not substantially similar to any work that has already been submitted for another qualification at any institution, except as declared in the title. It does not exceed the prescribed word limit of 60,000 words as specified by the Degree Committee for the School of Clinical Medicine.

Funding

I would like to thank the Biotechnology and Biological Sciences Research Council (BBSRC) for organising a doctoral training partnership programme at the interface of academia and industry, and to both the BBSRC and AstraZeneca for funding this project.

Acknowledgements

First and foremost, I owe the deepest gratitude to my supervisors Geoff Woods at CIMR and John Linley at AstraZeneca for opening the door to this opportunity. From my interest in neurogenetics and electrophysiology, you built a training path that showed me the strengths of combining clinical, academic and industry expertise to make a meaningful impact on society. Your patience and encouragement through the highs and lows meant the world to me, thank you for making this experience a dream come true – I'll never forget how a PCR works again!

To the Woods Lab past & present – Mike, Emily, Ichrak, Samiha, Yunisa, Dianah – you made every day fun and exciting, I couldn't have asked for a kinder group of people to work with so closely. Shoutout as well to Level 4 mates Seema, Jonny, Michael, Natalie plus my fellow Canterbridgean Biomed girls Lisa and Chloe – thank you for the drive-by laughs, rambles and lab/life advice, boosting morale at ridiculous o'clock when necessary. I am also hugely grateful to the AZ Neuro team who taught me so much about scientific rigour and the many hurdles to overcome when taking a target from discovery to the clinic; your balance of passion and pragmatism was so motivating to be around. Special thanks to NeuroGals Robyn, Diana and Rachel for your moral support at the rig, sharing many geeky conversations and all the baked goods.

The African proverb "It takes a village…" applies just as well to raising a researcher, particularly when having a broad skillset is increasingly important. I am especially grateful to these colleagues at CIMR who generously provided tutorials and technical advice – Mark Bowen and Matthew Gratian (microscopy), Robin Antrobus and Jack Houghton (proteomics), Randy Read and Luke Perrera (structural analysis). Similarly from AstraZeneca, thank you to Fiona Cusdin and Janette Dillon for guiding me through the pitfalls of working with Nav channels and the HEK JI TREX cell line, as well as Carl Matthews for advising on high-content imaging systems.

Even with such a supportive environment, I almost didn't make it this far. To the friends who kept my spirits high and heart full – Wally Gals, the Queen Square Nerd Herd and extended family of the SOAS Jindokai Dungeon – just looking at the group names made me laugh when I needed it. But I owe the biggest hugs to Stephen, Hutan, Chris, Nate, Mica, Cait, Joe, Rachel, Alex and Sharmin. Last but not least to my family, especially Ammamma and each of my parents; I would not be here without your dedication to giving us greater opportunities in life. Thank you for teaching me that we can always think positive.

"Turns out, life isn't a puzzle that can just be solved one time and it's done.
You wake up every day, and you solve it again."
Chidi Anagonye, The Good Place

Publications

Stouffer, K., Nahorski, M., Moreno, P., **Sarveswaran, N.**, Menon, D., Lee, M. and Woods, C.G. (2017). Functional SNP allele discovery (fSNPd): an approach to find highly penetrant, environmental-triggered genotypes underlying complex human phenotypes. *BMC Genomics*, 18(1).

Moss, C., Srinivas, S.M., **Sarveswaran, N.**, Nahorski, M., Gowda, V.K., Browne, F.M. and Woods, G. (2018). Midface toddler excoriation syndrome (MiTES) can be caused by autosomal recessive biallelic mutations in a gene for congenital insensitivity to pain, PRDM12. *British Journal of Dermatology*, 179(5)

Inamadar, A.C., Vinay, K., Olabi, B., **Sarveswaran, N.**, Bishnoi, A., Woods, C.G. and Moss, C. (2019). Extending the phenotype of midface toddler excoriation syndrome (MiTES): Five new cases in three families with PR domain containing protein 12 (PRDM12) mutations. *Journal of the American Academy of Dermatology*, 81(6)

Conference Presentations

The Challenge of Chronic Pain Conference 2019 (Poster)

"Mid-face Toddler Excoriation Syndrome (MiTES): A second phenotype caused by polyalanine tract expansions in *PRDM12*"

IASP 2020 Virtual World Congress on Pain (Virtual Poster)

"Using *SCN9A* mutations in congenital painlessness to reveal novel analgesic targets"

NGF Webinar Series – 6th May 2021 (Talk)

"The puzzle of PRDM12 in sensory neuron development"

Abstract

The nociceptive system is a neural pathway that underlies our capacity to feel pain when we are threatened by potential tissue injury. Congenital Insensitivity to Pain (CIP) arises when genetic mutations disrupt molecular components that are essential to the development or postnatal function of this system. Understanding how these mutations alter the encoded protein, and subsequently impact sensory neuron signalling, can reveal new strategies to modulate their activity in maladaptive pain disorders.

The primary aim of this thesis was to confirm pathogenicity of several novel missense mutations from *SCN9A*-CIP patients, representing localised structural changes to the voltage-gated sodium channel (VGSC) Nav1.7. Studies revealed that all mutants were non-conducting, independent of protein folding or membrane trafficking defects, implying critical intramolecular roles for the affected residues. Through this project I developed a workflow for rapid stable cell line generation and functional assessment that could be applied to the interpretation of other VGSC variants.

We extended this project to examine the interactomes of wild-type human Nav1.7 channels and a null N-terminal mutation in the HEK293 expression system. While this approach did not conclusively identify any protein-protein interactions disturbed by the mutation, our results support some of the mass spectrometry hits detected in a similar study of the *in vivo* mouse Nav1.7 interactome.

Lastly, we uncovered a surprising genotype-phenotype correlation in another CIP gene, *PRDM12*. Unlike other loss-of-function mutations in this gene that cause global, lifelong painlessness, homozygous polyalanine expansions within a discrete range lead to facially-localised, enhanced itch in childhood (Midface Toddler Excoriation Syndrome – MiTES). Observations of the CIP- and MiTES-associated polyalanine expansion mutants in a non-neuronal cell line hint at a subtle difference in PRDM12 availability that may influence the maturation of polymodal pain- and itch-sensing neurons.

Collaborative Contributions

- Clinical characterisation of *SCN9A*-CIP patients by Professor Geoff Woods
- Identification of *SCN9A* variants by the Cambridge University Hospitals Genomic Laboratory
- Generation of wild-type *SCN9A* plasmids by Dr Fiona Cusdin
- Automated electrophysiological data acquisition by Dr John Linley
- Mass spectrometry analysis by Dr Robin Antrobus and Dr Jack Houghton
- Clinical characterisation of *PRDM12*-MiTES patients led by Professor Celia Moss
- *PRDM12* analysis of select patients by Dr Mike Nahorski and Dr Yunisa Pamela

List of Abbreviations

AKAP	A Kinase-Anchoring Protein
AmpR	Ampicillin Resistance
APC	Automated Patch Clamp
BDNF	Brain-Derived Neurotrophic Factor
BSA	Bovine Serum Albumin
Ca^{2+}	Calcium Ion
CGRP	Calcitonin Gene-Related Peptide
CIP	Congenital Insensitivity to Pain
cKO	conditional Knockout
CMV/-TO	Human Cytomegalovirus promoter/with Tet Operators
CNS	Central Nervous System
Co-IP	Co-Immunoprecipitation
CsCl	Caesium Chloride
CsF	Caesium Fluoride
CTD	C-Terminal Domain
DMEM	Dulbecco's Modified Essential Medium
dNTP	Deoxynucleoside Triphosphate
DOR/KOR/MOR/NOR	Delta/Kappa/Mu/Nociceptin Opioid Receptors
DREZ	Dorsal Root Entry Zone
DRG	Dorsal Root Ganglia
DTT	Dithiothreitol
ER	Endoplasmic Reticulum
ERK1/2	Extracellular signal-Regulated Kinase 1/2
EUPC	Exclusive Unique Peptide Count
FAAH	Fatty Acid Amide Hydrolase
FBS	Fetal Bovine Serum
FHF	Fibroblast Growth Factor Homologous Factor
G_{max}	Maximal conductance
GOI	Gene Of Interest
GPCR	G Protein-Coupled Receptor
H3K9(me)	Histone H3 Lysine 9 (methylated)
HA	Hemagglutinin
HEK	Human Embryonic Kidney
HMT	Histone-lysine N-Methyltransferase
hNav	human Nav
IB4	Isolectin-B4
ICS	Intracellular Solution
I_{max}	Maximal current
INa_T	Transient sodium ion current
IP-MS	Immunoprecipitation-Mass Spectrometry
iPSCs	induced Pluripotent Stem Cells
KO	Knockout
LB-Amp	Luria Broth with Ampicillin
LC-MS/MS	Liquid Chromatography with tandem Mass Spectrometry
LFQ	Label-Free Quantitation

LOF	Loss-Of-Function
LTMR	Low-Threshold Mechanoreceptor
MAPK	Mitogen-Activated Protein Kinase
MEM	Minimum Essential Medium
MiTES	Midface Toddler Excoriation Syndrome
MSA	Multiple Sequence Alignment
Na^{2+}	Sodium Ion
NCCs	Neural Crest Cells
NDS	Normal Donkey Serum
NEAA	Non-Essential Amino Acids
NGF	Nerve Growth Factor
NMDA	N-Methyl-D-aspartate
NMIIa	Non-muscle Myosin Iia
NPB	Neural Plate Border
NSAIDs	Nonsteroidal Anti-Inflammatory Drugs
NTD	N-Terminal Domain
NTP	Non-Targeting Pool
PBS/-T/-Tx	Phospho-Buffered Saline/-Tween20/-Triton X-100
PCR	Polymerase Chain Reaction
PFA	Paraformaldehyde
PKA/C	Protein Kinase A/C
PPI	Protein-Protein Interaction
PRDM	PR homology domain-containing member
PTM	Post-Translational Modification
RE	Restriction Enzyme
RLC	Regulatory Light Chain
RPM	Revolutions Per Minute
scRNA-seq	single cell RNA sequencing
SDM	Site-Directed Mutagenesis
SOC	Super Optimal broth with Catabolite repression
TBS/-T	Tris-Buffered Saline/-Tween20
TetO	Tetracycline Operator
TetR	Tetracycline Repressor
TG	Trigeminal Ganglia
TH	Tyrosine Hydroxylase
Trk(-A/B/C)	Tropomyosin Receptor Kinase (A/B/C)
V_{50}	Voltage of half-maximal in-/activation
VGCC	Voltage-Gated Calcium Channel
VGPC	Voltage-Gated Potassium Channel
VGSC	Voltage-Gated Sodium Channel
vlPAG	ventrolateral Periaqueductal Gray
V_{rev}	Reversal Potential
WDR	Wide Dynamic Range
WGA-488	Wheat Germ Agglutinin conjugated to Alexa Fluor 488
WT	Wild-Type

Table of Contents

CHAPTER 1: Main Introduction

1.1 – Human Pain and Nociception

The most commonly cited definition of pain comes from the International Association for the Study of Pain, described as "an unpleasant sensory and emotional experience associated with, or resembling that associated with, actual or potential tissue damage"[1]. Nociception is the physiological process responsible for identifying harmful stimuli, which is almost always accompanied by the highly deterrent experience of pain. The molecular features and functional properties of nociceptors (the first order neurons in this sensory pathway) are highly conserved across species, underscoring the importance of this threat-detection system[2,3]. The way pain is perceived is dependent on several facets of neural activity including sensory discrimination, affective motivation and cognitive evaluation[4]. More simply put, it is a phenomenon influenced by the body, mind and socio-cultural factors; thus, while nociception-related behaviours are universally recognisable externally, pain perception is a highly subjective mental experience.

Despite its inherent unpleasantness, the ability to feel pain as a result of nociception has multiple adaptive benefits. When nociceptors detect physical stimuli that have the potential to cause tissue damage, their excitation and signal propagation prompts a rapid withdrawal response via spinal reflexes to prevent injury. In addition to this immediate protective function, pain acts as a learning signal; the sensation is closely associated with its environmental context, helping the individual learn to recognise and avoid subsequent situations that may cause harm. If a wound is acquired, pain serves a further purpose by promoting shielding and immobilisation of the injured tissue until it has fully healed. However, it is important to differentiate between physiologically useful pain that is spatially and temporally correlated with injury and healing processes, versus pathophysiological pain that manifests as hypersensitive signalling or even lacking any relationship with underlying injury.

Acute nociceptive pain as described above refers to the activation of specialised sensory neurons by a noxious stimulus and the consequent signalling to the central nervous system (CNS) that instates withdrawal behaviour and aversive emotional connotations. If there is a tissue injury, inflammation is a coinciding event whereby the release of chemical mediators meant to trigger wound repair also temporarily sensitise nociceptive fibres. However, in chronic inflammatory diseases such as arthritis, nociceptors are repeatedly sensitised such that inflammatory pain itself can be considered a chronic pain condition. Alternatively, neuropathic pain arises from abnormal activity in nociceptive neurons themselves due to primary lesions, genetic hyperexcitability disorders or metabolic alterations – all of

which produce burning, shooting sensations which are not associated with any somatic damage. In both chronic inflammatory and neuropathic pain, the persistence and/or unpredictable nature of pathophysiological pain has a severe impact on quality of life.

Chronic pain is clinically defined as “pain that persists or recurs for longer than 3 months and is associated with significant emotional distress or significant functional disability”. It can be further classified into 1 of 6 classes of chronic secondary pain when there is evidence of an underlying cause such as tissue trauma, a musculoskeletal condition or pain induced from cancer or its treatment[5]. Unsurprisingly, long-term pain that is disproportionate or unpredictable can have adverse effects on mood, sleep and all aspects of general health. In a survey across Europe, chronic pain was estimated to affect 19% of adults and although two-thirds of patients used analgesic drugs and/or non-pharmacological therapies, 40% of patients suffered from inadequate management of their pain[6]. At the socio-economic level, over 60% of individuals were unable to work effectively away from home, and 19% had even lost their jobs because of their pain[6]. With ageing populations growing around the world, the prevalence of conditions accompanied by secondary chronic pain also increases and thus the burden of chronic pain will continue to be a significant problem[7].

The health and social care costs of supporting patients with chronic pain often requires multidisciplinary management at secondary and tertiary levels[7]. Chronic pain can be understood through the biopsychosocial model given that biological factors, personal meaning and environmental context all uniquely interact and contribute to the patient’s experience of pain[8]. Educating patients on the neurobiology of pain and nociception, providing mental and physical tools to cope with flare-ups and insomnia, and supporting self-advocacy can help them live well with pain[9]. These specialist interventions are undoubtedly valuable in improving quality of life because of their holistic view of the affected individual, but unfortunately some patients still suffer from incurable pain.

Research into the biological basis of chronic pain has highlighted a vast array of molecular processes that can enhance pain, some of which are selectively expressed in certain disorders. Recent adjustments to diagnostic definitions[10] should help stratify clinical subtypes so that processes involved in the generation of chronic primary pain can be differentiated from those involved with secondary chronic pain. Understanding the molecular mechanisms that drive these diverse pain states will help to choose the most appropriate pain management strategy as early as possible, and potentially reveal novel targets that could provide more effective pain relief.

1.2 – Anatomical Components of the Nociceptive Pathway

The recognition of external or internal tissue-damaging stimuli coincides with painful sensations motivating us to modify our behaviour. The nociceptive pathway mediating this process can be simplified into three main neural components, as shown in Figure 1.1. The first order neuron is the nociceptor, which detects harmful stimuli exposed to the skin or internal organs. Signal transduction proteins transform the extracellular stimulus into an electrical signal that is propagated along the nociceptor axon to its central terminals, where they form synapses within a dense network of neurons in the dorsal spinal cord. The nociceptors release excitatory neurotransmitters that activate cognate receptors on spinal neurons, and with sufficient stimulation, the second order neuron of the ascending spinothalamic tract transmits the signal to thalamic and brainstem nuclei. From here, third and fourth order neurons convey the message to multiple brain regions involved in processing the sensory, emotional and cognitive aspects of pain perception.

In contrast to typical depictions of the unipolar neuron, nociceptors and other somatosensory neurons have a pseudounipolar morphology – a stem axon protrudes from the cell body which then splits into a T-junction where the two branches extend to peripheral and central targets[11,12] (see Figure 1.2A). Peripheral targets for innervation include visceral organs and skin tissue, whereas the shorter central projections terminate on specific sections of the dorsal spinal cord. The cell bodies of sensory nerves innervating the face are clustered within the trigeminal ganglia (TG), while those that innervate the rest of the body are clustered in dorsal root ganglia (DRG), as shown in Figure 1.2B. Pairs of ganglia afford sensation to either side of the body, present at each axial level and protected by bony structures of the skull or vertebrae. Small blood vessels are enmeshed within the ganglia to sustain the high energy demand required for the preservation and functional adaptation of such long neurons. These capillaries are fenestrated, with increased permeability allowing for more direct communication between sensory nerves and sensitising molecules in systemic circulation[13].

Somatosensory neurons within the DRG and TG can be categorized in a variety of ways, all of which bear relevance to their specialised functions (see Figure 1.2B). Historically, classification was based on the diameter of cell bodies, myelination status and a limited selection of molecular markers that could distinguish broad populations[14–16] – proprioceptors which recognise self-generated movement and body position; low-threshold mechanoreceptors (LTMRs) that respond to innocuous touch; and nociceptors which detect noxious stimuli. Proprioceptors and LTMRs (also known as Aα and Aβ nerve fibres) have larger cell bodies, are heavily myelinated, and are identified by the expression of neurotrophic tropomyosin receptor kinases (Trk) TrkC and TrkB respectively. Nociceptors include

thinly myelinated Aδ fibres and unmyelinated C fibres, both of which have the smallest cell bodies and express TrkA. The density of axonal myelination determines the transmission speed of electrical impulses. This is neatly illustrated by the type of pain perceived when different nociceptive fibres are stimulated – the conduction velocity of Aδ fibres is 5-40 m/s accounting for sharp first pain, while C fibres conduct action potentials at 0.5-2 m/s responsible for slow, dull pain[3]. Of note, facial proprioceptors are absent in the TG, instead located in the mesencephalic trigeminal nucleus[17].

The manner in which somatosensory neurons terminate in the periphery also helps to distinguish their functions. Nociceptive Aδ and C fibre peripheral terminals are found within the outermost layer of skin, the epidermis, branching into free nerve endings that express stimulus-specific receptors. They also terminate within the mucosa, muscle and vascular regions of visceral organs[18]. The peripheral terminals of Aβ LTMRs associate with non-neuronal cells in the lower dermal layer of skin to form highly organised and morphologically distinct end organs. These end organs respond to distinct qualities of innocuous touch (such as vibration or stretch) and vary in their sensory adaptation properties[19]. Proprioceptive neurons are found within skeletal muscle spindles, Golgi tendon organs and joints to monitor body movement and load[20].

The central branches of somatosensory neurons also terminate in separate areas of the spinal cord (see Figure 1.3A). C fibre nociceptor terminals are located in the most dorsal regions, lamina I and outer lamina II, while Aδ nociceptors terminate in lamina V[21] and Aβ LTMRs terminate in laminae III to VI[19,22]. In contrast, proprioceptors form synapses with motor neurons in lamina IX, or with interneurons in the intermediate zone and ventral spinal cord[23]. Excitatory and inhibitory interneurons exist throughout the spinal cord, forming microcircuits that process incoming signals and can mediate outputs onto ascending pathways[22,24,25]. The ascending spinothalamic tracts involved in nociception are comprised of spinal projection neurons originating from lamina I and V, branching into brainstem regions such as the parabrachial nucleus (PBN), periaqueductal gray (PAG) and rostral ventromedial medulla (RVM), before finally terminating within thalamic nuclei[21,26].

Neurons projecting from the PBN to the central and basolateral amygdala are important for generating negative emotions such as fear and intense discomfort[26,27]. Medial and posterior thalamic nuclei make connections with subcortical and cortical structures, engaging areas involved in autonomic regulation, memory and decision-making. Projections from the lateral thalamic nuclei to the somatosensory cortex discern the location and physical intensity of the stimulus. Concerted activity in these regions (see Figure 1.3B) is critical for forming an association between the incoming nociceptive signal and the

painful experience, so that the individual is motivated to avoid the same situation in the future[26,28]. Brain activity can also activate descending pathways which converge on the PAG, projecting onwards to the RVM and then spinal circuits, modulating their neuronal activity as to facilitate or inhibit incoming nociceptive signals[26].

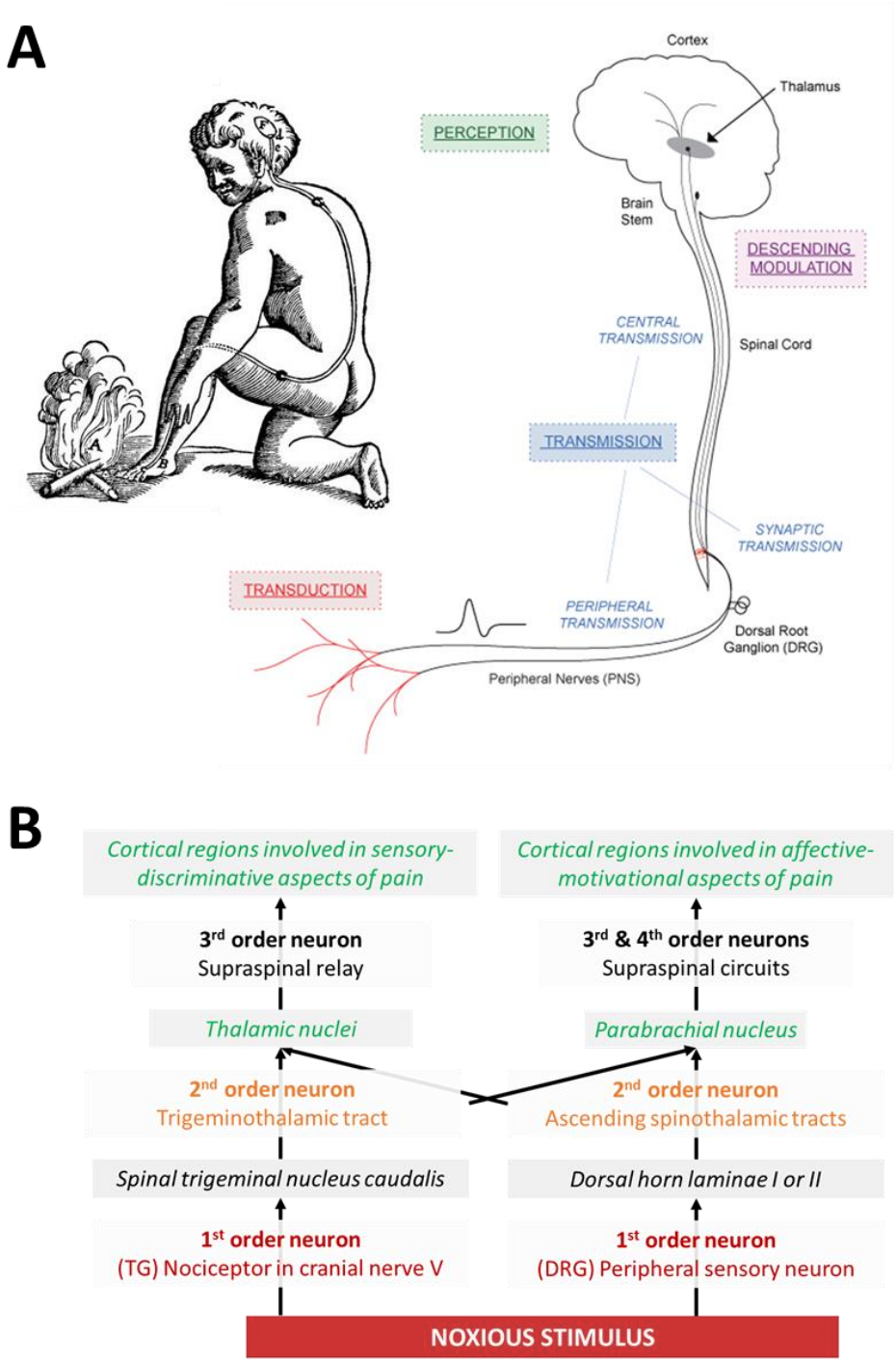

Figure 1.1: Organisation of the Nociceptive System
(A) Overview of major anatomical and functional components involved in nociception and pain perception; (B) Neural pathways and nuclei mediating nociceptive transmission from the trigeminal ganglia (TG) and dorsal root ganglia (DRG). *Adapted from Descartes, Traite de l'homme (1664); University of Wisconsin, Pain Pathway, (2010)*

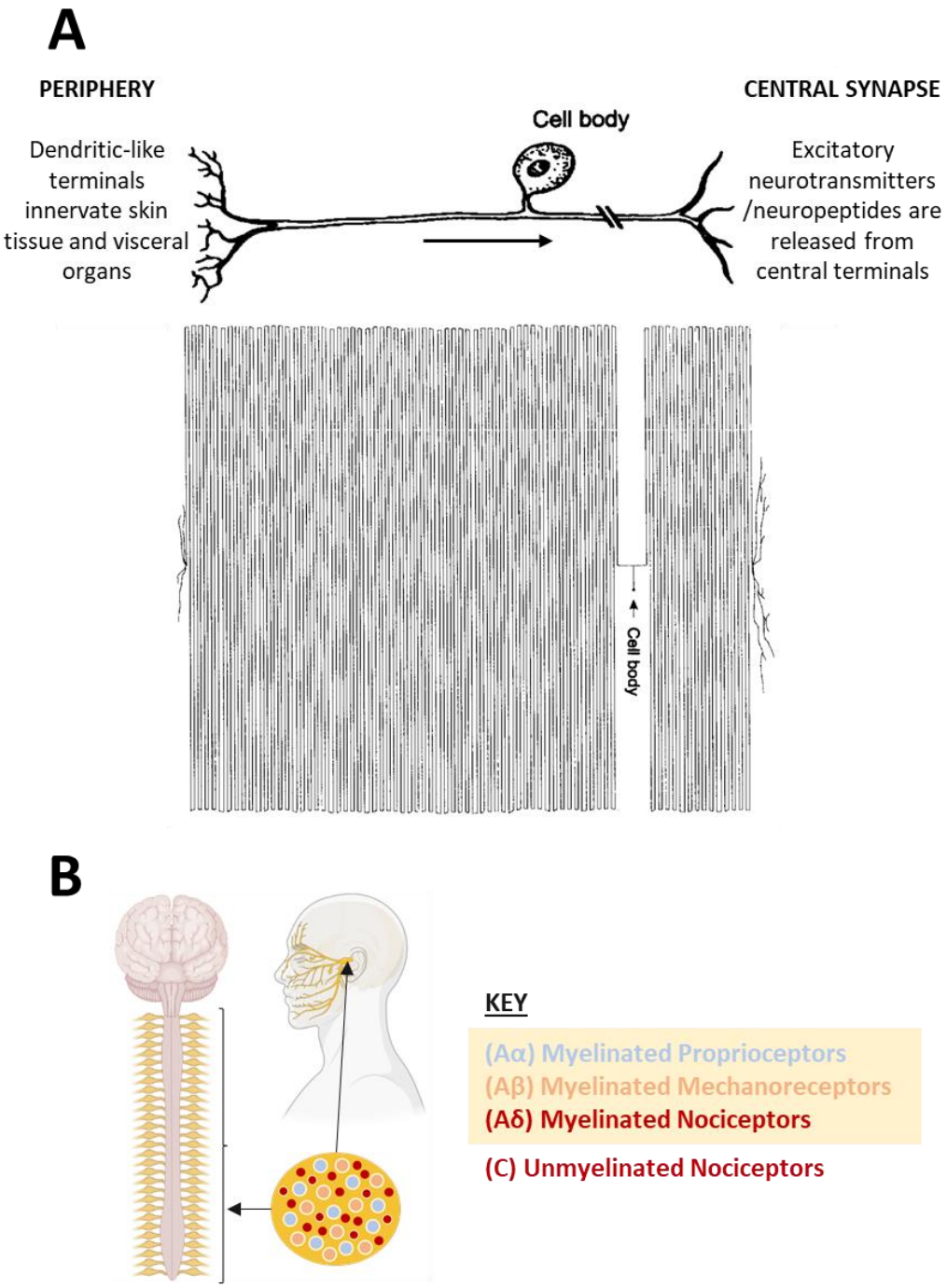

Figure 1.2: Morphological and Functional Classification of Somatosensory Neurons
(A) Somatosensory neurons exhibit pseudounipolar morphology, electrical transmission directed from peripheral to central terminals which synapse in the dorsal horn. (B) Somatosensory neurons can be divided into broad functional classes residing in the TG and DRG. *Figure created with Biorender.com and adapted from (1999) Devor.*

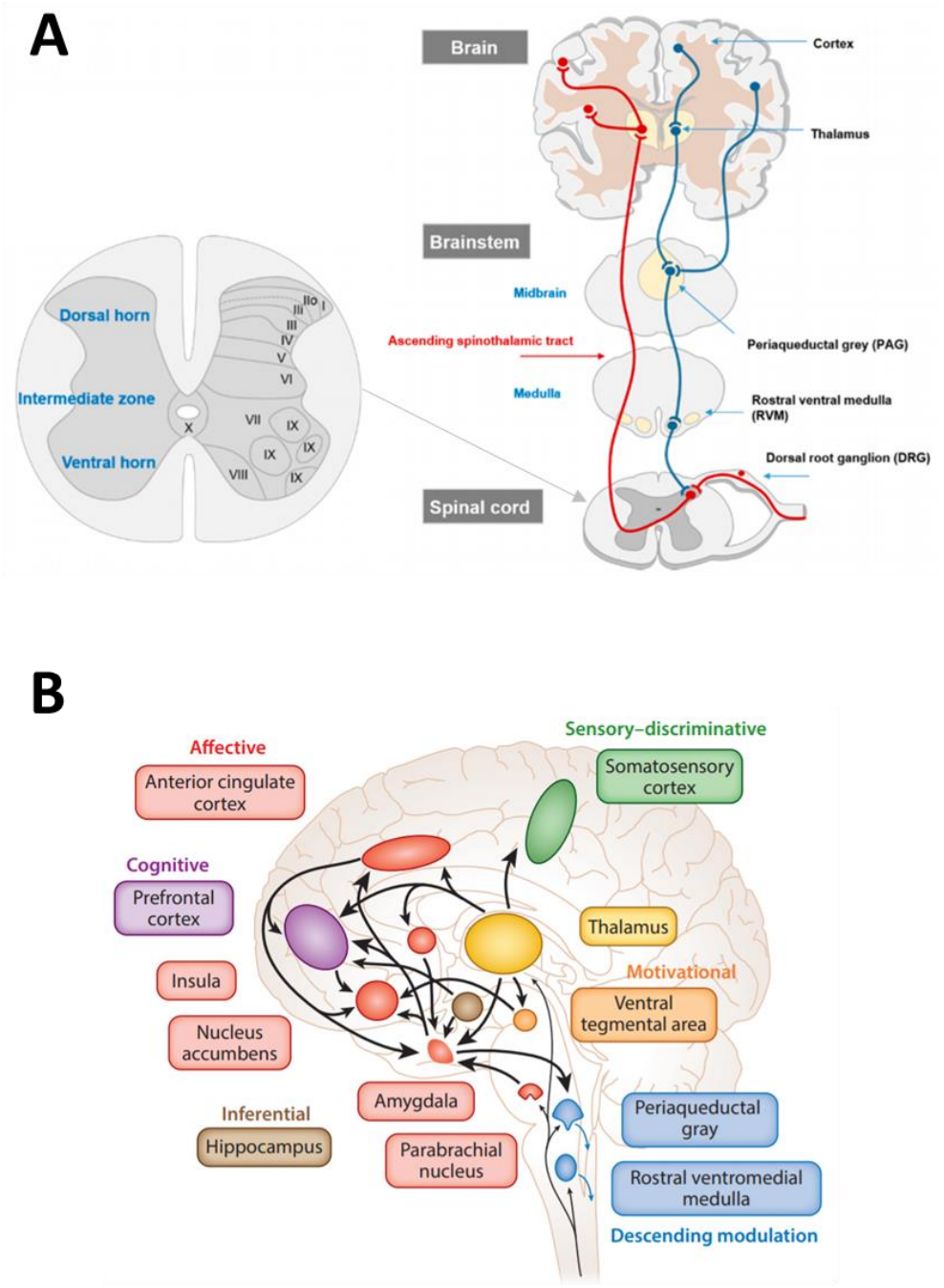

Figure 1.3: Spinal and Supraspinal Regions Involved in Pain Processing
(A) Laminar organisation of the spinal cord, plus important branchpoints of ascending and descending spinal modulatory pathways. (B) Major brainstem and cortical nuclei involved in central processing of various dimensions of pain. A*dapted from (2019) Corder.*

1.3 – Molecular Classification and Physiology of Nociceptors

In addition to the neurotrophin receptors TrkA-C, other neurochemical markers have been used in an attempt to isolate nociceptor subgroups that are associated with specific sensory modalities or chronic pain pathologies. The most common division is into peptidergic nociceptors positive for neuropeptides calcitonin gene-related peptide (CGRP) or substance P, versus non-peptidergic nociceptors positive for isolectin-B4 (IB4) or purinergic receptor P2X3R[29–31]. Other prominent markers include neurotrophin receptor Ret and enzyme tyrosine hydroxylase (TH)[32,33]. While non-peptidergic and peptidergic nociceptors can be separated in mice by their distinct patterns of marker expression and spinal laminar termination, comparative studies of rat and human sensory ganglia show considerable overlap of expression of neuropeptides with IB4 or P2X3R, cautioning the generalisation of nociceptor classes between species[34,35].

Nevertheless, recent single-cell transcriptome analyses in mice[36–38] and macaques[39] have revealed strong conservation of sensory neuron subtypes across species. When multiple markers and their mutually exclusive enrichment are taken into consideration, clustering methods defined 9-18 somatosensory subtypes based on unique RNA expression patterns (see Figure 1.4). In addition to TrkA-C divisions conforming to historical classification schemes, proprioceptors and various LTMR subgroups could be highlighted by the expression of neurofilament heavy polypeptide, plus calcium-binding proteins parvalbumin or calbindin. Polymodal nociceptors were consistently identified amongst the non-peptidergic groups, responsive to noxious mechanical, thermal and chemical stimuli as well as pruritogens (itch-generating stimuli). Peptidergic populations seemed largely comprised of Aδ mechanoreceptors and mechano-heat responsive C fibres. Two further functionally specialised classes that were consistently identified were the C-LTMRs involved in pleasant touch (unmyelinated, TrkA/B/C-negative, TH-positive) and cold-sensitive thermoreceptors enriched for signal transduction molecule TRPM8.

Responsiveness to a particular stimulus modality is defined by the expression of established transduction molecules. The detection of thermal stimuli is mediated by members of the transient receptor potential (TRP) channel family, tuned to respond to discrete temperature ranges within physiologically safe limits (15°C to 42°C) and dangerously cold or hot extremes[40]. Several TRP channels are also activated by chemical irritants, acidic pH, inflammatory mediators, as well as compounds associated with spicy-hot or ice-cool sensations such as capsaicin from chilli peppers or menthol from peppermint. Early psychophysical studies in humans demonstrated that intradermal injection of capsaicin or topical application of menthol causes nociceptive C fibres to fire, skin reddening due to

vasodilation and increased sensitivity to thermal and mechanical stimuli; all correlating with painful burning and/or cool sensations as described by subjects[41–44]. Capsaicin and menthol were later discovered to activate TRPV1 and TRPM8 cation channels respectively, depolarising the membrane potential closer to the action potential threshold[45,46].

The detection of harmful mechanical forces is not as well characterised. TRPA1 has been implicated in sensing noxious mechanical stimuli and mechanical hypersensitivity, although it may act as an integrator of noxious signals across multiple stimulus modalities[47]. The mechanosensor Piezo2 is responsive to low-threshold mechanical stimuli, which are typically perceived as innocuous when activated in cutaneous sensory neurons but painful when activated in corneal C fibres. Furthermore, the expression of Piezo2 in Aδ nociceptors that respond to high-threshold mechanical stimuli suggests it could be an important target for mechanical pain in certain physiological contexts[48,49]. Several background potassium-permeable channels may also be indirectly involved in mechanical pain perception, as their deletion results in hypersensitivity to mechanical stimuli[50–52]. Interestingly, pruriception (the sensation of itch) is exclusively encoded by a subset of polymodal Aδ and C fibres that express pruritogen-sensitive G protein-coupled receptors (GPCRs). Crucially, the combined function of metabotropic signalling via these GPCRs, and cation conductance via TRPV1 and TRPA1, is required to transmit itch sensations[53,54].

The generation of action potentials at the periphery, and their propagation towards the central synapse, is dependent on the function of voltage-gated sodium channels (VGSCs); predominantly on the co-ordinated activity of Nav1.7, Nav1.8 and Nav1.9[55] which are preferentially enriched in nociceptive neurons. Nav1.9 channels exhibit very slow activation and inactivation at hyperpolarised voltages, producing a persistent current that contributes to maintaining the resting membrane potential[56]. Nav1.7 is considered the “molecular gatekeeper of pain”[57]; small, slow receptor potentials produced by signal transducers activate Nav1.7, and the subsequent inward Na^+ current boosts the primary signal, further depolarising the neuron in order to activate Nav1.8. Nav1.8 activation produces a steep inward Na^+ current that forms the upstroke of the action potential in DRG neurons. During this period of membrane depolarisation, Nav1.8 channels are resistant to inactivation and recover quickly once inactivated, therefore able to support repetitive firing when nociceptor stimulation is prolonged[58,59]. Other VGSCs contributing to acute and chronic pain include Nav1.3, associated with particular pathophysiological pain states, while Nav1.1 and Nav1.6 are involved in visceral nociception; these are reviewed in detail elsewhere[60,61].

At the nociceptor central terminals, chemical transmission across the synapse is required to transfer input signals onto spinal circuitry. Action potentials reaching the presynaptic terminals depolarise the membrane sufficiently to activate N-type voltage-gated calcium channels (VGCCs). Elevated calcium ion concentration in this region, via VGCC conductance and/or intracellular signalling, triggers the release of excitatory molecules glutamate, CGRP and substance P[62]. Glutamate binding to ionotropic NMDA and AMPA receptors produces excitatory postsynaptic potentials in spinal neurons, while activation of glutamate-sensitive metabotropic receptors mGluR1 to mGluR8 is associated with maladaptive pain states[63]. CGRP and substance P act on postsynaptic neurokinin-1 and CGRP receptors, which prolongs membrane depolarisation of spinal neurons to facilitate NMDA receptor activation[64]. Neuropeptide receptors are also present on postcapillary blood vessels of the skin; neuropeptide release from nociceptor peripheral branches contributes to neurogenic inflammation characterised by the "wheal and flare" response – increased vascular permeability leading to plasma leakage and swelling, and vasodilation causing the reddening of skin surrounding the injured area[65].

The primary goal of nociceptor activation is to bring attention to a potential physical threat, and so polymodal nociceptors do not need to immediately distinguish the particular type of stimuli present. However, it is intriguing that pruriception and nociception are mediated by a shared set of sensory neurons since the sensations of pain and itch are quite distinct, as are their behavioural responses – common measures in mouse studies include flinching, withdrawal or wiping in response to pain versus scratching in response to itch. A recent study employed optogenetic and chemogenetic strategies to selectively activate nociceptive and pruriceptive signal transducers in the polymodal MrgprA3-positive population. Their results indicate that fast ionotropic signalling and slow metabotropic signalling via GPCRs recruit different peptide signalling pathways in spinal circuits, resulting in pain or itch behaviours respectively[66]. Whether this is due to differences in electrical firing patterns of the primary sensory neuron, or which central synapses are activated, remains to be investigated.

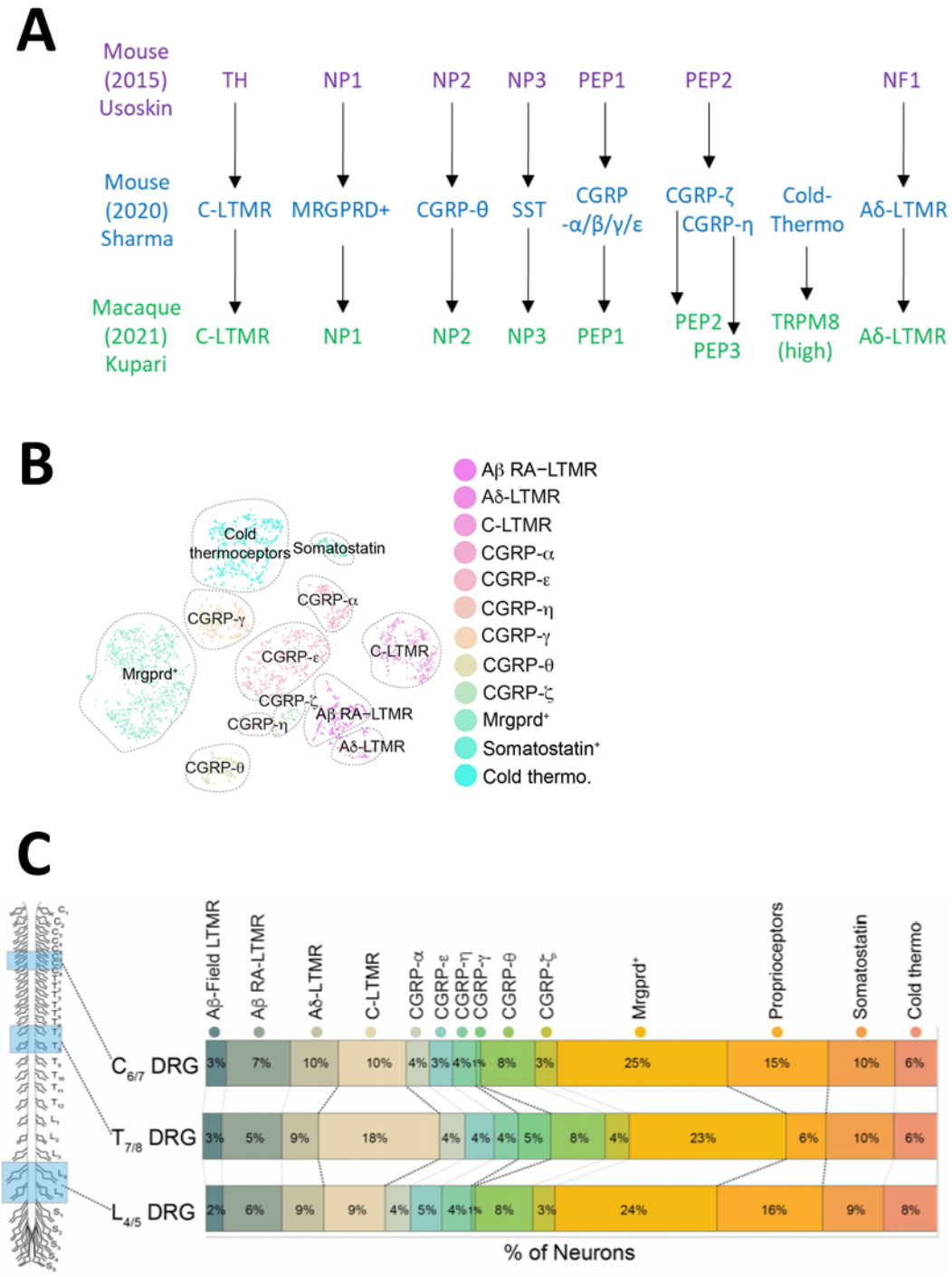

Figure 1.4: Molecular Classification of Somatosensory Neurons
(A) Transcriptomics analysis of DRG from mice and macaque identified up to 18 subtypes of somatosensory neuron, of which 9 exhibit cellular and molecular properties of nociceptors. (B) The breadth of DRG neuronal subtypes are also present in TG, excluding proprioceptors which are clustered in the mesencephalic trigeminal nucleus. (C) The proportion of neuronal subtypes present in DRG is similar across axial levels of the trunk. A*dapted from (2020) Sharma.*

1.4 – Pathophysiology of Chronic Pain

When we acquire an injury, two significant adjustments in sensory coding occur to indicate the area is vulnerable. If the wound is exposed to noxious stimuli again, the pain felt is heightened compared to an identical exposure on an undamaged area. In addition, light touch or mild warming around the site of injury can evoke pain[67]. The corresponding psychophysical phenomena are hyperalgesia, "increased pain from a stimulus that normally provokes pain", and allodynia, "pain due to a stimulus that does not normally provoke pain"[68]. Cellular correlates of hyperalgesia include lowering the action potential threshold and enhancing neuronal excitability, both increasing the likelihood and frequency of nociceptor firing. This is driven by inflammatory mediators released from damaged tissue; they activate specific receptors on nociceptors, which trigger short-term post-translational modifications and longer-term transcriptional changes of key excitability molecules such as ion channels[69]. Tactile allodynia on the other hand requires the integration of low-threshold mechanical input into nociceptive circuits; this is dependent on activation of TrkB-positive Aβ fibres[70,71], but how they gain access to nociceptive pathways is not clear.

In the acute injury setting, a vast array of chemical mediators are released from damaged keratinocytes and endothelial cells, as well as from immune cells that invade the injury site. This "inflammatory soup" consists of complex to simple algogenic molecules such as nerve growth factor (NGF), bradykinin, histamine, cytokines, prostaglandins, proteases, lipids, ATP and protons[72]. The cognate receptors for some of these molecules are constitutively expressed on nociceptors – e.g., purinergic 'P2X' receptors activated by ATP, or histamine and bradykinin-specific receptors. Metabotropic receptors initiate intracellular signalling cascades that activate local kinases and transcriptional effector molecules, while ionotropic receptor currents contribute to membrane depolarisation, both promoting pro-nociceptive signal transmission[72]. Hyperalgesia from acute injury is short-lived and subsides once the tissue is restored, reflecting the typically reversible nature of these molecular changes.

Acute nociception is protective, but when pain persists after an injury has healed it has no adaptive purpose. This transition from acute to chronic pain is driven by long-term sensitisation of nociceptors at the peripheral level, and of pro-nociceptive circuits in the CNS. Peripheral sensitisation is a normal response to acute tissue trauma but can be prolonged due to chronic inflammation[73,74]. Central sensitisation arises from changes in synaptic transmission in the spinal cord and brain, such that pro-nociceptive signalling is favoured over anti-nociceptive mechanisms[72,75]. This is dependent on sustained input from peripheral nociceptors that strengthen excitatory synapses, particularly the

potentiating influence of brain-derived neurotrophic factor (BDNF). BDNF promotes the recruitment of Ca^{2+}-permeable AMPA receptors on post-synaptic spinal neurons, leading to increased Ca^{2+} influx that enhances post-synaptic excitatory potentials and activates Ca^{2+}-dependent pro-excitatory effector pathways[76]. BDNF can also dampen inhibitory transmission in the spinal cord; as a result, the normal levels of activity of descending inhibitory pathways are no longer sufficient to suppress pro-nociceptive transmission[77–79].

Historically, the origin of chronic pain was classified as either chronic inflammatory pain or neuropathic pain. Chronic inflammation initiates positive feedback loops that maintain the long-term hyperexcitability of nociceptors through peripheral sensitisation, as well as stimulating the production of sensitising agents from non-neuronal cells. For example, substance P triggers histamine release from degranulated mast cells, while ATP triggers BDNF and cytokine release from activated microglia[72]. In contrast, neuropathic pain arises from a lesion or disease of the somatosensory nervous system itself, resulting in a combination of sensory loss and positive sensory signs such as spontaneous pain and paraesthesias. Associated pathologies include diabetic neuropathy, spinal cord injury and multiple sclerosis[69]. There is some overlap in molecular drivers of inflammatory and neuropathic pain, as the local increase in cytokines and neurotrophins contributing to regenerative responses (such as NGF and TNFα) also activate pro-inflammatory pathways[80,81]. However, neuropathic pain is marked by spontaneous electrical activity far from the peripheral terminals where action potentials are normally generated[82]; this adaptation is mediated by changes in ion channel expression that promote hyperexcitability. Two-pore domain potassium channels such as TRESK are downregulated resulting in a stable membrane depolarisation, while persistent Na^{+} influx via upregulated Nav1.3, Nav1.6 and Nav1.8 support ectopic spike generation[75].

Clinical definitions of chronic pain focus on severe pain that negatively impacts quality of life and that continues longer than would be expected for tissue damage from some triggering event to have resolved. However, chronic pain can also arise independently of an injury or primary condition. Recent developments in the International Classification of Diseases (ICD-11) categorize different types of chronic pain in a way that aims to be more clinically meaningful, and useful for informing research and health policy[5]. Chronic primary pain includes conditions where plasticity of the nociceptive system is thought to be the major driving factor – e.g., in fibromyalgia or complex regional pain syndrome. In contrast, chronic secondary pain is driven by a primary condition whose resolution should provide pain relief; this classification has six subgroups:

1) Chronic cancer-related pain (caused by the cancer itself or chemotherapy/radiotherapy)
2) Chronic post-surgical or post-traumatic pain
3) Chronic neuropathic pain
4) Chronic secondary headache or orofacial pain (such as dental pain or trigeminal neuralgia)
5) Chronic secondary visceral pain (caused by mechanical, vascular or inflammatory factors)
6) Chronic secondary musculoskeletal pain (caused by disease processes that directly affect bone and muscle)

Chronic pain is much more diverse than originally conceived, and so using this nomenclature can stratify patients with similar pathophysiology and shared experiences. This should help to home in on key molecular drivers of different types of chronic pain, and to identify patterns in effective pain management that best serve these distinct patient groups.

1.5 – Pharmacotherapy Options for Chronic Pain

While pain from acute injury or disease is temporary and treatable, chronic pain is much more difficult to manage. Several analgesic classes exist which are successful in relieving acute pain (summarised in Table 1.1), but long-term use for chronic pain is usually only effective in some individuals[83] and even then can be hampered by the development of adverse side effects[84]. If pain relief is inadequate with medical interventions, patients may be referred onto pain management programmes that focus on rehabilitation, providing psychological and practical tools for living well with pain[85]; however consistent infrastructure and staffing of these services is lacking[7].

However, certain drug classes demonstrate high efficacy for select chronic pain conditions. For adults with neuropathic pain, clinical guidelines in the UK recommend a choice from amitriptyline, duloxetine, gabapentin or pregabalin[86]. Switching within this group is encouraged if pain is not sufficiently alleviated or the drug cannot be tolerated at any of the titrated doses[87]. Further guidance proposed by international clinical consortia suggest prioritising specific treatments in the context of spinal cord injury[88], and present evidence on more specialist interventions to be considered if first line treatments are ineffective[89].

Table 1.1: Summary of analgesic drug classes
Adapted from (2017) British Medical Association[84]

ANALGESIC CLASSES	EXAMPLES
Simple analgesics	Paracetamol
Nonsteroidal anti-inflammatory drugs (NSAIDs)	Aspirin, Ibuprofen, Diclofenac, Celecoxib
Anti-epileptic drugs	Carbamazepine, Pregabalin, Gabapentin
Tri-cyclic antidepressants (TCAs)	Amitryptiline, Nortriptyline, Imipramine
Serotonin-noradrenaline reuptake inhibitors (SNRIs)	Duloxetine, Venlafaxine
Local anaesthetics	Lidocaine, Bupivacaine
Weak opioids	Codeine, Dihydrocodeine
Strong opioids	Morphine, Buprenorphine, Fentanyl, Methadone, Oxycodone, Tramadol
Compound analgesics	Co-codamol, co-codaprin

Analgesics available over the counter such as paracetamol (also known as acetaminophen), aspirin and ibuprofen are usually sufficient for mild to moderate acute pain. Nonsteroidal anti-inflammatory drugs (NSAIDs) inhibit the activity of cyclo-oxygenase enzymes 1 and 2 (COX-1 and COX-2). The latter is upregulated during inflammation to generate prostanoids – key agents in peripheral sensitisation of nociceptors. However, COX enzymes also have homeostatic roles in platelet activation, renal control

of blood pressure and mucus secretion in the gastrointestinal tract; as a result, continuous high doses risk provoking cardiovascular and gastrointestinal complications[90].

The mechanism of action behind paracetamol is more complex, acting at multiple levels of the nociceptive system. In the ventrolateral periaqueductal gray (vlPAG), fatty acid amide hydrolase (FAAH) conjugates arachidonic acid onto paracetamol to generate the metabolite AM404[91]. AM404 acts on both TRPV1 and CB1 receptors to promote the activation of descending inhibitory pathways[92], as well as interfering with the reuptake of anandamide, an endocannabinoid which has anti-anxiolytic properties[91]. AM404 has also been shown to inhibit prostaglandin synthesis in activated microglia[93], while in the periphery, AM404 action on TRPV1 receptors causes conduction block in nociceptors to prevent synaptic transmission[94]. Paracetamol can be safely combined with opioids or other analgesic classes in a multimodal approach to enhance pain relief and minimize side effects from the stronger agents.

Anti-epileptic drugs, tri-cyclic antidepressants (TCAs) and serotonin-noradrenaline reuptake inhibitors (SNRIs) are recommended as first line treatments for neuropathic pain[95], but are of limited benefit for other chronic pain conditions[84]. Sustained, low-dose administration of TCAs and SNRIs produce analgesia without affecting susceptibility to depression; pain relief appears to be mediated by the noradrenergic component of the descending inhibitory pathway, but may be modulated by serotonergic signalling[96]. In contrast, gabapentin and pregabalin exert their analgesic effects in a peripherally biased manner. By inhibiting the forward trafficking of the α2δ-1 subunit of VGCCs in injured DRG neurons, they limit excitatory neurotransmission onto the spinal cord[97]. In terms of common chronic pain disorders, the anticonvulsant carbamazepine is only recommended for trigeminal neuralgia in the UK[86]; however, it is also an effective treatment in some patients with rare GOF (gain-of-function) *SCN9A* and *SCN10A* mutations that cause extreme pain[98,99]. In both cases, carbamazepine inhibits VGSC activity to reduce the hyperexcitability of peripheral nociceptors. Local anaesthetics similarly inhibit VGSC activity, although their action on a multitude of ionotropic and metabotropic receptors contributes to analgesia[100]. Applied topically, they are used to relieve dental pain and to numb skin before surgical procedures, while acute and chronic post-surgical pain can be alleviated by intravenous lidocaine.

Opioids originated from alkaloids of the opium poppy, including natural derivatives codeine and morphine, to synthetic compounds such as oxycodone and fentanyl with optimised binding affinity and agonist action on opioid receptors; they range in strength, calculated as potency relative to oral

morphine[84]. Exogenous opioids and endogenous opioid peptides act on the four opioid receptors – mu, delta, kappa and nociceptin (MOR, DOR, KOR, NOR). All four GPCRs exhibit distinct levels of expression on nociceptors, in the spinal cord and in various brain regions, but all activate inhibitory signalling cascades to restrain neural excitation. At the peripheral level, inhibiting VGCCs impedes the release of excitatory neurotransmitters and neuropeptides. Opioid receptor signalling also activates G protein-gated inwardly rectifying potassium (GIRK) channels on postsynaptic spinal neurons, hyperpolarising the membrane potential to suppress excitatory inputs. MOR activation in the vlPAG and RVM drives the inhibition of dorsal horn activity via descending pathways, but all opioid receptors are involved to varying degrees in the central processing of nociceptive inputs, modulating sensory, affective, cognitive and motivational aspects of pain[101].

Opioid use is well established in managing acute pain following surgery or significant tissue trauma, or for severe cancer pain in palliative care[84]. However, marketing of new synthetic opioids in the 1990s downplayed their addictive potential and encouraged the long-term prescription of opioids to address chronic pain, advocating stepwise increases in opioid strength as pain intensity worsened[102]. This was in line with the World Health Organisation's analgesic ladder, a tool validated for the treatment of short-lived cancer pain, but the recommendations were inappropriate for the persistent and unpredictable nature of chronic pain[103]. Nevertheless, low doses of opioids used intermittently can provide considerable pain relief for a small proportion of chronic pain patients[104,105]. Risk factors must be thoroughly investigated before initiating prescriptions, and patients should be regularly monitored to recognise any potential for significant adverse events such as respiratory depression, endocrine abnormalities or hyperalgesia[105]. If necessary, discontinuation of opioid treatment must be done carefully to prevent further physical and psychological harm[106].

Results from the 2017 Public Health England survey indicate chronic pain affects 1 in 3 adults[107]. The annual economic burden, in terms of additional healthcare requirements and lost labour productivity, costs the UK at least £10 billion when considering back pain alone[108]. Given the limited efficacy and safety concerns around using available analgesics for prolonged periods, there is clearly an enormous unmet need for novel treatments that can specifically target chronic pain. Developing such analgesics would have a significant positive impact at the individual and societal level.

1.6 – Congenital Insensitivity to Pain (CIP)

Despite its unpleasantness, being born unable to feel pain poses a significant problem. Without this strongly aversive sensation, these individuals cannot easily differentiate harmful from harmless stimuli and are not motivated to adapt dangerous behaviour, even at the risk of tissue damage. As a result, they are susceptible to severe injuries from unintentional self-mutilation, burns and bone breaks, unless they are taught to recognise harmful situations through other contextual clues. An early diagnosis is key to supporting families manage the physical, behavioural and social aspects of this condition[109]. The study of affected cases has also provided valuable evidence of cellular mechanisms that are crucial for pain perception in humans, and therefore could be appealing targets for analgesic drug development[110,111].

The genome is a fundamental determinant of how effectively our molecular machinery operates, and consequently the performance of physiological systems. Human mutations that alter the activity of crucial proteins will cause cellular and system dysfunction, manifesting as clinically recognisable disease. Several genes cause insensitivity to pain (see Table 1.2), with a range of other clinical features depending on the function of the affected protein in other tissues. The cellular basis of painlessness can be categorised into one of four main mechanisms:

1) Degeneration of nociceptors causing progressive loss of pain sensation
2) Faults in electrochemical transmission from intact nociceptors onto spinal neurons
3) Defects in neurodevelopment of nociceptors
4) Enhancement of endogenous analgesic signalling

Mutations that cause postnatal degeneration of nociceptors include autosomal recessive mutations in *WNK1*, *FAM134B*, *KIF1A*, *IKBKAP* and *MPV17*, or autosomal dominant mutations in *SPTCL1*, *SPTCL2* and *ATL1*. The age at onset of these conditions varies from childhood to later decades in life depending on the rate of neurodegeneration. Painlessness is often accompanied by major autonomic and motor pathologies as well as generalised somatosensory neuropathy. Given the breadth and severity of these phenotypes, as well as the long-term effects on cellular integrity, it would be dangerous to attempt modulating their function simply to reduce pain. More information regarding the clinical presentation and reported variants associated with each disease can be accessed using the OMIM entry codes at https://omim.org/.

All conditions from groups 2-4 are apparent from birth and so can be classed under the umbrella of congenital insensitivity to pain (CIP). In the second group of painlessness disorders, nociceptors are intact but key components mediating neuronal excitability and/or synaptic transmission are faulty. In contrast, the third group is characterised by defects in differentiation and trophic signalling that stop nociceptors forming at all. In both cases, the propagation of input signals into CNS circuits is disrupted therefore preventing the perception of pain. The last group was recognised very recently through a single family with mutations in the pseudogene *FAAH-OUT* which enhance endocannabinoid signalling, relieving pain and anxiety[112]. The relationship between *SCN9A* knockout and endogenous opioid signalling suggests it may also belong to this group[113].

The clinical presentation, functional consequences of CIP variants and analgesic potential of CIP genes are reviewed briefly in the following text. The involvement of *SCN9A* and *PRDM12* mutations in somatosensory disorders are expanded upon in Chapters 2 and 4.

Bi-allelic loss-of-function (LOF) mutations in *SCN9A* is one of the most common causes of CIP[109]. Apart from the expected injuries due to lack of nociception, *SCN9A*-CIP patients are relatively normal with the only additional features being impaired smell and temperature sensation. As a result, the encoded VGSC Nav1.7 has drawn much interest from the pharmaceutical industry due to the inference that a drug inhibiting Nav1.7 activity could provide robust pain relief, with anosmia as the only side effect. Voltage-clamp studies have shown that CIP patient mutations reduce sodium ion conductance by 50-100% compared to wild-type channels. Initially this was thought to result in hypoexcitability of nociceptors, given the vast evidence base that gain-of-function mutations cause hyperexcitability and episodes of extreme pain. Indeed, neurographic recordings from a series of *SCN9A*-CIP patients revealed a complete absence of nociceptor conduction profiles.

Furthermore, iPSC-derived nociceptors from these patients required 1.5-fold higher current stimulus to initiate an action potential and exhibited much lower firing frequency in response to sustained depolarisation[114]. However, local neurogenic inflammation is intact in all *SCN9A*-CIP patients, suggesting there is at least sufficient local excitability to stimulate branches innervating vascular tissue. Targeting Nav1.7 on the central axon appears to be critical to reduce the release of excitatory neurotransmitters at the central synapse and prevent the transmission of nociceptive signals; this approach may be enhanced in combination with modulators of opioid signalling[113,115].

Table 1.2: Genetic Disorders of Painlessness
Adapted from (2020) Schon et al.[109]*, (2015) Nahorski et al.*[110] *and (2020) Drissi et al.*[111]
HSAN: Hereditary Sensory and Autonomic Neuropathy; **HSN:** Hereditary Sensory Neuropathy; **ER:** Endoplasmic reticulum; **AR:** Autosomal Recessive; **AD:** Autosomal Dominant

RECOGNISED PHENOTYPE	OMIM CODE	GENE	PROTEIN FUNCTION	MODE OF INHERITANCE	PREVALENCE*	PREDOMINANT MECHANISM
HSAN1A	162400	*SPTLC1*	Anabolic enzyme	AD	Common	Degeneration of nociceptors
HSAN1C	613640	*SPTLC2*	Anabolic enzyme	AD	Rare	
HSN1D	613708	*ATL1*	ER membrane regulator	AD	Very rare	
HSAN2A	201300	*WNK1*	Protein kinase	AR	Common	
HSAN2B	613115	*FAM134B*	ER membrane regulator	AR	Very rare	
HSN2C	614213	*KIF1A*	Microtubule motor	AR	Very rare	
HSAN3	223900	*IKBKAP*	Transcriptional regulator	AR	Common	
Navajo neurohepatopathy	256810	*MPV17*	Mitochondrial ion channel	AR	Common	
Channelopathy-associated insensitivity to pain	243000	*SCN9A*	Voltage-gated sodium channel	AR	Common	Faults in nociceptor transmission
HSAN7	615548	*SCN11A*	Voltage-gated sodium channel	AD	Very rare	
Marsili syndrome	147430	*ZFHX2*	Transcriptional regulator	AD	Single kindred	
HSAN4	256800	*NTRK1*	Neurotrophin receptor	AR	Common	Defects in nociceptor development
HSAN5	608654	*NGFβ*	Neurotrophin	AR	Very rare	
HSAN8	616488	*PRDM12*	Transcriptional regulator	AR	Rare	
Pain insensitivity	601273	*CLTCL1*	Clathrin heavy chain	AR	Single kindred	
Pain insensitivity	618377	*FAAH-OUT*	Catabolic enzyme	AD	Single kindred	Enhanced circulation of endocannabinoids

*****Common = >20 cases; Rare = 5-20 families; Very rare = <5 families; Single kindred = one family only

Both *SCN11A*-CIP and *ZFHX2*-CIP patients possess typical painless injuries such as fractures and cutaneous wounds, while proprioception and detection of low-threshold thermal and mechanical stimuli are unaffected, as are sense of smell and cognitive development. Skin and nerve biopsies have shown no evidence of neuropathy in either condition[116,117]. Gastrointestinal dysfunction has been noted across all four reported *SCN11A*-CIP cases, but the presence of other distinguishing features such as intense itch, increased sweating and motor neuron deficits varies[109]. In the single *ZFHX2*-CIP family, all six affected members share high thresholds to noxious thermal, mechanical and chemical stimuli. However, painlessness is not universal; pain from headaches and childbirth are perceived

intensely, and intradermal injection of capsaicin produced transient pain. The *ZFHX2*-CIP mutation may impact on some autonomic functions – most cases have deficiencies in thermoregulation and sweating, while strong odours and pain sometimes trigger fainting or vomiting[117].

The dominant missense mutations in *SCN11A* have been shown to cause GOF at the molecular level[116,118], changing the voltage-dependence of activation of the encoded channel Nav1.9. This alteration forces Nav1.9 to generate a persistent window current that depolarises the resting membrane potential, so much so that it prevents other Nav channels from activating and contributing to action potentials, therefore producing LOF at the cellular level. The dominant missense mutation in *ZFHX2* is also associated with reduced nociceptor responsiveness, demonstrated through the behaviour of transgenic mice in pain assays and calcium imaging of cultured DRG neurons in response to capsaicin exposure[117]. Nevertheless, given the incomplete painlessness observed in *ZFHX2*-CIP cases and the gastrointestinal problems of *SCN11A*-CIP, it is unlikely either protein would be pursued for analgesic drug development.

Genes that cause developmental CIP are crucial regulators of neurotrophic signalling during the embryonic specification and growth of nociceptors. *NTRK1* and *NGFβ* encode the tyrosine kinase receptor TrkA and its growth factor ligand NGF respectively, both of which must be functional to promote the survival and peripheral axon guidance of nociceptors during embryonic development[119]. *NGFβ* mutations that disrupt the cleavage of pro-NGF into its mature form prevent NGF from activating TrkA receptors[120,121]. *NTRK1* mutations that diminish TrkA plasma membrane expression, or its ability to activate the intracellular PLCγ signalling pathway via receptor phosphorylation, ultimately lead to reduced neurite outgrowth[122]. PRDM12 is a transcription factor that controls the initiation and maintenance of TrkA expression during the critical period of neural crest cell differentiation, so LOF mutations in both alleles leads to a complete absence of the nociceptor lineage while other somatosensory neurons are unaffected[123–125]. *CLTCL1* encodes the clathrin heavy chain protein CHC22, which appears to control the developmental timing of trophic neuropeptide release (including BDNF, VGF and NPY) until sensory neuron precursors are appropriately positioned to integrate other differentiation cues[126,127].

There is significant overlap in the clinical presentation of these conditions with some distinguishing features[109]. Intellectual disability to varying degrees is common in patients with *NGFβ*, *NTRK1* and *CLTCL1* mutations, likely due to the dependence of certain CNS neurons on NGF and BDNF signalling[126,128]. In contrast, *PRDM12* expression is limited to nociceptors so cognitive development of

these CIP patients is not impaired. Motor function, muscle strength and proprioception are normal across all four developmental CIP phenotypes. However, innocuous temperature sensation is sometimes reduced in *NGFβ*, *NTRK1* and *PRDM12* CIP cases, while lack of responsiveness to light touch is unique to *CLTCL1*-CIP. Another interesting aspect of *NGFβ*, *NTRK1* and *PRDM12* CIP patients is the increased susceptibility to S*taphylococcus aureus* infections, due to the role of NGF-TrkA signalling in the activation of macrophages and recruitment of neutrophils[129]. PRDM12 is not a universal regulator of TrkA expression, as the receptor is still expressed in the sympathetic ganglia of PRDM12-KO mice despite complete absence in DRG[124,125]. On the other hand, the involvement of PRDM12 in regulating immune cell expression of TrkA is yet to be ruled out.

Targeting these genes to permanently remove all nociceptors is clearly inappropriate as well as impossible outside of the embryonic window. However, both NGF and BDNF have been implicated postnatally in peripheral and central sensitisation. NGF released from damaged tissue binds to TrkA on nociceptors, activating intracellular signalling cascades that regulate post-translational modifications of local proteins and enhance the excitability of the peripheral terminal. Signalling endosomes that internalise the NGF-TrkA complex support long-term hyperexcitability by upregulating the transcription of ion channels and signal transduction molecules, therefore increasing the responsiveness of nociceptors to inflammatory mediators[130,131]. These signalling endosomes also boost CGRP and Substance P synthesis to promote peripheral inflammation and synaptic transmission at the spinal cord[132]. BDNF is co-released with excitatory neurotransmitters from central terminals following prolonged, high-frequency stimulation of nociceptors or exposure to NGF[133]. BDNF binding to TrkB receptors on spinal cord neurons triggers the phosphorylation of nearby glutamate receptors, potentiating their activity to strengthen synaptic transmission[134].

Increased NGF levels have been observed in tissue samples from patients with certain painful conditions[131], which has led to the development of small molecule inhibitors and therapeutic antibodies that negate NGF-TrkA activity. Several anti-NGF antibodies have reached clinical trials for a range of chronic pain indications, including Pfizer's Tanezumab which was shown to provide effective pain relief and improved join function when used in patients with moderate to severe osteoarthritic pain[132]. However, evidence of rapidly progressing osteoarthritis and destruction of healthy joints in some patients has prevented FDA approval of Tanezumab, even with mitigation measures such as low doses and frequent X-ray screening[135]. Nevertheless, clinical trials are still in progress for Tanezumab and other anti-NGF therapies to determine their safety and efficacy in conditions such as chronic lower back pain and neuropathic pain[132].

Due to their recent identification as CIP genes, there is no evidence so far that PRDM12[123] and CHC22[126] are involved in nociceptor sensitisation in humans. The highest expression of CHC22 postnatally is in skeletal muscle where it participates in trafficking of the glucose transporter GLUT4[136], but its expression in postnatal nociceptors is unknown. Whether the targeted induction of CHC22 expression in adult nociceptors could suppress BDNF release and prevent central sensitisation is yet to be investigated. In contrast, postnatal expression of PRDM12 in rodent and human nociceptors is well established[123,125] where it may continue to act as an epigenetic regulator[110]. Two groups have validated adult-onset *PRDM12* conditional knockout in DRG to conduct bulk DRG transcriptomics analysis, single-cell electrophysiology and pain behaviour assays[137,138]. Both studies found a core set of genes dysregulated upon *PRDM12* knockout, although electrophysiological and behavioural responses to noxious stimuli only mimicked human PRDM12-CIP patients in one of the mouse models. This may be attributed to differing genetic strategies for *PRDM12* knockdown, and suggesting blunt knockdown of PRDM12 activity could still be an effective analgesic strategy.

The *FAAH* gene encodes fatty-acid amide hydrolase (FAAH), a catabolic enzyme that breaks down endogenous ligands for cannabinoid receptors. Homozygous carriers of the common *FAAH* variant rs324420 request postoperative analgesia less than women with alternative *FAAH* genotypes[139], and exhibit more positive affective responses to placebo analgesia[140]. The variant lowers protein stability[141] which would increase levels of FAAH substrates in the brain, an effect associated with reduced pain, fear and anxiety in animal models[142]. A woman with CIP was recently identified who was heterozygous for the rs324420 variant as well as a novel microdeletion in a downstream pseudogene termed *FAAH-OUT*[112]. Her son also displayed pain insensitivity to a lesser degree and was found to be heterozygous for the microdeletion but possessed the wild-type allele at the rs324420 locus, while her unaffected daughter did not possess either variant. Blood concentration of FAAH-specific substrates such as anandamide were found to be significantly higher in the proband than in control individuals who were only heterozygous for the rs324420 variant, suggesting the *FAAH-OUT* microdeletion is a major contributor to the CIP phenotype. More work is needed to show how the molecular product of *FAAH-OUT* disrupts FAAH catabolic activity, but it is a promising avenue for research given the failure of small molecule inhibitors for pain relief in clinical trials[143].

1.7 – Thesis Scope and Objectives

While the gene-disease associations of *SCN9A*-CIP and *PRDM12*-CIP are well established, interrogating the loss-of-function mechanisms behind different variants can reveal novel strategies for modulating their activity. Similarly, refining genotype-phenotype correlations can provide insight into the functions of distinct protein domains at the molecular, cellular and physiological level. To this end, the objectives of this thesis were:

1. To confirm pathogenicity of six novel missense mutations identified from *SCN9A*-CIP patients, and establish the molecular mechanism behind their loss-of-function – focusing on protein folding, trafficking to the plasma membrane, and biophysical properties.

2. To determine whether an intracellular N-terminal Nav1.7 mutation (Leu75Pro) disrupts a protein-protein interaction that is essential for wild-type Nav1.7 function using co-immunoprecipitation and mass spectrometry.

3. To examine the relationship between *PRDM12* mutations and sensory neuron development; specifically, if there is a genotype-phenotype correlation between the length of polyalanine expansion mutations and two highly divergent conditions – CIP and MiTES.

CHAPTER 2: Mechanisms of Pathogenicity Behind Missense *SCN9A*-CIP Mutations

2.1 INTRODUCTION

2.1.1 – The Voltage-Gated Sodium Channel Family

The generation and transmission of electrical signals in the nervous system is mostly dependent on voltage-gated sodium channels (VGSCs) and voltage-gated potassium channels. Activation of VGSCs permits sodium ion influx that rapidly depolarises the cell membrane from its resting voltage and contributes to the rising phase of the action potential. Inactivation of VGSCs terminates the signal and is followed by potassium ion efflux, resetting the equilibrium of charges across the membrane in anticipation of the next action potential.

There are nine members in the human VGSC family of α-subunits (Nav1.1 to Nav1.9) encoded by separate genes – *SCN1A*-*SCN5A* for Nav1.1-Nav1.5 and *SCN8A*-*SCN11A* for Nav1.6-Nav1.9. Each gene translates into a single polypeptide chain that folds into 24 transmembrane segments which can be separated into four structurally homologous domains. The four domains arrange themselves around a central pore that is selectively permeable to sodium ions, with conductance being controlled by structural elements that determine voltage sensing, sodium ion selectivity, and voltage-dependent gating[144]. The α-subunits can associate with auxiliary β-subunits either through non-covalent bonds with β1 or β3, or covalent disulfide bonds with β2 or β4. Whilst β-subunits have been shown to support forward trafficking and cell surface expression of the channel, as well as modify its biophysical properties[145], the presence of the α-subunit alone at the cell membrane is sufficient for conductance. The nine VGSC subtypes are enriched in specific adult tissues though their spatial expression can be altered during development and disease-related processes. Consequently, genetic mutations causing gain-of-function (GOF) or loss-of-function (LOF) are associated with Mendelian disorders of excitability, with clinical manifestations centred around the primary tissue[146,147].

Nav1.1, Nav1.2, Nav1.3 and Nav1.6 are predominantly expressed in the central nervous system, although levels of expression differ between neuronal cell types (e.g., excitatory vs inhibitory interneurons), developmental stages (embryonic vs postnatal), and membrane subdomains (e.g., dendrites, axon initial segment and nodes of Ranvier). Pathogenic mutations in these channels are related to a range of epilepsy syndromes as well as autism spectrum disorder[148,149]. Nav1.4 is found at the neuromuscular junction of skeletal muscle; mutations that increase cell excitability impair muscle relaxation whereas those that decrease cell excitability cause muscle paralysis[149]. Nav1.5 is the

primary VGSC in the heart and so its dysfunction is associated with several cardiac arrhythmias[150]. Nav1.7, Nav1.8 and Nav1.9 are enriched in the peripheral nervous system, particularly in nociceptive neurons; thus hyperexcitability mutations cause neuropathic pain disorders, whereas hypoexcitability mutations cause congenital painlessness[151,152].

Studying Nav channelopathies that are associated with pain-related phenotypes has led to an understanding of each VGSC's unique biophysical profile, and how their integrated activity controls nociceptor excitability (see Section 1.3). GOF mutations in *SCN9A* to *SCN11A* (encoding Nav1.7 to Nav1.9) enhance their tendency to activate, or interfere with their inactivation, so that nociceptors are more prone to firing action potentials. Associated conditions include inherited erythromelalgia (IEM), paroxysmal extreme pain disorder (PEPD) and small fibre neuropathy (SFN)[151]. In contrast, LOF *SCN9A* mutations reduce Nav1.7 conductance and thus hinder the amplification of generator potentials[114,153], while certain GOF *SCN11A* mutations depolarise the resting membrane potential such that other Nav channels are inactivated; both result in congenital insensitivity to pain (CIP) at the clinical level[116,118].

2.1.2 – Structure-Function Relationships of Nav Channels

From measuring ionic contributions to the action potential in squid axons, Alan Hodgkin and Andrew Huxley derived mathematical expressions to describe the time course of voltage-sensitive potassium and sodium ion currents. These equations predicted that Na^+ conductance was controlled by the co-ordination of three activating components (m-gates) and one inactivating component (h-gate), so that the neuronal membrane was only permeable to sodium ions when the three m-gates were open, and blocked when the h-gate rapidly shut[154]. This theoretical model of a voltage-sensitive and sodium-selective channel was built upon through biophysical studies by Bertil Hille and Clay Armstrong, who proposed the voltage-dependent gating particles must accommodate a transmembrane pore with size and chemical properties that determine ion selectivity[155]. Molecular cloning of VGSC cDNAs uncovered the existence of multiple channel subtypes with highly homologous secondary structures and critically conserved residues; however, electrophysiological study of individual subtypes in heterologous expression systems (without interference from the assorted ion channel currents in native tissues) revealed subtle differences between them[156,157].

Human VGSCs are produced from a single chain of 1700-2000 amino acids that folds into four structurally homologous domains (DI – DIV), each domain consisting of six α-helical transmembrane segments (S1 – S6) and connected by alternating intracellular and extracellular loops (see Figure 2.1). The S5 and S6 segments from each domain form the walls of the central pore, closed off from the cytoplasm by an intracellular gate that opens upon channel activation. The extracellular S5-S6 loops form a funnel-like vestibule that attracts cations towards the ion selectivity filter, through which only sodium ion flow is permitted. The S1 to S4 segments form the outer voltage-sensing modules which shift vertically through the membrane in response to local changes in membrane potential. Finally, the intracellular S4-S5 linkers play a critical role in co-ordinating the movements of the main functional modules, so that voltage sensor activation is coupled to opening the pore[144,158].

The pore is the central axis around which the VGSC is built, providing an energetically favourable pathway for charged sodium ions to pass across the lipid membrane. The extracellular funnel is formed from the disordered S5-S6 'pore loops', drawing hydrated cations close to the pore edge. The loops dip partially into the transmembrane space, where each domain contributes a single residue to the sodium ion selectivity filter – DEKA (domains: I = aspartic acid; II =glutamic acid; III = lysine; IV = alanine). The pore is filled with water and narrowest at the selectivity filter, exhibiting over 10-fold preference for sodium ion permeation over other biologically relevant metal ions: $Na^+ > K^+ > Ca^{2+} >> Cl^-$ (~1.00:0.08:0.02:<0.01)[144]. The width of this site favours hydrated sodium ions over the larger

potassium ion[159,160], but the presence of the domain III lysine residue is also crucial for sodium over potassium ion selectivity; substitutions to alternative positively charged, hydrophobic or larger aromatic residues result in almost equivalent permeability to sodium or potassium ions[161]. The amino acid composition of the filter also determines selectivity of monovalent sodium ions over divalent calcium ions and negatively charged chloride ions[159,161,162].

Below the filter is a larger central cavity which is closed off from the cytoplasm by an activation gate[163]. In the human Nav family, conserved aromatic residues from the base of each S6 segment make the activation gate (domains: I = tyrosine; II, III & IV =phenylalanine)[164]. The S4-S5 linkers form a constricting collar around the base of the S6 segments at rest; this loosens upon channel activation, allowing a subtle turn of the S6 segments to shift the large, hydrophobic side chains of the activation gate away from the lumen of the pore[163,165]. Hence, distal conformational changes in the voltage sensors are communicated via the S4-S5 linker to open the intracellular end of the conduction pathway in a voltage-sensitive manner.

The concentration of charged amino acids in S1-S4 mediate the voltage-sensitive action of VGSCs. Primary sequence analysis showed a consistent motif in each S4 segment, where positively charged arginines or lysines are positioned at every third residue with hydrophobic residues in between. This pattern is not present in S1-S3 segments, although S1 and S3 favour negatively charged residues, while S2 segments contain a mixture of both charges. This is in stark contrast to the absence of charged residues in the S5 and S6 segments[156,166]. It is energetically costly for charged residues to occupy the hydrophobic transmembrane environment, but by forming ion pairs between oppositely charged residues in proximal segments, the electrostatic forces are neutralised, and the protein structure remains stable. The 'sliding-helix' model of voltage-sensing relates this static structural data with Hodgkin & Huxley's model of gating particles to explain the conformational shifts required for VGSC activation and inactivation.

At rest, the net negative charge at the intracellular membrane surface pulls the positive S4 gating charges towards the cytoplasm, holding the channel in a closed state as the activation gate has sealed the conduction pathway. Local depolarisation releases this electrostatic force, allowing the voltage sensors to move upwards in the membrane and activating the channel. Voltage sensor movement changes the orientation of the S4-S5 linker such that the base of the S6 segments rotate apart like a camera shutter, increasing the inner diameter of the pore and opening the activation gate for sodium ion conductance. The outward movement of S4 segments is rapid but controlled, rotating in relation

to the S1-S3 segments so that S4 gating charges exchange ion pairs from the intracellular to extracellular negative clusters in S1-S3[144,163].

In vertebrate VGSCs, the voltage sensors of domains I and II activate first, followed by domain III and then IV; sequential activation of domains I-III corresponds to Hodgkin & Huxley's m-gates while domain IV acts as the h-gate mediating fast inactivation. This is due to an "IFMT" motif (isoleucine, phenylalanine, methionine, threonine) on the intracellular linker between domains III and IV being pulled towards a hydrophobic pocket close to the activation gate; this tightens the diameter of the pore at the intracellular edge, effectively blocking conductance[163,167]. Recovery from the fast inactivated state occurs within milliseconds; the downward movement of voltage sensors from domains III and IV displaces the fast inactivation particle from its binding pocket, followed by the sensors in domains I and II as the membrane repolarises to the resting potential[168].

VGSCs also exhibit slow inactivation, a property that builds up over repeated channel activations to reduce channel availability and avoid excitotoxicity. The structural basis for this phenomenon appears to be an asymmetric collapse of the pore, with two opposing S6 segments moving towards the central axis and two moving away; this distorts the shape of the pore at the ion selectivity filter, along the central cavity and at the activation gate, preventing hydrated sodium ions from passing through[163,169]. Reduced mobility of the voltage sensors is also implicated in slow inactivation; immobilisation of the sensors from domains I and II correlate closely with entry into slow inactivation, while remobilisation of the domain III sensor drives recovery, which requires an extended period at the resting membrane potential[170]. The order and mechanism by which the two modules become trapped remains elusive.

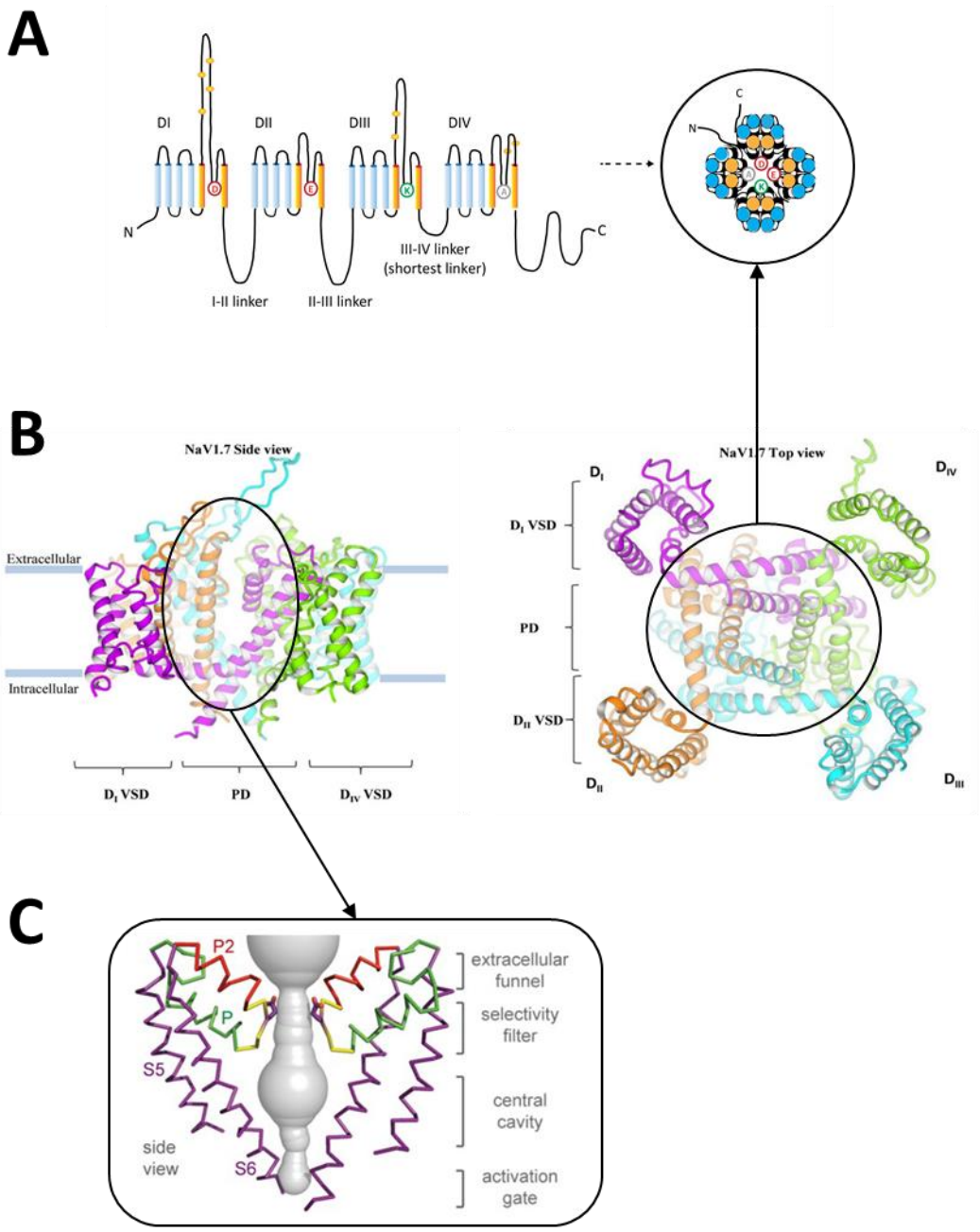

Figure 2.1: Structural organisation of Nav channels and important pore sub-domains. Representations of VGSC structure include (A) transmembrane topological diagrams, with S1 to S4 segments in light blue and S5 to S6 segments in orange; (B) models of the 3D folded channel, based on atomic co-ordinates of Nav protein structures; (C) contributions of the S5 and S6 segments to forming the wall of the pore (carbonyl backbone traces in purple), and volume of the permeation pathway (grey). *Adapted from Fux et al. (2018); Kapetis et al. (2016); Catterall & Swanson (2015).*

2.1.3 – Molecular Determinants of Nav1.7 Function and Subcellular Localisation

Two further aspects of the α-subunit structure are relevant to Nav1.7 function. Homodimers of Nav1.5 and Nav1.7 were recently discovered, held together via their domain I-II intracellular linkers through the 14-3-3 protein and direct α-subunit interactions[167,171]. Cell lines stably expressing wild-type Nav1.7 produced identical currents whether the dimers were present or disrupted by a pharmacological 14-3-3 binding inhibitor, difopein. Upon coupling wild-type channels with channels with patient mutations (i.e., mimicking a heterozygous genotype), pathogenic persistent currents emerged, or current density decreased, in the GOF and LOF conditions respectively. These effects were abolished by difopein treatment, recovering close to homozygous wild-type function[167]. Functional coupling is particularly relevant to *SCN9A* GOF mutations that cause painful disorders, which are always dominant alleles. Reducing persistent currents by inhibiting dimer formation may therefore produce a meaningful reduction in nociceptor excitability and pain sensation.

The other modulatory feature of Nav1.7 structure and function arises from two alternative splicing events[172]. The first choice is from mutually exclusive exons termed 5N and 5A due to their enrichment in neonatal vs adult tissues. Their encoded protein sequences only differ by two residues; 5N places a leucine at the top of the S3 segment in domain I, and an asparagine five amino acids away in the S3-S4 linker, whereas these two residues in 5A are replaced by valine and aspartic acid respectively[173]. The leucine to valine substitution reduces the size of the side chain but both amino acids share similar biochemical properties. The asparagine to aspartic acid substitution is less conservative, imparting a negative charge in the extracellular region and potentially removing an N-linked glycosylation site. The second splicing event differs by the use of alternative splice donor sites in exon 11, resulting in a short (11S) or long (11L) form[172,173]. The extension adds a series of 11 amino acids “VIIDKATSDDS” into the intracellular linker connecting domains I and II.

All splice isoforms of *SCN9A* (5N11S/5N11L/5A11S/5A11L) are expressed at the RNA level in adult human DRG tissue[172]. The encoded proteins produce currents of similar magnitude and possess similar gating kinetics apart from an alteration to fast inactivation in 5N vs 5A isoforms. The exon 5 duplication of *SCN9A* was identified in structurally equivalent exons of five other VGSC genes[174], with the adult variant of Nav1.1, Nav1.2 and Nav1.7 conferring slower recovery from fast inactivation and lowered channel availability following trains of short depolarisations[173,175]. Intriguingly, the effects of some GOF *SCN9A* mutations on channel gating and cellular excitability are enhanced on the 5A variant background, which may explain the later onset of pain symptoms in these cases[176,177].

Equivalents of the exon 11 addition in *SCN9A* have been found in *SCN1A* (VIIDKPATDDN) and *SCN8A* (VKIDKAATDDS)[172], as well as more extensive variation of the domain I-II linker in *SCN3A*[178]. Exon 11 isoforms of Nav1.7 display similar properties at baseline, but are differentially modulated by interacting proteins[173,179]. For example, phosphorylation of 11S isoforms by protein kinase A (PKA) causes a hyperpolarising shift in activation when compared to its dephosphorylated state. This modulation was absent in 11L isoforms, possibly due to a structural change in the domain I-II linker that obscures phosphorylation sites or disrupts the binding site for a PKA scaffolding protein[173,180].

The Navβ1 subunit has also been shown to modulate Nav1.7, significantly increasing current density when co-expressed with each splice variant. The influence of β1 on Nav1.7 gating parameters could be separated into a hyperpolarising shift of voltage-dependent activation mediated by exon 5 (larger in 5N than 5A isoforms), and a depolarising shift in voltage-dependent inactivation mediated by exon 11 (larger in 11L than 11S isoforms). The magnitude of the change in channel availability, and thus current density, in the presence of β1 is dependent on which splice isoform is present; the largest being a 6-fold increase in current density at -20 mV when the 5N11L isoform was expressed[179].

With regards to tissue-specific expression, the cDNA for Nav1.7 was first cloned from a human neuroendocrine cell line, hence an early name for the channel being 'hNE'. mRNA transcripts were detected in mammalian adrenal and thyroid glands, but absent from the brain, heart and other major organs where different VGSC subtypes had been identified[166]. The rodent orthologue PN1 was shown to be highly expressed in the peripheral nervous system, restricted to sensory and sympathetic neurons rather than glial cells[181]. In rodent DRG, *in situ* RNA analysis showed *SCN9A* transcripts were enriched in both myelinated and unmyelinated TrkA-positive sensory neurons (i.e., Aδ and C nociceptors)[182,183]. More recent single-cell transcriptomics analyses have also detected low levels of *SCN9A* in Aβ LTMR fibres, but it is virtually absent in proprioceptors[36,184,185].

At the subcellular level, Nav1.7 protein has been detected along the whole length of nociceptor axons from peripheral terminals innervating the skin to the pre-synaptic central terminals at the dorsal horn. They are also detected at the nodes of Ranvier in small diameter myelinated axons, bounded by caspr-positive paranodal regions[186]. Nav1.7 appears to be concentrated in somatic and axonal intracellular pools[181,187], but distributed as relatively sparse nanoclusters in the cell membrane; however delivery to the cell surface is upregulated in the presence of inflammatory mediators[187]. A recent study showed Nav1.7 may also be transferred across the central synapse and localised onto the dendrites of post-synaptic spinal neurons in lamina II of the dorsal horn, where it modulates the action potential

threshold and neuronal firing properties[188]. Nav1.7 has recently been detected in third order neurons of the nociceptive pathway that connect discrete structures of the parabrachial nucleus and thalamus to the amygdala, responsible for the aversive quality of nociceptive inputs[189].

The abundant expression of Nav1.7 in human DRG supports its importance in sensory neuron excitability. *SCN9A* is the predominant subtype expressed, making up over 40% of the total of all VGSC subtype transcripts[190], while Nav1.7 protein is detected in approximately 90% of all sensory neurons[191]. As with rodent systems, Nav1.7 expression extends from DRG along central axons and into laminae I and II of the spinal cord[35]. At the peripheral terminals, Nav1.7 is found in the epidermal layer and upper epidermis but absent from Meissner's corpuscles, a peripheral end organ innervated by Aβ fibres[192]. Nociceptors derived from human induced pluripotent stem cells (iPSCs) exhibit a similar subcellular distribution of Nav1.7 as seen in primary cultures of rodent DRG neurons – the channel is concentrated in the cell soma, but puncta are visible along unmyelinated axons or localised to nodal regions in myelinated co-cultures[114].

The delivery of VGSCs to the plasma membrane is regulated by specific interactions along the secretory pathway[193]. VGSC polypeptides are translated at ribosomes associated with the rough endoplasmic reticulum (ER), followed by protein folding and core glycosylation within the ER. Molecular chaperones such as calnexin monitor the assembly of nascent channels, directing misfolded proteins for degradation. Correctly folded proteins are inserted into the ER membrane and transported to the Golgi, where they undergo further glycosylation. The trafficking endosomes that carry Nav channels from ER to Golgi to plasma membrane move along microtubule tracks, dependent on direct or indirect interactions between the channel and kinesin motors. Upon reaching the cell surface, endosomes must fuse with the plasma membrane where channels may be anchored by other transmembrane and cytoskeletal factors[193,194].

Compared to other sensory Nav channels, few specific regulators of Nav1.7 transport are known[195]. For example, both the kinesin KIF5B and adaptor protein p11 support the forward trafficking of Nav1.8, but an equivalent role for Nav1.7 has been dismissed[196,197]. However, beta subunits β1 and β3 have been shown to promote Nav1.7 localisation to the membrane via alternative glycosylation routes[198], and in cultured DRG neurons, Nav1.7 is transported primarily via Rab6A-positive vesicles[187]. CRMP2 is another key regulator of Nav1.7 membrane localisation, driving the balance between membrane insertion versus ubiquitin-mediated internalisation[199,200].

2.1.4 – Pathogenicity of *SCN9A*-CIP Mutations – LOF at the Molecular Level

Soon after dominant GOF mutations in *SCN9A* were discovered to cause extreme pain disorders[201,202], homozygous truncating mutations were mapped to *SCN9A* in three families with CIP[153]. Their painless phenotype was unique in that they had normal intelligence and autonomic function, and initially without evidence of peripheral sensory neuropathy. Subsequent case reports highlighted anosmia as an additional distinguishing feature of this form of CIP[203,204]. The *SCN9A*-CIP mutations were predicted to cause LOF at the molecular level via nonsense-mediated mRNA decay, or from premature truncation of the protein sequence before the third domain – therefore lacking half of the α-subunit structure. Channel function was assessed by voltage-clamp electrophysiology in HEK293 cells, which have sufficient cellular machinery to produce fully functional WT Nav1.7 channels and is well established in biophysical characterisation of mutant VGSCs. While the wild-type channels produced robust currents with the expected voltage-dependent profile, Nav1.7 CIP mutants produced negligible current, equivalent to background when no α-subunits were expressed[153].

CIP is an incredibly rare condition, and aside from the neurotrophin receptor gene *NTRK1*, LOF mutations in *SCN9A* have emerged as one of its most common causes[109]. These include truncations due to nonsense substitutions, frameshifts and mis-splicing[203,205,206]; an in-frame deletion that extracted a string of amino acids from the translated protein[207]; or missense substitutions that alter single functionally critical residues in an otherwise fully folded channel[114,207–209]. *SCN9A*-CIP is inherited in an autosomal recessive manner, meaning patients can carry different LOF mutations in each allele. Because patients display such a distinct clinical phenotype, most reported mutations have been associated with disease based on expected segregation of variants in the affected family, population frequency data and predictions from bioinformatic tools[210].

Of the mutations that have been functionally assessed *in vitro*, electrophysiological analysis has shown that Nav1.7 mutants with truncations before the C-terminal tail are completely non-conducting[114,153,211,212]. In contrast, the nonsense mutation Leu1831X displayed a 3-fold reduction in peak current density as well as subtle changes in activation and inactivation that would reduce channel availability and therefore excitability at the cellular level. This mutation retains all four VSDs, the ion selectivity filter and gating components of the α-subunit, only excluding the last 146 residues of the C-terminus, thus illustrating the functional importance of the C-terminal domain[208]. This CIP patient was compound heterozygous for Leu1831X and Ala1236Glu, a missense mutation that also exhibited partial LOF with over 6-fold decrease in peak current density and a small but significant

hyperpolarising shift in fast inactivation. The genotype of this patient was the first indication that a substantial but incomplete LOF in both alleles may be sufficient for congenital analgesia in humans[208].

Of the nine *SCN9A*-CIP missense mutations published (illustrated in Figure 2.2 and listed in Table 2.1), seven have been functionally assessed by whole-cell voltage-clamp electrophysiology on a HEK293 cell background. Substitutions of Arg896Gln or Arg896Trp in the DII:S5-S6 pore-loop, and Gly1725Arg at the top of the DIV:S6 transmembrane helix, all resulted in virtually complete loss of conductance[114,207]. Four missense mutations caused a 50-90% reduction in peak current density – Arg99His and Trp1775Arg in the intracellular N-terminal and C-terminal tails; Trp917Gly in the DII:S5-S6 pore-loop; and Ala1236Glu in DIII:S2 transmembrane helix[208,209]. Lys376Gln and Cys1719Arg are located in the S5-S6 pore-loops of domain I and domain IV respectively, but the mechanisms behind their LOF have not been investigated[213,214]. In addition to electrophysiology, semi-quantitative methods have sometimes been used to demonstrate a reduction in total protein expression and plasma membrane localisation compared to wild-type control constructs[207,209].

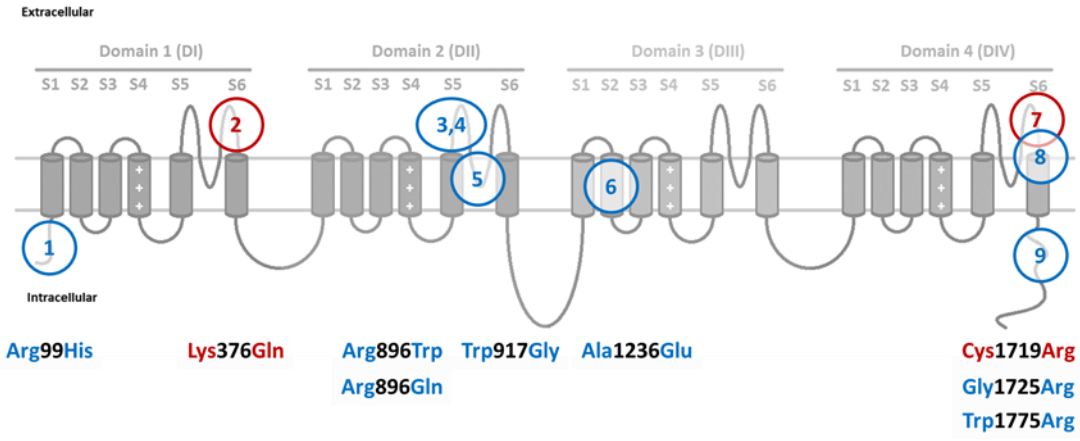

Figure 2.2: Genetic and structural locations of novel *SCN9A*-CIP patient mutations
Locations of published missense *SCN9A*-CIP patient mutations. Only those in blue have been functionally characterized; see Table 2.1 for patient histories and details of functional assessment.

Table 2.1: Published Missense *SCN9A*-CIP Mutations

All amino acid numbering based on the 11S splice variant

ICC: immunocytochemistry; **WB:** western blot; **WC-VC:** whole-cell voltage-clamp electrophysiology; **PC12:** rat-derived pheochromocytoma cell line; **HEK293/-A/-T:** human embryonic kidney cell lines; **n.s.:** not statistically significant

MISSENSE MUTATION	SECOND MUTATION	REFERENCE	ICC	WB	WC-VC	COMPARISON TO WILD-TYPE
Arg896Gln	*Arg896Gln*	(2010) Cox[207]	☑ PC12		☑ HEK293A	▪ [ICC] Reduction in plasma membrane localisation ▪ [WC-VC] Complete loss of sodium conductance
Trp1775Arg	*Splice-site**	(2015) Emery[208]			☑ HEK293	▪ [WC-VC] >65% reduction in peak current density ▪ [WC-VC] 11.8 mV depolarized shift of $V_{1/2}$ activation
Arg1236Glu	*Leu1831X*				☑ HEK293	▪ [WC-VC] >85% reduction in peak current density ▪ [WC-VC] 9.6 mV hyperpolarized shift of $V_{1/2}$ fast inactivation
Arg896Trp	*Intronic variant***	(2019) McDermott[114]			☑ HEK293T	▪ [WC-VC] Complete loss of sodium conductance
Gly1725Arg	*Tyr897X*				☑ HEK293T	▪ [WC-VC] Negligible sodium conductance
Arg99His	*Trp917Gly* ***	(2020) Sun[209]	☑ HEK293	☑ HEK293	☑ HEK293	▪ [WC-VC] ~50% reduction in peak current density ▪ [WC-VC] ~2 mV depolarized shift of $V_{1/2}$ activation (n.s.) ▪ [WC-VC] ~2 mV hyperpolarized shift of $V_{1/2}$ fast inactivation (n.s.) ▪ [WB] ~50% reduction in total protein expression ▪ [ICC] ~55% reduction in Nav1.7-specific fluorescence
Trp917Gly	*Arg99His* ***		☑ HEK293	☑ HEK293	☑ HEK293	▪ [WC-VC] ~90% reduction in peak current density ▪ [WB] No significant difference in total protein expression ▪ [ICC] No significant difference in Nav1.7-specific fluorescence
Cys1719Arg	*Splice-site**	(2011) Staud[213]	No functional assessments – diagnosis based on clinical phenotype, plus segregation of genetic variants and disease in affected case only consistent with autosomal recessive inheritance.			
Lys376Gln	*Frameshift* ****	(2014) Shorer[214]				
Arg896Trp	*Arg896Trp*	(2021) Palma[215]				

* Different splice-site mutations: predicted to trigger nonsense-mediated mRNA decay in (2015) Emery et al.[208]; shown to skip exon 17 in (2011) Staud et al.[213]

** Intronic variant of unknown significance

*** Both missense mutations in the same proband

**** Chromosomal alteration (c.1124delG) causes a frameshift and premature truncation in DI:S6

2.1.5 – Phenotypic Features of *SCN9A*-CIP in Humans

Congenital onset of painlessness is usually identified by lack of distress from the teething period onwards, which results in self-mutilation of the lips and tongue. Affected children may also be unbothered by needles during immunisations or other medical procedures. Patients possess a variety of painless injuries from bruises and cuts to amputated digits, burn wounds and bone fractures[109]. Injuries tend to be poorly healed due to the absence of pain that would otherwise prompt taking time out to recover; for example, repetitive fractures can lead to Charcot's joints and the eventual loss of limb use unless the patient learns to recognise other signs of injury and to carefully monitor their behaviour[206,216]. Medical histories and quantitative sensory testing have determined that these individuals can detect changes in mechanical and thermal stimulus intensity into noxious ranges[114,153,203], but without the aversive character of pain they are not motivated to modify their behaviour. However, one *SCN9A*-CIP case has described feeling a "tingling" sensation when exposed to noxious stimuli and learned by experience to avoid such situations[216]. Light touch, vibration sensing and proprioception are all unaffected, reiterating the unique significance of Nav1.7 function in nociceptors. Temperatures within safe limits are also perceived normally[114,153,203].

SCN9A-CIP can be clinically differentiated from other genetic causes of painlessness if the patient is anosmic and has no deficits in cognitive development or in motor, autonomic and gastrointestinal function. If other family members are affected, the pedigree would indicate an autosomal mode of inheritance which should be verified by targeted gene sequencing[109]. The corneal blinking reflex and ability to form tears (dependent on parasympathetic nerves and sensory reflex arcs) are thought to be intact in most *SCN9A*-CIP patients[109], however due to corneal nociceptor dysfunction, trauma to the eyes can reduce corneal responses[204,207]. Visceral pain is also absent as illustrated by pain-free abdominal surgeries and pregnancy[203,204]. Curiously, three female *SCN9A*-CIP patients have been reported to experience pain of visceral, headache or neuropathic nature after childbirth[212,217] – despite never feeling pain before, their behaviour and verbal descriptions clearly reveal severe discomfort. Why pain emerges after this event is unclear although some have hypothesised that endogenous opioid signalling, which appears to be mis-regulated upon Nav1.7 LOF[113,218], may be drastically altered during recovery from labour[212].

In neurodevelopmental forms of CIP caused by *NTRK1*, *NGFβ* and *PRDM12* mutations, nociceptors fail to form as established by skin and nerve biopsies[123,219,220]; evidence of neuropathy in *SCN9A*-CIP however is more contentious. In earlier case series, patients appeared to have the normal complement of myelinated and unmyelinated nerve fibres present in sural nerve biopsies[153,203,207]. In

addition, sensory nerve conduction velocity is frequently within normal ranges[114,153,203,206], although sensory nerve amplitudes were slightly reduced in two cases which was attributed to damage from surgeries and past injuries[114,204]. Several other patients had absent or noticeably reduced action potentials in some sensory nerves but normal recordings in others; whether these also correlated with older tissue traumas was not elaborated on[207]. Histamine response tests in *SCN9A*-CIP patients produced the "wheal and flare" typical of neurogenic inflammation[114,203,207]; this response is dependent on the activation of histamine receptors on peripheral terminals innervating the skin, plus sufficient membrane excitability for the axon reflex arc to stimulate local vascular tissue[65].

Unexpectedly, an almost complete lack of nociceptive fibres crossing into the epidermis has been observed in all five *SCN9A*-CIP cases who have had skin biopsies taken[114,204,206]. Microneurographic recordings from three of these inidviduals[114] (a more precise technique for studying small fibre dysfunction than nerve conduction studies[221]) revealed a complete absence of nociceptor conduction profiles whereas C-fibre thermoreceptive and low-threshold mechanoreceptive transmission were unaffected. Curiously, histamine-induced flare responses were still intact. Thus, partial denervation may be a true feature of *SCN9A*-CIP, but whether loss of Nav1.7 activity is involved in a neurodevelopmental defect in axon guidance or die-back of peripheral terminals is unknown.

2.1.6 – Physiological Basis of Painlessness in *SCN9A*-CIP

Several *SCN9A* knockout mouse models have been generated to investigate the physiological basis of painlessness. As in humans, global *SCN9A* embryonic-knockout mice were anosmic, indicating the critical role for Nav1.7 in olfactory signal transmission is conserved between species[222,223]. With assisted feeding at the neonatal stage, adult knockouts grew to comparable size of wild-type mice and displayed normal movement and tactile sensitivity. Transient swelling and skin flare were observed following injection with complete Freund's adjuvant and histamine respectively, indicating neurogenic inflammation was intact, although unlike CIP patients, global knockout mice exhibit normal innervation of the epidermis as demonstrated by PGP9.5 staining. Behavioural assays demonstrated a complete loss of acute nociception in mechanical, thermal and chemical modalities, as well as inflammation-induced hypersensitivity to thermal stimuli[222]. Whole-cell patch-clamp analysis showed that dissociated DRG neurons from knockout mice still expressed a TTX-sensitive current, likely from Nav1.1, Nav1.3 or Nav1.6[60,190,224]. However, in a skin-nerve preparation where C fibre responses could be isolated, mechanical stimulation of knockout animals produced a 6-fold lower action potential frequency than in wild-type controls[222]. This data mirrors the clinical picture of human *SCN9A*-CIP patients, implying that a significant but incomplete reduction in nociceptor firing may be sufficient to alleviate acute nociceptive and longer-term inflammatory pain.

Conditional *SCN9A* knockout mice have also been used to study the role of Nav1.7 in nociception, however they do not recapitulate all features of CIP patients. Mice with *SCN9A* embryonic-knockout from Nav1.8-expressing cells (representing a large proportion of nociceptors), could tolerate noxious blunt pressure up to the maximum cut-off point. However, these mice retained their sensitivity to noxious punctate mechanical stimuli[225,226], analogous to pinprick pain which is tolerated in humans with *SCN9A*-CIP[114,203,206]. Sensitivity to noxious thermal stimuli also varied depending on the behavioural assay used. Knockout mice displayed increased withdrawal latencies compared to wild-type mice in the Hargreave's test, but produced similar responses to wild-type mice in the hot plate assay[225,226]. It was later shown that responses to thermal stimulation in the latter assay are mediated supraspinally and depend on the integration of nociceptive and sympathetic input, whereas the Hargreave's test assesses spinal reflex responses. Hence, thermal insensitivity in the hot plate assay has only been observed when Nav1.7 is deleted from both sensory and sympathetic neurons[222,227].

Reducing nociceptor input into the spinal cord via Nav1.7 inhibition was also shown to abolish the development of mechanical and thermal allodynia[225,226,228] as well as spontaneous pain induced by formalin injection[222,226,227]. With regards to chronic pain, sensitivity to noxious stimuli before and after

spinal nerve ligation has been used to track the development of neuropathic pain following nerve injury. Surprisingly, nociceptor-specific knockout of Nav1.7 had no effect on the emergence and time course of mechanical allodynia up to 4 weeks following nerve injury[226,227]. However, removal of Nav1.7 from both sensory and sympathetic neurons lessened the degree of mechanical hypersensitivity within the first week, and these knockout mice recovered baseline function 10 days after injury; in contrast, wild-type mice continued to exhibit significant mechanical hypersensitivity for 28 days without improvement[227]. These results complement human data that suggest peripheral Nav1.7 modulation could reduce chronic pain in inherited and acquired neuropathies[229–231].

Electrophysiological studies have produced somewhat conflicting results as to the impact of Nav1.7 on nociceptor excitability. *In vivo*, Nav1.7 knockout in mechano-sensitive nociceptors did not affect the action potential threshold at peripheral terminals, but slowed axonal conduction velocity by ~20% which was attributed to the stronger depolarisation required to activate Nav1.8[232]. In contrast, patient-derived iPSC nociceptors with *SCN9A* mutations did exhibit an increased rheobase, resulting in a lower action potential frequency in response to suprathreshold current stimuli and longer ramp currents[114]. This difference may be due to the human *in vitro* model not expressing the full complement of channels as in native tissue, or a true species difference in nociceptor electrogenesis.

Surprisingly, in another study of peripheral Nav1.7 knockout mice, nociceptor excitability up to the cell body was unaltered (assessed *in vivo* by calcium imaging and extracellular DRG recordings), despite these knockout mice displaying an equivalent analgesic phenotype as *SCN9A*-CIP humans. Instead, the absence of functional Nav1.7 was shown to reduce excitatory neurotransmission by increasing the presynaptic current threshold required for glutamate release at central terminals. This was associated with a reduction in spinal responses to noxious thermal and mechanical stimulation of nociceptors, specifically the number of evoked spikes in wide dynamic range (WDR) neurons[113]. A deficit in excitatory neuropeptide release and spinal responses has been observed in other studies of Nav1.7 knockout mice, as well as after pharmacological inhibition of Nav1.7 in wild-type mice[115,225,227], indicating synaptic transmission at the central synapse is the pivotal site producing painlessness.

A further discovery from this body of work was the interplay between Nav1.7-specific conductance and opioidergic signalling in producing painless phenotypes. The endogenous opioid proenkephalin, a precursor to enkephalin peptides, was previously shown to be upregulated at the mRNA level in Nav1.7 knockout mice which coincided with a 2-fold increase in Met-enkephalin peptides at the nociceptor central terminals. The transcriptional change was specifically modulated by intracellular

sodium ion concentration as opposed to calcium ions, a classical second messenger, and was not observed in Nav1.8 or Nav1.9 knockouts that also display a CIP phenotype. Strikingly, the opioid antagonist naloxone reversed thermal and mechanical analgesia in Nav1.7 knockout mice, demonstrated by behavioural assays and enhanced electrical activity of spinal WDR neurons. A *SCN9A*-CIP patient also temporarily regained pain sensation following intravenous naloxone treatment, recognised by verbal reports and psychophysical study[218].

In addition, transcripts for the serotonin receptor 5-HT4 were lowered in nociceptors from Nav1.7 knockouts; the activation of this GPCR stimulates PKA activity, augmenting Nav1.8 currents and pro-nociceptive transmission. The change in 5-HT4 expression in Nav1.7 knockout mice led to a reduction of PKA activity, which was further dampened by fentanyl and DAMGO, a non-specific opioid receptor agonist and MOR-specific agonist respectively[233]. These results suggest the absence of Nav1.7 current leads to transcriptional changes that promote anti-nociceptive adaptations of peripheral nociceptors. In support of this theory, the upregulation of proenkephalin alone does not produce analgesia; knockout of *NFAT5*, a putative transcriptional repressor of the *PENK* gene, increases *PENK* mRNA levels but had no effect on pain thresholds in these mice[234].

However, the contribution of opioid signalling to painlessness in *SCN9A*-CIP humans is not universal. Naloxone treatment in 2 of 3 patients led to a temporary recovery of pain sensation, whereas there was no effect in the third[113,218]. This deviation may be explained by the patient genotypes; those affected by naloxone possessed mutations that would cause complete LOF in both their Nav1.7 mutant alleles, either due to nonsense-mediated decay or non-conducting channels[113,114,204,205,218]. The third patient was compound heterozygous for the nonsense mutation R830X and a late frameshift mutation (FS1773) in the C-terminal domain[113,216]; the former mutation completely abolished conductance while the latter mutant channel was still partially functional but displayed an 8-fold reduction in current density[114]. Yet in human iPSC-derived nociceptors with CRISPR-mediated knockout of Nav1.7, *PENK* mRNA levels were not altered and naloxone had no effect on cell excitability, although neurotransmitter release was not measured in this model[114]. Taken together, this data suggests a complete absence of Nav1.7 current is required for opioid-mediated adaptation *in vivo*, but this mechanism may not be recapitulated in current stem cell-derived models.

2.2 OBJECTIVES

In this project, we sought to expand our understanding of how Nav1.7 function may be disrupted by localised changes in protein structure. Six novel missense mutations in *SCN9A* were identified from patients diagnosed with CIP. The unique clinical phenotype in these patients, and the presence of these missense mutations in trans with a second *SCN9A* mutation, provided strong grounds for their pathogenicity (see Figure 2.3A-B).

In silico analysis tools were employed to evaluate the following:

I. How conserved are the affected residues, across species and within the VGSC family?
II. Where are the affected residues located within the tertiary folded structure of hNav1.7?
III. How do the biochemical properties of the native and substituted amino acids differ?

While bioinformatics analysis can be informative, limits in our understanding of the complex structure-function relationships of voltage-gated ion channels mean false predictions can be made[235]. Therefore, to prove the missense mutations are pathogenic (i.e., cause a change in molecular function that could impair nociceptor signalling), I developed *in vitro* assays investigating several essential aspects of Nav1.7 function in transiently transfected cells, which were later confirmed in stable cell lines (see Figure 2.3C).

Of note, five of our CIP mutations were studied in both transient and stable expression systems. The sixth mutation (A1687P) was identified in early 2019, by which time I had moved onto the stable cell line generation. The R896W and G1725R mutations were independently studied by McDermott et al. who also found these mutants to be non-functional[114].

In vitro assays were used to answer the following questions for each mutation:

I. Does the subcellular distribution of wild-type and mutant channels differ?
II. Are mutant channels able to localise to the plasma membrane?
III. If so, do they display any differences in biophysical profile compared to wild-type channels?

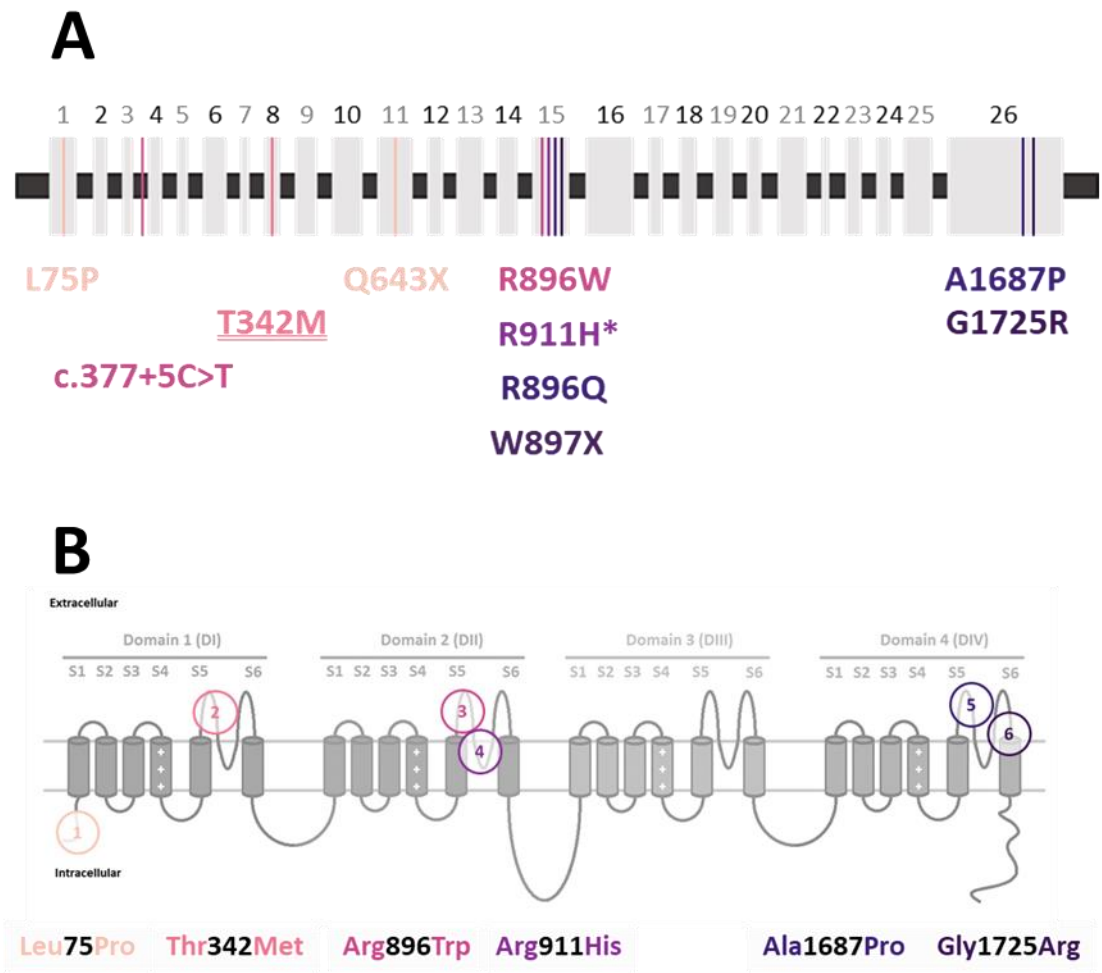

Figure 2.3: Objectives for *SCN9A*-CIP mutation characterisation
(A) Genomic locations of *SCN9A*-CIP mutations used in this project – matching colours indicate compound heterozygous mutations in the same patient (see also Table 2.3). The T342M mutation was inherited homozygously while R911H was the only *SCN9A* mutation identified in that patient. (B) Protein structure locations of missense mutations studied in this project. (C) Molecular approaches for the functional assessment of these mutations. *Figure created with BioRender.com.*

2.3 METHODS

2.3.1 – Clinical Information and Genetic Data on *SCN9A*-CIP Cases

Cases were referred through a specialist NHS clinic for genetic pain disorders at Addenbrooke's Hospital, Cambridge, UK. Detailed phenotype characterisation and clinical examination was carried out (see Table 2.2), indicating *SCN9A*-CIP as the most plausible diagnosis[109]. Exome sequencing and electronic filtration to a pain gene panel revealed *SCN9A* mutations in both alleles for 5 of 6 cases, which were confirmed by Sanger sequencing in the NHS Genetics laboratory (see Table 2.3). Annotation of the amino acid number affected is based on the *SCN9A* isoform with the short form of exon 11 – i.e. missing the peptide sequence 'VIIDKATSDDS' at residues 648-658 from the canonical sequence.

Table 2.2: Clinical information on new *SCN9A*-CIP cases
Y: Yes; **N**: No; **T**: too young to test

CLINICAL FEATURES OF CIP	*SCN9A*-CIP CASE					
	1	2	3	4	5	6
Impaired pain sensation	Y	Y	Y	Y	Y	Y
Impaired temperature sensation	N	N	N	N	N	N
Painless fractures and/or Charcot's joints	N	Y	Y	N	Y	Y
Self-mutilating injuries	N	N	N	N	N	N
Corneal injuries	N	N	N	N	Y	N
Anosmia	Y	Y	Y	T	T	Y
Frequent *Staphylococcus aureus* infections	N	N	N	N	N	N
Sweating dysfunction – anhidrosis or hyperhydrosis	N	N	N	N	N	N
Delayed cognitive development	N	N	N	N	N	N
Gut dysfunction	N	N	N	N	N	N
Pruritis	N	N	N	N	N	N

Table 2.3: Genotype of new *SCN9A*-CIP cases

Case	*SCN9A* Mutation Genotype	Nucleotide Change	Protein Change
1	Compound Heterozygous	c.224T>C	Leu75Pro
		c.1927C>T	Gln643X
2	Homozygous	c.1025C>T	Thr342Met
3	Compound Heterozygous	c.2686C>T	Arg896Trp
		c.377+5C>T	Splice-site*
4	Sole mutation**	c. 2732G>A	Arg911His
5	Compound Heterozygous	c.5059G>C	Ala1687Pro
		c.2687G>A	Arg896Gln
6	Compound Heterozygous	c.5173G>C	Gly1725Arg
		c.2691G>A	Trp897X

(*): Splice-site mutation was confirmed as pathogenic in (2018) Shaikh et al.[205]
(**): Child has formal CIP diagnosis, but too young to test for anosmia

2.3.2 – *In Silico* Pathogenicity Prediction and Sequence Conservation Analysis

Canonical protein sequences were acquired from UniProt[236] for members of the human VGSC family and for Nav1.7 across several species – accession codes are listed in Table 2.4. Multiple sequence alignments (MSAs) were generated using the EMBL-EBI Clustal Omega tool[237] to compare amino acid conservation at the mutation locations – MSAs can be viewed in Appendices C-E. Sequence conservation figures were produced using Jalview software[238]. The online PolyPhen-2 tool was run to predict pathogenicity of missense mutations, using UniProt accession code Q15858-3 as the input (http://genetics.bwh.harvard.edu/pph2/) and configured for output from the HumVar-trained model[239].

Table 2.4: UniProt accession codes for Nav channel MSAs

GENE	ORGANISM	SPECIES	ACCESSION CODE
SCN9A	Human	*Homo sapiens*	Q15858
SCN9A	Macaque	*Macaca mulatta*	F7A8X1
SCN9A	Cattle	*Bos taurus*	M0QVY7
SCN9A	Opossum	*Monodelphis domestica*	F6QVC1
SCN9A	Chicken	*Gallus gallus*	E1C4S2
SCN9A	Rat	*Rattus norvegicus*	O08562
SCN9A	Mouse	*Mus musculus*	Q62205
para	Fly	*Drosophila melanogaster*	P35500
SCN1A	Human	*Homo sapiens*	P35498
SCN2A			Q99250
SCN3A			Q9NY46
SCN4A			P35499
SCN5A			Q14524
SCN8A			Q9UQD0
SCN10A			Q9Y5Y9
SCN11A			Q9UI33

2.3.3 – Structural Modelling of Human Nav1.7 Channel

The structure for human Nav1.7- β1-β2 complex, bound to a combination of animal toxins, was recently solved by cryo-electron microscopy[240]. Using the structure visualisation software Chimera[241], a single model was chosen (Protein Data Bank ID code 6J8G) to pinpoint potential changes in local structure caused by our CIP mutations. Beta subunits, toxins, and glycosylation groups were hidden, leaving only the Nav1.7 chain visible. Amino acid sidechains were mutagenized using the default Dunbrack rotamer library[242]. Multiple sequence alignment of Nav1.7 splice variants with the sequence of the resolved structure is presented in Appendix E to identify locations of the *SCN9A*-CIP mutations.

2.3.4 – *SCN9A* Plasmids Used for Transient and Stable Expression

SCN9A transcripts and the encoded Nav1.7 protein can exist as 4 possible isoforms depending on the alternative splicing of exons 5 and 11. Nav1.7 isoforms encoded from adult versus neonatal exon 5 (5A vs 5N) differ by two amino acids – '5A' encodes Val201 and Asp206, whereas '5N' encodes Leu201 and Asn206. Exon 11 long versus short isoforms (11L vs 11S) differ by the presence or absence respectively, of the sequence 'VIIDKATSDDS' within the domain I:II intracellular loop[172,173,177].

The *SCN9A* plasmids used in this project, see Figure 2.4A, encode the 5N11S isoform which was codon-optimised for expression in mammalian systems, and were kindly gifted by Fiona Cusdin (MedImmune, UK). An N-terminal FLAG tag and PreScission Protease recognition sequence precede the *SCN9A* gene, followed by a flexible linker, thrombin cleavage site and poly-histidine tag at the C-terminal end, see Figure 2.4B. Both plasmids employ a high-copy number origin of replication site derived from the pBR322 plasmid. The *ampR* gene confers resistance to ampicillin and carbenicillin antibiotics, which were used for selection of successfully transformed bacteria during plasmid propagation.

Where pcDNA4/TO_SCN9A was transiently transfected into HeLa and HEK293 cell lines, constitutive expression of the *SCN9A* insert was driven by the CMV promoter. In contrast, once the pJTI-R4-DEST-SCN9A plasmids had been integrated into the HEK JI TREX cell line, *SCN9A* expression is initially repressed due to the stable expression of the tetracycline repressor protein (TetR) in the parental HEK JI TREX cell line. TetR homodimers bind to a single tetracycline operator (TetO) sequence, blocking gene transcription. Adding tetracycline or doxycycline compounds to cell culture media de-represses gene expression; this is due to the higher affinity binding between TetR homodimers and the antibiotic, causing a conformational change in TetR that releases it from the TetO sequence[243].

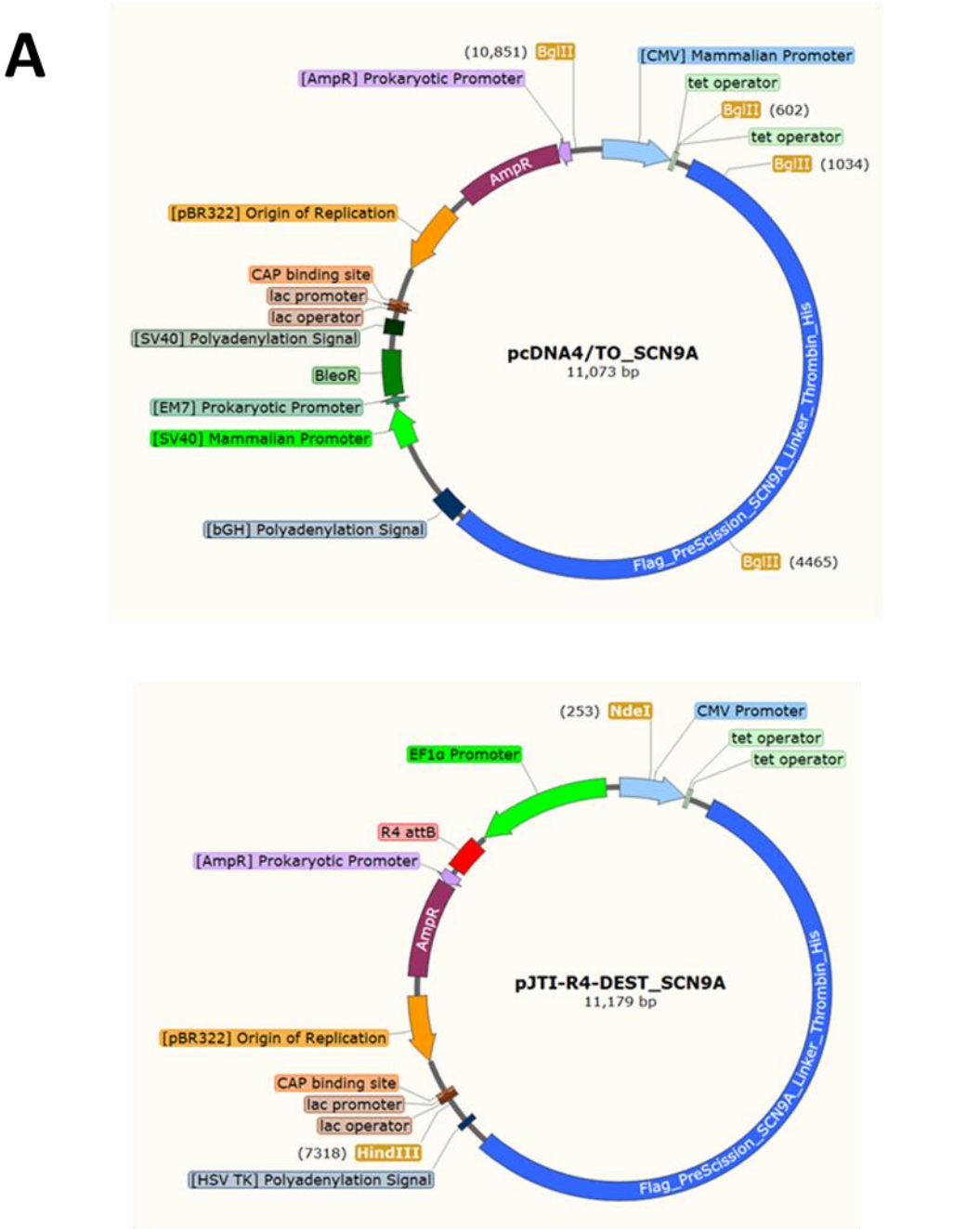

Figure 2.4: *SCN9A* plasmid maps and encoded hNav1.7 construct
(A) Both plasmids were kindly gifted by Fiona Cusdin, encoding an identical Nav1.7 channel construct as illustrated in (B). The pcDNA4/TO plasmids were used for transient transfection, while the pJTI-R4-DEST plasmid was used to generate HEK JI TREX Nav1.7 stable cell lines.

2.3.5 – Bacterial Propagation of *SCN9A* Plasmids

For initial experiments using the pcDNA4/TO_SCN9A plasmid, propagation was first attempted in XL10-Gold Ultracompetent cells with 4% (v/v) β–mercaptoethanol (Agilent Technologies) according to the manufacturer's protocol. Transformed bacteria were plated onto agar plates of Luria Broth with ampicillin (LB-Amp) and grown in a standing incubator at 37°C, 5% CO_2 overnight. Inoculated mini-cultures and maxi-cultures were grown in a shaking incubator set to 37°C, 5% CO_2 and 220 rpm.

Despite variations in temperature and duration of incubation at each growth stage, plasmid yield was either negligible or produced large-scale rearrangements in the wild-type plasmid. The optimisation process is outlined in results section 2.4.3. Therefore, I switched to using MAX Efficiency Stbl2 Competent cells (Invitrogen) as recommended in the literature[244]. This protocol successfully mitigated our propagation issues and produced the best quality and yield of plasmid DNA in the shortest timeframe.

For the transformation procedure, 50 ng plasmid was added to 25 µl Stbl2 cells and mixed gently by swirling the tube. Cells were kept on ice for 25 minutes, then briefly heat-shocked at 42°C for 40 seconds, before sitting on ice for a further 2 minutes. After adding 400 µl SOC media (super optimal broth with catabolite repression), the cells were then incubated in a 37°C shaking incubator for 90 minutes. Transformed bacteria were plated onto LB-Amp agar plates for incubation in a standing incubator at 37°C overnight.

Single colonies were used to inoculate 5 ml LB-Amp mini-cultures the next day and incubated for 6 hours in a shaking incubator at 37°C. Plasmid DNA was extracted and prepared using the QIAprep spin miniprep kit (Qiagen) for diagnostic restriction enzyme digests and sequence verification where required. LB-Amp maxi-cultures were inoculated using 2-5 ml from individual mini-cultures and incubated overnight in a shaking incubator at 37°C. Plasmid DNA was extracted and prepared using the Genopure Plasmid Maxi Kit (Roche). All bacterial cultures were grown in LB with 100 µg/ml working concentration ampicillin.

To check whether plasmid DNA had undergone any major duplications or rearrangements, diagnostic restriction enzyme digests were conducted as detailed in Table 2.5. For pcDNA4/TO_SCN9A plasmids, complete digestion with the BglII restriction enzyme (NEB) at 37°C for 2 hours produced bands at approximately 6.5 kb, 3.5 kb, 800 bp and 450 bp when run against the Hyperladder 1 kb molecular weight marker (Bioline). This was in keeping with virtual restriction digest calculating four fragments

at 6386, 3431, 824 and 432 bp. For pJTI-R4-DEST_SCN9A plasmids, a double digest was conducted with the NdeI and HindIII-HF restriction enzymes (NEB) at 37°C for 2 hours. Both enzymes cut the pJTI-R4-DEST_SCN9A plasmid at single sites, producing two fragments of 7065 and 4114 bp.

Table 2.5 Reaction Components & Thermocycling Protocol for RE Digests of *SCN9A* Plasmids

Restriction Enzyme Digest Components for pcDNA4/TO_SCN9A plasmid			
COMPONENT		**VOLUME (µl)**	
PCR grade water		Make up to total volume = 50.0	
10X NEBuffer 3.1		5.0	
BglII (10.0 U/µl)		1.0	
Plasmid DNA		Volume for 1.0 µg	
Thermocycling Parameters			
STAGE	**TEMP (°C)**	**TIME**	**CYCLES**
Incubation	37	2 hours	---
Hold	4	∞	---
Restriction Enzyme Digest Components for pJTI-R4-DEST_SCN9A plasmid			
COMPONENT		**VOLUME (µl)**	
PCR grade water		Make up to total volume = 25.0	
10X CutSmart Buffer		5.0	
NdeI (20.0 U/µl)		0.5	
HindIII-HF (20.0 U/µl)		0.5	
Plasmid DNA		Volume for 500 ng	
Thermocycling Parameters			
STAGE	**TEMP (°C)**	**TIME**	**CYCLES**
Incubation	37	2 hours	---
Enzyme Heat Inactivation	80	20 mins	---
Hold	4	∞	---

2.3.6 – Plasmid Sequence Verification

All plasmid maxi-preps were sequence verified before use in molecular biology experiments. Sequencing primers were designed to cover the entire *SCN9A* insert and immediately surrounding regions of the plasmid backbone (see Appendix B). Sanger sequencing was initially done manually in-house using the Big Dye Terminator v.3.1 cycle sequencing kit and ABI 3730xl DNA analyser (Applied Biosystems). We later moved to using the Genewiz commercial Sanger sequencing service.

DNA inputs for Sanger sequencing were prepared in 96-well plates as described in Table 2.6, followed by an ethanol purification protocol to remove salts and phenol from the PCR products. First, sodium acetate-ethanol solution was added to PCR products and left at room temperature for 5 minutes.

Plates were spun at 4000 rpm for 30 minutes in a Beckman centrifuge to pellet the precipitated DNA, and then spun inverted on absorbent paper at 400 rpm for 1 minute to remove the supernatant. Pellets were washed with 200 µl of 70% (v/v) ethanol and spun at 4000 rpm for 15 minutes. Supernatant was removed as before followed by a second 70% ethanol wash and spin. After the final removal of supernatant, 10 µl HiDi Formamide (Applied Biosystems) was added to each well and plates were run on the DNA analyser.

Table 2.6: Reaction Components & Thermocycling Protocol for Sanger Sequencing Inputs

ABI Sanger Sequencing Reaction Components			
COMPONENT		**VOLUME (µl)**	
PCR grade water		5.25	
Sequencing Primer (20 µM)		1.0	
Plasmid DNA Template (200 ng/µl)		1.0	
BigDye™ Buffer (5X)		2.0	
BigDye™ Terminator 3.1 Ready Reaction Mix		0.75	
Thermocycling Parameters			
STAGE	**TEMP (°C)**	**TIME**	**CYCLES**
Initiation	96	1 minute	---
Denaturation	96	10 seconds	X25
Annealing	50	5 seconds	
Extension	60	4 minutes	
Hold	4	∞	---

2.3.7 – Plasmid Mutagenesis

All novel CIP mutations were introduced into the wild-type version of pcDNA4/TO_SCN9A and pJTI-R4-DEST_SCN9A plasmids using the QuikChange II XL site directed mutagenesis kit (Agilent Technologies), which is optimised for larger and more difficult constructs. The online QuikChange Primer Design Program was used to generate optimal mutagenesis primers, with considerations to primer length, melting temperature, GC content and terminal base choice. Mutagenesis primers are listed in Table 2.7; those for A1236E and A1687P substitutions were only used for the pJTI-R4-DEST_SCN9A plasmid.

Mutagenesis reactions were prepared and run as described in Table 2.8. The reaction products were subsequently incubated with 1 µl DpnI enzyme at 37°C for 1 hour to digest non-mutagenized template DNA. The isolated mutagenized constructs were then transformed into Stbl2 cells, grown to maxi-culture stage and sequence verified as described in Sections 2.3.5 and 2.3.6.

Table 2.7: SDM Primers for *SCN9A* Constructs

PRIMER ID	PRIMER SEQUENCE
L75P-F	GTGTCCGAGCCCCCGGAAGATCTGGAC
L75P-R	GTCCAGATCTTCCGGGGGCTCGGACAC
T342M-F	AACCCCGACTACGGCTACATGAGCTTCGACACC
T342M-R	GGTGTCGAAGCTCATGTAGCCGTAGTCGGGGTT
R896W-F	CTGCACCCTGCCCTGGTGGCACATGAA
R896W-R	TTCATGTGCCACCAGGGCAGGGTGCAG
R911H-F	GCTTTCTGATCGTGTTTCATGTGCTGTGTGGCGAGTGG
R911H-R	CCACTCGCCACACAGCACATGAAACACGATCAGAAAGC
A1236E-F	TGCTGCTGAAGTGGATCGAGTACGGCTATAAGACCTAC
A1236E-R	GTAGGTCTTATAGCCGTACTCGATCCACTTCAGCAGCA
A1687P-F	ATCACCACCTCCCCCGGCTGGGATG
A1687P-R	CATCCCAGCCGGGGGAGGTGGTGAT
G1725R-F	GCAACCCCAGCGTGCGCATCTTCTACTTC
G1725R-R	GAAGTAGAAGATGCGCACGCTGGGGTTGC

Table 2.8: Reaction Components & Thermocycling Protocol for SDM of *SCN9A* Constructs

Mutagenesis Reaction Components			
COMPONENT		**VOLUME (µl)**	
PCR grade water		38.0	
Reaction Buffer (10X)		5.0	
Plasmid DNA Template (10 ng/µl)		1.0	
Forward SDM Primer (125 ng/µl)		1.0	
Reverse SDM Primer (125 ng/µl)		1.0	
dNTP mix		1.0	
QuikSolution Reagent		3.0	
PfuUltra Polymerase		1.0	
Thermocycling Parameters			
STAGE	**TEMP (°C)**	**TIME**	**CYCLES**
Initiation	95	1 minute	---
Denaturation	95	50 seconds	X19
Annealing	60	50 seconds	
Extension	68	11 minutes	
Final Extension	68	7 minutes	
Hold	4	∞	---

2.3.8 – General Maintenance of Cell Lines

HeLa and HEK293 cell lines were used at CIMR for transient expression studies. HeLa cells were cultured in Minimal Essential Media (MEM) with 10% Fetal Bovine Serum (FBS), both from Sigma. HEK293 cells were cultured in Dulbecco's Modified Essential Media (DMEM) from Gibco with 10% FBS (Sigma). All cells were grown in 75 cm^2 tissue-culture treated flasks, incubated at 37°C, 5% CO_2, and split when sub-confluent at a 1:10 ratio twice a week with Trypsin-EDTA solution (Corning). To plate cells for experiments, cells were gently dissociated to ensure a homogeneous suspension, then 10 µl was taken and mixed with 10 µl trypan blue stain (Invitrogen). Both chambers of a Countess Cell Counting Chamber Slide (Invitrogen) were loaded with 10 µl trypan blue-stained cells, for live cell concentration measurements using a Countess II Automated Cell Counter (Applied Biosystems). An average of the two measurements was taken for dilution calculations as required per experiment.

For high-throughput imaging and manual patch clamp electrophysiology studies at AstraZeneca, several cell lines were used. Both HeLa and HEK293 cell lines were maintained in MEM (Gibco), supplemented with 10% FBS and 1% non-essential amino acids (NEAAs). The HEK hNav.7 cell line, stably expressing untagged human Nav1.7, was cultured in DMEM/F-12 (Gibco) with 10% FBS and 1% NEAAs. The HEK JI TREX Nav1.7-FLAG stable cell line, with doxycycline-inducible expression of FLAG-tagged Nav1.7, was grown in DMEM (Gibco) with 10% dialysed FBS, 1% NEAAs, 5 µg/ml Blasticidin S (Gibco) and 1 mg/ml Geneticin (Gibco).

All cells were maintained in 175 cm^2 tissue-culture treated flasks. Cells were split upon reaching ~75% confluency with 2 ml Accutase (Sigma) and cell suspensions were prepared as above for manual cell counting using C-Chip disposable haemocytometers (NanoEntek). To induce gene expression in the HEK JI TREX Nav1.7-FLAG stable cell line, doxycycline hydrochloride (MP Biomedicals) was used at a final concentration of 1 µg/ml in cell culture media for 16-24 hours before experiments. Fresh aliquots at stock concentration 1 mg/ml were used per experiment.

Generation of new wild-type and mutant HEK JI TREX Nav1.7-FLAG stable cell lines at AstraZeneca is described in detail in the next section. Once transferred to CIMR, cells were maintained in high glucose DMEM with L-glutamine (Sigma) supplemented with dialysed FBS (Sigma), 1% NEAAs (Sigma), 5 µg/ml Blasticidin S (Alfa Aesar) and 2 mg/ml G418 disulfate (Alfa Aesar). Standard FBS can contain tetracycline from the animal's diet, therefore dialysed FBS was essential to prevent basal gene expression.

2.3.9 – Generation of HEK JI TREX Nav1.7-FLAG Stable Cell Lines

To generate cell lines stably expressing Nav1.7, I used the Jump In T-REx HEK 293 kit (Thermo Scientific) as summarised in the schematic diagram and timeline in Figure 2.5. The wild-type pJTI-R4_DEST_SCN9A plasmid encoded an identical Nav1.7 construct to that used in transient expression experiments. For each Nav1.7 mutant cell line, the pJTI-R4-DEST_SCN9A plasmid was mutagenized, propagated and sequence verified as described in Sections 2.3.5 - 2.3.7, including a previously characterised *SCN9A*-CIP mutant A1236E[208] as an additional control for electrophysiological analysis. The commercially available pJTI R4 EXP CMV-TO EmGFP pA vector was used as a positive control during cell line generation.

The HEK JI TREX parental cell line has been engineered to carry a single retargeting acceptor site '*attP*' which allows for site-specific homologous recombination with plasmids carrying the partner '*attB*' site, but only catalysed in the presence of R4 integrase[245]. Alongside the *attP* site is the promoter-less *NeoR* gene, which would otherwise confer resistance to neomycin and G418 antibiotics. The final critical feature in this system is the stable expression of the TetR protein, as explained in Section 2.3.4. The pJTI-R4-DEST vector allows for Gateway cloning in one's gene of interest (GOI) under the control of the CMV promoter and two TetO sequences (CMV-TO). In addition to the *attB* site, the donor plasmid also carries the mammalian EF1α promoter sequence from human elongation factor 1 alpha.

Upon co-transfection of pJTI-R4-DEST_SCN9A and pJTI-R4-Int (encoding R4 integrase) plasmids into HEK JI TREX parental cells, the recombination event unravels the donor sequence such that EF1α is now positioned upstream of *NeoR* to constitutively drive its expression, and the CMV-TO driven *SCN9A* construct is simultaneously integrated into the cell genome. The recombination event splits the original attachment sites to form '*attL*' and '*attR*' sites, resulting in unidirectional genome integration when the corresponding excisionase enzyme is absent. Cells are subsequently put under selective pressure of neomycin/G418; only cells that have undergone successful integration at the *NeoR* site should survive, forming the basis of a polyclonal but isogenic cell population.

A kill curve was run to determine the optimal antibiotic concentration for selection of transformed cell colonies. Two 6-well plates were prepared with 2 ml HEK JI TREX cell suspension plated at a seeding concentration of 6 x 10^5 cells/ml in each well, grown in Geneticin-free culture medium. The next day, one plate was co-transfected with the wild-type pJTI-R4-DEST_SCN9A and pJTI-R4-Int plasmids, while the second plate underwent a mock transfection lacking any plasmid DNA. After 24 hours, the 6 wells per plate were transferred to individual T25 flasks in selection media with increasing concentrations

of Geneticin: 0, 1, 2, 4, 8 and 16 mg/ml. Media was changed every 2-3 days and flasks were monitored daily for cell death and colony growth over 3-4 weeks. Observations and advice from colleagues familiar with the Jump-In system determined 2 mg/ml as the optimal dose for slow growing colonies.

Transfection complexes were prepared per well as recommended in the system manual; total 2.5 µg DNA at a 1:1 molar ratio of pJTI-R4-Int and pJTI-R4-DEST_SCN9A plasmids was diluted in 0.5 ml OptiMEM (Gibco), followed by additions of 2.5 µl Plus Reagent and 6.25 µl Lipofectamine LTX (Invitrogen). The mixture was incubated for 30 minutes at room temperature before being added dropwise to cells. Four transfection controls were run alongside the experimental *SCN9A* transfections: 1) mock transfection as described above, 2) OptiMEM alone, 3) transfection with wild-type *SCN9A* plasmid but lacking R4 Integrase, 4) complete transfection complex with the EmGFP positive control vector. Media changes and monitoring were conducted as for the kill curve. After 5-10 days, sufficient colony growth was observed for cells to be resuspended and plated in T175 flasks. Once confluent, cell stocks were frozen down at the first passage in Recovery Cell Culture Freezing Medium (Gibco) and maintained as described in the previous section.

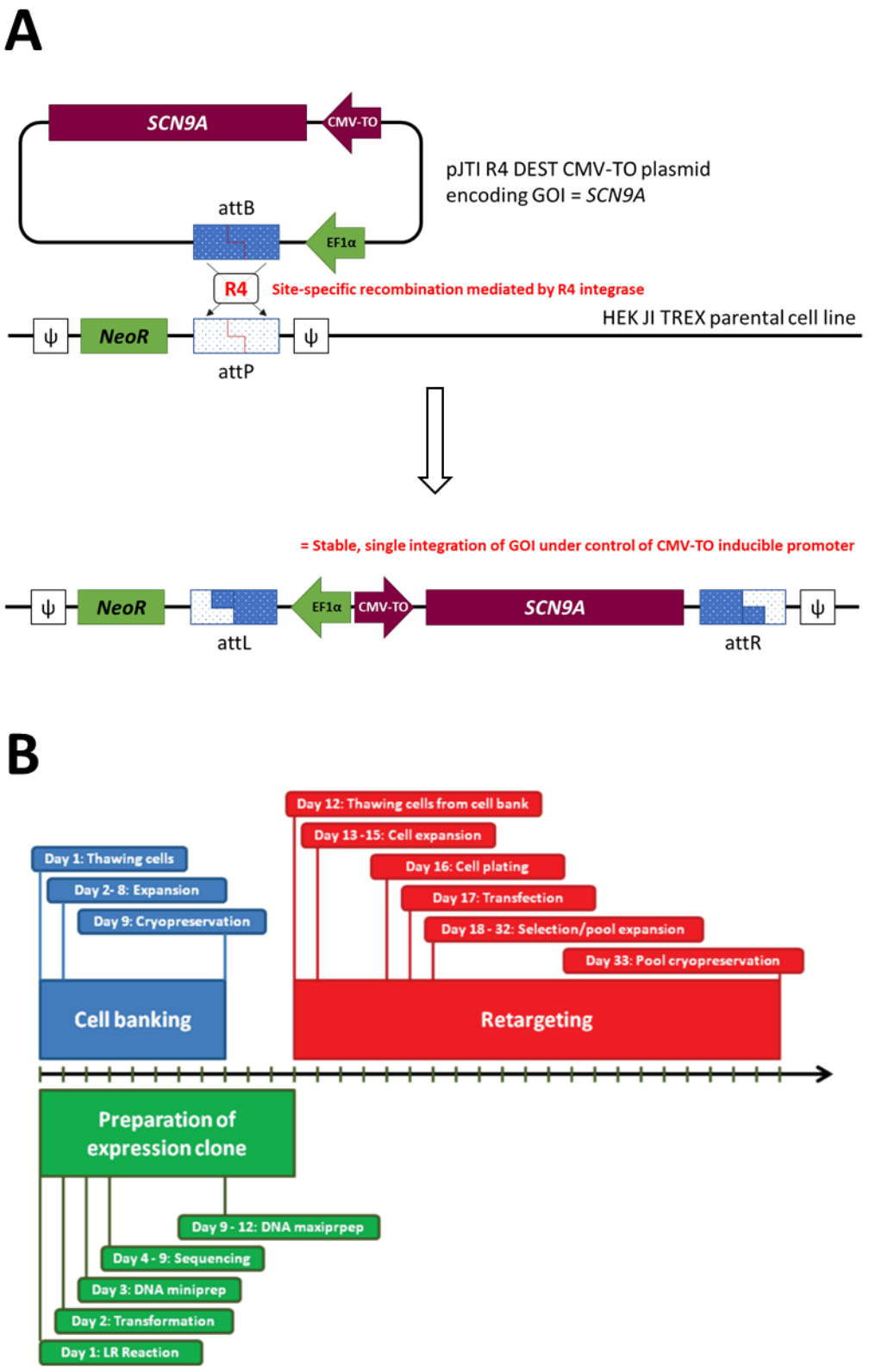

Figure 2.5: Site-specific recombination technology for HEK JI TREX stable cell line generation
Site-specific, R4-mediated homologous recombination technology shown in (A) is exploited to produce polyclonal, stable cell lines using the HEK JI TREX system. The timeline for cell line generation (B) is taken from the manufacturer's Jump-In T-REx HEK293 Retargeting Kit User Guide.

2.3.10 – Nav1.7 Subcellular Localisation Studies Using Confocal Microscopy

Nav1.7 subcellular localisation in the endoplasmic reticulum (ER) was assessed by fixed-cell immunocytochemistry and visualisation using confocal microscopy. Preliminary studies were conducted on transiently transfected HeLa cells with pcDNA4/TO_SCN9A plasmids, and observations were confirmed in the HEK JI TREX Nav1.7-FLAG stable cell lines.

Coverslips were sterilised with 70% ethanol, coated with poly-L-lysine solution (Sigma) and placed in individual wells of a 6-well plate. For transient expression studies, a 2 ml suspension of HeLa cells was plated at a seeding concentration of 1.5 x 10^5 cells/ml in each well. Cells were transiently transfected the next day using FuGENE HD transfection reagent (Promega) at a 3:1 ratio of reagent to DNA. For each well, 2 µg of DNA was diluted in 100 µl of OptiMem (Gibco) and mixed gently, followed by the addition of 6 µl FuGENE HD. The transfection solutions were gently mixed again and incubated at room temperature for 15 minutes before dropwise addition onto corresponding wells. Plasmid DNA concentration and purity was checked before each transfection.

At 48 hours post-transfection, media was removed and cells were washed thrice in 0.1% Tween-20 phospho-buffered saline solution (PBS-T), and again between the following sequential incubations at room temperature: 1) fixation with 4% paraformaldehyde solution in PBS (PFA) (Thermo Scientific) or chilled methanol for 10 minutes; 2) permeabilisation with a 0.3% Triton X-100 solution in PBS (PBS-Tx) (Sigma) for 10 minutes; 3) blocking non-specific antibody binding with a 10% normal donkey serum (NDS) (Sigma) and 10% bovine serum albumin (BSA) (Sigma) solution made in PBS-T for 30 minutes; 4) primary antibody co-stains for 1 hour; 5) fluorescently-conjugated secondary antibody staining for 1 hour. Coverslips were mounted onto slides using Prolong Diamond Antifade Mountant with DAPI (Invitrogen) and stored at 4°C.

For imaging experiments on stable cell lines, the immunocytochemistry protocol was slightly adapted. Cells were plated as above in growth medium with 1 µg/ml doxycycline. After 24 hours, media was removed and cells were washed thrice in PBS, and again between the following sequential incubations at room temperature: 1) fixation with 4% PFA for 10 minutes; 2) permeabilisation with a 0.1% PBS-Tx for 10 minutes; 3) blocking non-specific antibody binding with a 10% NDS and 10% BSA solution made in PBS-Tx for 1 hour. After removing the blocking buffer, cells were incubated with primary antibodies at 4°C overnight. The next day, cells were washed thrice in PBS followed by incubation with fluorescently conjugated secondary antibodies for 1 hour at room temperature. After the final PBS

washes, coverslips were mounted onto slides using Prolong Diamond Antifade Mountant with DAPI (Invitrogen) and stored at 4°C.

Nav1.7-FLAG was detected using mouse anti-FLAG (Clontech, #635691) in transiently expressing HeLa cells and mouse anti-Nav1.7 (Merck, #MABN41) in stable HEK JI TREX lines; identical Nav1.7 staining patterns were observed with both antibodies. Rabbit anti-KDEL (Abcam, #ab176333) was used as a marker for the endoplasmic reticulum. Donkey anti-rabbit AF488 (Invitrogen) and donkey anti-mouse AF546 (Invitrogen) secondaries were used for fluorescent detection.

All images were acquired using the LSM880 confocal microscope (Zeiss) with a 63x magnification, planar-apochromatic, 1.4NA oil immersion lens. Excitation by Diode 405 nm, Argon 488 nm and Diode 561 nm lasers was used for the detection of DAPI staining, AF488 and AF546 fluorophores respectively. The Airyscan detector feature was used to improve signal-to-noise ratio in images taken of stable cell lines[246].

2.3.11 – Nav1.7 Plasma Membrane Localisation Studies Using Widefield Imaging

Nav1.7 plasma membrane localisation was observed by fixed-cell immunocytochemistry and visualisation using the ImageXpress Micro XLS Widefield High-Content Analysis System (Molecular Devices), allowing for unbiased and automated image acquisition across multiple sites per well. MetaXpress image analysis software can identify individual cells per image by nuclear staining and programmable measurements. Custom modules can be used to create masks of various cell compartments based on high-contrast, specific fluorescence of chosen markers in FITC and/or Cy5 imaging channels.

Optimisation of plasma membrane markers was attempted in HeLa, HEK293 and HEK JI TREX Nav1.7-FLAG cell lines, plated at a seeding density of 5,000 cells/well in PDL-coated, optically clear bottom 96-well plates (Perkin Elmer). Transient transfection of HEK293 cells was done after 1 day in vitro, using the FuGENE 6 transfection reagent (Promega) in a 3:1 ratio of reagent to DNA, made up to 100 µl with OptiMem (Gibco).

After 24 hours transfection, media was removed and cells were washed in HBSS (Gibco) before being fixed for 10 minutes with 4% PFA or ice-cold methanol. Cells were washed twice with 0.1% PBS-Tx, followed by a 10 minute incubation at room temperature to permeabilise cells. Cells were then incubated with a 5% NDS (Abcam), 0.1% PBS-Tx blocking buffer for 1 hour at room temperature. Primary antibodies were diluted in blocking buffer for a further 1 hour incubation at room temperature. Cells were then washed thrice before being incubated with fluorescently conjugated secondary antibodies in blocking buffer for another hour; Hoechst stain (Invitrogen) was added during the final 10 minutes of this incubation. Finally, cells were washed thrice again in PBS-Tx and stored in PBS for imaging the same day.

Fixation method was chosen based on plasma membrane marker choice – 4% PFA for fluorescently conjugated wheat germ agglutinin (WGA-488) (Invitrogen, W11261) or ice-cold methanol for rabbit anti-Na^+K^+ ATPase antibody (Abcam, #ab76020). Mouse anti-FLAG (Clontech, #635691) was used to detect Nav1.7-FLAG in co-staining images presented here; identical staining patterns were observed with mouse anti-Nav1.7 (Merck, #MABN41). Donkey anti-rabbit AF488 (Invitrogen) and donkey anti-mouse AF647 (Invitrogen) secondaries were used for fluorescent detection. Hoechst stain was used for labelling nuclei, freshly prepared at 2 µg/ml in PBS. All images were acquired at 60X magnification with a planar-apochromatic objective. Illumination settings were programmed to DAPI, FITC and Cy5 for Hoechst, AF488 and AF647 fluorophore detection respectively.

2.3.12 – Nav1.7 Cell-Surface Biotinylation

To compare levels of proportions of plasma membrane-localised Nav1.7 between WT and mutants, the Pierce Cell Surface Protein Isolation Kit (Thermo Scientific) was used. Specific chemical properties of the labelling reagent, Sulfo-NHS-SS-Biotin, are exploited to selectively isolate surface-localised proteins, see Figure 2.6. Crucially, the negatively charged sulfonate group prevents permeation through the cell membrane. The N-hydroxysuccinimide (NHS) ester reacts with primary amines, commonly outward facing, positively charged side-chain groups of Lysine residues, to form a stable amide bond. The biotin group is used to extract labelled proteins via a streptavidin column, and the disulfide bond is cleaved in reducing conditions to remove biotin from surface proteins at the final elution step.

For transient transfections, HEK293 cells were plated at 1.5 x 10^5 cells/ml per 100 mm dish and transfected the next day at a 3:1 ratio of 56 µl FuGENE HD to 19 µg plasmid DNA in a total volume of 879 µl OptiMEM. After 24 hours transfection, biotinylation was performed according to manufacturer's instructions. For HEK JI TREX Nav1.7-FLAG cell lines, cells were plated at 1.5 x 10^5 cells/ml per 100 mm dish, and Nav1.7 expression was induced with doxycycline the next day; after 24 hours, biotinylation proceeded as described.

Briefly, cells were washed twice with ice-cold PBS and then incubated with 0.25 mg/ml EZ-Link Sulfo-NHS-SS-Biotin per dish, for 30 minutes at 4°C. The reaction was stopped with the provided quenching solution containing 100 mM glycine. Cells were then pelleted and washed twice in ice-cold TBS, re-suspended in 500 µl lysis buffer, and disrupted by sonication. Cell lysis proceeded on ice for 30 minutes with periodic vortexing. A 100 µl aliquot of lysed cells was set aside as the "total" fraction. The remainder of the lysed cells were added to a NeutrAvidin agarose column and incubated for 1 hour at room temperature to bind the biotinylated surface proteins. After 3 washes with wash buffer, the column was heated for 5 minutes at 95°C and biotinylated proteins ("surface" fraction) were eluted in 400 µl NuPAGE LDS sample buffer (Invitrogen) containing 50mM dithiothreitol (DTT). EDTA-free Protease Inhibitor Mini Tablets (Thermo Scientific) were added to the supplied lysis and wash buffers.

Due to limited availability of kits during the covid-19 pandemic, experiments comparing transient and stable expression of WT Nav1.7, and for replicates assessing surface-localised A1687P mutant Nav1.7 were scaled down. This meant per condition, 2 wells of a 6-well plate were biotinylated (approximately three-fold reduction in surface area) and half volumes of assay reagents were used.

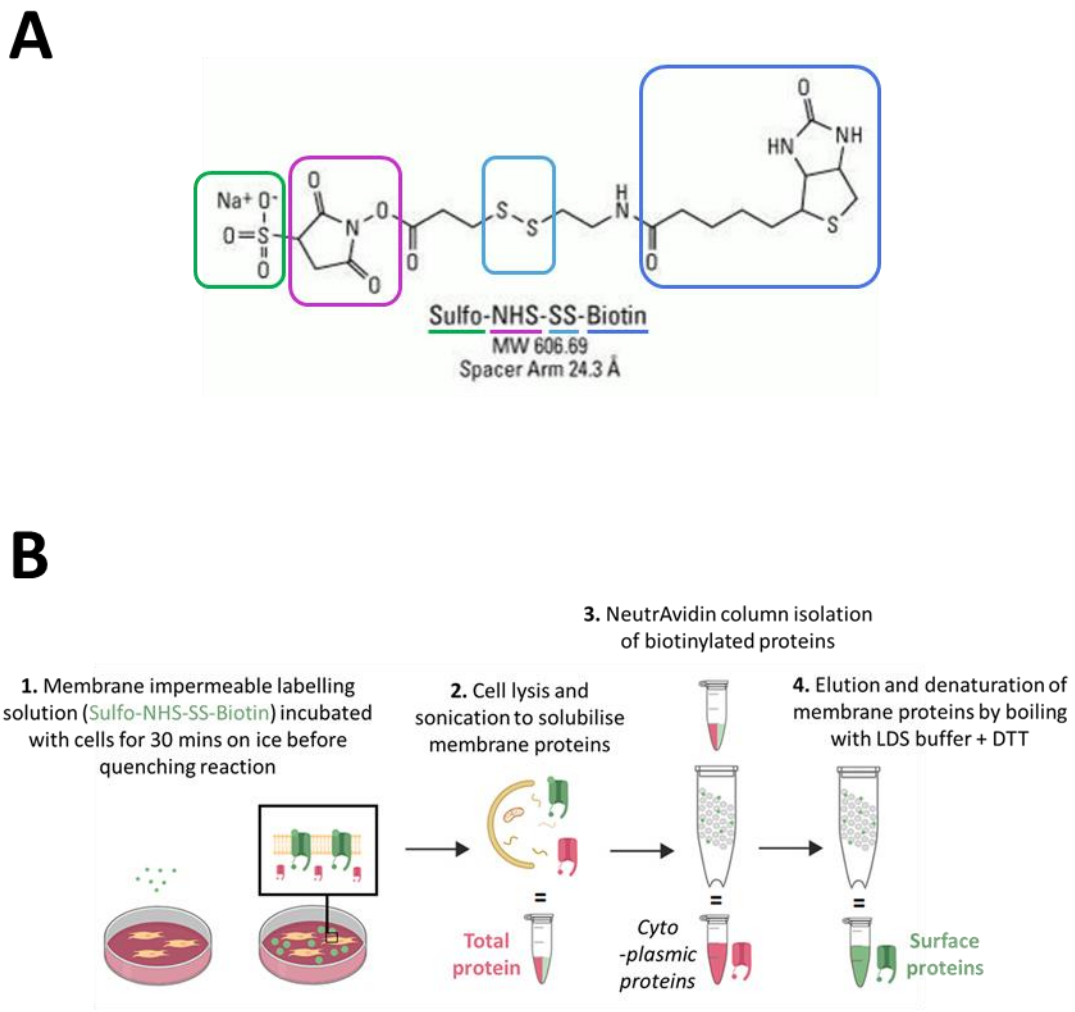

Figure 2.6: Cell-surface biotinylation assay
Schematic overview of (A) key biochemical principles and (B) protocol steps, that allow for the selective isolation of cell-surface proteins. *Figure created with BioRender.com.*

2.3.13 – Western Blots and Band Densitometry Analysis

Samples from cell-surface biotinylation experiments were analysed by western blot and band densitometry. Input samples were prepared in LDS sample buffer with 2.5% β-mercaptoethanol and incubated for 10 minutes at 70°C; these conditions were optimised to produce the tightest bands for densitometry analysis. As transiently transfected Nav1.7 protein levels could not be controlled between genotypes and experiments, equal volumes of total and surface fractions from each dish were loaded per gel against a 10 to 250 kDa prestained protein ladder (Thermo Scientific).

Precast 3-8% Tris-Acetate Protein Gels (Invitrogen) were run in NuPAGE Tris-Acetate SDS Running Buffer (Invitrogen) at 120V for 1.5-2 hours. Gels were transferred at 120V for 1.5 hours, onto 0.45 µm pore size PVDF membranes (GE Healthcare) in NuPAGE Transfer Buffer (Invitrogen) with 20% methanol. NuPAGE Antioxidant (Invitrogen) was added to both the running and transfer buffers according to the NuPAGE Technical Guide; the antioxidant prevents re-oxidation of proteins during electrophoresis and transfer, which appeared to reduce the extent of band smearing of high molecular weight proteins. For later experiments comparing WT Nav1.7 transient versus stable expression and A1687P mutation replicates, gels were transferred at 20V for 13 minutes using the iBlot2 dry transfer system and PVDF membranes.

Blots were washed thrice for 5 minutes each in Tris-buffered saline with 0.1% Tween20 (TBS-T), then incubated for 1 hour at room temperature with a blocking buffer of 5% Marvel Milk and 1% BSA in TBS-T. Membrane segments were incubated with primary antibodies, on a rocker overnight at 4°C. The next day, blots were washed thrice for 5 minutes each in PBS-T before incubating with secondary antibodies for 1 hour at room temperature. After the final washes, membranes were immersed in Amersham ECL Prime Western Blotting Detection Reagent (GE Healthcare) for 1 minute, drip-dried and immediately imaged using the ChemiDoc MP Imaging System and Image Lab software (Bio-Rad).

All antibodies were diluted in blocking buffer. Membranes were probed with mouse anti-Nav1.7 (Merck, #MABN41), rabbit anti-Na^+K^+ ATPase (Abcam, #ab76020), mouse anti-actin (Sigma, #A2228) and rabbit anti-calnexin (Abcam, #ab13504). Intracellularly restricted proteins actin and calnexin were used as negative controls of biotinylation, while Na^+K^+ ATPase was used as a positive control. HRP-linked secondary antibodies, anti-mouse IgG (Cell Signaling Technology, #7076) and anti-rabbit IgG (Cell Signaling Technology, #7074) were used for chemiluminescent detection.

Images were taken at exposures before bands became saturated and exported in TIFF format for densitometry analysis in ImageJ. Surface band signal was divided by the total band signal to give the percentage proportion of surface-localised protein. Results are expressed as mean averages with with error bars representing standard error of the mean (SEM). Statistical tests were performed in GraphPad Prism 9 (GraphPad Software) with corrections chosen assuming unequal standard deviations and statistical significance set to $P < 0.05$. For comparing Nav1.7 mutations to WT in the transient expression system, Brown-Forsythe and Welch ANOVA test with Dunnett's T3 correction was chosen. For comparing WT Nav1.7 in the transient versus stable expression systems, values were expressed as mean ± SEM, and an unpaired, two-tailed t-test with Welch's correction was chosen to test statistical significance.

2.3.14 – Manual Patch Clamp Electrophysiology

Cells expressing WT or mutant Nav1.7 were manually patch clamped in the whole-cell configuration[247]. Sterilised coverslips were coated with poly-D-lysine solution and placed in individual wells of a 24-well plate. Cells were plated at low seeding density to ensure individual cells could be selected for patch clamping at 24-72 hours after plating of stable cell lines or post-transfection of HEK293 cells. All cells were maintained in antibiotic-free medium in 37°C, 5% CO_2 incubators, until coverslips were required for recordings. The HEK hNav1.7 stable cell line was used to confirm our experimental setup produced values for WT Nav1.7 comparable to the literature. For profiling Nav1.7 mutants, HEK293 cells were transiently co-transfected with pcDNA4/TO_SCN9A plasmids and pmaxGFP (Lonza) using FuGENE 6 (Promega) or by electroporation with AMAXA Cell Line Nucleofector Kit V (Lonza).

For chemical transfection, FuGENE complexes were assembled the day after plating as recommended online (https://www.promega.com/techserv/tools/FugeneHdTool/) for a 3:1 ratio of plasmid DNA to transfection reagent. Co-transfections of total 0.5 µg DNA per well were calculated based on a 3:1 molar ratio of SCN9A and GFP vectors respectively. Electroporation-based transfections were conducted the same day as plating. First, 1 x 10^6 cells per sample were re-suspended in 100 µl Supplemented Nucleofector solution, followed by addition of total 2.5 µg DNA at a 3:1 molar ratio of SCN9A to GFP plasmids. The suspension was moved to a cuvette for electroporation using the Nucleofector 2b device (Lonza) and pre-programmed electrical pulse parameters for HEK ATCC cells. Immediately after, 500 µl fresh culture media was added to cells, then further diluted to total 5 ml. Of this suspension, 100 µl was added per coverslip/well and topped up with media.

The recording chamber (Warner Instruments, #RC-24N) was set up on an inverted microscope (Nikon, #Eclipse TS100), fit with filter cubes and connected to an LED Fluorescence Excitation System (CoolLED, #pE-2) to identify fluorescent cells. The headstage (Molecular Devices, #CV-7B) was manoeuvred above the chamber with coarse controls, and then into bath solution and approaching cells using a micromanipulator (Burleigh, #PCS-500). The complete rig was placed within a Faraday cage on an air table (both TMC) to minimise electromagnetic noise and vibrational disturbances. The Multiclamp 700B amplifier and Digidata 1440A digitizer (both Molecular Devices) were used for taking current measurements, maintaining voltage-clamp and operating protocols.

Clean silver wire was sanded and chlorided by immersion in sodium hypochlorite solution for 1 hour, then washed briefly in sterile water before connection to the patch-clamp amplifier forming the measurement electrode. An Ag/AgCl pellet was used as the reference electrode, placed in the agar

bridge well of the recording chamber. Micropipettes of 1-4 MΩ resistance were produced using GC120F-10 borosilicate glass capillaries (Harvard Apparatus) and the p-97 micropipette puller (Sutter Instruments). Micropipette shanks were dipped in Sigmacote (Sigma) after filling with intracellular solution to reduce pipette capacitance in recordings[248].

Patch clamp recordings were conducted at room temperature, with extracellular bath solution and coverslips replaced in the recording chamber every hour of the session. Composition of intracellular and extracellular solutions are described in Table 2.9. Gigaseal formation and stability of the whole-cell configuration was most successful in convex, oval-shaped and medium-sized (~10-30 pF) cells. After making contact with the cell membrane, the holding potential was set to -60 mV to assist seal formation with high electrical resistance, before rapid negative pressure was applied using a 2 ml syringe to transition into the whole-cell configuration. Cells were given 3-5 minutes to stabilise in whole-cell mode, and stimulation proceeded once leak current was under 200 pA.

Table 2.9: Solutions for Manual and Automated Patch Clamp

Intracellular Solution			
COMPONENT	**CONCENTRATION (mM)**	**pH**	**OSMOLARITY (mOsm)**
Sodium chloride (NaCl)	10	7.3 (CsOH-titration)	Manual: 275 – 285 Auto: 305 – 315
Caesium fluoride (CsF)	140		
Calcium chelating agent (EGTA)	2		
pH buffer (HEPES)	10		
Extracellular Solution			
COMPONENT	**CONCENTRATION (mM)**	**pH**	**OSMOLARITY (mOsm)**
Sodium chloride (NaCl)	140	7.4 (NaOH-titration)	295 – 305
Potassium chloride (KCl)	2		
Calcium chloride ($CaCl_2$)	2		
Magnesium chloride ($MgCl_2$)	1		
pH buffer (HEPES)	10		

2.3.15 – Automated Patch Clamp Electrophysiology

For high-throughput assessment of biophysical properties of Nav1.7 mutants, the HEK JI TREX Nav1.7-FLAG stable cell lines were studied by automated patch clamp (APC) electrophysiology. In APC, cell suspensions are discharged over planar recording chips and settle onto sites assisted by negative pressure. Similar to manual patch, increasing negative pressure and rapid suction facilitate seal formation and membrane rupture. Notably in APC, the experimenter has no control over which cells attach to recording sites; thus, it is critical that the control and experimental variables, in this case expression of Nav1.7 WT versus mutants, are consistent across as many cells as possible.

QPlates used on the Sophion QPatch16 platform (Sophion Bioscience), can accommodate up to 16 cells being recorded simultaneously in the whole-cell configuration. As shown in Figure 2.7, intracellular and extracellular solutions are contained in separate compartments of the QPlate with their own channels for precise application of test and wash solutions where necessary. Reference (REF) and measurement (MEAS) electrodes are integrated per measurement site, and as new QPlates are used for each experiment, do not require ongoing maintenance.

HEK JI TREX Nav1.7-FLAG cell lines had been grown in T-25 flasks with or without induction by doxycycline for 24 hours. Cells were gently detached from flasks using Accutase, resuspended in serum-free FreeStyle Expression Medium (Gibco) and centrifuged at 800 RPM for 3 minutes. The pellets were gently resuspended by pipetting in FreeStyle media supplemented with 20 mM HEPES and trypsin inhibitor, then filtered through a 40 µm cell strainer and added to 96-well compound plates for use in experiments.

Automated electrophysiology experiments were performed in conjunction with John Linley (AstraZeneca, Cambridge, UK). All voltage-clamp protocols and composition of recording solutions were identical to those for manual patch clamp, although intracellular solution was made hyper-osmotic to extracellular solution in APC studies. Series resistance compensation was set to 70%.

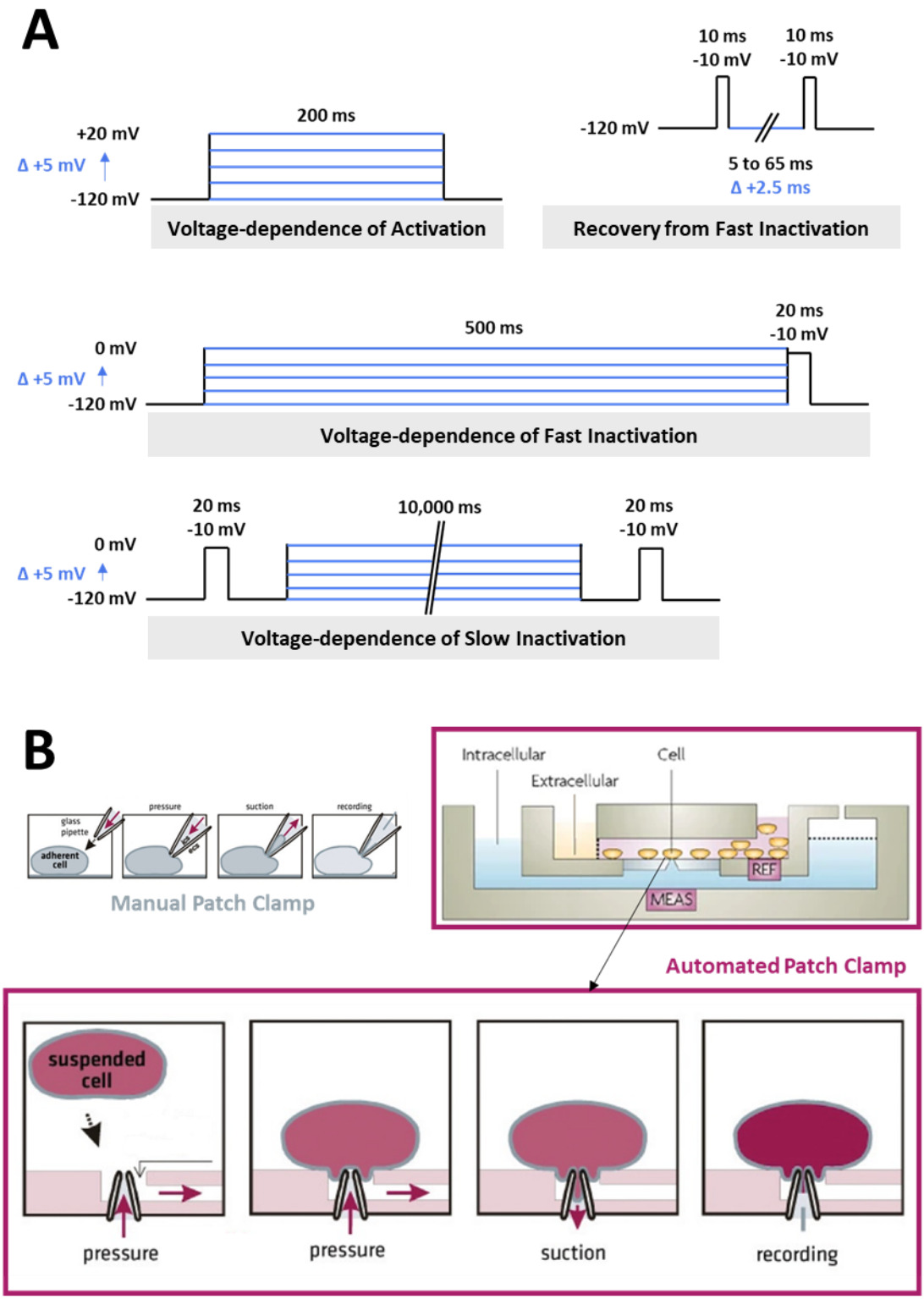

Figure 2.7: Protocols for manual and automated whole-cell voltage-clamp
(A) Voltage-clamp protocols designed to profile several biophysical properties of Nav1.7 by both manual and automated whole-cell electrophysiology; (B) Comparison of cell selection and seal formation procedures in manual versus automated patch-clamp techniques.

Image adapted from web page: "An Automated Approach To Solving Pharma's Cardiac Toxicity Conundrum" - https://www.ddw-online.com/an-automated-approach-to-solving-pharmas-cardiac-toxicity-conundrum-1292-201304/ *and (2008) Dunlop et al.* High-throughput electrophysiology: an emerging paradigm for ion-channel screening and physiology

2.3.16 – Voltage-Clamp Protocols

Programming of voltage-clamp protocols and data acquisition was performed using Clampex software (Molecular Devices), as illustrated in Figure 2.7A. Online P/N leak subtraction was executed before protocol sweeps, opposite in polarity to the waveform, where N=3 for activation and fast inactivation protocols and N=2 for the recovery from fast inactivation protocol. Prediction and correction modes for series resistance compensation were set to 70% to minimise voltage drop errors; liquid junction potentials were not corrected for.

A pulse protocol was performed on each cell first to test whether any Nav1.7 current was expressed, consisting of a 20 ms hyperpolarisation to -120 mV to ensure recovery from fast inactivation, followed by a 30 ms pulse to -10 mV. Each sweep of the following protocols began with cells being hyperpolarised to -120 mV for 50 ms and concluded by holding cells at -80 mV for several seconds between sweeps, to ensure all channels were available for activation at the start of the protocol in each sweep.

To assess voltage-dependence of activation, cells were depolarised in 5 mV steps from -110 to +20 mV for 200 ms to elicit transient Na^+ currents (INa_T). For voltage-dependence of fast inactivation, the same steps were applied for 500 ms to activate channels, followed immediately by a 20 ms pulse at -10 mV to measure available INa_T from non-inactivated channels. To determine kinetics of recovery from fast inactivation, two -10 mV pulses were applied to cells for currents to be measured (I1 and I2), between which was a single step at -120 mV for channels to recover from fast inactivation, whose duration ranged from 5 to 65 ms and increased by 2.5 ms each sweep.

For voltage-dependence of slow inactivation, a 20 ms pulse at -10 mV was applied to cells to elicit the maximum reference current (P1) then held at -120 mV for 50 ms for channels to recover from fast inactivation, followed by sustained depolarisation steps for 10 seconds. Cells were then held again at 50 ms at -120 mV to ensure the currents measured during the second -10 mV pulse (P2) were only from channels recovered from slow inactivation.

2.3.17 – Patch Clamp Data Analysis

Data were handled in Clampfit (Molecular Device) and Sophion Analyzer (Sophion) software for manual and automated patch clamp respectively. Raw data were exported to Microsoft Excel for normalisation, conductance and other calculations. Statistical analysis, curve-fitting and graph generation were completed in GraphPad Prism. Statistical comparisons of biophysical measurements produced with CsF- versus CsCl-based intracellular solutions, and at 48 hours versus 72 hours post-transfection by AMAXA electroporation, were performed using unpaired, two-tailed t-tests with Welch's correction. For peak current measurements from HEK JI TREX-Nav1.7-FLAG cell lines, Brown-Forsythe and Welch one-way ANOVA test was chosen, with Dunnett T3 correction for multiple comparisons. Results in the main text are depicted as mean averages ± SEM.

Currents from the voltage-dependence of activation protocol were transformed into conductance values using equation {1} below, where G represents conductance in Siemen units (S), I is current measured in picoamperes (pA), V is the membrane potential clamped at each voltage step in millivolts (mV) and V_{rev} is the reversal potential. Individual reversal potentials were generated per cell by fitting a linear regression across current datapoints at voltage steps 0 to 20 mV, then calculating the voltage at which there is no net flow of sodium ions (i.e. y=0).

$$G = \frac{I}{(V - V_{rev})} \quad \{1\}$$

For graphing voltage-dependences of activation and fast inactivation, conductance and current were normalised so that the value at each voltage step was expressed as a fraction of the peak amplitude. Boltzmann curves were fit using equation {2} for activation and {3} for inactivation, where "bottom" and "top" values were made constants equal to 0.0 and 1.0 respectively. G/G_{max} represents the available fraction of normalised conductance whereas I/I_{max} is the available fraction of normalised current. V50 in this context is the voltage of half-maximal conductance or current, V is the voltage step and k is the slope factor. The reported mean average V_{50} and k values were derived from Boltzmann curves fit for G-V and I-V data per individual cell.

$$G/G_{max} = Bottom + \frac{Top - Bottom}{1 + exp(\frac{V50 - V}{k})} \quad \{2\}$$

$$I/I_{max} = Bottom + \frac{Top \times Bottom}{1 + exp(\frac{V50 - V}{k})} \quad \{3\}$$

For voltage-dependence of slow inactivation, I2 was divided by I1 at each sweep to calculate the relative Na^+ current available after slow inactivation at increasing membrane potentials. Boltzmann curves were fit using equation {3} as described above. For recovery from fast inactivation, P2 was divided by P1 at each sweep to determine the fraction of current available as the cell was held at the recovery potential for increasing lengths of time. This curve was fit using equation {4} for one phase association from which k, tau and half-time values were derived per cell then averaged.

$$^{P2}/_{P1} = Y0 + (Plateau - Y0) \times (1 - \exp(-k \times time)) \qquad \{4\}$$

2.4 RESULTS

2.4.1 – *In silico* pathogenicity predictions of novel *SCN9A*-CIP mutations

Six missense mutations were identified from *SCN9A*-CIP patients, with residue annotation based on the 11S splice variant of Nav1.7 – Leu75Pro, Thr342Met, Arg896Trp, Arg911His, Ala1687Pro and Gly1725Arg, see Figure 2.3C. Sequence conservation analysis revealed complete conservation of each of the native residues when compared to Nav1.7 species orthologues, from large mammals to rodents as well as in the single voltage-gated sodium channel α-subunit from flies, as shown in Figure 2.8.

Multiple sequence alignment of the human Nav (hNav) family as shown in Figure 2.8 revealed 100% conservation of the following four native residues in Nav1.7 to their hNav paralogs – Leu75 in the N-terminal tail; Thr342 in the domain I:S5-S6 pore loop; Arg911 in the domain II:S5-S6 pore loop; Ala1687 in the domain IV:S5-S6 pore loop and final residue participating in the ion selectivity filter. The two remaining mutated amino acids in Nav1.7 were almost completely conserved across the human Nav family with the exception of Nav1.9 where Arg896 in the domain II:S5-S6 pore loop is a Histidine residue, and Gly1725 within the domain IV:S6 transmembrane segment is an Alanine.

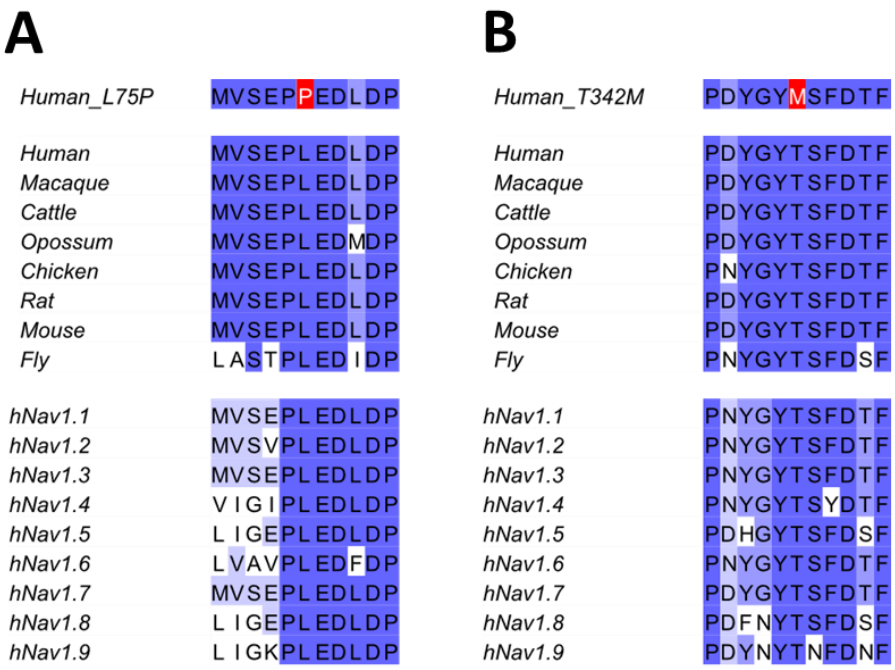

Figure 2.8: Nav1.7 sequence conservation across species and within the human Nav family
Multiple sequence alignments were produced for Nav1.7 channel sequences across species (including the single fly sodium channel gene) and for the human Nav family. Each *SCN9A*-CIP missense mutation is highlighted in red on the top line: (A) Leu75Pro, (B) Thr342Met, (C) Arg896Trp, (D) Arg911His, (E) Ala1687Pro, (F) Gly1725Arg

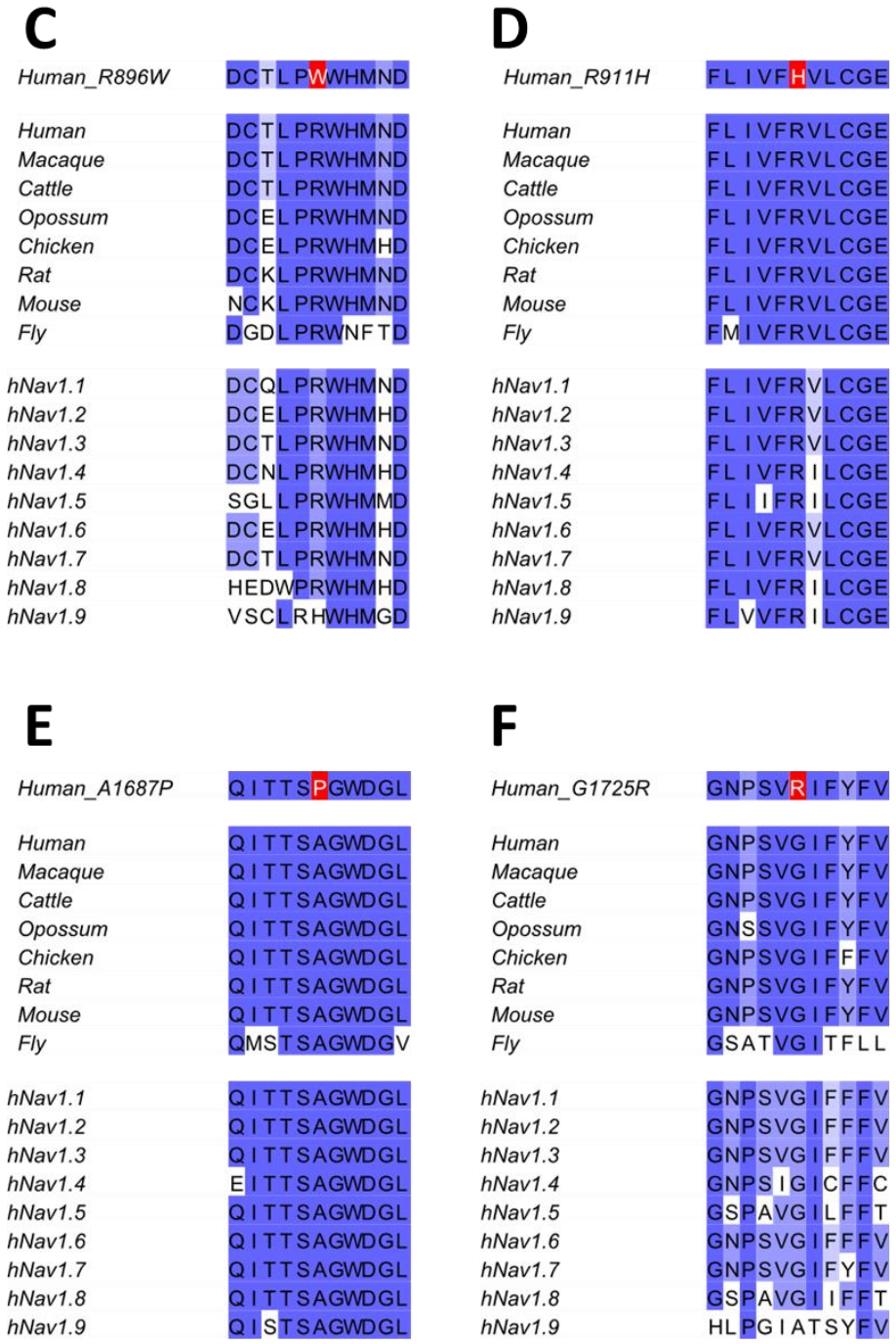

Figure 2.8: Nav1.7 sequence conservation across species and within the human Nav family
Multiple sequence alignments were produced for Nav1.7 channel sequences across species (including the single fly sodium channel gene) and for the human Nav family. Each *SCN9A*-CIP missense mutation is highlighted in red on the top line: (A) Leu75Pro, (B) Thr342Met, (C) Arg896Trp, (D) Arg911His, (E) Ala1687Pro, (F) Gly1725Arg

Pathogenicity predictions in Table 2.10 were obtained using the PolyPhen-2 tool with the HumVar prediction model which is trained to differentiate rare mutations that may cause drastic effects on protein function from mildly deleterious but abundant polymorphisms[249]. All *SCN9A*-CIP mutations were classified as probably damaging with the highest probability score of 1.000 given to mutations Thr342Met, Arg896Trp and Arg911His. The probability scores for Leu75Pro, Ala1687Pro and Gly1725Arg were slightly lower but still below the false positive rate threshold for the HumVar model.

Table 2.10: *In silico* Predictions of Pathogenicity of Novel *SCN9A*-CIP Mutations

***SCN9A* MUTATION**	**PREDICTION**	**PROBABILITY SCORE**
Leu75Pro	Probably Damaging	0.980
Thr342Met	Probably Damaging	1.000
Arg896Trp	Probably Damaging	1.000
Arg911His	Probably Damaging	1.000
Ala1687Pro	Probably Damaging	0.995
Gly1725Arg	Probably Damaging	0.996

2.4.2 – Locations of mutated residues within 3D Nav1.7 structure

The *SCN9A*-CIP mutations were visualised within the recently resolved hNav1.7 structure in an inactivated state, to compare the local environment of native residues and possible consequences of sidechain substitutions, coloured in red. The N-terminal tail density was insufficient to be resolved and so the Leu75Pro mutation is not presented. Thr342Met is displayed in Figure 2.9A-B looking at the channel from above (i.e. extracellular side) at a slight tilt; Arg896Trp is displayed looking at the channel from the side in Figure 2.9C-D; Arg911His, Ala1687Pro and Gly1725Arg are displayed looking directly into the pore from the extracellular side in Figures 2.9E-J.

Thr342 is located within the pore loop of the first domain, in close proximity to a sharp turn. Substitution to the larger, hydrophobic Methionine residue is shown in Figure 2.9B. Importantly, this mutation did not disrupt an O-linked glycosylated site as the only glycosylated residues resolved in this structure were at Asparagines 283, 1352, 1366 and 1375[240].

From annotation of the 11S Nav1.7 splice variant from Klugbauer et al.[166], Arg896 and Arg911 were predicted to be located between the domain II:S5-S6 transmembrane segments, i.e., within the pore loop. This was confirmed for both residues in the 3D structural model, see Figures 2.9C and 2.9E, and notably Arg911 was positioned within a portion of the pore loop with alpha-helical structure while Arg896 was in a disordered region. Arg911 was also only four residues away from Glu916, the second residue participating in the ion selectivity filter; the intervening residues are highlighted in yellow in Figure 2.9F. Both positively charged Arginines were substituted with the equally large and hydrophobic Tryptophan and Histidine residues respectively.

Ala1687 is the smallest and only uncharged residue contributing to the ion selectivity filter, in concert with Asp361, Glu916 and Lys1395. Substitution to the equally small and uncharged Proline is displayed in Figure 2.9H with the sidechain connected twice to the protein backbone. This mutation appeared not to interfere in the diameter of the permeation pathway. Gly1725 is located at the top of the final alpha-helical transmembrane segment in a tight turn. Substitution to the much larger and positively charge Arginine is shown in Figure 2.9J, with the new sidechain protruding towards the domain IV pore loop.

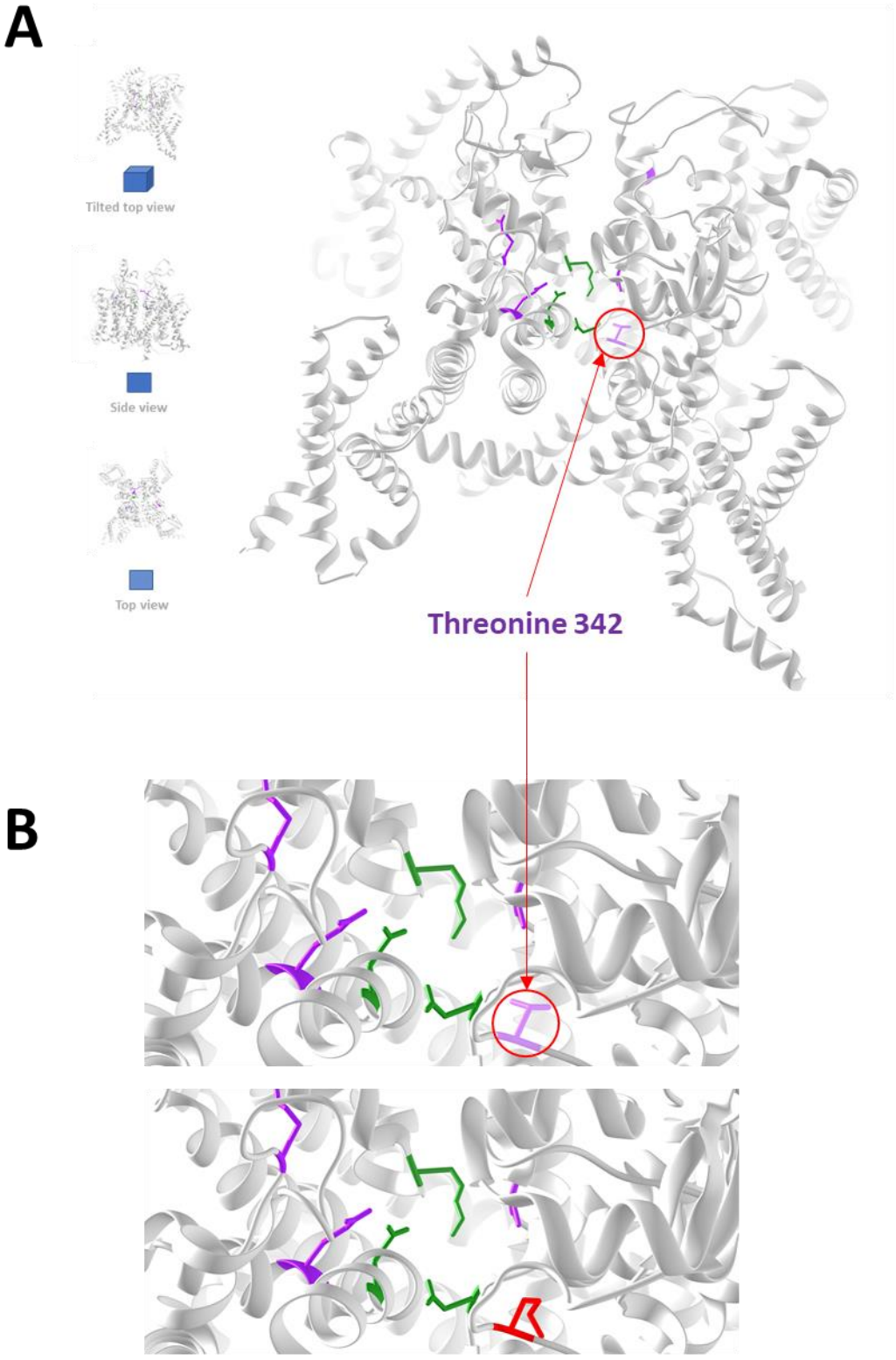

Figure 2.9: Human Nav1.7 atomic model highlighting amino acid substitutions from CIP patients
The hNav1.7 chain from PDB model 6J8G from (2019) Shen et al. is shown, with sidechains displayed in purple for the native residues at mutated locations. The three unaffected amino acids contributing to the ion selectivity filter are coloured green. Zoomed insets illustrate substitution with *SCN9A*-CIP mutations in red: (B) Thr342Met, (D) Arg896Trp, (F) Arg911His, (H) Ala1687Pro, (J) Gly1725Arg

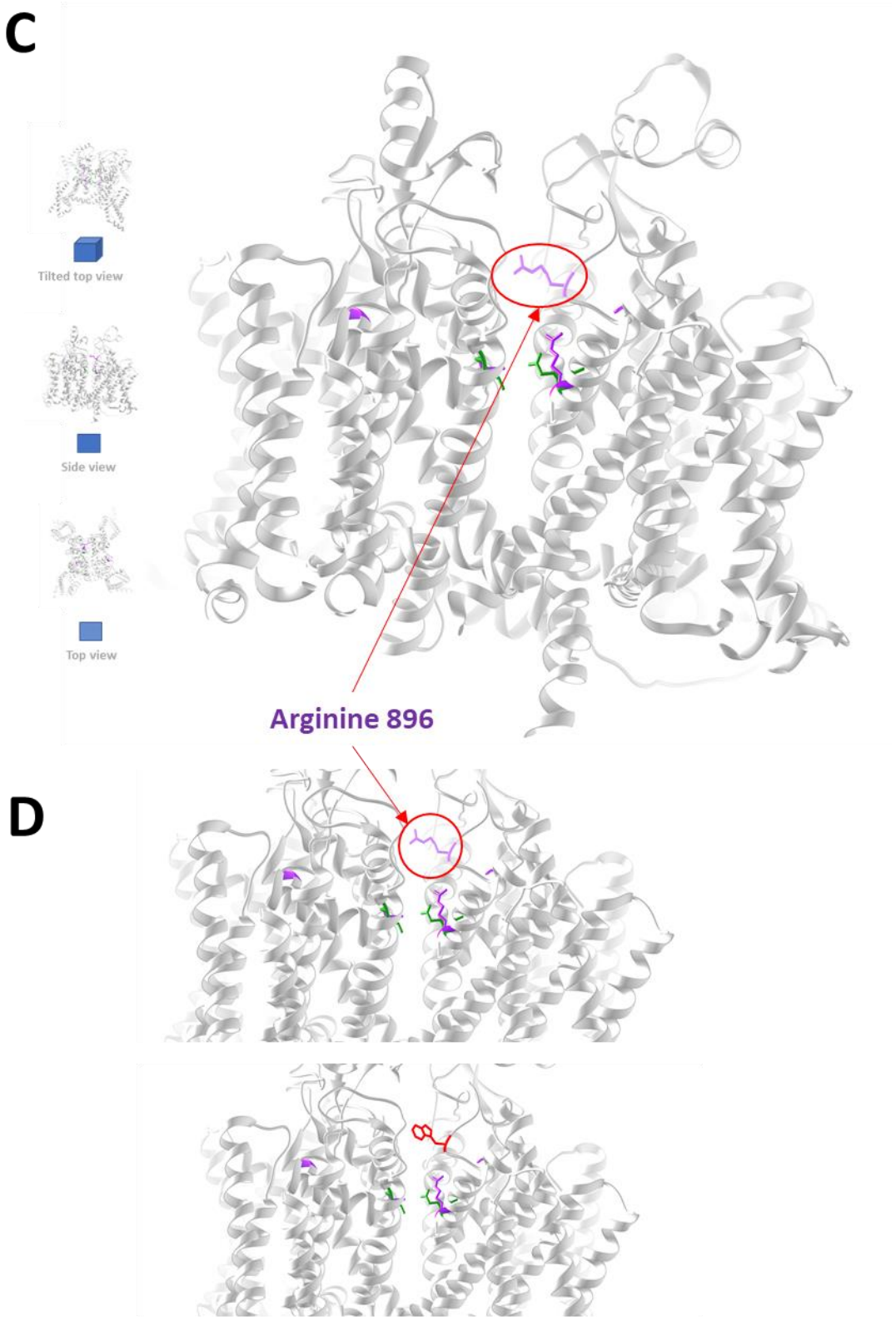

Figure 2.9: Human Nav1.7 atomic model highlighting amino acid substitutions from CIP patients
The hNav1.7 chain from PDB model 6J8G from (2019) Shen et al. is shown, with sidechains displayed in purple for the native residues at mutated locations. The three unaffected amino acids contributing to the ion selectivity filter are coloured green. Zoomed insets illustrate substitution with *SCN9A*-CIP mutations in red: (B) Thr342Met, (D) Arg896Trp, (F) Arg911His, (H) Ala1687Pro, (J) Gly1725Arg

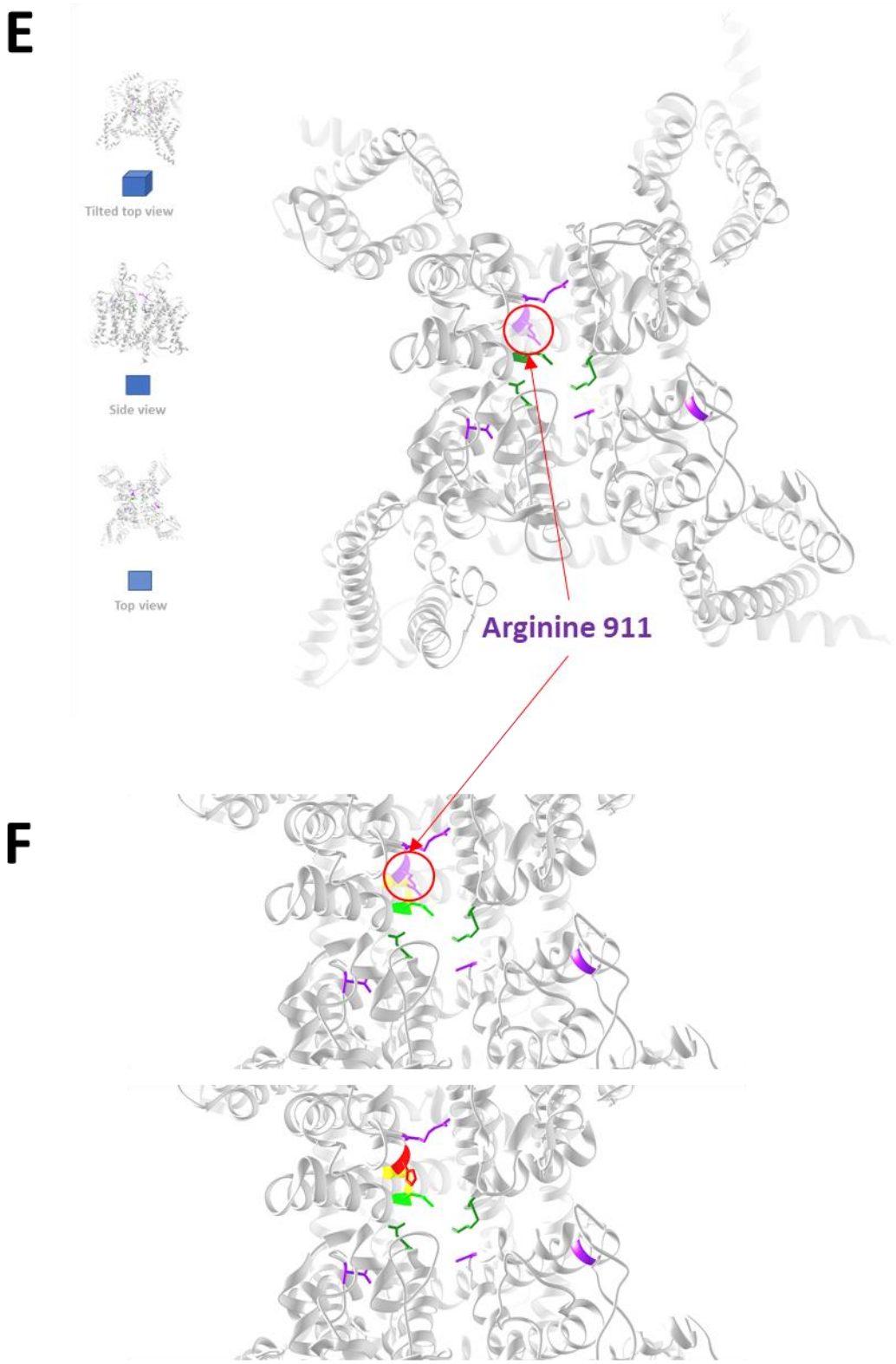

Figure 2.9: Human Nav1.7 atomic model highlighting amino acid substitutions from CIP patients
The hNav1.7 chain from PDB model 6J8G from (2019) Shen et al. is shown, with sidechains displayed in purple for the native residues at mutated locations. The three unaffected amino acids contributing to the ion selectivity filter are coloured green. Zoomed insets illustrate substitution with *SCN9A*-CIP mutations in red: (B) Thr342Met, (D) Arg896Trp, (F) Arg911His, (H) Ala1687Pro, (J) Gly1725Arg

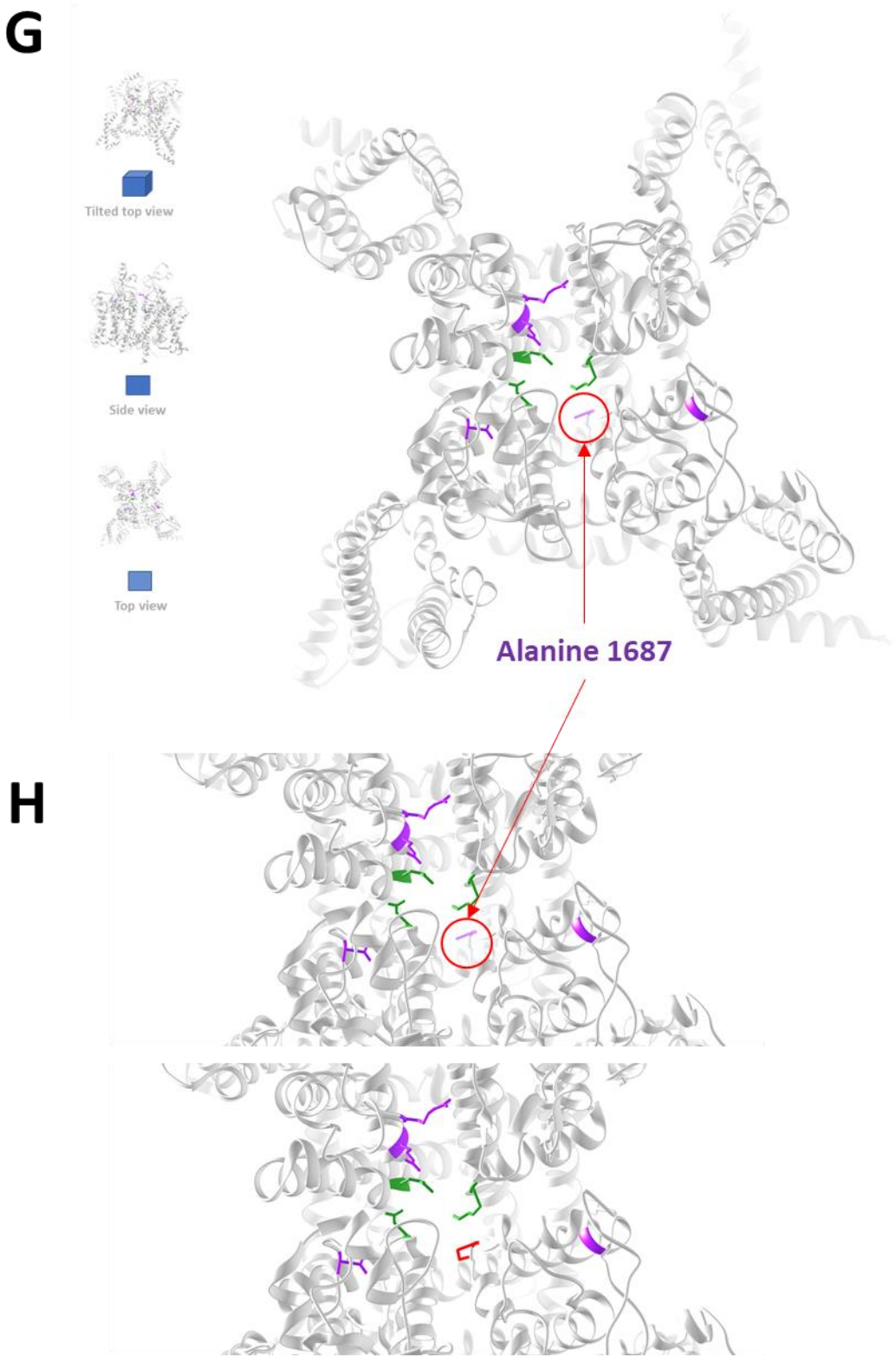

Figure 2.9: Human Nav1.7 atomic model highlighting amino acid substitutions from CIP patients
The hNav1.7 chain from PDB model 6J8G from (2019) Shen et al. is shown, with sidechains displayed in purple for the native residues at mutated locations. The three unaffected amino acids contributing to the ion selectivity filter are coloured green. Zoomed insets illustrate substitution with *SCN9A*-CIP mutations in red: (B) Thr342Met, (D) Arg896Trp, (F) Arg911His, (H) Ala1687Pro, (J) Gly1725Arg

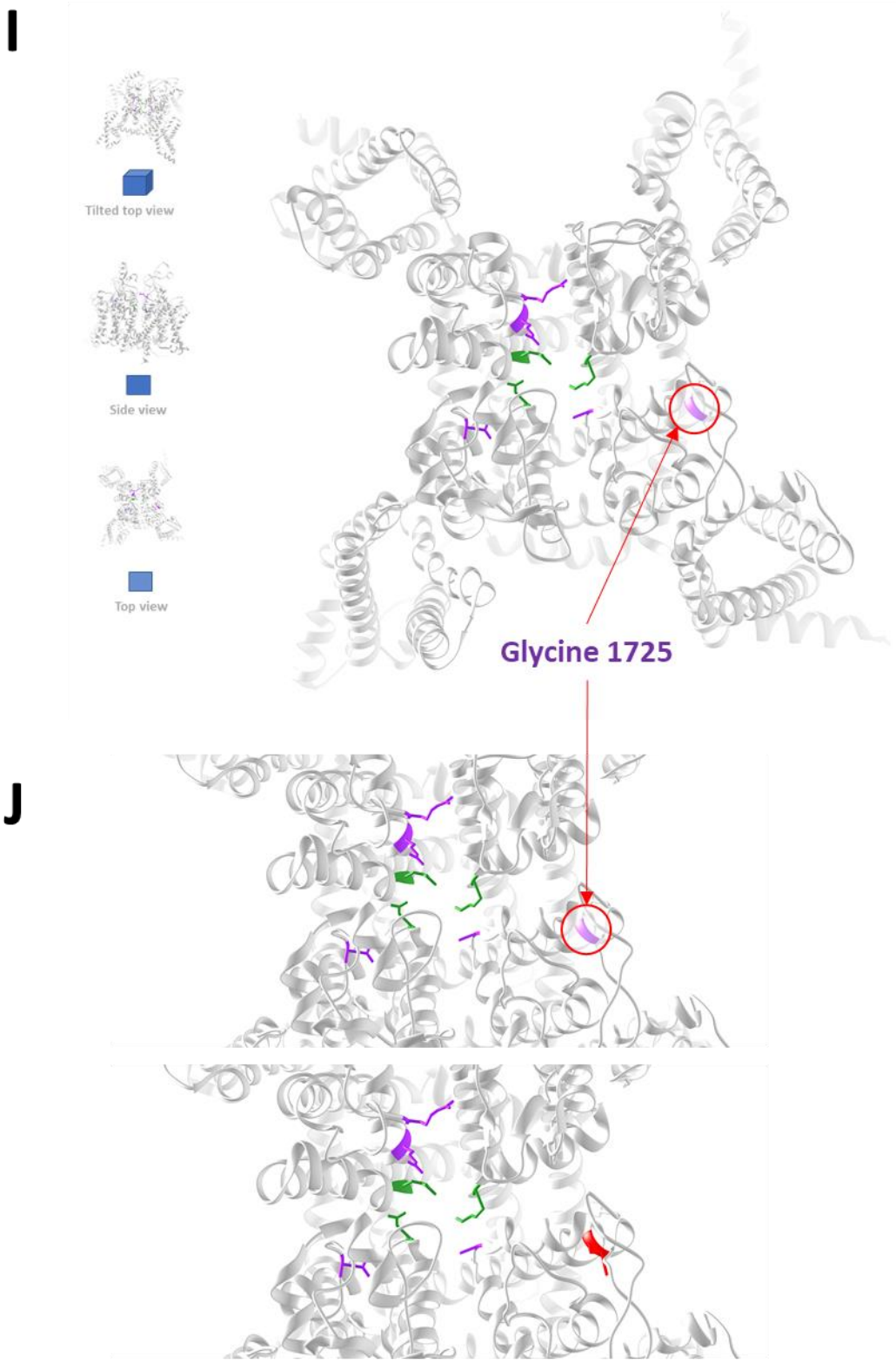

Figure 2.9: Human Nav1.7 atomic model highlighting amino acid substitutions from CIP patients
The hNav1.7 chain from PDB model 6J8G from (2019) Shen et al. is shown, with sidechains displayed in purple for the native residues at mutated locations. The three unaffected amino acids contributing to the ion selectivity filter are coloured green. Zoomed insets illustrate substitution with *SCN9A*-CIP mutations in red: (B) Thr342Met, (D) Arg896Trp, (F) Arg911His, (H) Ala1687Pro, (J) Gly1725Arg

2.4.3 – Optimisation of *SCN9A* plasmid propagation

VGSC plasmids are notoriously difficult to reproduce and sub-clone given their high susceptibility to large-scale duplications or rearrangements. Transformation of the pcDNA4/TO_SCN9A transient expression construct was initially attempted in XL10-Gold Ultracompetent cells, with all growth stages from LB-agar plates to mini- and maxi-cultures conducted at 37°C. Diagnostic digests with restriction enzyme BglII consistently produced higher bands which were not observed in positive control digests of the original plasmid aliquot (data not shown), suggesting rearrangements had occurred. The process was repeated with all stages conducted at 30°C; in this case fewer, slow-growing colonies were observed and picked 6 days post-transformation, but maxi-prepped DNA still produced the higher bands after BglII digest.

Following suggestions from a methods paper on Nav channel plasmid preparation[244], Stbl2 cells were chosen for transformation and an optimisation experiment was designed to compare the effect of maxi-culture temperature on plasmid rearrangement in the two bacterial cell types, see Figure 2.10A. Only the maxi-culture temperature was varied in order to produce *SCN9A* constructs in the shortest timeframe possible. The BglII digest in Figure 2.10B illustrates the results of this experiment. XL10-Gold cells maxi-cultured at 30°C were of insufficient yield for BglII digest, but of the remaining conditions, only the Stbl2 maxi-cultures grown at 30°C produced the expected band fragments at 6.5 kb and 3.5 kb. The smaller fragments at 800 and 450 bp were too small to visualise on this gel. Sequencing verified the full-length of the WT *SCN9A* insert and absence of any additional mutations.

This was the protocol followed for preparation of wild-type and mutagenised pcDNA4/TO_*SCN9A* and pJTI-R4-DEST_*SCN9A* constructs. For the latter vector, a double enzyme digest with NdeI and HindIII-HF produced the expected bands of 4114 bp for the plasmid backbone, 7065 bp and 1687 bp for the *SCN9A* and *emGFP* inserts respectively, see Figure 2.10C.

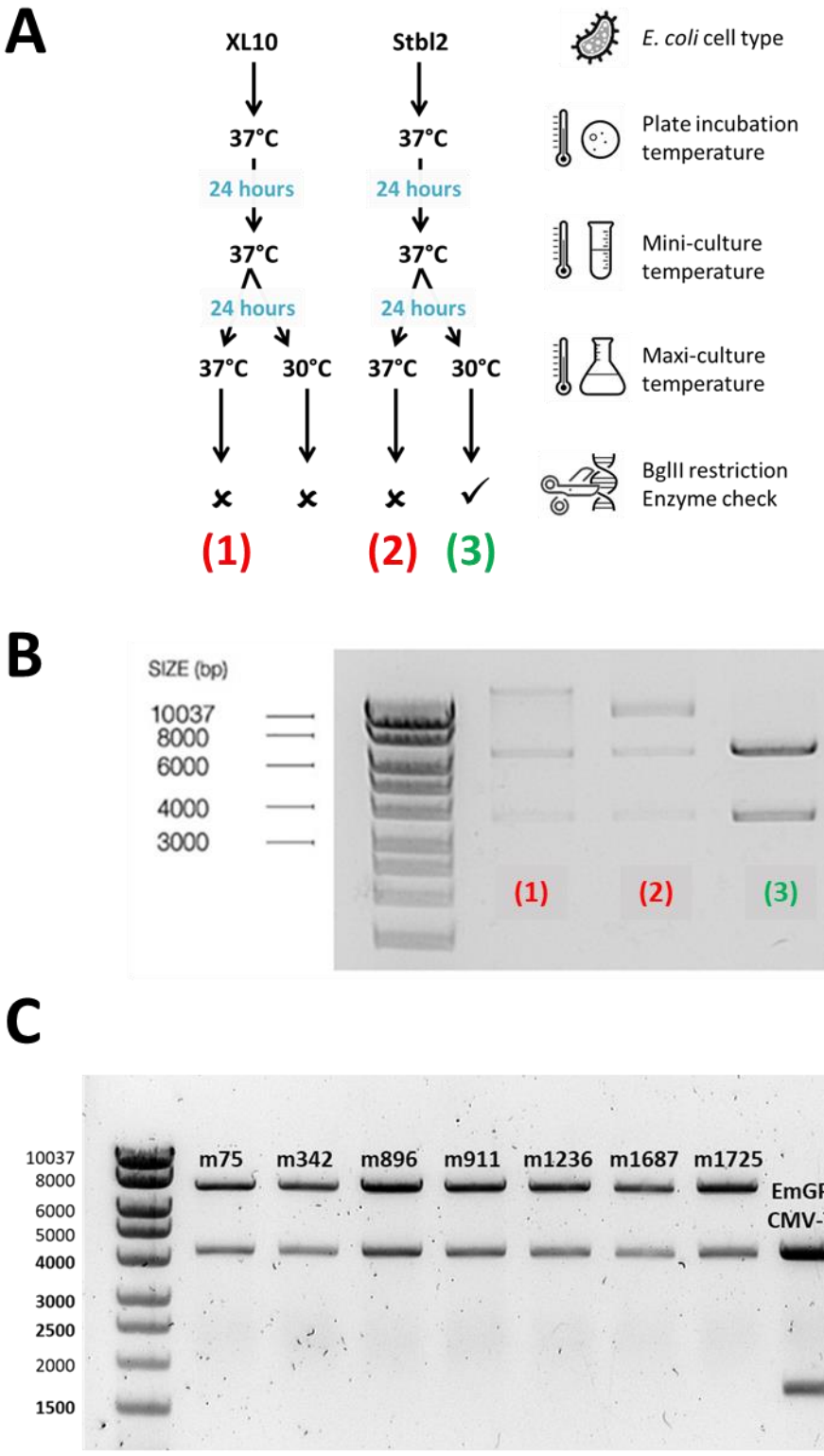

Figure 2.10: Optimisation of *SCN9A* plasmid propagation in bacterial cultures
Due to recurrent rearrangements of *SCN9A* during plasmid propagation, an optimisation experiment was designed, shown in (A). The BglII digest in (B) demonstrates the two correctly sized bands when plasmids were maxi-cultured in Stbl2 cells at 30°C, whereas higher bands were produced in XL10 cultures. This method was also reliable for pJTI-R4-DEST_SCN9A plasmids, as demonstrated by NdeI & HindIII-HF double digest producing plasmid backbone and insert fragments observed in (C).

2.4.4 – Validation of *SCN9A* integration into HEK JI TREX-Nav1.7-FLAG cell lines

HEK JI TREX parental cells were co-transfected with R4 integrase and pJTI-R4-DEST_*SCN9A* vectors to generate stably expressing Nav1.7-FLAG cell lines. Massive cell death was observed upon changing to Geneticin selection media after the transfection, but colonies could be observed under the microscope within 2-3 days and by eye within 7 days post-transfection as shown in Figures 2.11A-B. Once cells were confluent enough to freeze down stocks, cells were plated at the first passage to test induction of gene expression by doxycycline and correct protein production by western blot and probing with anti-Nav1.7 antibody. Figure 2.11C shows absence of Nav1.7 expression in each cell line when cell culture media did not contain doxycycline, compared to presence of Nav1.7 expression when the drug was added. Inducible expression was also confirmed in the A1236E and EmGFP control cell lines (data not shown).

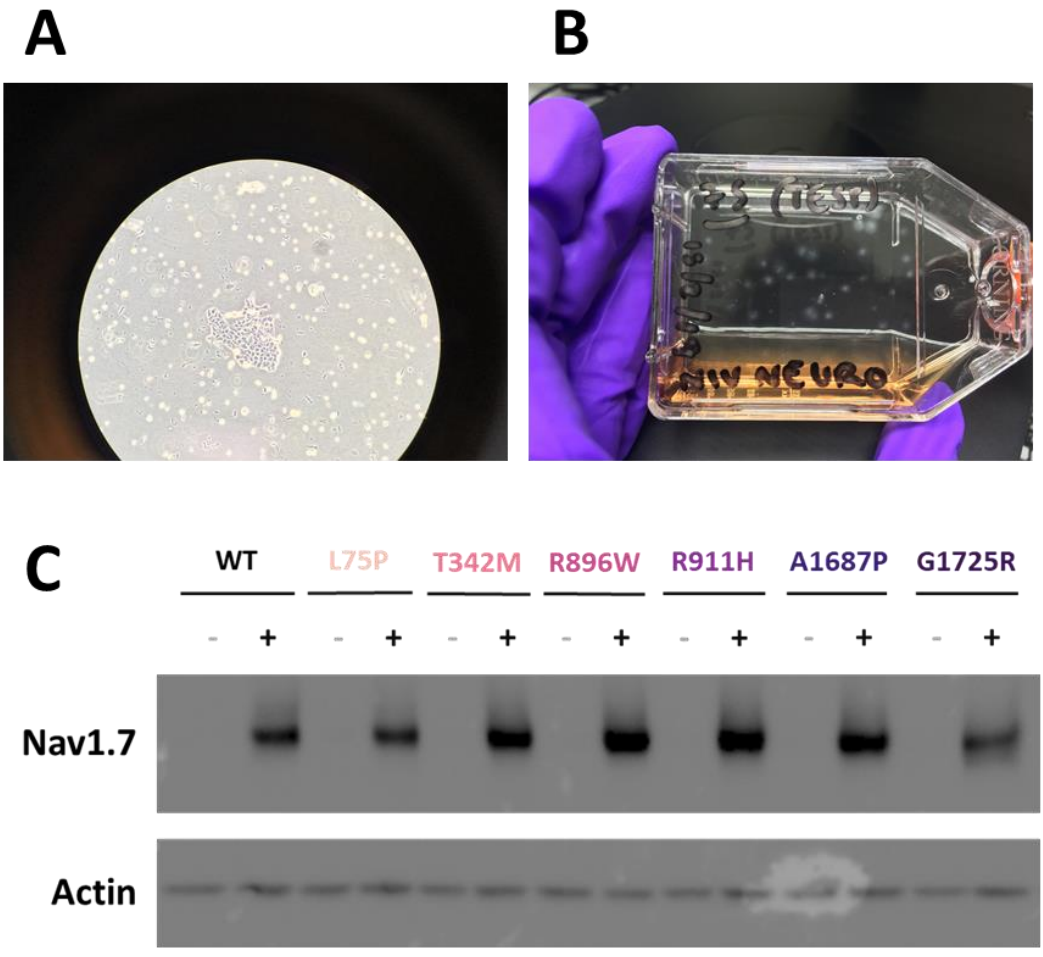

Figure 2.11: Validation of inducible expression in HEK JI TREX-Nav1.7-FLAG cell lines
Generation of polyclonal stable cell lines was based on Geneticin-selection of successfully transfected cells with the pJTI-R4-DEST_*SCN9A* cassette. Colonies were visible under the microscope (A) within 2-3 days of transfection and by eye after a week (B). Cell lysates from uninduced (-) versus induced (+) cells were probed with anti-Nav1.7 to confirm full-length Nav1.7-FLAG protein was produced (C).

2.4.5 – Subcellular localisation of Nav1.7 in transient & stable expression systems

Confocal microscopy was used to determine if any of the mutant channels exhibited major localisation defects within the protein maturation pathway. The wild-type or mutant FLAG-tagged channels were transiently transfected into HeLa cells and co-stained for Nav1.7-FLAG and the ER compartment. Representative images of each condition in Figure 2.12 show there were no differences in subcellular distribution of wild-type and mutant channels as all genotypes displayed diffuse, intracellular expression with no obvious enrichment at the cell perimeter.

Whilst there was no evidence of complete ER retention in any of the Nav1.7 genotypes, occasionally Nav1.7 staining produced a tubule-like arrangement (see middle R911H-transfected cell in Figure 2.12) or concentrated in the perinuclear region (see top-left R896W-transfected cell in Figure 2.12). In the few cells where these phenotypes were observed, the ER distribution was also abnormal and overlapping with the Nav1.7 stain. However, both morphologies were seen in all genotypes and was not magnified in any particular mutant condition.

In HEK JI TREX-Nav1.7-FLAG stable cell lines, where expression of WT or mutant Nav1.7 is driven by a single copy of the *SCN9A* insert, channel distribution was similarly diffuse as in HeLa cells and without obvious plasma membrane enrichment, see Figure 2.13. This staining pattern was observed in all Nav1.7 genotypes, suggesting the rare anomalies seen in HeLa cells may have been an artefact of over-expression by transient transfection.

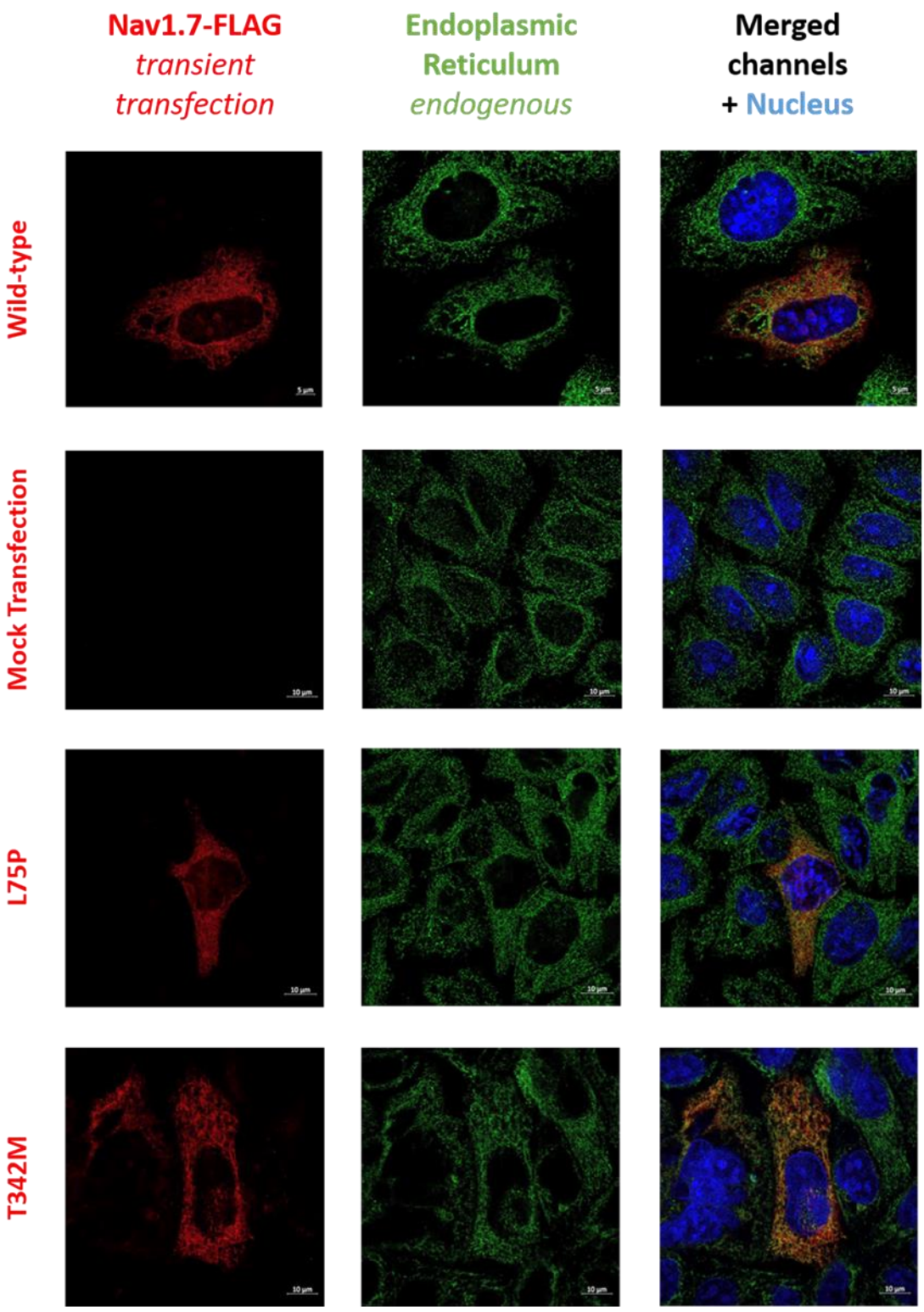

Figure 2.12: Nav1.7 mutants are not retained in the ER in a transient expression system
Transient transfection of WT and mutant Nav1.7 in HeLa cells produced a diffuse intracellular staining pattern that showed little overlap with ER marker anti-KDEL. Rare tubular and aggregate phenotypes were not unique to any genotype and were considered artefacts of over-expression.

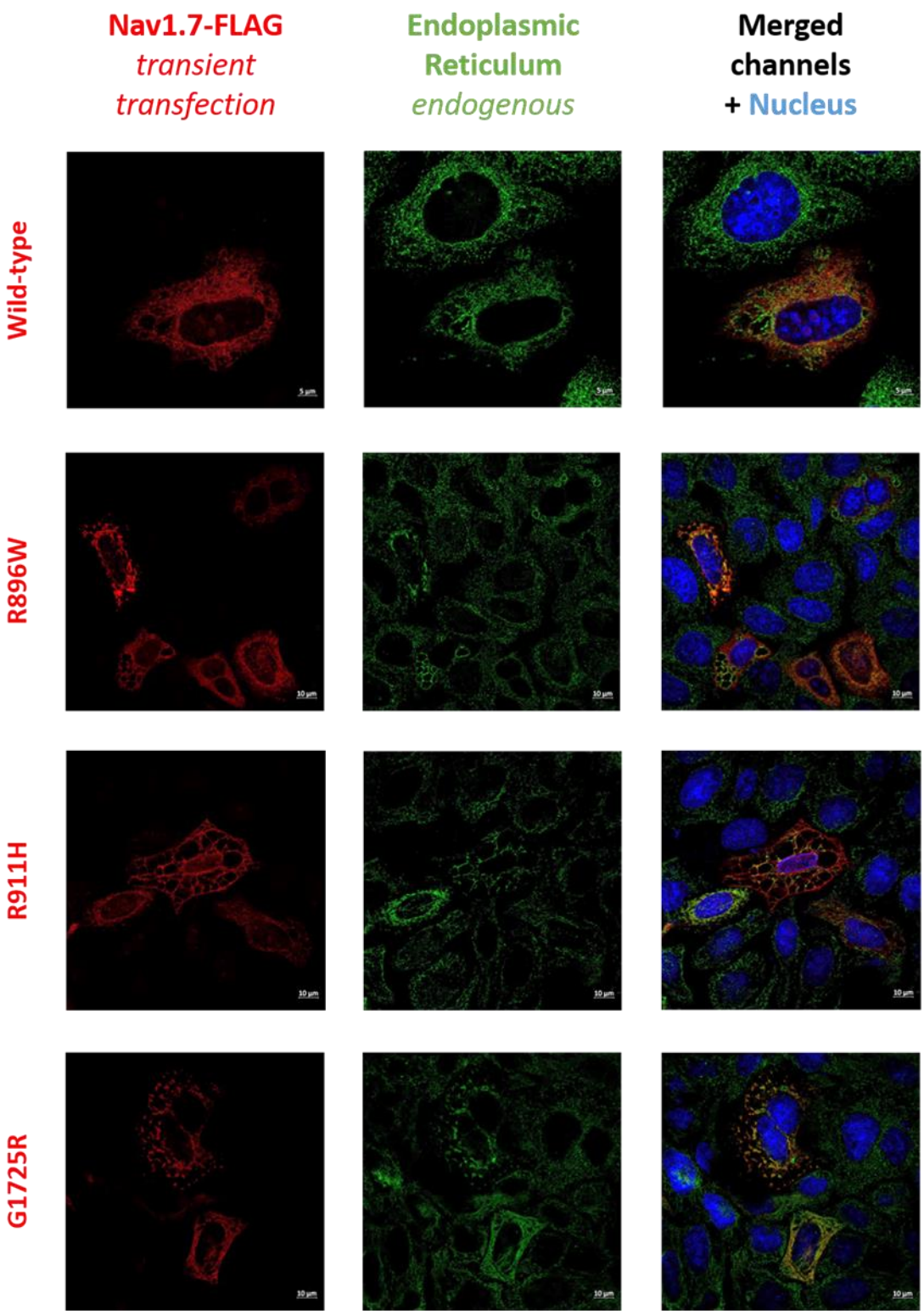

Figure 2.12: Nav1.7 mutants are not retained in the ER in a transient expression system
Transient transfection of WT and mutant Nav1.7 in HeLa cells produced a diffuse intracellular staining pattern that showed little overlap with ER marker anti-KDEL. Rare tubular and aggregate phenotypes were not unique to any genotype and were considered artefacts of over-expression.

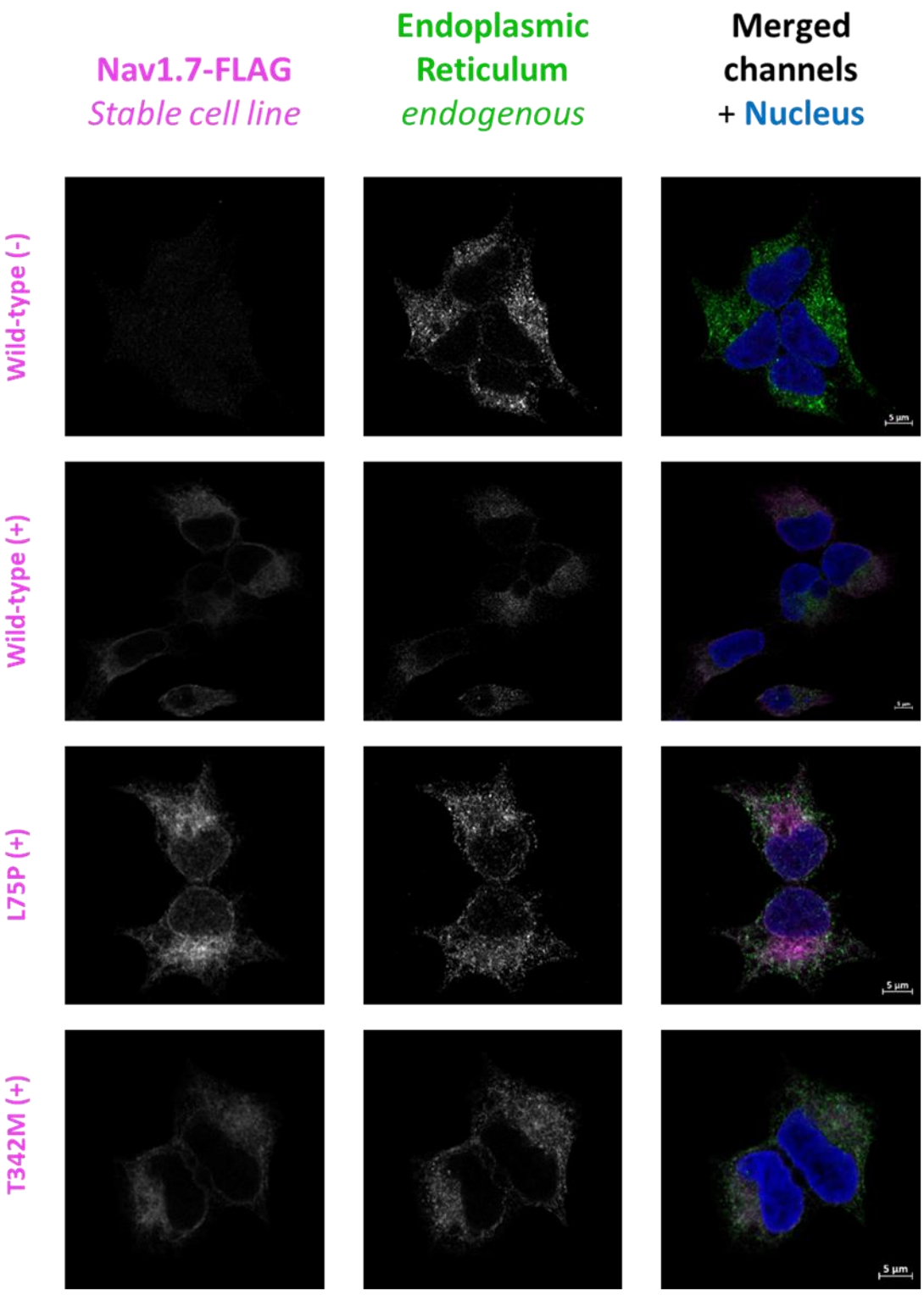

Figure 2.13: Nav1.7 mutants were not retained in the ER in a stable expression system
In HEK JI TREX-Nav1.7-FLAG stable cell lines, expression of WT or mutant Nav1.7 is driven by a single copy of the *SCN9A* insert. Nav1.7 distribution was diffuse in the cytoplasm and without major overlap with ER marker anti-KDEL, as was observed in HeLa cells.

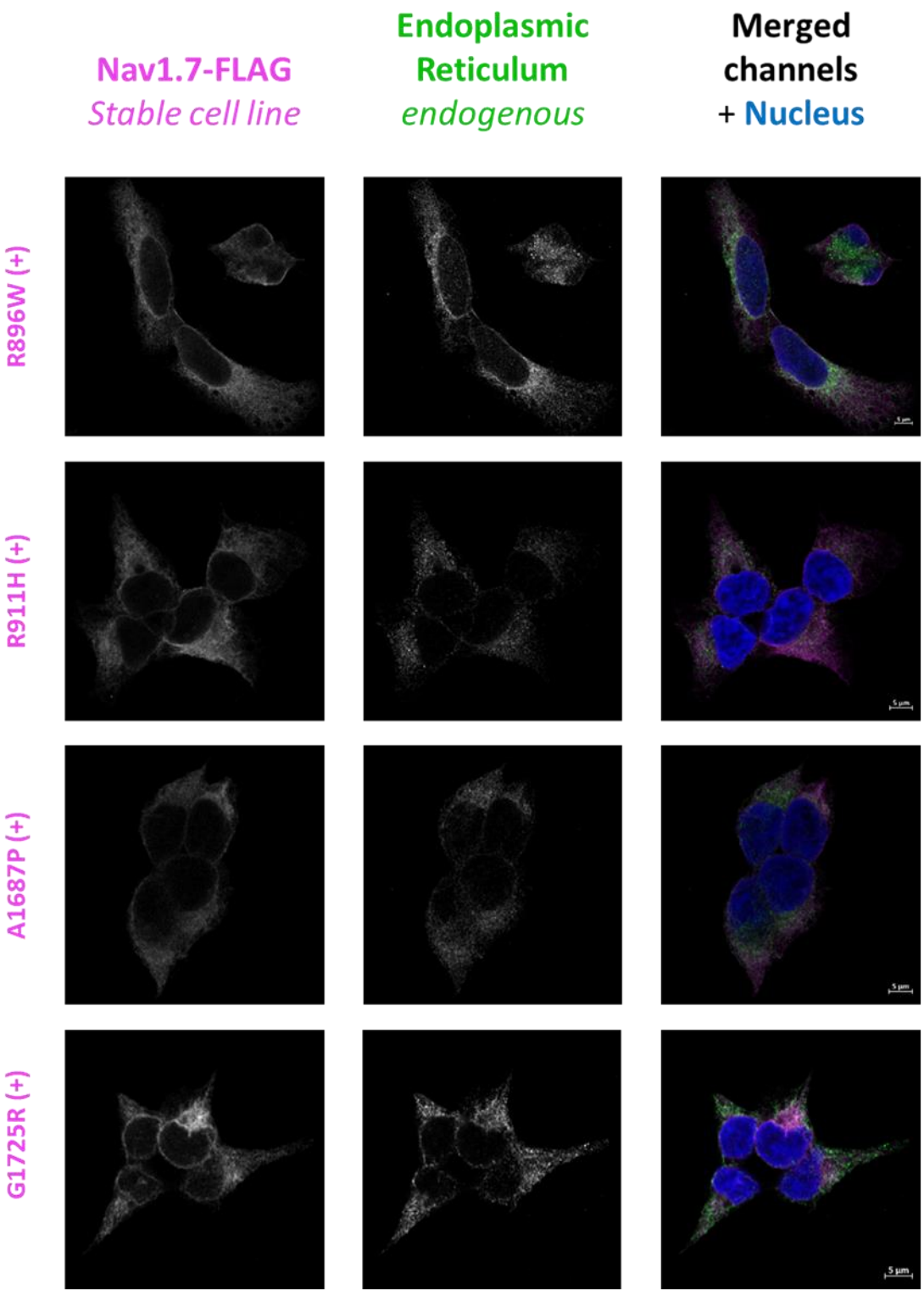

Figure 2.13: Nav1.7 mutants were not retained in the ER in a stable expression system
In HEK JI TREX-Nav1.7-FLAG stable cell lines, expression of WT or mutant Nav1.7 is driven by a single copy of the *SCN9A* insert. Nav1.7 distribution was diffuse in the cytoplasm and without major overlap with ER marker anti-KDEL, as was observed in HeLa cells.

2.4.6 – Nav1.7 plasma membrane localisation by immunocytochemistry

Whilst there was no distinct enrichment of Nav1.7 at the plasma membrane, this would not discount the presence of concentrated Nav1.7 puncta in the membrane. An image segmentation approach with automated analysis was considered in an attempt to make quantitative comparisons of the proportion of membrane-localised Nav1.7 between WT and mutants. MetaXpress software would use the fluorescence intensity of a plasma membrane marker to produce a mask of this region. Nav1.7 fluorescence intensity could then be measured within this compartment and expressed as a fraction of total cell intensity. In order to produce reliable segmentation masks, the marker would need to stain the entire border of the cell and demonstrate high contrast in fluorescence between the cell membrane and intracellular compartment.

Figure 2.14A illustrates staining with a fluorescently-conjugated lectin, wheat germ agglutinin 488 (WGA-488), which requires the whole staining protocol to occur on ice to prevent endocytosis and labelling of intracellular organelle membranes. Whilst WGA-488 produced a strong, membrane-specific signal in HeLa cells, the extended incubations on ice repeatedly led to detachment of HEK293 cell lines, even from PDL-coated surfaces. Adjustments to this protocol such as shorter incubations on ice, fixation before versus after WGA-488 staining, or alternative permeabilization agents slightly improved HEK293 cell attachment but still produced sub-membranous, endosomal-like staining. To isolate the cell membrane from intracellular puncta would require additional customisation of image analysis modules in MetaXpress. Instead, a monoclonal rabbit anti-Na^+K^+ ATPase antibody was chosen as an alternative plasma membrane marker. Fluorescent detection was dependent on polyclonal anti-rabbit secondaries conjugated to Alexa Fluor 488. Figure 2.14B shows limited membrane staining in HeLa cells, whereas the fluorescence intensity was much stronger and specific in HEK background cell lines; however in the latter case, staining was most uniform in cells abutted against each other whereas labelling of free membrane edges was inconsistent.

Before pursuing further optimisation, HEK293 cells were transiently transfected with pcDNA4/TO_*SCN9A* constructs to see how much Nav1.7 was present in line with the plasma membrane. Figure 2.14C shows only a few puncta were observed in the membrane, a tiny fraction of the total protein expressed per cell; this pattern was also observed in mutant transfections (data not shown). Given the minute proportions of channel that were membrane-localised relative to in the cytoplasm, differences at such small orders of magnitude were unlikely to be significant. Instead, these studies were discontinued in favour of the cell-surface biotinylation approach.

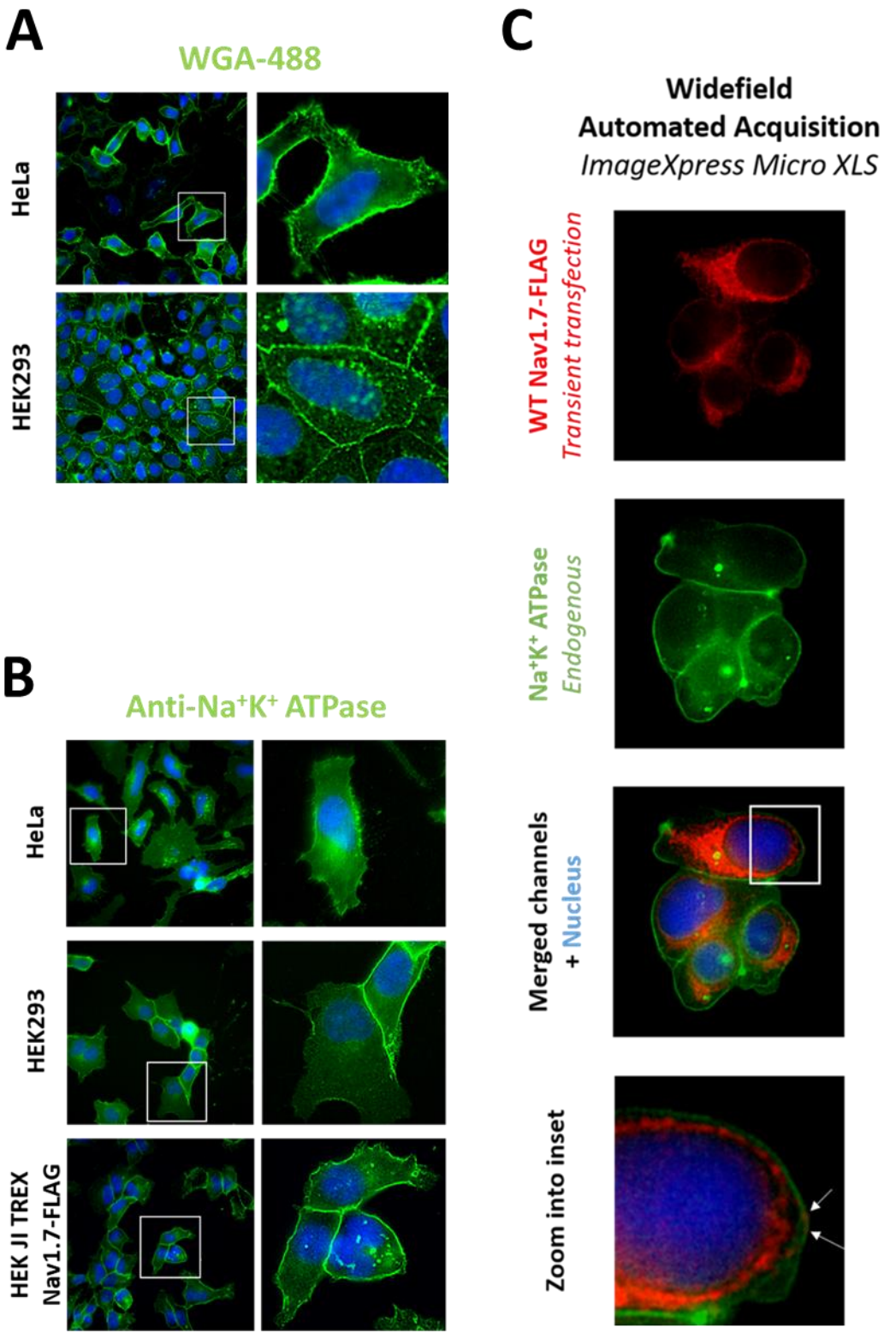

Figure 2.14: Plasma membrane marker optimisation for cell segmentation analysis
A fluorescently-conjugated lectin (A) and antibody-based detection of transmembrane protein Na^+K^+ ATPase (B) were used in different cell lines to determine their suitability as a plasma membrane marker for automated cell segmentation analysis. However, transient transfection of Nav1.7 in HEK293 cells (C) revealed only few Nav1.7 puncta could be detected at the plasma membrane.

2.4.7 – Nav1.7 plasma membrane localisation by cell-surface biotinylation

Cell-surface biotinylation assay and densitometry analysis of immunoblots has proven to be a sensitive technique to determine differences in the proportion of surface-localised Nav1.7 when comparing the effects of Nav1.7 membrane trafficking partners[198,250]. This approach was used to make quantitative comparisons between WT and mutants in a transient expression system and then to confirm absence or presence of membrane-localised Nav1.7 in the stable cell lines.

For transient experiments, samples were collected from independent experiments of HEK293 cells transfected with WT or mutant Nav1.7 (WT and L75P – n=4; T342M, R896W, R911H, G1725R – n=3). Samples representing total and surface-localised proteins were taken as described in Section 2.3.12. In addition to studying Nav1.7 expression, blots were probed for Na^+K^+ ATPase as a positive control for cell-surface protein biotinylation, whilst β-Actin or Calnexin were used as negative controls to verify the biotinylated membrane protein fraction was not contaminated with intracellular proteins.

A representative blot in Figure 2.15A shows that all Nav1.7 mutant channels were able to reach the membrane. Quantification of surface-localised Nav1.7 was highly variable between individual experiments and across genotypes, however there was no statistically significant difference between any particular mutant compared to the WT (L75P: $p = 0.212$; T342M: $p = 0.496$; R896W: $p = 0.315$; R911H: $p = 0.360$; G1725R: $p = 0.487$). These results were corroborated in the HEK JI TREX-Nav1.7-FLAG cell lines as shown in Figure 2.16A, with additional assessment of the newly identified A1687P mutation; repeat experiments of this mutation, shown in Figure 2.16B, confirmed the validity of this result. Thus, we concluded that none of the mutations cause defects in forward trafficking of Nav1.7 to the cell membrane, when expressed in the absence of known trafficking partners in HEK background cell lines.

To demonstrate the variability inherent to cell-surface biotinylation assays when used with transient expression systems, new samples were taken from three individual experiments comparing WT Nav1.7 membrane localisation when expressed transiently versus stably. The blot in Figure 2.17A shows the total expression of Nav1.7 fluctuated between transient transfections but appeared consistent in stable cell lines. The levels of membrane-localised Nav1.7 were uniform across the transient and stable transfection conditions, although the intensity of the transient surface samples were stronger which may indicate saturated binding to the streptavidin column.

Quantification of these results shown in Figure 2.17B-C revealed a statistically significant difference in the proportion of WT Nav1.7 at the membrane depending on the expression system used (Transient: 59.2 ± 6.1 versus Stable: 17.6 ± 1.8; $p = 0.0497$). Endogenous levels of Na^+K^+ ATPase were expected to be consistent between experiments, any variation likely an effect of biotinylation efficiency. This was verified by statistical testing (Transient: 24.8 ± 3.6 versus Stable: 32.6 ± 5.4; $p = 0.5332$). This result highlights transient transfection efficiency as a potential confounding factor when using cell-surface biotinylation to make quantitative comparisons of membrane-localised proteins between genotypes or other conditions.

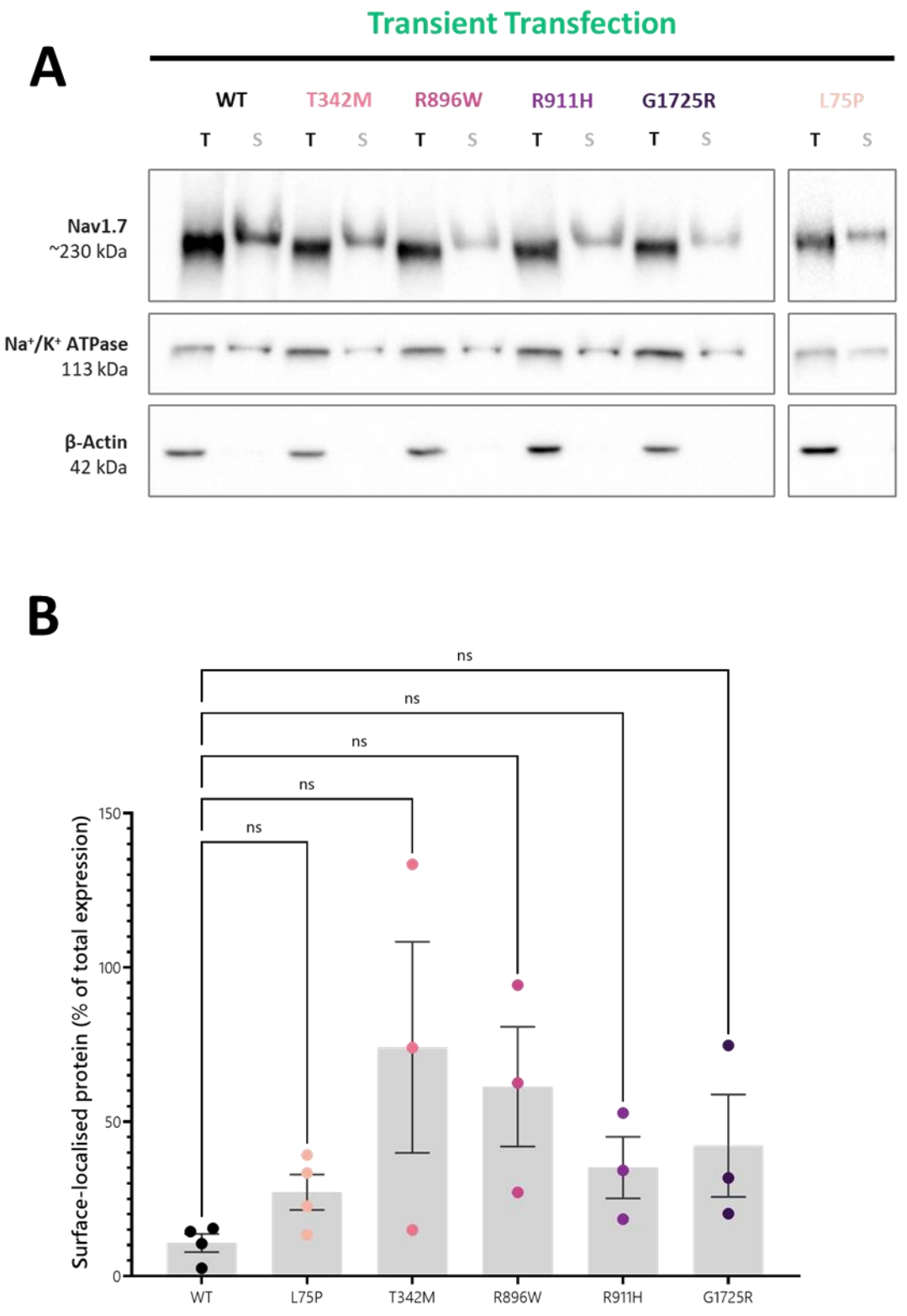

Figure 2.15: All Nav1.7 mutants reached the plasma membrane in a transient expression system
Nav1.7 was transiently transfected into HEK293 cells for use in a cell-surface biotinylation assay. (A) Western blot of total (T) and surface-localised (S) samples shows that all channels were able to reach the plasma membrane. Densitometry analysis graphed in (B) revealed high variability in the proportion of all channels that reached the membrane, but none were significantly different to WT.

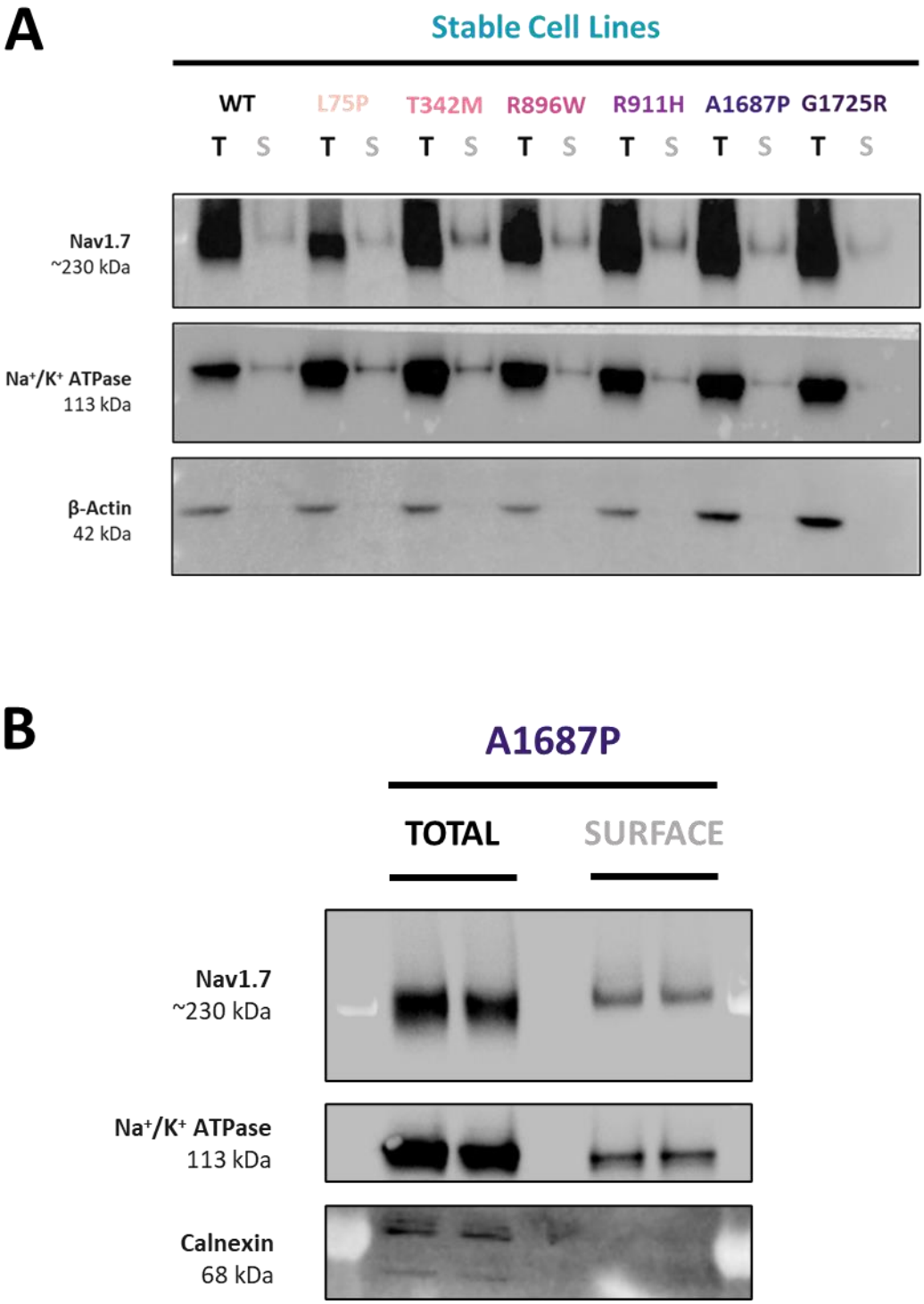

Figure 2.16: All Nav1.7 mutants reached the plasma membrane in a stable expression system
(A) The cell-surface biotinylation assay was repeated on HEK JI TREX-Nav1.7-FLAG stable cell lines, confirming the presence of all channels at the plasma membrane. (B) The Ala1687Pro mutation was newly identified after transient expression experiments, so this assay was repeated twice more on the A1687P stable cell line to ensure it was a reliable result.

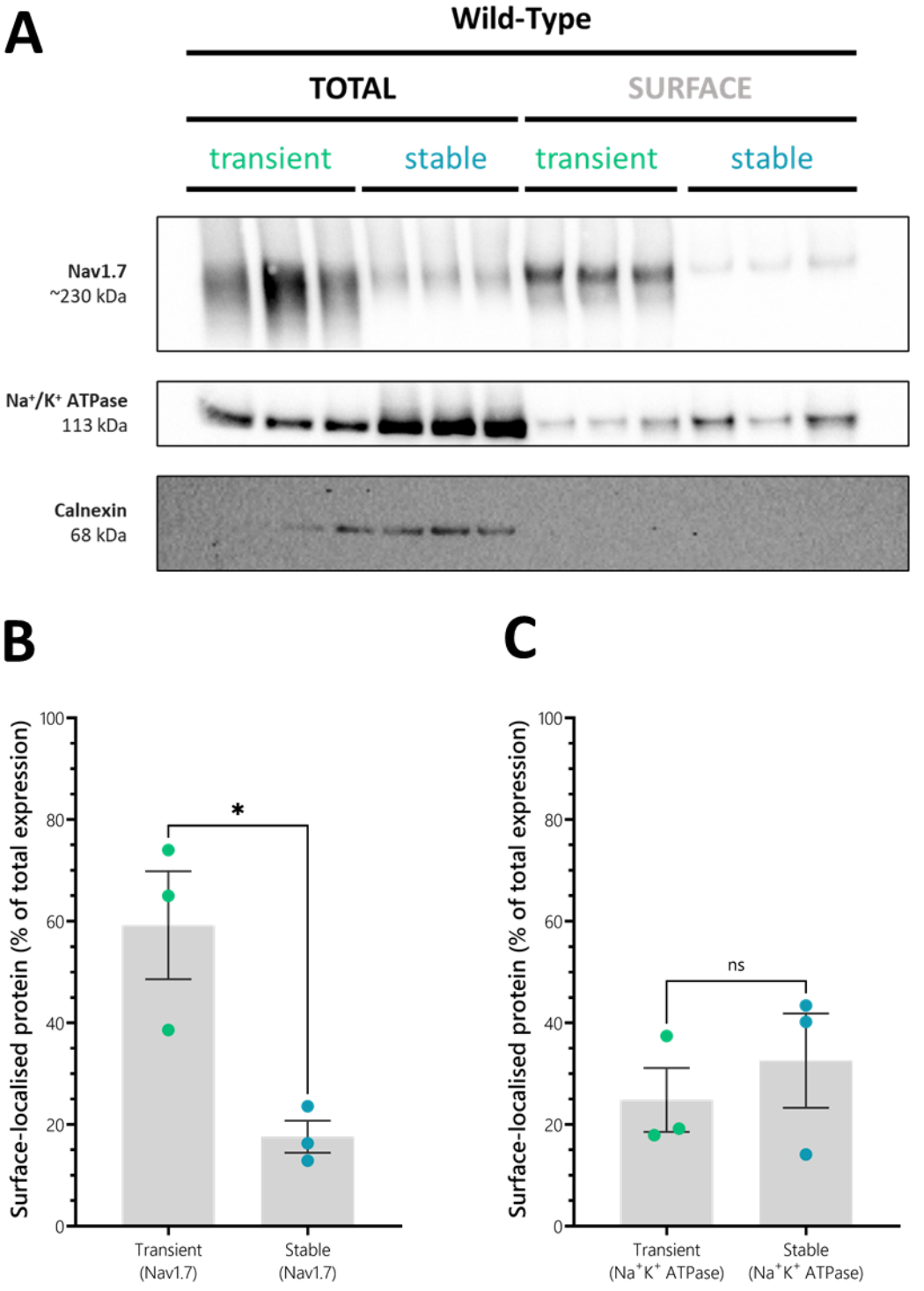

Figure 2.17: Cautionary notes on using cell-surface biotinylation for quantitative comparisons
(A) Cell-surface biotinylation experiments on transiently versus stably expressed Nav1.7 in HEK background cell lines (n=3) were directly compared by densitometry analysis to quantify the proportion of total WT Nav1.7 (B) and Na^+K^+ ATPase (C) localised to the plasma membrane. Levels of surface-localised Na^+K^+ ATPase were not significantly different between the two conditions. However, the lack of control in transient transfection of Nav1.7 resulted in highly variable assessments of this surface-localised population, which were significantly different to stable transfection conditions despite expression of an identical protein.

2.4.8 – Nav1.7 biophysical profiling by manual & automated voltage-clamp

The final assay of Nav1.7 function was electrophysiological profiling of channel properties. HEK293 cells stably expressing untagged, WT Nav1.7 were used for preliminary characterisation to ensure values were comparable to the literature (see Appendix A). The results of these manual patch clamp studies are presented in Figure 2.18 and Table 2.11.

Intracellular solutions (ICS) with either CsF (140 mM) or CsCl (125 mM) as the dominant anion were to be compared but maintaining a stable gigaohm seal for the duration required to record multiple protocols proved difficult with CsCl-based solution. Therefore, this comparison was only made with respect to voltage-dependence of activation. Although CsCl-based ICS produced a depolarising shift in voltage-dependence of activation (see Figure 2.18A), the difference in V_{50} (CsF: -28.8 ± 1.3 mV versus CsCl: -17.7 ± 5.0 mV; p = 0.2542) and slope factor values (CsF: 3.5 ± 0.3 versus CsCl: 4.7 ± 1.6; p = 0.5845) for the two solutions were not statistically significant and equivalent to those reported in the literature. Voltage-dependence of fast inactivation with CsF-based ICS (V_{50}: -70.5 ± 1.4 mV) was also similar to reported values, therefore we took the CsF-based ICS forward for subsequent studies.

As the transient Nav1.7 construct was not fluorescently tagged, HEK293 cells were co-transfected with a GFP-expressing plasmid, with the assumption that fluorescent cells would have taken up both vectors. Figure 2.19A illustrates the hit rate of measuring WT Nav1.7 currents in fluorescent cells at multiple timepoints when transient transfection was performed by chemical versus electroporation methods. This proved to be most efficient at 48-72 hours post transfection with the AMAXA electroporation method. The voltage-dependence of activation was slightly hyperpolarised from 48 to 72 hours, however this difference was not statistically significant (48h V_{50}: -16.7 ± 0.9 mV versus 72h V_{50}: -19.7 ± 1.9 mV; p = 0.2047). The difference in peak current expressed at -5 mV was also not statistically significant between the two timepoints (p = 0.5107).

In HEK293 cells transiently expressing Nav1.7 mutants L75P and R911H, no Na^+ currents were measured at 48 or 72 hours post-transfection, which would be consistent with the LOF phenotype in the CIP patients. However, given that 65% fluorescent cells in the WT condition did not express sodium ion currents at 48 hours post-transfection and 17% at 72 hours post-transfection, there was a concern that the absence of current in the mutant conditions could be due to unsuccessful take-up of Nav1.7 plasmid. This meant subtle changes in the biophysical profile of mutant channels might be missed by chance and would require many tens of cells to be measured per genotype to be confident of the result. At this point, the decision was made to generate the HEK JI TREX-Nav1.7-FLAG stable cell lines

for higher-throughput analysis. Previous recordings of an identical WT construct on the QPatch instrument by John Linley (AstraZeneca, Cambridge, UK), shown in Figure 2.19E, demonstrated normal channel function and suitability of this approach to characterise the *SCN9A*-CIP mutants.

With the newly generated HEK JI TREX-Nav1.7-FLAG cell lines described in Section 2.3.9, automated patch clamp analysis was performed. For the WT cell line (see Figure 2.20A), the half-maximal value for voltage-dependence of activation (V_{50} = -30.5 ± 0.2 mV; k = 3.0 ± 0.2) was very close to that measured by manual patch clamp in transiently transfected HEK293 cells using FuGENE HD (V_{50}: -28.8 ± 1.3 mV; k = 3.5 ± 0.3). However, none or negligible currents were measured from all other cell lines with induced protein expression – i.e., the novel *SCN9A*-CIP mutations, published partial LOF mutant A1236E and the EmGFP control cell line (see Figure 2.20B-C and Table 2.12). Thus, the mechanism of pathogenicity behind all novel missense *SCN9A*-CIP mutations was a complete loss of ion conducting ability.

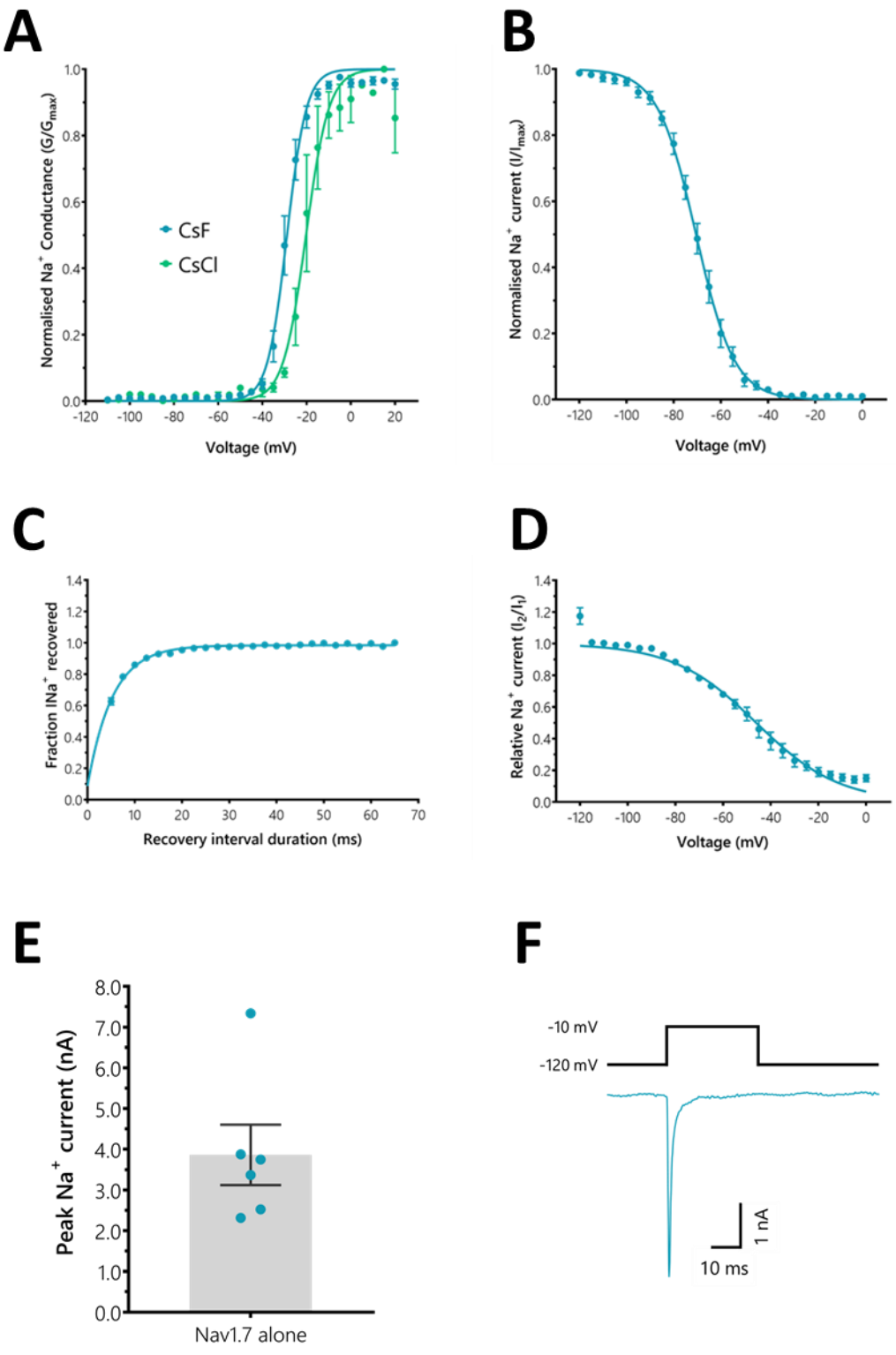

Figure 2.18: Biophysical properties of WT Nav1.7 determined by manual patch clamp
Averaged results of voltage-clamp protocols applied to HEK293 stable cell lines expressing untagged WT Nav1.7: (A) voltage-dependence of activation, (B) voltage-dependence of fast inactivation, (C) Recovery from fast inactivation, (D) voltage-dependence of slow inactivation. All protocols apart from voltage-dependence of activation were solely conducted with CsF-based intracellular solution. Peak sodium currents plotted in (E) and an example trace is shown in (F). Error bars represent SEM.

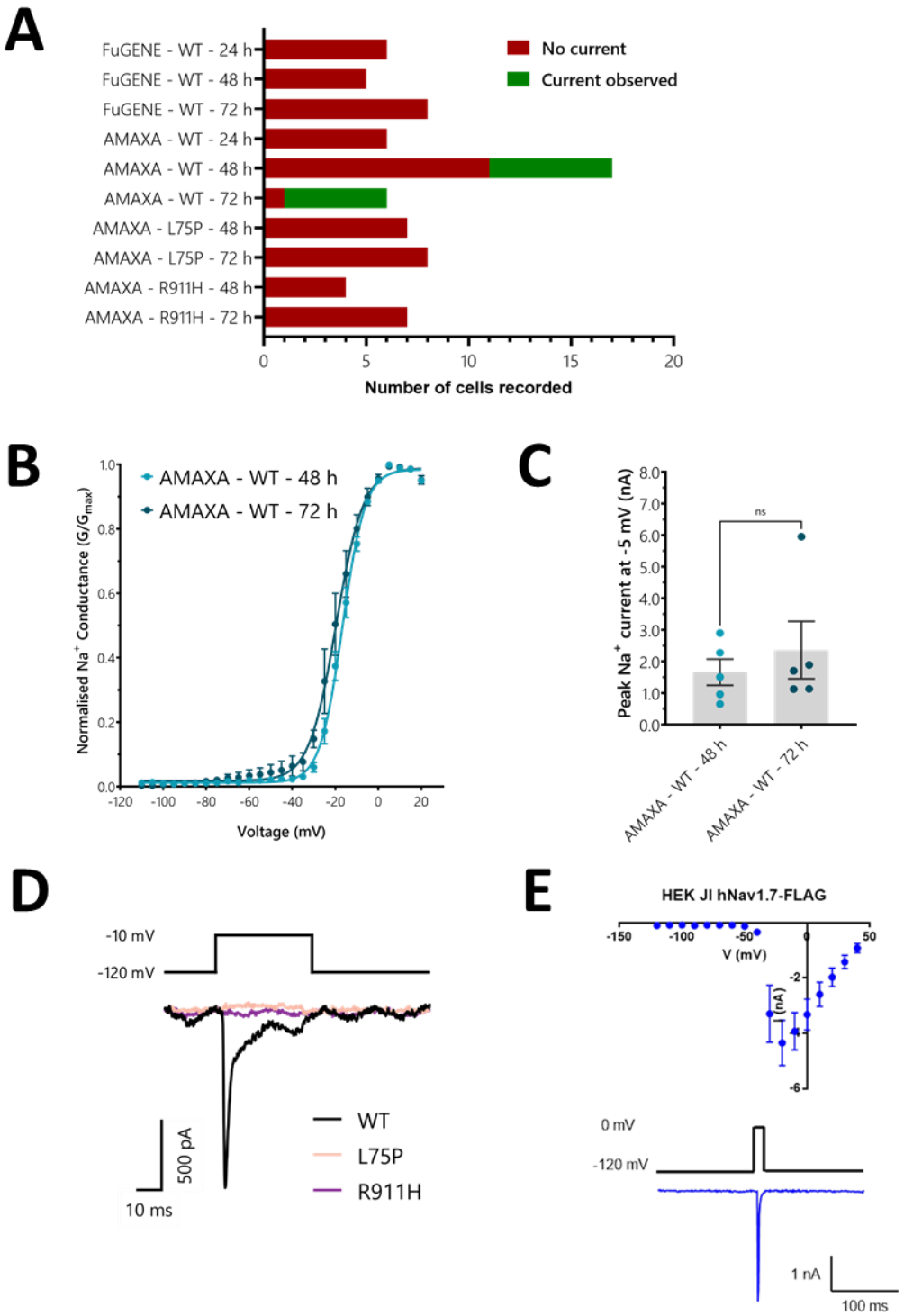

Figure 2.19: Limitations of profiling putative LOF Nav1.7 mutants in a transient expression system (A) Hit rate for measuring sodium currents at 24-72 hours post-transfection from transiently transfected HEK293 cells by FuGENE chemical transfection versus AMAXA electroporation. Voltage dependence of activation (B) and peak currents at -5 mV (C) from WT channels were compared at 48 versus 72 hours post AMAXA-based transfection to diagnose any pertinent differences. (D) Example traces of sodium currents measured from transiently expressed WT Nav1.7 or mutants L75P or R911H. Due to concerns in interpreting LOF mechanisms from potentially untransfected cells, HEK JI TREX-Nav1.7-FLAG cell lines were generated for high-throughput QPatch analysis. Functional characterisation of this WT cell line was previously demonstrated by John Linley in (E).

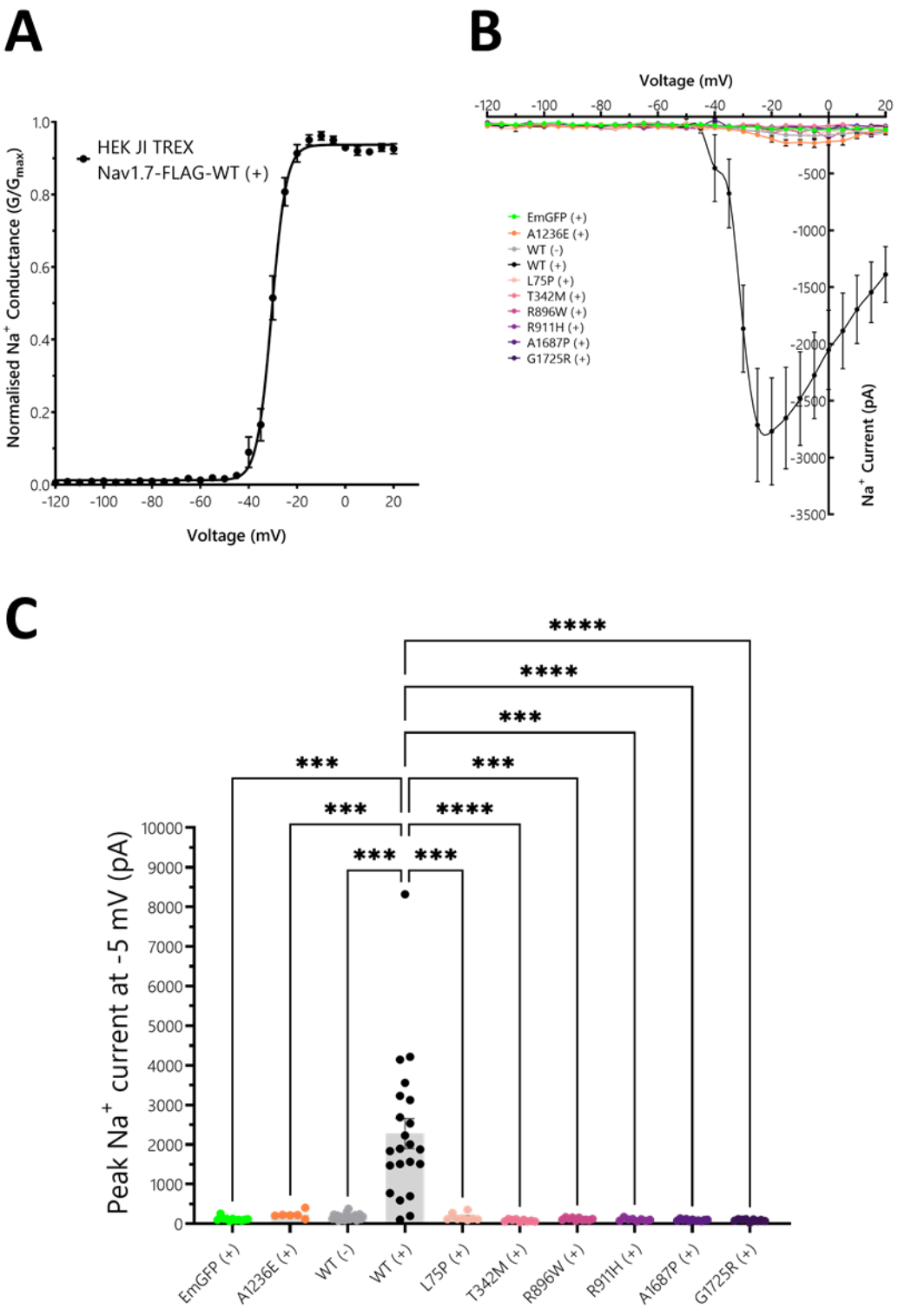

Figure 2.20: All novel Nav1.7 mutants were non-conducting in a stable expression system
(A) WT HEK JI TREX-Nav1.7-FLAG cells produced robust sodium currents measured with the QPatch automated patch clamp system, from which voltage-dependence of activation was determined. The I-V relationship for all cell conditions measured is plotted in (B) and peak current at -5 mV in (C). Doxycycline induction of protein expression is indicated by "(+)" following the cell line tested. Negligible currents were measured for all novel *SCN9A*-CIP mutants as well as published partial LOF mutant Ala1236Glu and negative controls EmGFP(+) and WT(-).

Table 2.11: Biophysical properties of WT Nav1.7 expressed in different conditions, measured by manual patch clamp

	ACTIVATION			FAST INACTIVATION			RECOVERY FROM FAST INACTIVATION				SLOW INACTIVATION		
	V_{50} (mV)	Slope	n	V_{50} (mV)	Slope	n	Tau (ms)	Half-time (ms)	Slope	n	V_{50} (mV)	Slope	n
- HEK hNav1.7 stable cell line - Untagged WT Nav1.7 - CsCl intracellular solution - Manual patch-clamp	-17.7 ± 5.0	4.7 ± 1.6	2										
- HEK hNav1.7 stable cell line - Untagged WT Nav1.7 - CsF intracellular solution - Manual patch-clamp	-28.8 ± 1.3	3.5 ± 0.3	10	-70.5 ± 1.4	-7.9 ± 0.6	7	5.3 ± 0.2	3.7 ± 0.1	0.2 ± 0.0	3	-50.0 ± 2.8	-17.2 ± 1.2	3
- HEK293 cell line - WT Nav1.7-FLAG - Transient transfection (48 h) - AMAXA electroporation - CsF intracellular solution - Manual patch-clamp	-16.7 ± 0.9	5.5 ± 0.4	5										
- HEK293 cell line - WT Nav1.7-FLAG - Transient transfection (72 h) - AMAXA electroporation - CsF intracellular solution - Manual patch-clamp	-19.7 ± 1.9	6.1 ± 1.0	5										
- HEK JI TREX-Nav1.7 stable cell line - WT Nav1.7-FLAG - CsF intracellular solution - Automated patch-clamp	-30.5 ± 0.2	3.0 ± 0.2	20										

Table 2.12: Peak current amplitudes at -5 mV of WT and mutant Nav1.7 in stable cell lines

HEK JI TREX Cell Line	Dox Induction	Peak Current at -5 mV (pA)	# cells	One-way ANOVA comparison to WT (+)
Nav1.7-WT	(+)	2275.8 ± 380.1	22	
EmGFP	(+)	117.7 ± 15.0	11	p = < 0.001
Nav1.7-A1236E	(+)	231.0 ± 38.8	6	p = < 0.001
Nav1.7-WT	(-)	168.8 ± 15.0	23	p = < 0.001
Nav1.7-L75P	(+)	167.9 ± 33.3	8	p = < 0.001
Nav1.7-T342M	(+)	82.1 ± 9.3	9	p = < 0.001
Nav1.7-R896W	(+)	119.0 ± 10.1	10	p = < 0.001
Nav1.7-R911H	(+)	103.2 ± 12.3	8	p = < 0.001
Nav1.7-A1687P	(+)	92.5 ± 6.5	11	p = < 0.001
Nav1.7-G1725R	(+)	87.1 ± 9.6	9	p = < 0.001

2.5 DISCUSSION

In this project, we have established the LOF mechanism behind six missense mutations associated with the *SCN9A*-CIP phenotype: a complete loss of conductance due to localised structural changes in otherwise fully folded and plasma membrane-localised mutant channels. This molecular mechanism is shared by previously reported missense LOF mutations that abolish conductance or significantly reduce current density. Sequence analysis revealed low tolerance for substitutions at these locations given the virtually complete conservation of native residues in Nav1.7 orthologues and paralogues within the hNav family. Structural modelling illustrated the clustering of LOF mutations in the S5-S6 pore loops and extracellular vestibule, underscoring the importance of maintaining specific biochemical features within the pore region. This study also adds evidence that the intracellular N-terminal tail plays an important role in modulating Nav1.7 function.

Exogenous expression of our WT and mutant FLAG-tagged Nav1.7 constructs in human cell lines resulted in a concentrated intracellular pool, a similar distribution to that observed of untagged Nav1.7 expressed in HEK293 cells[209] or tagged constructs in undifferentiated PC12 cells[207]. We found no obvious difference in subcellular distribution when comparing WT and mutant channels, particularly in the stably expressing cell lines, that was suggestive of a defect in secretory trafficking. Moreover, co-staining with anti-KDEL as a marker of the endoplasmic reticulum[251] illustrated negligible overlap between Nav1.7 constructs and the ER. Some abnormal distributions such as tubule-like staining or concentrated perinuclear foci were observed on rare occasions in transiently transfected HeLa cells. However, their absence in the stably transfected HEK cell lines suggests these were overproduction artifacts; true trafficking deficient ion channels tend to form small aggregates and display retention within the secretory pathway more consistently across transiently transfected cells[252].

To participate in action potential generation, Nav1.7 channels must localise to the cell membrane. HEK JI TREX cells stably expressing the WT Nav1.7-FLAG construct had previously been shown to express robust Na^+ currents, confirming HEK293 cells possess all the necessary machinery to produce functional channels and export them to the plasma membrane. Initial attempts to assess cell surface localisation by confocal microscopy showed that both WT and mutant channels localised as sparse puncta within the membrane compartment. This staining pattern did not change whether paraformaldehyde or methanol was used as the fixative. Cell permeabilization could not be avoided due to the lack of a suitable extracellular targeted antibody, though it is possible a weaker Triton-X solution or gentler detergent such as saponin could have changed the amount of Nav1.7 detected in the membrane[253,254]. However, a similar absence of plasma membrane enrichment has been observed

in fixed-cell imaging of transfected mammalian cell lines and live-cell imaging of fluorescently tagged Nav1.7 in rodent sensory neurons[187,207,209], suggesting only a small proportion of channels are membrane-localised. We concluded that quantifying differences in fluorescence intensity in our *in vitro* model was unlikely to provide a meaningful comparison, compared to microscopy approaches at single-molecule resolution[187], and proceeded with a biochemical assay.

Cell-surface biotinylation has been used to quantify changes in the proportion of membrane-localised Nav1.7 in the presence of beta subunits and trafficking partner CRMP2[198,250], but not to compare WT to mutant channels. We found all six missense mutants reached the cell membrane, though the proportion of this population varied considerably between transient transfections; therefore, drawing quantitative conclusions from the transient transfection data would be problematic without a control for measuring transfection efficiency. Due to the single integration of the WT or mutant *SCN9A* construct into HEK JI TREX cell lines[255], differences in the proportion of surface-localised Nav1.7 could be more reliably attributed to an effect of the mutation rather than differences in transfection efficiency. Indeed, quantification of the WT Nav1.7 stable cell line indicated about 20% of the total number of channels expressed reached the cell surface, whereas this value varied from <10% to 75% across all WT transient transfections. Given that most reported Nav1.7 LOF mutants are non-conducting, we decided to move on to biophysical analysis of the mutant channels but return to quantification of plasma membrane localisation if there was evidence of reduced current density that might be correlated with a decrease in cell surface expression[256].

Manual voltage-clamp studies were conducted in HEK293 cells expressing WT or mutant Nav1.7, with a CsF-based intracellular solution to maximise recording time in the whole-cell patch-clamp configuration. A GFP plasmid was co-transfected in transient expression experiments to identify transfected cells. Chemical co-transfection with FuGENE HD was attempted first, with a 3:1 ratio of Nav1.7 to GFP vectors to increase the take-up and translation of Nav1.7; however, no WT currents were observed in fluorescent cells up to 72 hours post-transfection. Switching to electroporation resulted in measurable WT Nav1.7 currents from 48 hours post-transfection, with the hit rate increasing over time. In both cases, GFP fluorescence was observed from 24 hours post-transfection onwards. This data suggests electroporation improved co-transfection efficiency but that the GFP plasmid may have outcompeted the Nav1.7 plasmid for transcriptional machinery earlier in the post-transfection period, since both genes were driven by the CMV promoter[257].

Testing *SCN9A*-CIP mutations Leu75Pro and Arg911His using the electroporation approach revealed neither generated any current, suggesting they were non-conducting. This was particularly surprising

for the N-terminal mutation Leu75Pro – while N-terminal mutations in VGSCs have been reported to change channel availability, they have never been shown to abolish ion conductance[209,258,259]. Given that there was no way to be certain that fluorescent cells also co-expressed mutant Nav1.7 channels, and because some Nav1.7 LOF mutants retain partial function[208,209], we considered whether subtle changes in function might be missed by assuming non-excitable cells were a result of the mutation rather than failed transfection or translation in the recorded cells. Therefore, we decided to generate stable cell lines using the HEK JI TREX system, including the published Ala1236Glu mutant as a positive control exhibiting partial LOF, and employed automated patch-clamping to speed up data acquisition.

Induction of channel expression in the WT HEK JI TREX-Nav1.7-FLAG cell line consistently produced peak currents in the nanoampere range. In contrast, peak currents at -5 mV were negligible in negative controls (WT Nav1.7 uninduced: 168.8 ± 15.0 pA; EmGFP: 117.7 ± 15.0 pA) and the novel Nav1.7 mutants (ranging from 82.1 ± 9.3 to 167.9 ± 33.3 pA), whereas the Ala1236Glu mutant generated a small but perceptible current as expected. Taken together, our results indicate the primary mechanism of pathogenicity behind our *SCN9A*-CIP mutations is a loss of sodium ion conducting ability. Degradation due to major protein misfolding was not explored since we could detect full-length Nav1.7 mutants in whole cell lysates of the stable cell lines with an anti-Nav1.7 antibody directed against the C-terminal epitope. Moreover, Nav1.7 mutants were detected at the plasma membrane in cell-surface biotinylation experiments using the same antibody. Given the absence of insoluble, intracellular aggregates (a hallmark of misfolded ion channels[260,261]), it appears the mutants form structurally stable channels that are efficiently trafficked to the membrane, but the mutations interfere with a critical aspect of VGSC function.

The most straightforward mutation to understand is Ala1687Pro, which alters the composition of the DEKA ion selectivity filter and prohibits sodium ion permeation. The charged D/E/K residues have been proposed to form the sodium ion binding site based on size and electrostatic interactions[161], as point substitutions of these residues significantly reduce sodium ion selectivity over other metal ions[160–162,262]. Alanine has typically been considered the least important residue within the filter due to its small size and lack of charge, although these properties are important alongside the D/E/K residues for the exclusion of divalent calcium ions[162]. Point mutagenesis of the alanine to negatively charged glutamic acid or aspartic acid has been shown to reduce single-channel sodium conductance, attributed to the introduction of a carbonyl group which could hinder the passage of hydrated sodium ions[262,263]. The Ala1687Pro mutation is relatively conservative in terms of biochemical properties as both residues are small and uncharged. However, proline is known to force kinks in local structure due to the side chain connecting with the protein backbone twice. Furthermore, the homologous mutation

in Nav1.1 (A1724P) has been reported in a patient with intractable childhood epilepsy; although lacking functional analysis, it is in keeping with the association between *SCN1A* LOF mutations and Dravet syndrome[148,264]. These findings suggest the alanine to proline substitution may have a deleterious impact on the shape of the selectivity filter such that the passage of any ion is obstructed.

The Nav1.7 permeation pathway may also be permanently disrupted by the Arg911His mutation. This arginine is located four residues above the domain II glutamic acid of the selectivity filter; the proximity and opposite charges of the Arg911 and Glu916 sidechains form a salt bridge that appears to stabilise the orientation of the glutamic acid towards the centre of the pore. The Arg911His mutation would normally be considered a neutral substitution as both amino acids are equally large and the histidine residue can exist in a positively charged state in certain chemical environments[265]. However, it is more likely to be uncharged when exposed to the extracellular fluid with pH ~7.3[266,267], which would disrupt the salt bridge with Glu916. Missense mutations of the homologous arginine to histidine or cysteine in Nav1.1 (Arg946) and Nav1.2 (Arg937) were also shown to cause a complete loss of conductance[259,268,269], while those in Nav1.5 (Arg893) were associated with the cardiac LOF phenotype Brugada syndrome in 5 unrelated individuals[270]. Taken together, this data emphasises the importance of the arginine at this location across the human VGSC family.

Substitutions of the Nav1.7 Arg896 residue to tryptophan or glutamine have been shown to cause a complete LOF in independent studies[114,207]. The Arg896Gln mutation was non-conducting in HEK293 cells and displayed a reduced capacity to reach the plasma membrane in PC12 cells when assessed by fixed-cell confocal microscopy[207]. The Arg896Trp mutation was solely characterised by whole-cell voltage-clamp, and was in agreement with our findings[114]. Mutations of the homologous arginine in Nav1.5 (Arg878) to cysteine or histidine have been reported in Brugada syndrome and sick sinus syndrome patients, while functional analysis established the Arg878Cys mutant is non-conducting and excluded trafficking defects[256,270,271]. These mutations point again to a critical role of the native arginine residue; given its position bridging the disordered pore loops of domain II and III, the arginine may be involved in non-covalent interactions that stabilise the extracellular vestibule to optimally guide solvated sodium ions towards the pore.

The structural impact of the Thr342Met and Gly1725Arg mutations on Nav1.7 function are less clear. Thr342 is located on the D1:S5-S6 pore loop, although it is further from the permeation pathway than the previously described mutations. In Nav1.5, the Thr351Ile was found to cause minor misfolding which led to a reduction of membrane-localised channels and ~75% reduction in peak whole-cell Na^+ currents in HEK293 cells; the trafficking defect was partially corrected *in vitro* by incubation with

mexiletine and resulted in altered but measurable whole-cell currents[272]. In Nav1.1, Thr363Pro and Thr363Arg were also associated with Dravet syndrome phenotypes, although the mechanism and magnitude of LOF are unknown[264,273]. While the loss of this threonine across hNav channels may be universally pathogenic, the absence of a trafficking defect and complete loss of conductance caused by the Nav1.7 Thr342Met mutation indicates the effect on protein structure depends more on the properties of the substituted amino acid.

A similar trend exists for missense mutations in equivalent positions as the Nav1.7 Gly1725Arg mutation, located on the top of the DIV:S6 transmembrane segment. While the Nav1.7 CIP-mutant is non-conducting[114], the Nav1.5 Gly1748Asp mutant associated with Brugada syndrome exhibited an >80% reduction in peak current due to a trafficking defect, as well as substantial changes to multiple voltage-dependent parameters[274]. A different substitution in Nav1.1 (Gly1762Glu) has been reported in a patient with a sub-phenotype of Dravet syndrome but lacks functional data[275]. The native glycine residue is small and uncharged, conferring high conformational flexibility in this part of the protein. Therefore, mutation to any one of these large, charged amino acids is understandably disruptive; in the case of Nav1.7, the Gly1725Arg mutation may lock the DIV:S6 segment in place, preventing the radial turn necessary to open the intracellular activation gate[165].

The final *SCN9A*-CIP mutation, Leu75Pro, is located on the intracellular N-terminal tail and is the first patient mutation from this region, across the hNav family, that has been proven to abolish channel function. It is unclear how this region contributes to VGSC gating and conductance but the association of over 20 N-terminal missense mutations each in Nav1.1 and Nav1.5 with a range of LOF and GOF disorders illustrates its functional importance[147]. Few have been biophysically characterised, but these studies show the N-terminus can impact channel function in a variety of ways. LOF mutations significantly reduced current density in whole-cell patch-clamp studies without affecting voltage-dependent properties (Arg99His in Nav1.7[209]), or reduced channel availability by altering the kinetics of inactivation (Asp12Asn and Asp82Gly in Nav1.2[259]). In contrast, a Nav1.7 GOF mutation, (Q10R) hyperpolarised voltage-dependence of activation resulting in inherited erythromelalgia[258].

The N-terminal region has not been resolved in crystal structures of human VGSCs[240,276–278] as it appears to be highly flexible outside of the cell environment; however, it has been partially captured at low resolution in Na_vPaS, a eukaryotic VGSC from the American cockroach[279] (see Figure 2.21). Parts of the N-terminus form alpha helices that are oriented parallel to the cell membrane, and the whole region docks below the voltage-sensing unit of domain I. Comparing the entire length of Nav1.7 and Na_vPaS N-terminal domains shows very little sequence conservation, although the “PLED” sequence

in which the Leu75Pro mutation occurs is identical. Expanding this to “PLEDFDPFY” in Na_vPaS and the corresponding sequences across the hNav family reveals a highly conserved motif, which forms a small loop pointing the side chains of positively charged (glutamic acid, aspartic acid) and hydrophobic (leucine, phenylalanine, tyrosine) residues in alternating directions.

It has been suggested that the N-terminus binds to cytoskeletal protein interaction sites or hydrophobic pockets in the lipid membrane to ensure the channel is properly tethered *(N. Yan, personal communication; April 7th, 2021).* The Leu75Pro substitution would likely force another tight turn in this loop, adjusting the orientation of these residues so that the motif is no longer recognised by its receptor site. The exact nature of this interaction and why it is essential to Nav function remains to be explored. The next chapter addresses one hypothesis: that the Nav1.7 Leu75Pro mutation may disrupt a critical protein-protein interaction.

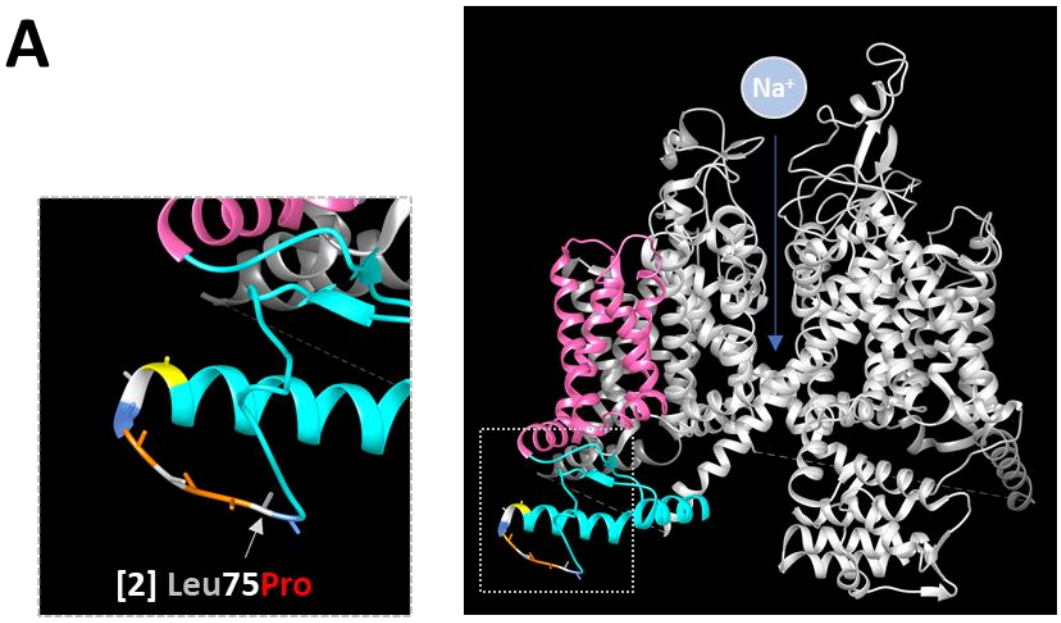

1	2	3	4	5	6	7	8	9
P	L	E	D	F/L	D	P	F/Y	Y
turn	*hydrophobic*	(+)	(+)	*hydrophobic*	(+)	*turn*	*hydrophobic aromatic*	*phosphorylation*

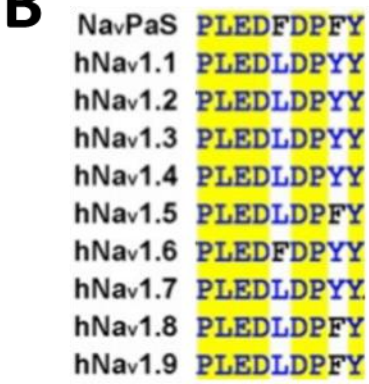

Figure 2.21: Structural features of the VGSC N-terminal tail
(A) Structural model of the eukaryotic VGSC Na_vPaS (PDB code: 5X0M). Residues 47-127 of the N-terminal tail were resolved (cyan) and located below the domain I voltage-sensing module (pink). The "PLEDFDPFY" motif is highlighted in the inset with amino acid sidechains coloured according to their biochemical properties, detailed in the grid. (B) Multiple sequence alignment of the Na_vPaS "PLEDFDPFY" motif across the hNav family illustrates strong conservation. Adapted from *Structure of a eukaryotic voltage-gated sodium channel at near-atomic resolution*. Reprinted with permission from AAAS.

CHAPTER 3: Interactome Study of a Loss-of-Function N-terminal Mutation in Nav1.7

3.1 INTRODUCTION

3.1.1 – Functional Roles of the Tail Domains in Human Nav Channels

A notable evolutionary feature of eukaryotic Nav channels is their arrangement from a single polypeptide chain rather than the homotetrameric structure of prokaryotic VGSCs. In bacterial Nav channels, each monomer subunit is equivalent to one of the six transmembrane subdomains of eukaryotic channels. The bacterial subunits possess identical free N- and C-terminal tails, whereas eukaryotic channels possess inter-domain linkers with divergent lengths and sequences, and single N-terminal and C-terminal tails extending from domain I and IV respectively. These linkers and tail domains are important sites for protein-protein interactions (PPIs), post-translational modifications (PTMs) and intramolecular interactions that modulate VGSC function[158,163,280].

In human Nav channels, both the N-terminal and C-terminal tail domains (NTD and CTD) are involved in localising channels to the plasma membrane and even specific subdomains. The intracellular tail sequences are the least conserved parts of the channel when compared across the hNav family, which reflect adaptations to expression in distinct cellular environments. For example, Nav1.2 is enriched along axons of unmyelinated cortical neurons while Nav1.6 localisation is restricted to dendritic and somatic regions. Studies of channel chimeras found that swapping either of the Nav1.6 tail domains onto Nav1.2 forced the same spatial restrictions onto Nav1.2 and excluded it from the axon, while swapping both Nav1.2 terminal domains simultaneously onto Nav1.6 allowed Nav1.6 access onto axonal membranes[281]. Limiting ion channel localisation to specific compartments can arise from non-specific delivery but targeted endocytosis, as has been suggested for Nav1.2[282]. An alternative mechanism is by programmed sorting based on interactions with trafficking partners; in the case of Nav1.5, its NTD mediates an interaction with cytoskeletal factor α1-syntrophin to enhance membrane expression in cardiac myocytes[283].

The C-terminus has also been implicated in regulating fast inactivation in a channel-specific manner; swapping the Nav1.2 CTD with Nav1.3, Nav1.5 or Nav1.6 exchanged their fast inactivation kinetics[284–286], while Nav1.4 and Nav1.5 mutations in this region are commonly associated with changes in fast inactivation parameters[287,288]. The structural basis for this functional connection was recently determined for Nav1.4 and Nav1.5. When Nav channels are at rest or during the early stages of activation, the fast inactivation motif in the DIII-IV linker interacts with the C-terminus. In some VGSC subtypes, this interaction is stabilised by additional PPIs with calmodulin and fibroblast growth factor

homologous factor (FHF) proteins. In wild-type (WT) channels, domain IV voltage sensor activation overcomes these forces and releases the inactivation particle in a controlled manner to constrict the pore. Consequently, mutations that weaken any of these intramolecular or protein-protein interactions reduce the precision of this conformational change, resulting in persistent currents[289,290]. While the calmodulin-binding IQ domain is shared by most of the hNav family[291], additional binding sites on the C-terminus seem to underlie subtype-specific differences in how calmodulin regulates Nav channel behaviour[292–294].

The Nav1.7 CTD has been swapped into Nav1.8 and Nav1.9 to increase their surface expression in HEK293-based cell lines. The critical regulatory site was refined to the more proximal portion of the CTD tail, although excluded the IQ domain for Nav1.9. The chimeras displayed similar biophysical profiles to their parent channels, apart from voltage-dependence and kinetics of fast inactivation which were closer to Nav1.7 values[295–297]. These results indicate a sequence or structural element unique to the Nav1.7 CTD facilitates forward trafficking to the membrane in non-neuronal cells. The differences in fast inactivation mirror patterns observed in other channel chimeras which could be mediated by intramolecular and/or protein-protein interactions with calmodulin or FHF proteins[291,298]. The importance of the Nav1.7 NTD is less clear, as no conserved functional role has yet been observed.

3.1.2 – Protein Partners Mediating Secretory Trafficking of Nav1.7

As a transmembrane protein, Nav1.7 must be embedded in a lipid bilayer to maintain its structural integrity. Consequently, its orientation in transport vesicles and at the cell surface positions the intracellular tail domains and linkers towards the cytoplasm where they are subject to regulatory interactions. The binding partners that mediate Nav channel transport through the secretory pathway and to membrane subdomains are relatively well characterised for some subtypes[195,299,300], and are beginning to be uncovered for Nav1.7 (see Figures 3.1 & 3.2A).

Following biosynthesis and tertiary folding in the endoplasmic reticulum (ER), VGSCs undergo glycosylation in the ER and Golgi network, inserting charged glycan moieties on the channel surface. This modification has been shown to affect channel gating and plasma membrane localisation in various VGSC subtypes[301–304]. When Nav1.7 is expressed alone in HEK293 cells, core glycosylated (~250 kDa) and fully glycosylated (~280 kDa) isoforms have been identified at the cell surface[198]. When beta subunits β2 or β4 were co-expressed, the same glycoforms were identified and there was no change in current density or gating properties. In contrast, the presence of β1 or β3 significantly increased Nav1.7 current density, and was associated with faster rates of activation and depolarising shifts in voltage-dependence of inactivation. Curiously, β1 or β3 co-expression led to the formation of an intermediate glycosylation state (~260 kDa). This intermediate glycoform was enriched at the cell surface when β1 was present, whereas β3 promoted surface localisation of the core glycoform. These results suggest β1 and β3 direct Nav1.7 towards alternative glycosyltransferase or glycosidase enzymes, perhaps in the ER where β1-Nav1.5 and β3-Nav1.8 interactions were demonstrated[305,306].

To reach the plasma membrane, VGSCs must be exported from the Golgi and targeted towards the cell surface. Several Nav1.7 binding partners have been separately identified that may together facilitate the sorting of Nav1.7 vesicles for forward trafficking. A live-cell imaging study of cultured DRG neurons showed Nav1.7 is selectively co-transported with Rab6A, which mediates anterograde transport towards axon terminals[187]. However, a substantial proportion of Nav1.7-positive vesicles were negative for Rab6A or the other Rab proteins tested, suggesting other Rab family members could also be involved[307]. Given that the speed of vesicle movement was consistent with carriage by a kinesin motor, and was halted upon microtubule destabilisation[187], a kinesin was proposed to drive Rab6A-Nav1.7 vesicular transport. Nav1.7 has been found to interact with KIF3A[308] and KIF5B[309] in mouse DRG, although the latter interaction is absent in rat DRG[196,310]. This may be due to a species difference, or differences in the composition of lysis buffer, influencing the Nav1.7-KIF5B interaction directly or indirectly via an essential adaptor such as ankyrin-G[311]. Both ankyrin-G and Nav1.7 are upregulated in

painful human neuromas[312,313], and an interaction between them in mouse DRG was recently validated[309]; the binding site is most likely via a conserved motif in the domain II-III linker[314].

Multiple studies have implicated KIF5B in the movement of Rab6-positive vesicles towards the cell periphery[315–317], though additional kinesins are involved in vesicle budding and supporting microtubule binding[315,317]. Rab6A and KIF5B were also shown to co-localise with non-muscle myosin II (NMII) at the Golgi. Interestingly, the Rab6A-NMII interaction was necessary for the fission of Golgi vesicles moving in both anterograde (towards the plasma membrane) and retrograde (towards the ER) directions, whereas KIF5B only pulled Rab6A-positive vesicles towards the cell surface[315]. NMIIa and NMIIb subtypes also interact with Nav1.7 and Nav1.8 in rat DRG, and over-expression of NMIIb with Nav1.8 in the rodent neuronal cell line ND7/23 enhanced current density three-fold[310]. NMIIb is also associated with short range, post-Golgi transport of Kv2.1 channels; its depletion in cultured hippocampal neurons by shRNA led to Kv2.1 trafficking defects and reduced Kv2.1 total expression, possibly due to channel degradation[318]. Taken together, the sequential interactions of Rab6A, NMII and KIF5B with Nav1.7 may enable the sorting of nascent channels towards the secretory pathway.

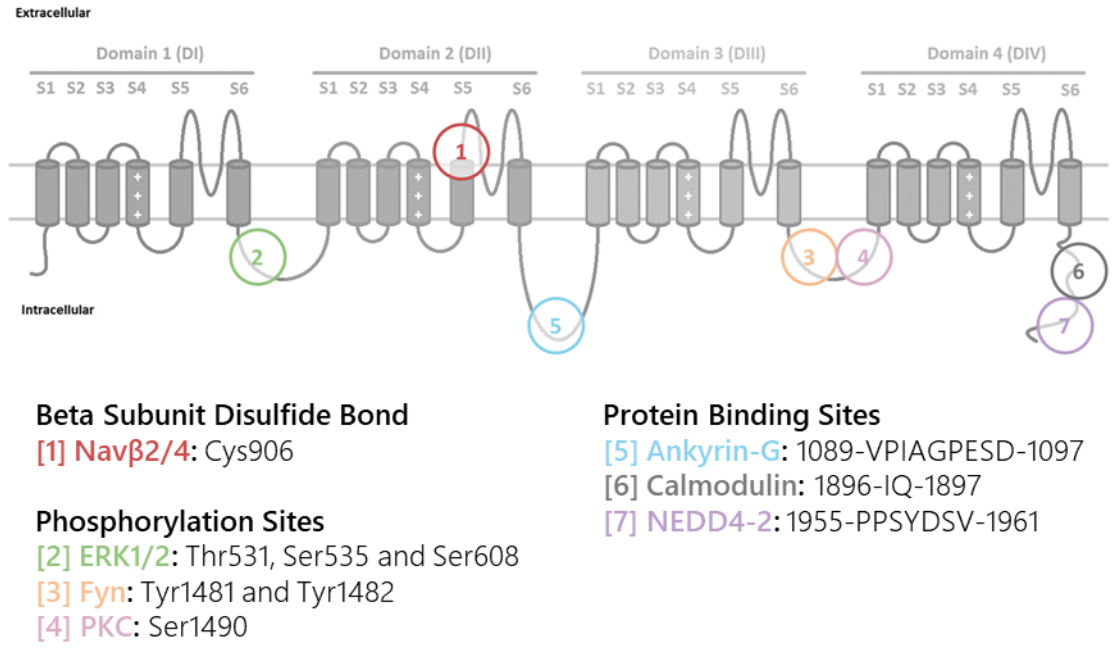

Figure 3.1: Nav1.7 protein-protein interaction sites and post-translational modifications
Locations of experimentally confirmed binding sites and phosphorylated residues on Nav1.7. Residue numbering is based on the 11L splice variant.

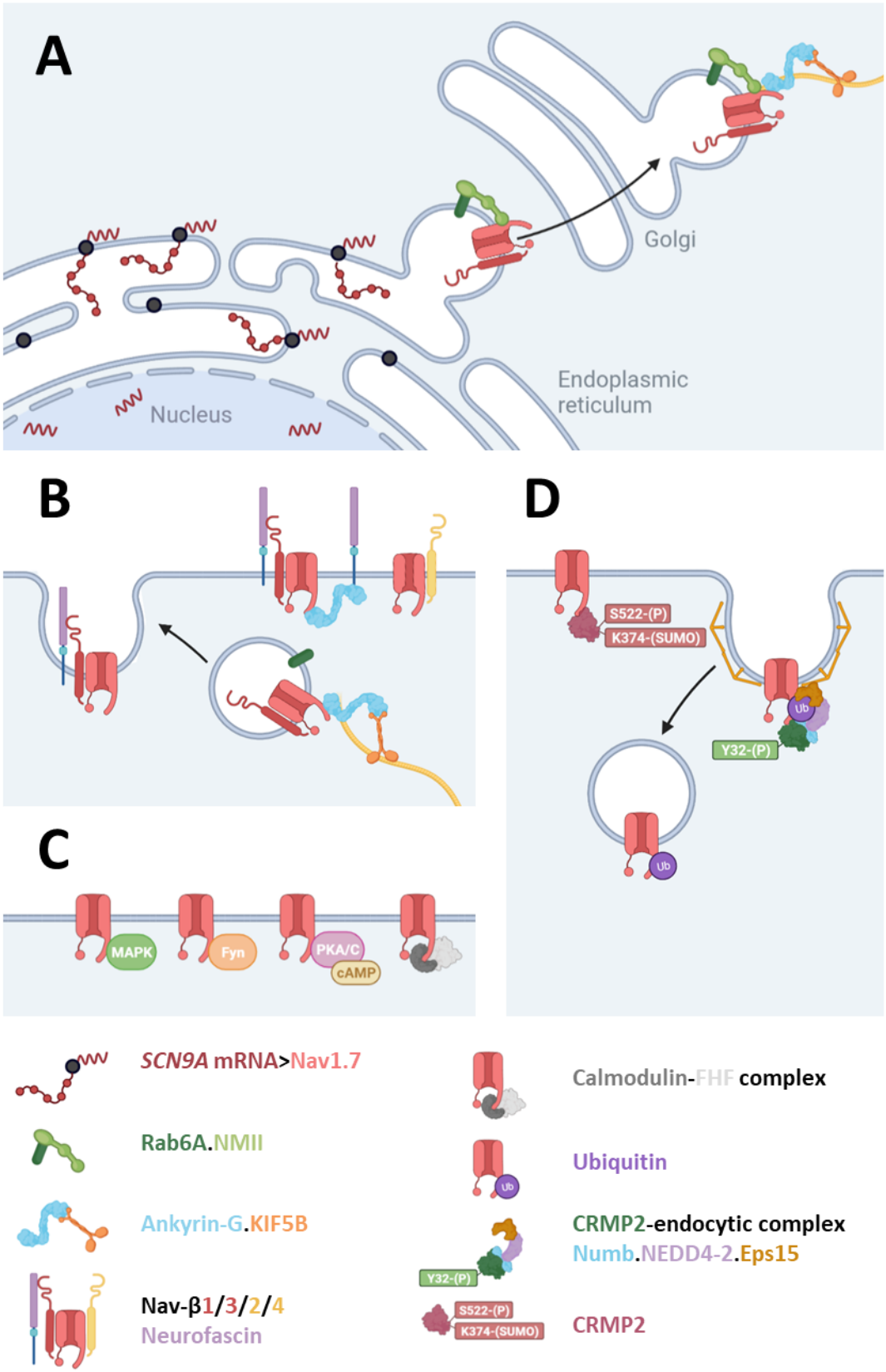

Figure 3.2: Protein-protein interactions regulating Nav1.7 localisation and channel availability
Nav1.7 protein complexes involved in (A) secretory transport, (B) stabilising plasma membrane localisation, (C) modulating gating properties, and (D) clathrin-mediated endocytosis. *Figure produced with Biorender.com.*

3.1.3 – Protein Partners Regulating Nav1.7 Localisation at the Plasma Membrane

Upon reaching the cell surface, vesicle fusion inserts Nav1.7 into the plasma membrane (see Figure 3.2B). Interactions with other transmembrane proteins and cytoskeletal components can direct channel insertion to specific subdomains and promote the association of larger regulatory complexes. A periodic actin-spectrin cytoskeleton structure was recently discovered in axons across the nervous system, including in fixed sciatic nerve preparations and unmyelinated DRG neuron cultures[319,320]. It has been proposed to act as an organisational platform for signalling molecules to support action potential generation and propagation[321,322]. Live-cell imaging studies of unmyelinated DRG neuron cultures show Nav1.7 channels accumulate in nanoclusters along the axon but do not exhibit the same patterned localisation[187], indicating the periodic cytoskeleton does not intrinsically impose a regular membrane distribution of Nav1.7.

Physical interactions between Nav1.7 and the Nav beta subunits β1-β3 have been demonstrated by co-immunoprecipitation (co-IP) and structural studies[240,309]. The β1 and β3 subunits were shown to increase Nav1.7 localisation at the plasma membrane[198], although dynamic studies are needed to determine whether the beta subunits enhance forward trafficking or anchoring at the cell surface. Nav1.7 also associates with neurofascin[309], a neuronal-specific cell adhesion molecule, which may further form heterotrimeric complexes with β1 or β3 subunits[323]. In myelinated DRG neurons, neurofascin is one of the earliest components localised to nodes of Ranvier, drawing in other factors such as Nav channels and ankyrin-G[324]. Consequently, postnatal knockdown of *NFASC* moderately lowered the expression of these components at peripheral nodes and reduced conduction velocity[325]. The specific VGSC subtype was not determined in these studies but could include Nav1.1, Nav1.6, Nav1.7 or Nav1.8[60]. Neurofascin is likely targeted to the plasma membrane independently of Nav1.7 but functions to stabilise channel localisation at nodes of Ranvier[326].

Nav1.7 internalisation is initiated by signalling molecule CRMP2 (see Figure 3.2D). CRMP2 itself is subject to a complex hierarchy of PTMs which control the recruitment of ubiquitinating[327] and endocytic machinery[328]. Cdk5-mediated phosphorylation of serine522 and Ubc9-dependent SUMOylation of lysine374 prevent CRMP2 from associating with the endocytic complex. Conversely, Fyn-mediated phosphorylation of tyrosine32 biases CRMP2 interactions toward Nav1.7 internalisation[328,329]. In this state, CRMP2 first engages the adaptor protein Numb which attracts the E3 ubiquitin-ligase NEDD4-2 to the PPxYxxV-motif in the Nav1.7 CTD (see Figure 3.1). Monoubiquitinated Nav1.7 is then recognised by Eps15 which promotes the assembly of clathrin-coated endosomes. A physical interaction between CRMP2 and Nav1.7 has been demonstrated by co-

IP[309,328]. Although the binding site has not been determined, binding affinity was significantly reduced with the SUMOylation-deficient CRMP2 mutant[328].

This regulatory pathway occurs *in vitro* and *in vivo*[200,328] and may be differentially involved in distinct chronic pain conditions[330–332]. Intriguingly, the interplay of CRMP2 and Nav1.7 signalling in neuropathic pain appears to be influenced in a sex-specific manner[200,333]. Nevertheless, an exciting development from this body of work was the generation of a therapeutic peptide that inhibits CRMP2 SUMOylation by Ubc9, subsequently reducing Nav1.7 membrane localisation and current density, and alleviating behavioural signs of neuropathic pain in rats of both sexes[329,334].

3.1.4 – Protein Partners Modulating Nav1.7 Gating Properties

Multiple protein kinases act on Nav channels (see Figures 3.1 & 3.2C), imparting negatively charged phosphate groups onto distinct residues. These local changes in charge density can influence intramolecular interactions or the affinity for protein binding partners in order to alter gating behaviour[180,335,336].

Nav1.7 is a substrate for extracellular signal-regulated kinase 1/2 (ERK1/2), a member of the mitogen-activated protein kinase (MAPK) family. Pro-inflammatory mediators activate intracellular signalling cascades that lead to the phosphorylation of MAPKs, allowing them to phosphorylate a wide range of targets[180]. The co-localisation of activated MAPKs with Nav1.7 was first observed in patient samples and experimental models of painful neuromas[313,337]. Nav1.7 phosphorylation by ERK1/2 hyperpolarizes the voltage-dependence of activation and fast inactivation, increasing the firing frequency of DRG neurons. This functional modulation is dependent on phosphorylation of three residues in the domain I-II linker: threonine531, serine535 and serine608[338]. In a model of migraine, IL-6 application induced facial allodynia in awake rats and hyperexcitability in cultured trigeminal sensory neurons; these effects were associated with an enhanced interaction between Nav1.7 and ERK1, and alleviated by an inhibitor of MAPK phosphorylation[339]. The p38 MAPK was also visualised with Nav1.7 in neuroma studies[313,338] although Nav1.7 may not be its direct target; rather, p38 activation downstream of protein kinase C was shown to increase total Nav1.7 expression, possibly via a transcriptional mechanism, in a rodent model of painful diabetic neuropathy[340,341].

Protein Kinases A and C (PKA and PKC) also modify Nav1.7 properties. In *Xenopus* oocytes, activated PKA reduced Nav1.7 peak currents and increased those for Nav1.8 without changing gating parameters; an effect attributed to altered membrane trafficking[342]. In contrast, PKA activation in the human tsA201 cell line led to a negative shift in Nav1.7 voltage-dependence of activation, but without an effect on current magnitude. Notably, the modulation in human cells was specific to Nav1.7 splice variants with the short form of exon 11, as Nav1.7-11L splice variants were not affected by PKA activation[173]. The authors proposed extension of the domain I-II linker obscured a binding site for an A kinase-anchoring protein (AKAP), as AKAP-15 had been shown to bind in this vicinity and was necessary for PKA-mediated modulation of Nav1.2[343]. A recent Nav1.7 interactome study identified AKAP-12 as a putative binding partner (see next section). Although requiring further validation, it is worth noting that their *SCN9A* construct encoded the 11S splice variant[153,309], supporting the previous hypothesis. PKC activation in human cells expressing Nav1.7 depolarised both activation and fast inactivation, and significantly increased gating kinetics. These effects were dependent on the

phosphorylation of serine1479 in the domain III-IV linker[344]. PKC activity has also been shown to enhance the effects of pathogenic Nav1.7 mutations[344,345].

Fyn kinase interacts with Nav1.7 to phosphorylate tyrosine residues 1470 and 1471 in the domain III-IV linker[346]. A constitutively active form of Fyn increased total Nav1.7 expression and its membrane localisation, correlating with increased current density, in both HEK293 and ND7/23 cells. While effects on gating parameters differed depending on cell background[346], Fyn-mediated regulation of Nav1.7 is more complex *in vivo*, as direct phosphorylation of Nav1.7 is expected to enhance neuronal excitability whereas its action on CRMP2 promotes channel internalisation. The Nav1.7-Fyn binding site was not determined, but likely involves proline-rich motifs that act as SH3-binding domains. A comprehensive study of Fyn binding sites in Nav1.5 revealed four proline-rich motifs in the domain I-II linker and C-terminus that were necessary for the interaction[347]. While none of these interfaces are conserved within the hNav family, a distinct proline-rich motif in the domain I-II linker of Nav1.2 was also shown to be necessary to pulldown Fyn, drawing attention to this region[348]. However, the above studies did find the same tyrosines in the domain III-IV linker were responsible for Fyn-mediated changes in channel behaviour, and highlighted additional conserved residues in the tail domains that may be relevant to Nav1.7 modulation[347–349].

Certain protein-protein interactions at the cell surface have been shown to alter Nav1.7 function. FHF2A and FHF2B splice variants (also known as FGF13) were shown to have different effects on Nav1.7 gating properties but both contributed to hampering channel activation in HEK293 cells and DRG neurons[298]. However, the effects on fast inactivation seen in the human cell line were absent in the primary neuronal cultures[298]; this was surprising given the established relationship between FHF proteins Nav channel behaviour, as well as evidence of calmodulin binding to Nav1.7[291]. Conflicting results were presented in another study, where FHF2B increased Nav1.7 peak currents in HEK293 cells without altering voltage-dependence of activation or fast inactivation, and FHF2 knockout in Nav1.8-positive neurons reduced stimulus-evoked neuronal firing and behavioural responses to heat stimuli[350]. Further investigations are needed to fully understand FHF-mediated regulation of Nav1.7.

In addition to guiding glycosylation status and membrane localisation, Nav beta subunits also impact Nav1.7 gating properties. Association of VGSC α-subunits with β1 or β3 is non-covalent and may depend on extracellular, transmembrane or intracellular interfaces, whereas β2 or β4 form an extracellular disulfide bond via a cysteine residue in the domain II pore module of the α-subunit (see Figure 3.1)[145,240]. Co-expression of the β1 or β3 subunits with Nav1.7 increases current density due to enhanced membrane localisation and gating changes that would increase channel

availability[179,198,336,351,352]. While full-length β2 and β4 subunits have no such effect[198,336,353], the cleaved β4 C-terminus was shown to interfere with Nav1.7 fast inactivation in exogenous expression systems, although it is not known whether this event occurs *in vivo*[353]. *SCN2B* mutations from patients with painful neuropathies can however enhance Nav1.7 currents by altering its gating properties or potentially by increasing forward trafficking or stabilisation at the membrane[354,355].

3.1.5 – Unbiased Mapping of the Nav1.7-Interactome *in vivo*

Unbiased interactome studies of Nav channels have uncovered novel PPIs that have important functional implications using yeast two-hybrid and affinity purification with mass spectrometry[356,357]. The latter approach was recently taken to characterise the interactome of mouse Nav1.7[309,358].

In this study, an epitope-tagged Nav1.7 knock-in mouse was generated by targeting a tandem affinity purification (TAP) tag to the 3' end of the *SCN9A* locus. The tag had no effect on the voltage-dependence or kinetics of Nav1.7 gating *in vitro*, and homozygous knock-in mice displayed comparable pain behaviours to WT mice, indicating the epitope tag did not impart a change in channel function. In addition to known expression in DRG and the sciatic nerve, Nav1.7 was detected by immunohistochemistry in the hypothalamus, the olfactory bulb and the lumbar enlargement of the spinal cord. Samples from these tissues were lysed in 1% CHAPS buffer to preserve transmembrane protein conformations, followed by co-IP to pulldown protein complexes.

The TAP tag fused onto the Nav1.7 C-terminus consisted of a polyhistidine tag and then a FLAG-epitope tag, with a TEV protease cleavage site in between. This allowed for a two-step purification procedure to enrich for high-affinity bait-specific interactions, but since low-affinity transient interactions can be lost, the authors opted for a single-step protocol using anti-FLAG antibody-coupled magnetic beads. The isolated complexes from knock-in vs WT mice were analysed by mass spectrometry and quantified based on a spectral counting method (as *in vivo* proteomics studies are not amenable to metabolic/chemical labelling approaches) to identify Nav1.7-specific interactions.

Hydrolase enzymes, cytoskeletal proteins and transporters were the most common protein classes identified within the Nav1.7 interactome. Twelve candidates were validated by western blot, being pulled down with Nav1.7 at endogenous levels in DRG. Those already known to have functional relationships with VGSCs included the Navβ3 subunit, cell adhesion molecule neurofascin, cytoskeletal tether ankyrin-G, microtubule motor KIF5B, protein kinase scaffolding protein AKAP-12 and signalling molecule CRMP2. Several novel PPIs were also detected such as secretory cargo-sorting protein TMED10, cell adhesion molecule neurotrimin and amino acid transporter LAT1.

Altogether, this paper presented the first attempt at unbiased mapping of the Nav1.7 interactome in physiologically relevant tissues, highlighting established and newly recognised binding partners that may allow for indirect regulation of Nav1.7 function.

3.2 OBJECTIVES

Compared to other regions of the typical Nav channel (e.g., voltage-sensor segments, pore loops, inactivation particle etc.), there is no consensus as to the functional role of the N-terminal tail. However, the presence of numerous disease-related mutations in this region[147], some of which have been shown to alter current density or voltage-dependent gating[209,258,259], demonstrates its ability to modulate channel function. The *SCN9A*-CIP mutation Leu75Pro abolishes Nav1.7 conductance without affecting cell-surface localisation in HEK293 cells, revealing an essential role for this residue in Nav1.7 function at the plasma membrane.

The Leu75Pro mutation is located within a highly conserved motif across the hNav family. This motif forms a disordered portion of the N-terminal tail, exposed to the cytoplasm in the eukaryotic Na_vPas structure rather than buried beneath a voltage-sensor domain (see Figure 3.3A), thus well placed to interact with intracellular proteins. Therefore, we considered whether the Leu75Pro mutation disrupts a critical protein-protein interaction at the plasma membrane (e.g., tethering to the cytoskeleton) that may control the motion of the N-terminal tail to facilitate ion conductance.

Given that the molecular loss-of-function could be observed in the HEK JI TREX-Nav1.7-FLAG cell background, we set the following experimental objectives for *in vitro* studies (see Figure 3.3B):

A. Conduct co-immunoprecipitation with mass spectrometry (IP-MS) experiments to investigate potential differences between WT and Leu75Pro Nav1.7 interactomes.
B. Validate candidates of interest from mass spectrometry by western blot.
C. Knockdown potential hits in the WT HEK JI TREX-Nav1.7-FLAG cell line and profile the effects on Nav1.7 function by whole-cell voltage-clamp.
D. If hit PPIs are disrupted by the Leu75Pro mutation, or knockdown in the WT cell line alters Nav1.7 function, confirm physiological relevance of interactions by co-IP in rodent DRG and/or demonstrate co-localisation by immunohistochemistry in human DRG.

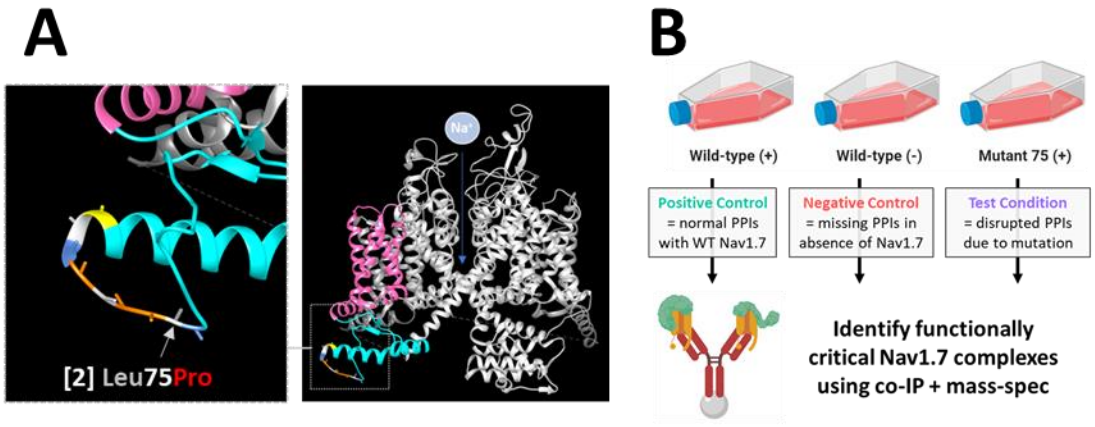

Figure 3.3: Investigating interactomes of WT hNav1.7 and the LOF N-terminal mutant, Leu75Pro
(A) Location of the PLEDLPFY motif (in blue, grey, orange & yellow; sidechains displayed as sticks) in the N-terminal tail (cyan) of Na_vPas. The domain I voltage-sensor segments are coloured pink.
(B) Experimental design for IP-MS studies of the hNav1.7 interactome in HEK JI TREX-Nav1.7-FLAG cell lines. (-) and (+) indicate uninduced or doxycycline-induced expression of *SCN9A* respectively.

3.3 METHODS

3.3.1 – Cell Preparation for IP-MS Experiments

The HEK JI TREX-Nav1.7-FLAG cell lines for WT and Leu75Pro mutant were maintained as described in Section 2.3.8. Cells were grown in five T-175 flasks per condition until almost confluent then Nav1.7 expression was induced with doxycycline 16-24 hours before the co-IP protocol. The three conditions per IP-MS experiment were WT uninduced, WT induced and mutant induced – WT(-), WT(+) and 75(+) respectively.

3.3.2 – Co-immunoprecipitation

Co-IP of hNav1.7 protein complexes from HEK JI TREX-Nav1.7-FLAG cell lines was conducted using the Dynabeads Co-Immunoprecipitation Kit and DynaMag-2 Magnet (both Invitrogen). Antibodies were covalently coupled to M-270 Epoxy-coated magnetic beads – purified mouse monoclonal anti-Nav1.7 (Merck, #MABN41) and anti-FLAG (Cell Signaling Technology, #8146S) were both tested, but the former was taken forward for IP-MS experiments as Nav1.7-FLAG pulldown was more efficient. Antibody-coupled beads were prepared fresh for the day of co-IP experiments, at a concentration of 7 µg antibody per mg beads and 1.5 mg antibody-coupled beads per condition as recommended. Coupling was carried out overnight in a shaking incubator at 37°C and 225 RPM, followed by washing in 0.05% Tween-20 supplemented wash buffers.

Cells were washed with PBS, trypsinised and re-suspended in culture medium, spun down at 300 x *g* for 5 minutes, and then washed and centrifuged again. After aspirating the PBS, the weight of the cell pellet was calculated, followed by lysis on ice for 15 minutes at a 1:9 ratio of cell mass to extraction buffer volume. The co-IP kit supplies a low stringency IP buffer containing 110 mM potassium acetate and 0.5% Triton X-100, which was minimally modified with 100 mM sodium chloride and EDTA-free Pierce protease and phosphatase inhibitors (Thermo Scientific), then referred to as the extraction buffer (also known as the lysis buffer). The lysed cell suspensions were centrifuged at 2600 x *g* for 5 minutes and the supernatant was transferred for use in co-IP. A tenth of this "input" fraction per condition was set aside for western blotting.

The remaining volume of input was incubated with antibody-coupled beads for 45 minutes on a roller at 4°C, after which an aliquot of this suspension was set aside as the "flowthrough" fraction for quality control blots. The antibody-coupled beads (with captured Nav1.7 complexes) were separated from the solution using the DynaMag rack and subjected to three washes with extraction buffer followed by a final incubation with 0.02% Tween-20 wash buffer for 5 minutes at room temperature. The

purified protein complexes were then isolated in 60 µl elution buffer as the “eluate” fraction for immunoblotting or mass-spectrometry.

3.3.3 – Western Blot and Coomassie Staining for Co-IP Optimisation

A preliminary co-IP was conducted to compare the effectiveness of the anti-Nav1.7 versus anti-FLAG antibodies for pull down of Nav1.7-FLAG in WT(+) versus WT(-) conditions. Equal volumes of input, flowthrough and eluate fractions were loaded onto NuPAGE 3-8% Tris-Acetate gels (Invitrogen), followed by gel electrophoresis and wet transfer onto 0.45 µm PVDF membranes as described in Section 2.3.13. Nav1.7 bands were detected using the Merck anti-Nav1.7 antibody. For determining if the mass of cell input was sufficient for mass-spectrometry, another gel was run and stained with InstantBlue Protein Stain (Expedeon Protein Solutions) for 1.5 hours at room temperature, then visualised using the ChemiDoc MP Imaging System and Image Lab software (Bio-Rad).

3.3.4 – Mass Spectrometry and Label Free Quantitation Analysis

Sample processing and liquid chromatography with tandem mass spectrometry (LC-MS/MS) was conducted by Robin Antrobus, while label free quantitation (LFQ) analysis was conducted by Jack Houghton, both of the CIMR Core Proteomics Facility.

Eluted samples from co-IP experiments were electrophoresed on 10% NuPAGE Bis-Tris gels, followed by staining with SimplyBlue SafeStain (both Invitrogen). Each lane was then excised and cut into 4 equal sized pieces. Gel segments were reduced in 10 mM dithiothreitol solution for 30 minutes at 56°C, alkylated in iodoacetamide solution for 30 minutes in the dark, followed by a pre-incubation with 12.5 ng/µl trypsin solution for 20 minutes on ice. Excess trypsin solution was removed and replaced with 50 mM ammonium bicarbonate solution for overnight digestion at 37°C. Peptides were dehydrated by vacuum drying and resuspended in 20 µl injection solvent (3% acetonitrile, 0.1% trifluoroacetic acid in ultrapure water), of which 10 µl was injected for LC-MS/MS analysis.

Peptides were separated using the UltiMate™ 3000 RSLCnano liquid chromatography system (Thermo Scientific), fitted with an Acclaim™ PepMap™ C18 trap column (100 µM diameter, 2 cm length, 5 µm particle size, 100 Å pore size) for pre-concentrating peptides, and an EasySpray PepMap analytical column (75 µM diameter, 50 cm length, 2 µm particle size, 100 Å pore size). Peptides were eluted over 171 minutes at 40°C, using a gradient of 3-95% solvent B (solvent A: 0.1% formic acid; solvent B: 20% acetonitrile, 0.1% formic acid). Peptides were fed into the EASY-Spray™ Source emitter (Thermo Scientific) at a flow rate of 300 nl/min for electrospray ionisation. Ionised peptides then entered the

Orbitrap Fusion™ Lumos™ mass analyser (Thermo Scientific), which was operated in positive ion mode.

The Orbitrap detector resolution was set to 120,000 and the total LC-MS/MS run time was 60 minutes. The "top N" algorithm, a data-dependent acquisition approach, was applied to collect peptide sequence data[359]. During the MS1 survey scan, mass spectra of peptide ions within a mass-to-charge ratio (m/z) range of 375 to 1,500 m/z were isolated. The most abundant (top N) peptide ions over 3 second cycles were selected for fragmentation by higher-energy C-trap dissociation (HCD; collision energy set to 35%), to produce the MS2 spectra from which amino acid sequences could be inferred. The precursors for MS2 analysis were isolated in 1.6 m/z windows for optimal separation of peptides co-eluting at the same time, thus generating clean MS2 spectra.

Raw spectral files across the five IP-MS experiments were analysed with MaxQuant (version 1.6.6.0). The Andromeda search engine was used to make spectrum-peptide matches based on the following parameters:

(i) Human database (UniProt reference proteome downloaded 18 Dec 2018 containing 21066 proteins) with additional inbuilt MaxQuant contaminant database (containing 246 common contaminants)
(ii) Trypsin-specific digestion with up to 2 missed cleavages allowed
(iii) Methionine oxidation and N terminal acetylation as variable modifications
(iv) Cysteine carbamidomethylation as a fixed modification
(v) Precursor ion tolerance: 20 ppm in the preliminary search, 4.5 ppm in the main search
(vi) Label-free quantification (MaxLFQ algorithm) and match between runs enabled

The false discovery rate filter was set to < 1%. Proteins with three valid values were included, while reverse sequences and contaminants were excluded. Batch correction was carried out on protein LFQ values using the "ComBat" algorithm and post-processing was carried out using R with bespoke scripts incorporating the "limma" statistical package.

3.3.5 – Candidate Prioritisation from IP-MS Pilot Based on EUPC Analysis

To meet the objectives for this project in identifying and validating potentially critical functional partners of Nav1.7, at least 3 IP-MS experimental replicates were required to identify significant hits by LFQ analysis. Due to manufacturing issues with liquid chromatography columns and restricted access to labs during the covid-19 lockdowns, there was a 14-month delay in running sufficient replicate experiments and data analysis to identify putative hits. As this situation became apparent, several hits were chosen from the first IP-MS experiment based on 3 criteria:

1) The Exclusive Unique Peptide Count (EUPC) value for a given protein was less than 5 in the WT(-) condition and more than 7 in the WT(+) condition – i.e., sparsely present or absent from Nav1.7-co-IP when the channel is absent, but with at least a two-fold increase in the number of unique peptides identified from Nav1.7-co-IP when the channel is expressed.
2) Independent, published evidence of an interaction with Nav1.7
3) Enriched mRNA expression in DRG sensory neurons from adolescent mice using the http://mousebrain.org/genesearch.html tool[185]

With respect to criterion 1, fold change values were calculated using the equation '(B – A)/A' where 'A' represents the EUPC value for a given protein in the WT(-) sample and 'B' represents the same for either the WT(+) or 75(+) samples. To allow fold-change calculation for proteins with null expression values in the WT(-) sample, a negligible value of '0.1' was added to all EUPCs.

3.3.6 – Western Blot Validation of Select IP-MS hits

Non-muscle myosin IIa (NMIIa), AHNAK and AHNAK2 were prioritised for further investigation. The following antibodies were optimised for use in western blots: rabbit polyclonal anti-AHNAK (Proteintech, #16637-1-AP), rabbit polyclonal anti-AHNAK2 (Proteintech, #17682-1-AP) and anti-NMIIa (Abcam, #ab55456). The AHNAK antibodies were used at a 1 in 1000 dilution while the anti-NMIIa antibody solution was made to a final concentration of 2.5 µg/ml. Due to batch issues with the anti-AHNAK2 antibody, protein-level studies of AHNAK2 had to be withdrawn.

Sample preparation, gel electrophoresis and membrane transfer were performed as described in Section 2.3.13 with some key differences. Gel electrophoresis was conducted at 125V for 6 hours in the cold room to maximise separation of the AHNAK proteins (~600 kDa) from NMIIa and Nav1.7 (both ~250 kDa). Nitrocellulose membranes bound AHNAKs more efficiently than PVDF membranes in wet transfer conditions (data not shown), so were used throughout. To improve the transfer of high

molecular weight proteins in wet transfer conditions, the transfer buffer was supplemented with 0.1% sodium dodecyl sulfate (SDS) and methanol concentration was reduced to 10%.

Membrane transfer conditions were optimised to improve protein binding and detection. A 10X dilution series of whole-cell lysate was run on NuPAGE 3-8% Tris-Acetate gels (Invitrogen) and transferred in different conditions (see Section 3.3.4). Starting total protein concentration was determined using the Bio-Rad Protein Assay (Bio-Rad), dilutions of bovine serum albumin as protein standards, and the Spark multimode plate reader (Tecan) for colorimetric detection. In addition, PFA fixation of membranes was performed immediately after transfer for 30 minutes at room temperature to minimise protein loss during washes.

Preliminary blots indicated endogenous AHNAK, AHNAK2 and NMIIa levels in input fractions were very high and were suspected to be low in the co-IP fractions. Therefore, the minimum volume of inputs and maximum volume of co-IP fractions were loaded onto gels for the final IP-MS validation blot; 1.0 µl and 16.25 µl respectively. This adjustment was made in an attempt to avoid saturation of the input signals masking the whole blot and preventing visualisation of low-level protein expression in the co-IP fractions.

3.3.7 – siRNA Dosage Optimisation

SMARTpool siRNAs were obtained from Horizon Discovery for the following genes – GAPDH (#D-001830-10-05), MYH9 (#L-007668-00-0005), AHNAK (#L-014285-01-0005), AHNAK2 (#L-022014-01-0005), and a negative control Non-Targeting Pool (#D-001810-10-05). Transfection complexes were prepared in DharmaFECT1 (Horizon Discovery) and OptiMEM (Gibco) at siRNA concentrations from 12.5 to 100 nM and incubated for 30 minutes at room temperature in separate wells of a 24-well plate. The WT Nav1.7 inducible cell line was plated on top in antibiotic-free culture medium (i.e., lacking Geneticin and Blasticidin) at a seeding density of 50,000 cells/well. Untreated cells were included as an additional negative control.

Triplicate plates were prepared to test mRNA-level and protein-level knockdown at 24, 48 and 72 hours, and experiments were run in triplicate. Nav1.7 expression was induced with doxycycline at 24 hours post-transfection. Cells were lysed for mRNA and protein level quantification in RNA lysis buffer from the RNeasy Plus kit (Qiagen) and RIPA buffer with EDTA-free protease and phosphatase inhibitor tables (all from Sigma) respectively. However, due to limited availability of mRNA isolation kits and limited lab access during the covid-19 pandemic, mRNA and protein level knockdown could only be quantitatively assessed in one experimental replicate each.

3.3.8 – Total mRNA Isolation, cDNA Conversion and RT-qPCR

Total mRNA isolation was performed according to manufacturer's instructions of the RNeasy Plus kit (Qiagen). siRNA-treated cells were lysed with RLT Plus Buffer with β-mercaptoethanol and pellets were stored at -80°C until processing. RNA was eluted in RNase-free water and stored at -80°C until cDNA conversion. RNA concentration was quantified using the NanoDrop spectrophotometer (Thermo Scientific) before conversion to cDNA using the QScript cDNA synthesis kit (Quantabio) and recommended protocol.

Primers for RT-qPCR were designed using the GenScript tool (https://www.genscript.com/tools/real-time-pcr-taqman-primer-design-tool) and their reference transcripts are listed in Table 3.1. RT-qPCR reactions were prepared in triplicate using the LightCycler 480 SYBR Green I Master Mix (Roche) and were run on the CFX384 Real-Time PCR System (Bio-Rad). Reaction composition and thermocycling parameters are given in Table 3.2.

Table 3.1 – qPCR primers for MYH9, AHNAK and AHNAK2 mRNA quantification

PRIMER ID	PRIMER SEQUENCE	TRANSCIPT ID
MYH9-F	TGAATCTGGAGCTGGCAAGA	ENST00000216181.11
MYH9-R	CGAATGAATTTGCCGAAGCG	
AHNAK-F	ATGTCTCAGGACCCAAGGTG	ENST00000378024.9
AHNAK-R	ATTCAGGTCCACATCAGGCA	
AHNAK2-F	AGGATGAAGAGTGGGCTTCC	ENST00000333244.6
AHNAK2-R	ACATCCGTGTCCTCCTTCTC	

Table 3.2: Reaction Components & Thermocycling Protocol for qPCR

qPCR Reaction Components			
COMPONENT		**VOLUME (µl)**	
2X LightCycler 480 SYBR Green I Master Mix		5.0	
Target Primer – FWD (10 µM)		1.0	
Target Primer – REV (10 µM)		1.0	
PCR grade water		1.0	
cDNA template		2.0	
Thermocycling Parameters			
STAGE	**TEMP (°C)**	**TIME**	**CYCLES**
Pre-Incubation	95	5 minutes	---
Amplification	95	10 seconds	X 45
	51	10 seconds	
	72	10 seconds	
Melting Curve	95	5 seconds	---
	65	5 seconds	---
	+ Δ5°C steps	Continuous	---
END	95°C	---	---

3.3.9 – siRNA-Knockdown Data Analysis

Raw RT-qPCR data was exported to Microsoft Excel to calculate the ΔΔCt value for each siRNA condition according to the equation below, where ΔCTE represents the difference between Ct values of the gene of interest and GAPDH in the experimental treatment (i.e., NMIIa or AHNAK/2 siRNAs at increasing doses at different timepoints), and ΔCTC represents the same difference in the control treatment (i.e., cells treated with 50 nM non-targeting siRNA pool).

$$\Delta\Delta Ct = \Delta CTE - \Delta CTC \quad \{5\}$$

The most efficient knockdown dose at mRNA level was chosen to test protein-level knockdown by western blot and band densitometry analysis as described in Section 2.3.13. Both sets of data were charted in Graphpad software.

3.3.10 – Manual Patch Clamp in siRNA-treated cells

The WT HEK JI TREX-Nav1.7-FLAG cell line was used to profile the effects of double AHNAK knockdown on Nav1.7 biophysical properties. AHNAK and AHNAK2 were knocked down with 50 nM each SMARTpool siRNAs, and 50 nM non-targeting pool was used as the negative control. PDL-coated coverslips were placed in individual wells of a 24-well plate and siRNA transfection complexes were prepared as stated in Section 3.3.7. Cells were plated on top in antibiotic-free culture medium at a seeding density of 50,000 cells/well, and Nav1.7 expression was induced after 24 hours. Patch clamp recordings were performed at 48-72 hours post-transfection in the manual patch clamp set up described in [Section 2.3.14] to assess voltage-dependence of activation and fast inactivation using the protocols and analysis parameters described in sections 2.3.16-17. Statistical comparisons were made using unpaired, two-tailed t-tests with Welch's correction in Graphpad software, and results are expressed as mean averages ± SEM.

3.4 RESULTS

3.4.1 – Optimisation of Cell Input and Antibody Choice for IP-MS Experiments

Nav1.7 protein pulldown from HEK JI TREX-Nav1.7-FLAG cells lines was tested using anti-Nav1.7 versus anti-FLAG antibodies. The anti-FLAG antibody would isolate Nav1.7 constructs from the fusion FLAG tag on the Nav1.7 N-terminal tail, whereas the anti-Nav1.7 antibody targets amino acids 1751-1946 of the human Nav1.7 C-terminal tail. As shown in the eluate ("E") lanes of Figure 3.4A, Nav1.7-FLAG protein pulldown was much more effective using the anti-Nav1.7 antibody, with little protein lost in flowthrough washes. Therefore, this antibody was taken forward for IP-MS experiments. Notably, some Nav1.7 protein was expressed in the uninduced WT condition indicative of leaky transgene expression[360] in the absence of doxycycline competition with the TetR protein.

A large-scale co-IP experiment was run using cell input from 10 confluent T-175 flasks and samples were loaded onto a Coomassie stained gel to determine if this Nav1.7 expression was enriched enough for mass-spectrometry analysis (see Figure 3.4B). The molecular weight of untagged Nav1.7 is estimated to be 226 kDa, whilst the tagged Nav1.7 construct encoded in the stable cell lines was detected on western blots at just over 250 kDa. Review of the Coomassie stained gel by our Core Proteomics team determined that the smudge in the eluate lane at this molecular weight was most likely the pulled down Nav1.7 protein and deemed sufficient cell input for mass-spectrometry analysis. Due to the length of time required to culture such large amounts of cells for 3 conditions (i.e., WT(-), WT(+) and 75(+)), cell input was halved to 5 confluent T-175 flasks per condition.

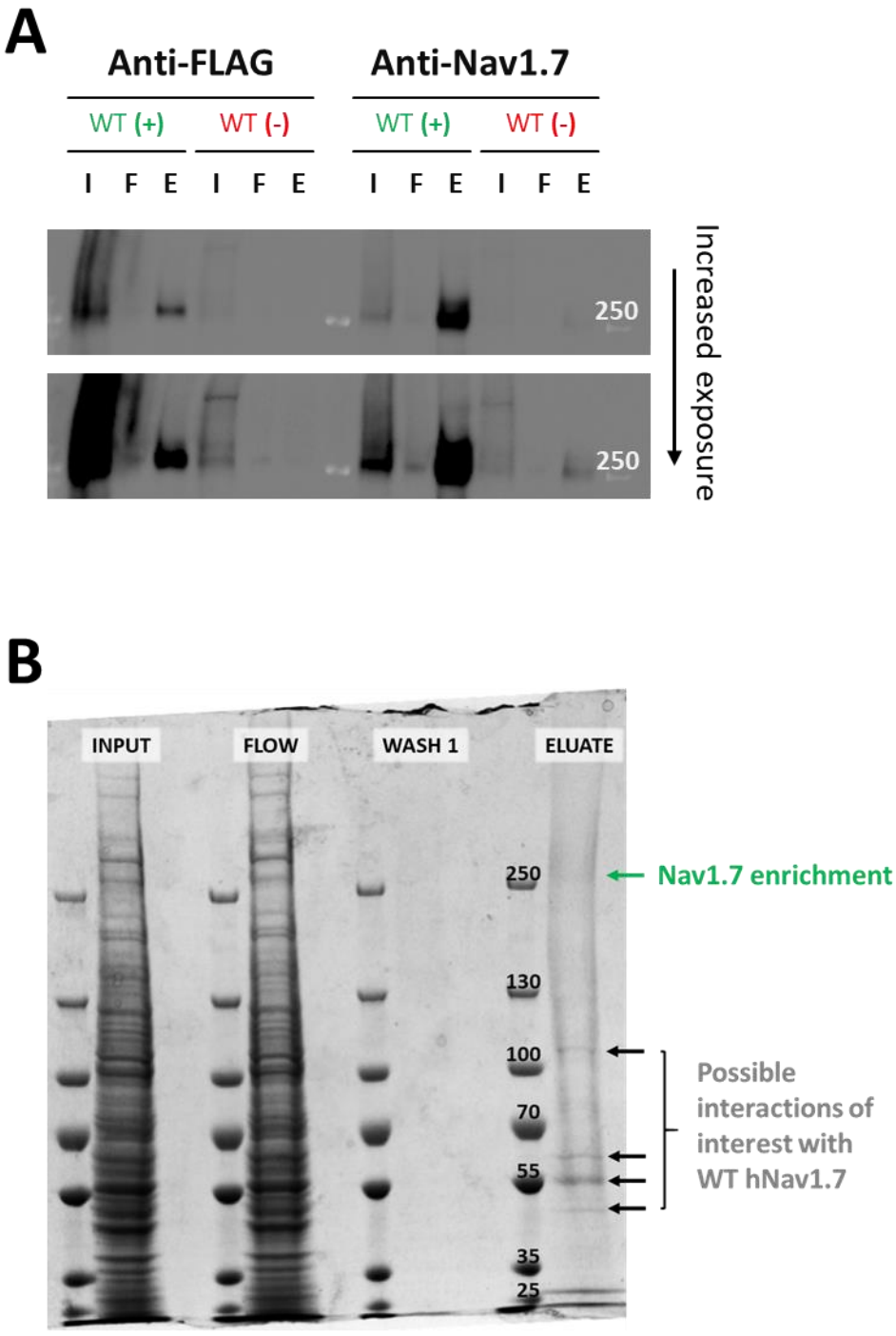

Figure 3.4: Optimisation of co-IP input for mass spectrometry
(A) Co-immunoprecipitation was tested to compare the efficiency of Nav1.7-FLAG pulldown by anti-FLAG versus anti-Nav1.7 antibodies from the induced "(+)" WT HEK JI TREX-Nav1.7-FLAG cell line. Uninduced "(-)" condition was used as a negative control. Input ("I"), flowthrough ("F") and eluate ("E") fractions were probed by western blot and illustrate better pulldown with the anti-Nav1.7 antibody, with minimal protein lost in the flowthrough. (B) A large-scale co-IP was run separately for Coomassie staining to determine if there was enough Nav1.7 protein for mass-spectrometry analysis.

3.4.2 – Prioritised hits from pilot IP-MS Experiments – NMIIa, AHNAK and AHNAK2

Given the severe delays in running replicate IP-MS experiments during the covid-19 pandemic, several hits were prioritised from the pilot IP-MS results, as described in Section 3.3.5 and Figure 3.5A. The prioritisation criteria were designed to identify proteins enriched in WT(+) complexes but were absent when channel expression was not induced in the WT(-) condition and "dropped out" when the L75P mutant channel was expressed, indicating binding may have been disturbed by the N-terminal mutation. Due to leaky expression of Nav1.7 in the WT(-) condition as a possible confounding factor, proteins with a minimal number of peptides were included in the prioritised hit list in Table 3.3.

This list was processed using the STRING functional enrichment analysis tool (https://string-db.org/) to build a PPI network, displayed in Figure 3.5B, which highlights the way proteins may interact with each other to form macromolecular complexes. Two proteins stood out due to independent reports of an interaction with Nav1.7 in DRG tissue – AHNAK was reported in the TAP-tagged mouse study by Kanellopoulos et al.[309] and non-muscle myosin IIa (NMIIa) was found to interact with Nav1.7 by Dash et al.[310]. AHNAK2 was also pulled down with WT Nav1.7 and as a structural homologue of AHNAK, was also prioritised for further study.

AHNAK was recently found to form a cytoskeletal scaffold, together with annexin A2 and p11, to bring alpha and beta subunits of L-type voltage-gated calcium channels in close proximity of each other in excitatory neurons and inhibitory interneurons in the brain[361]. The p11 protein has previously been found to bind to the N-terminal tail of Nav1.8 in a region that includes the Nav1.7 PLED motif[197] and p11 modulates Nav1.8 membrane localisation[362]. When comparing mRNA expression of these genes in adolescent mice using the mousebrain genesearch tool, they were all enriched in sensory neuron subtypes compared to other neuronal tissues, see Figure 3.6. Of special interest, *AHNAK* mRNA expression was strongest in non-peptidergic neurons whereas *AHNAK2* was enriched in the neurofilament class of DRG neurons, hinting they may play non-redundant roles in different sensory neuron subtypes.

Table 3.3 - Prioritised Hits from IP-MS Experiment 1 Based on EUPC Values

Due to technical and pandemic-related delays, candidate Nav1.7-binding partners were chosen from the pilot IP-MS experiment based on criteria laid out in Section 3.3.5. All proteins meeting criterion (1) – i.e., EUPC value of <5 in the WT(-) sample and >7 in the WT(+) sample – are listed here.

Proteins with null expression values in the WT(-) sample are separated in the bottom set. A negligible value of 0.1 was added to all EUPCs to allow fold change calculations when the EUPC for a protein in the WT(-) sample = 0.

The magnitude of fold-change comparing EUPCs in WT(+) or 75(+) samples to the WT(-) sample is colour coded such that the largest (most positive) to smallest (most negative) fold changes are indicated from darkest to lightest shades respectively.

			EXCLUSIVE UNIQUE PEPTIDE COUNT (EUPC)				
GENE	PROTEIN NAME (UNIPROT)	MOLECULAR WEIGHT (kDa)	WT(-)	WT(+)	75(+)	Fold Change WT(+) v WT (-)	Fold Change 75(+) v WT (-)
SCN9A	Sodium channel protein type 9 subunit alpha	226	4.1	35.1	29.1	7.56	6.10
AHNAK	Neuroblast differentiation-associated protein AHNAK	629	3.1	70.1	5.1	21.61	0.53
LMNA	Prelamin-A/C	74	1.1	21.1	3.1	18.18	1.82
EPPK1	Epiplakin	556	1.1	18.1	1.1	15.45	0.00
HSPA1A	Heat shock 70 kDa protein 1A	70	4.1	16.1	11.1	2.93	1.71
HSPA8	Heat shock cognate 71 kDa protein	71	1.1	15.1	6.1	12.73	4.55
HSPA5	Endoplasmic reticulum chaperone BiP	72	2.1	14.1	6.1	5.71	1.90
LGALS7	Galectin-7	15	2.1	12.1	3.1	4.76	0.48
PLEC	Plectin	532	1.1	12.1	0.1	10.00	-0.91
POF1B	Protein POF1B	68	4.1	11.1	7.1	1.71	0.73
EEF1A1	Elongation factor 1-alpha 1	50	3.1	11.1	7.1	2.58	1.29
SERPINB3	Serpin B3	45	3.1	11.1	1.1	2.58	-0.65
CALML5	Calmodulin-like protein 5	16	2.1	10.1	1.1	3.81	-0.48
HSPB1	Heat shock protein beta-1	23	2.1	10.1	4.1	3.81	0.95
ENO1	Alpha-enolase	47	5.1	9.1	5.1	0.78	0.00
RBM14	RNA-binding protein 14	69	2.1	9.1	5.1	3.33	1.43
PKP1	Plakophilin-1	83	4.1	8.1	8.1	0.98	0.98
TPI1	Triosephosphate isomerase	31	4.1	8.1	8.1	0.98	0.98
IDE	Insulin-degrading enzyme	118	1.1	8.1	0.1	6.36	-0.91
PKM	Pyruvate kinase PKM	58	1.1	8.1	3.1	6.36	1.82
MYH9	Myosin-9	227	0.1	21.1	0.1	210.00	0.00
EVPL	Envoplakin	232	0.1	20.1	1.1	200.00	10.00
ACTN4	Alpha-actinin-4	105	0.1	18.1	2.1	180.00	20.00
PPL	Periplakin	205	0.1	17.1	1.1	170.00	10.00
HERC2	E3 ubiquitin-protein ligase HERC2	527	0.1	15.1	28.1	150.00	280.00
IQGAP1	Ras GTPase-activating-like protein IQGAP1	189	0.1	14.1	0.1	140.00	0.00
IVL	Involucrin	68	0.1	12.1	0.1	120.00	0.00
P4HB	Protein disulfide-isomerase	57	0.1	11.1	0.1	110.00	0.00
SPTAN1	Spectrin alpha chain, non-erythrocytic 1	285	0.1	11.1	1.1	110.00	10.00
FLNB	Filamin-B	278	0.1	10.1	1.1	100.00	10.00
SERPINB5	Serpin B5	42	0.1	10.1	0.1	100.00	0.00
YWHAZ	14-3-3 protein zeta/delta	28	0.1	9.1	0.1	90.00	0.00
EEF2	Elongation factor 2	95	0.1	9.1	3.1	90.00	30.00
PGK1	Phosphoglycerate kinase 1	45	0.1	9.1	0.1	90.00	0.00
RAB1B	Ras-related protein Rab-1B	22	0.1	9.1	0.1	90.00	0.00
TUBB	Tubulin beta chain	50	0.1	9.1	2.1	90.00	20.00
AHNAK2	Protein AHNAK2	617	0.1	8.1	0.1	80.00	0.00
PPP1R12A	Protein phosphatase 1 regulatory subunit 12A	115	0.1	8.1	1.1	80.00	10.00
VCP	Transitional endoplasmic reticulum ATPase	89	0.1	8.1	3.1	80.00	30.00

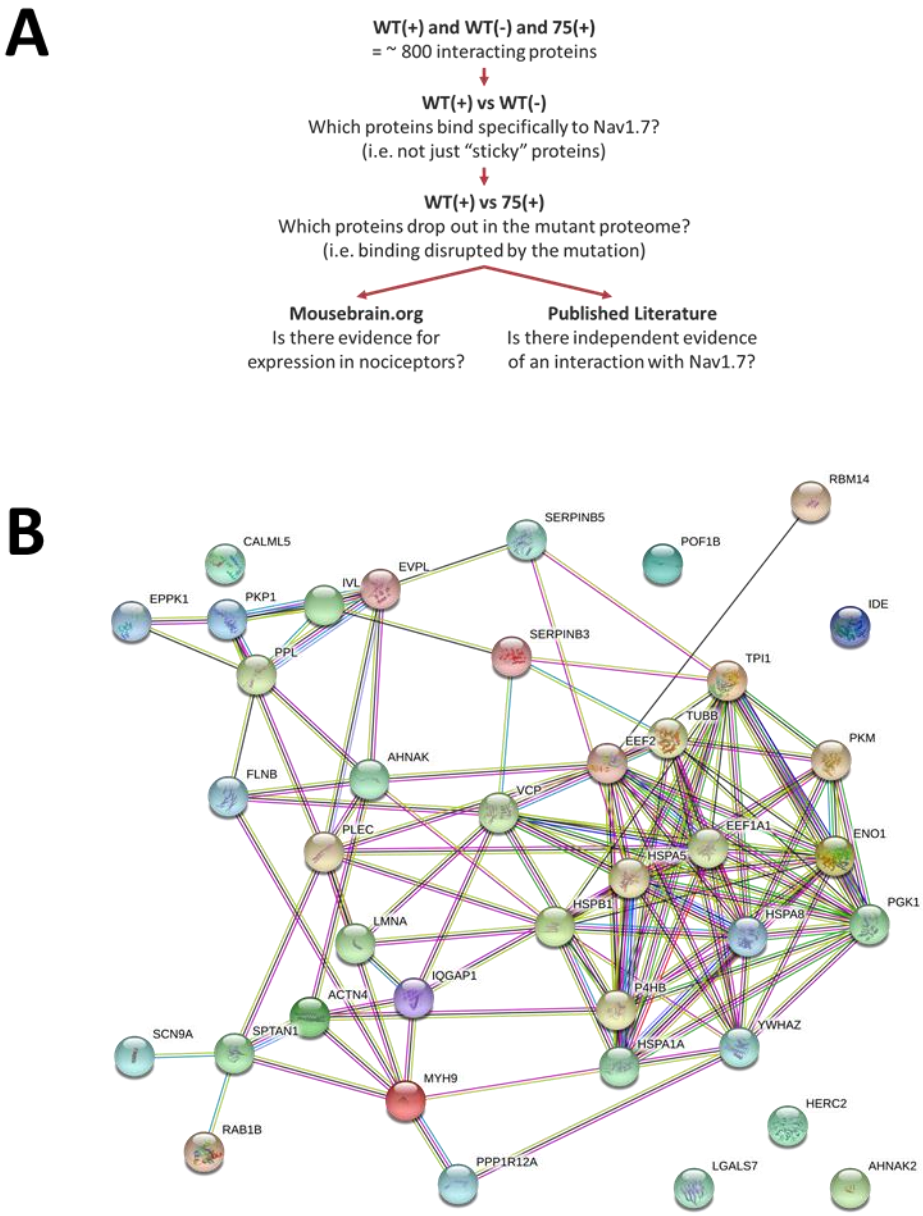

Figure 3.5: Hit prioritisation approach and results from IP-MS Experiment 1
(A) Decision tree of principles used to identify physiologically relevant binding partners of hNav1.7 that may be disrupted by the N-terminal mutation Leu75Pro. (B) 38 proteins of interest were identified based on exclusive unique peptide counts in the WT(+), WT(-) and 75(+) proteomes. Functional network analysis of these proteins was performed using the online tool https://string-db.org/.

A

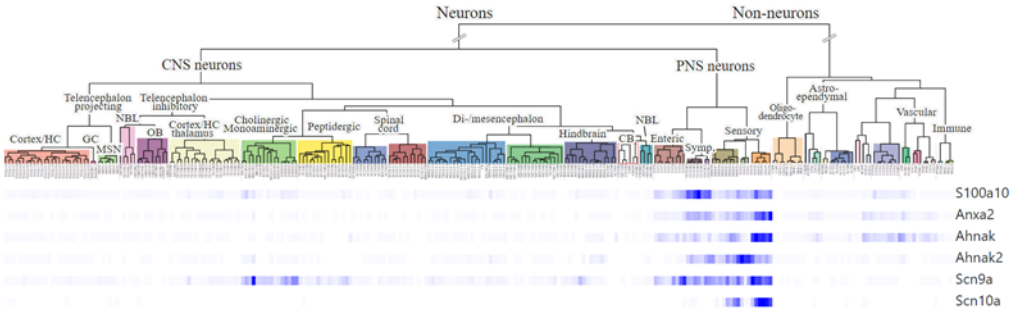

Index	Name	Description	S100a10	Anxa2	Ahnak	Ahnak2	Scn9a	Scn10a
198	PSPEP8	Peptidergic (TrpM8), DRG	4.81	4.25	0.0704	3.64	1.82	0.00
199	PSPEP7	Peptidergic (TrpM8), DRG	2.39	0.907	0.202	0.954	1.42	0.0788
200	PSPEP6	Peptidergic (TrpM8), DRG	3.89	2.52	0.723	1.30	1.80	0.00
201	PSPEP5	Peptidergic (PEP1.2), DRG	3.74	3.07	0.733	1.47	1.43	0.199
202	PSPEP2	Peptidergic (PEP1.3), DRG	7.44	5.85	1.35	3.94	2.92	1.56
203	PSPEP4	Peptidergic (PEP1.1), DRG	5.17	3.49	2.94	2.37	1.34	1.16
204	PSPEP3	Peptidergic (PEP1..4), DRG	6.67	6.16	2.48	3.43	1.67	2.51
205	PSPEP1	Peptidergicv (PEP2), DRG	14.5	9.36	1.65	6.64	3.14	3.28
206	PSNF3	Neurofilament (NF2/3), DRG	9.13	6.36	0.451	9.58	1.64	0.613
207	PSNF2	Neurofilament (NF4/5), DRG	8.67	5.01	0.262	7.47	0.351	0.0350
208	PSNF1	Neurofilament (NF1), DRG	6.95	4.11	0.131	7.79	1.95	0.0263
209	PSNP1	Non-peptidergic (TH), DRG	11.5	7.07	5.86	5.56	5.48	1.08
210	PSNP2	Non-peptidergic (NP1.1), DRG	27.7	17.4	8.00	2.53	4.00	3.71
211	PSNP3	Non-peptidergic (NP1.2), DRG	16.1	18.2	6.33	2.73	4.14	5.28
212	PSNP4	Non-peptidergic (NP2.1), DRG	13.0	23.8	6.80	1.93	2.76	5.47
213	PSNP5	Non-peptidergic (NP2.2), DRG	13.6	14.9	5.57	2.90	3.25	4.99
214	PSNP6	Non-peptidergic (NP3), DRG	20.0	31.1	7.14	1.51	3.87	4.00

Figure 3.6: *In silico* mRNA analysis of *AHNAK* and *AHNAK2* in nociceptor subtypes
AHNAK has been shown to form scaffolding complexes with Annexin A2 (*ANXA2*) and p11 (*S100A10*) proteins to anchor voltage-gated calcium channels, and the latter protein regulates Nav1.8 membrane localisation. Results from the https://mousebrain.com/genesearch online tool revealed mRNA expression for this set of proteins as well as AHNAK2 and Nav1.7 were enriched in sensory neuron subtypes compared to the rest of the nervous system.

3.4.3 – Western Blot Validation of Putative hNav1.7 Interaction Partners

The identification of proteins in IP-MS experiments is dependent on the assignment of peptides from mass-spectrometry samples. To validate the presence of whole proteins in Nav1.7 complexes, co-IP experiments were repeated at the same scale followed by probing of western blots for NMIIa and AHNAK. In preliminary blots, it was clear that endogenous levels of both proteins were very high such that if proteins were present in the co-IP fractions at very low levels, these bands became hidden as the luminol signal from the input lanes saturated the entire blot (data not shown). Therefore, membrane transfer conditions were optimised to ensure maximal protein transfer at low total protein concentrations. Figure 3.7A shows the dry transfer method followed by 0.4% PFA fixation substantially enhanced signal detection for all proteins of interest, AHNAK in particular.

Figure 3.7B shows the final blot examining the presence of each protein at endogenous levels in the cell input versus pulldown with Nav1.7 in co-IP fractions. Na^+K^+ ATPase was used as a loading control for input samples and as a negative control in co-IP fractions since it was not identified in Nav1.7 complexes by mass-spectrometry. Nav1.7 was robustly expressed in WT(+) and 75(+) inputs although noticeably lower in the L75P mutant cell line, and was effectively pulled down in co-IPs. A small amount of Nav1.7 was expressed in the WT(-) condition and was pulled down by co-IP as to be expected.

Endogenous levels of AHNAK and NMIIa were detected in cell inputs; however, AHNAK could not be detected in any of the co-IP fractions before the segment became saturated, whereas NMIIa was present in all co-IP fractions. Both of these results were contrary to what was expected from EUPC analysis of mass-spectrometry data; that proteins would be present in the WT(+) co-IP but absent from WT(-) and 75(+). A final attempt was made to detect AHNAK2 with a newly available antibody (Abcam, #ab70053 at 1 in 500 dilution), but this was also unsuccessful. This data confirmed human NMIIa as a protein binding partner of human Nav1.7 but was inconclusive with regards to the validity of AHNAK or AHNAK2 binding to Nav1.7.

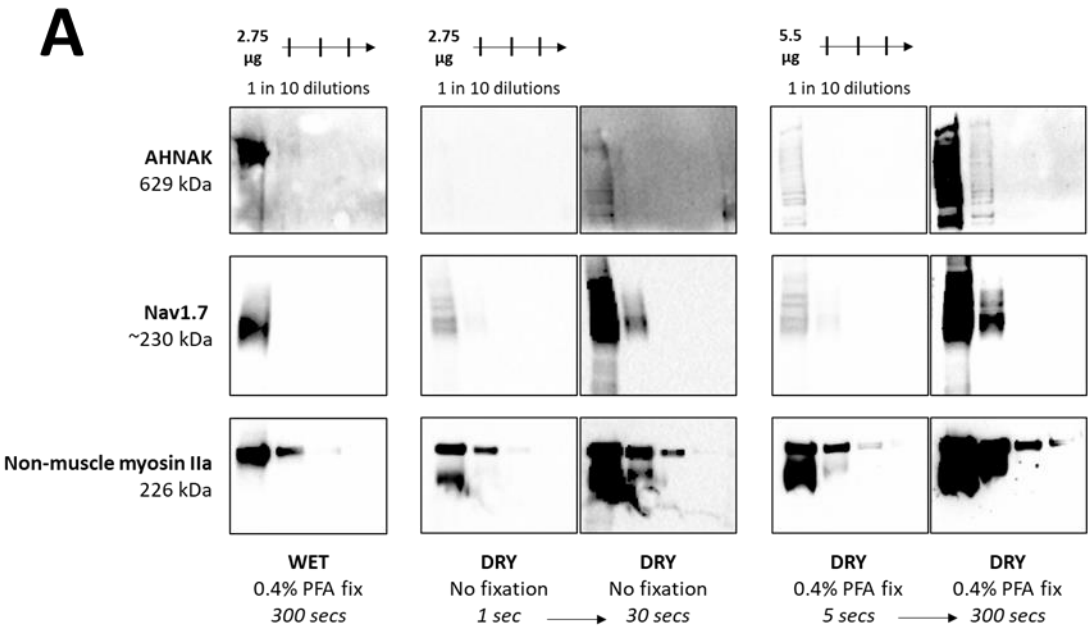

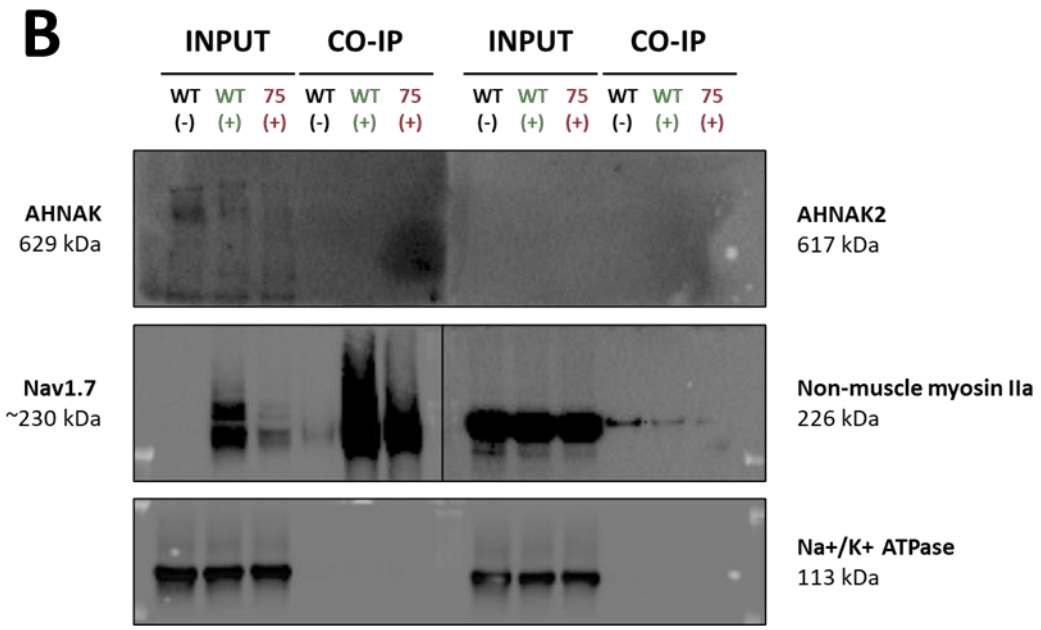

Figure 3.7: Attempted validation of hNav1.7 interaction partners AHNAK, AHNAK2 and NMIIa
(A) To maximise protein transfer and detection of low levels of AHNAK and NMIIa protein, several membrane transfer conditions were tested of whole cell lysates from induced WT HEK JI TREX-Nav1.7-FLAG cells; dry transfer followed by 0.4% fixation was most effective. (B) Whole cell input and co-IP eluates were probed by western blot for target and control proteins to determine if they were selectively present in WT(+) co-IP but absent in WT(-) and 75(+) co-IPs. Nav1.7 and Na^+K^+ ATPase expression appeared in the expected fractions, however AHNAK was not detected in any of the co-IPs while NMIIa was present in all three. AHNAK2 could not be detected due to defective antibody.

3.4.4 – NMIIa and AHNAK siRNA Dosage Optimisation in HEK JI TREX Cell Line

To investigate the effects of protein partner knockdown on Nav1.7 biophysical function, siRNA treatments were first optimised to identify the dose and timepoint at which knockdown of NMIIa, AHNAK and AHNAK2 was most efficient. Given the hypothesis that AHNAK and AHNAK2 may play non-redundant roles in anchoring Nav1.7, knockdown of both proteins simultaneously was tested. Three different doses of target siRNAs were applied and expression of target mRNAs was measured at 24-72 hours. The non-targeting pool (NTP) was used at 50 nM as a negative control. Following mRNA analysis, the optimal dose was chosen to compare protein knockdown at 48 and 72 hours.

Figure 3.8A shows *MYH9* (the gene encoding NMIIa) mRNA expression was reduced approximately 0.8-fold within 24 hours of treatment, at siRNA doses 25 to 100 nM. Expression levels were lowered further at 48 hours but started to increase again by 72 hours. *MYH9* knockdown was most effective after 48 hours treatment with 50 nM SMARTpool siRNA – a 0.94-fold difference. When taking this dose forward for protein expression studies (see Figure 3.8B), a slight decrease in NMIIa was visible at 48 and 72 hours, relative to the 3 negative controls – untreated cells, NTP siRNA-treated cells and GAPDH siRNA-treated cells. GAPDH was also used as a positive control for siRNA transfection, and this segment shows a significant though incomplete knockdown of GAPDH, indicating the transfections had technically worked. Nav1.7 and Na^+K^+ ATPase proteins were not affected by siRNA treatments and as expected, bands were more intense at 72 hours due to cell growth. However, as NMIIa protein levels were still substantial after siRNA treatment, further study of this target was dismissed.

Double knockdown of *AHNAK* and *AHNAK2* (dA) was assessed in a similar manner to *MYH9* as above, however each siRNA SMARTpool was applied at doses 12.5 to 50 nM. As shown in Figure 3.9A, Expression levels of *AHNAK* mRNA were hardly affected within 24 hours, and strangely *AHNAK2* mRNA appeared to increase approximately 3-fold with siRNA treatment. A profound decrease in mRNA levels was observed by 48 hours and began to increase again by 72 hours post-siRNA treatment. The most effective knockdown was observed at 48 hours with 50 nM each siRNA SMARTpool, which resulted in over 0.95-fold decrease in mRNA levels of both *AHNAK* and *AHNAK2*.

Protein knockdown by western blot could not be assessed for AHNAK2 as no adequate antibody was available, however AHNAK protein levels were examined at 48 and 72 hours after 50 nM dA siRNA treatment. Given the discrepancy in mRNA and protein knockdown for NMIIa, AHNAK protein knockdown was also assessed in cells were treated with 100 nM AHNAK (A1) siRNA. Untreated and NTP siRNA-treated cells were used as negative controls, in which equivalent AHNAK levels can be seen

in Figure 3.9B. Protein knockdown was substantial with both AHNAK treatments, as presented in Figure 3.9C, reaching 80-95% knockdown by 72 hours. Nav1.7 and Na^+K^+ ATPase proteins were unaltered by any siRNA treatments.

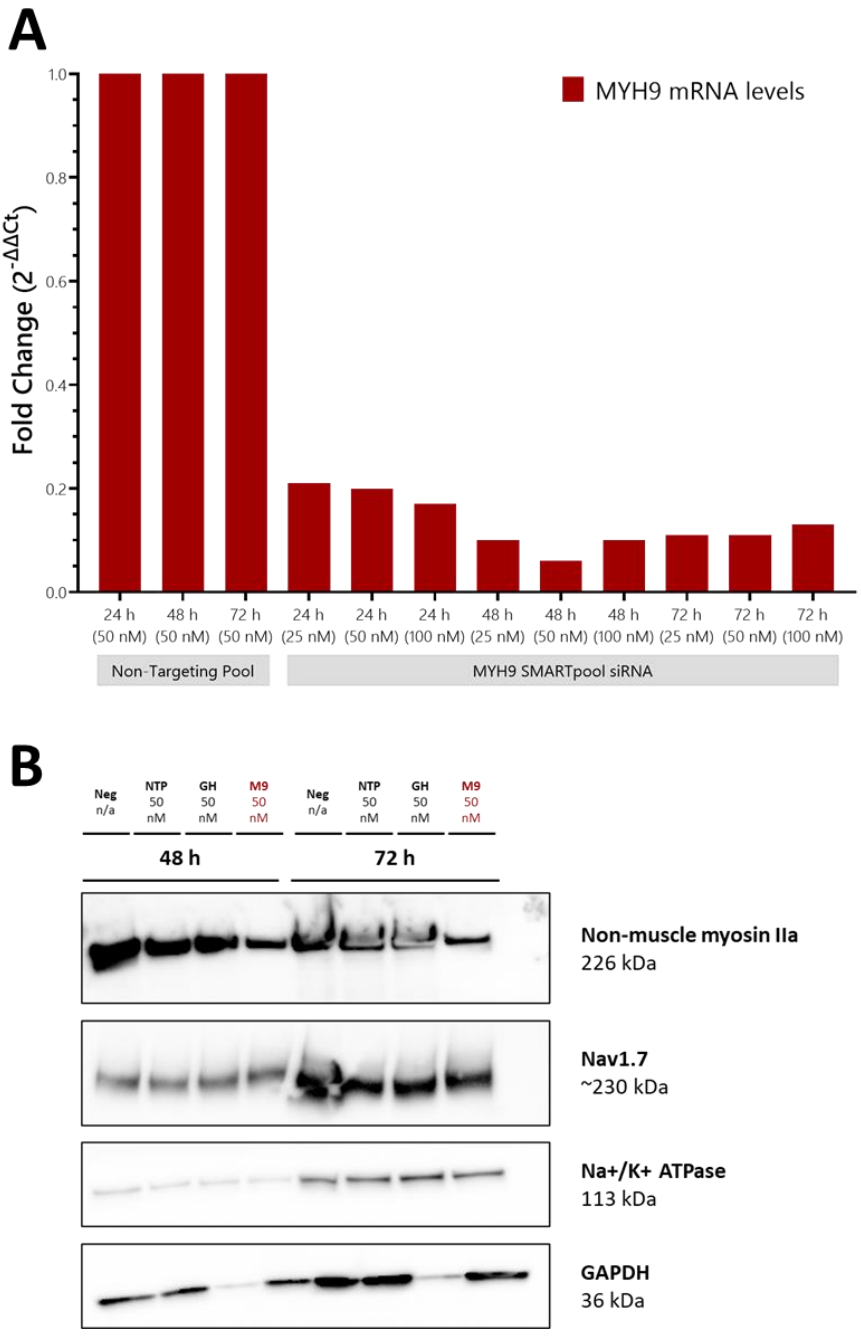

Figure 3.8: siRNA-mediated knockdown of NMIIa
(A) Knockdown of *MYH9* mRNA by SMARTpool siRNAs was tested at 25, 50 and 100 nM at 24-, 48- and 72-hours post-treatment. Quantification by RT-qPCR showed knockdown was most effective after 48 hours with 50 nM siRNA. (B) NMIIa protein knockdown with 50 nM siRNA was incomplete at 48- and 72-hours post-treatment, therefore electrophysiological analysis of WT Nav1.7 in the context of NMIIa knockdown was not pursued.

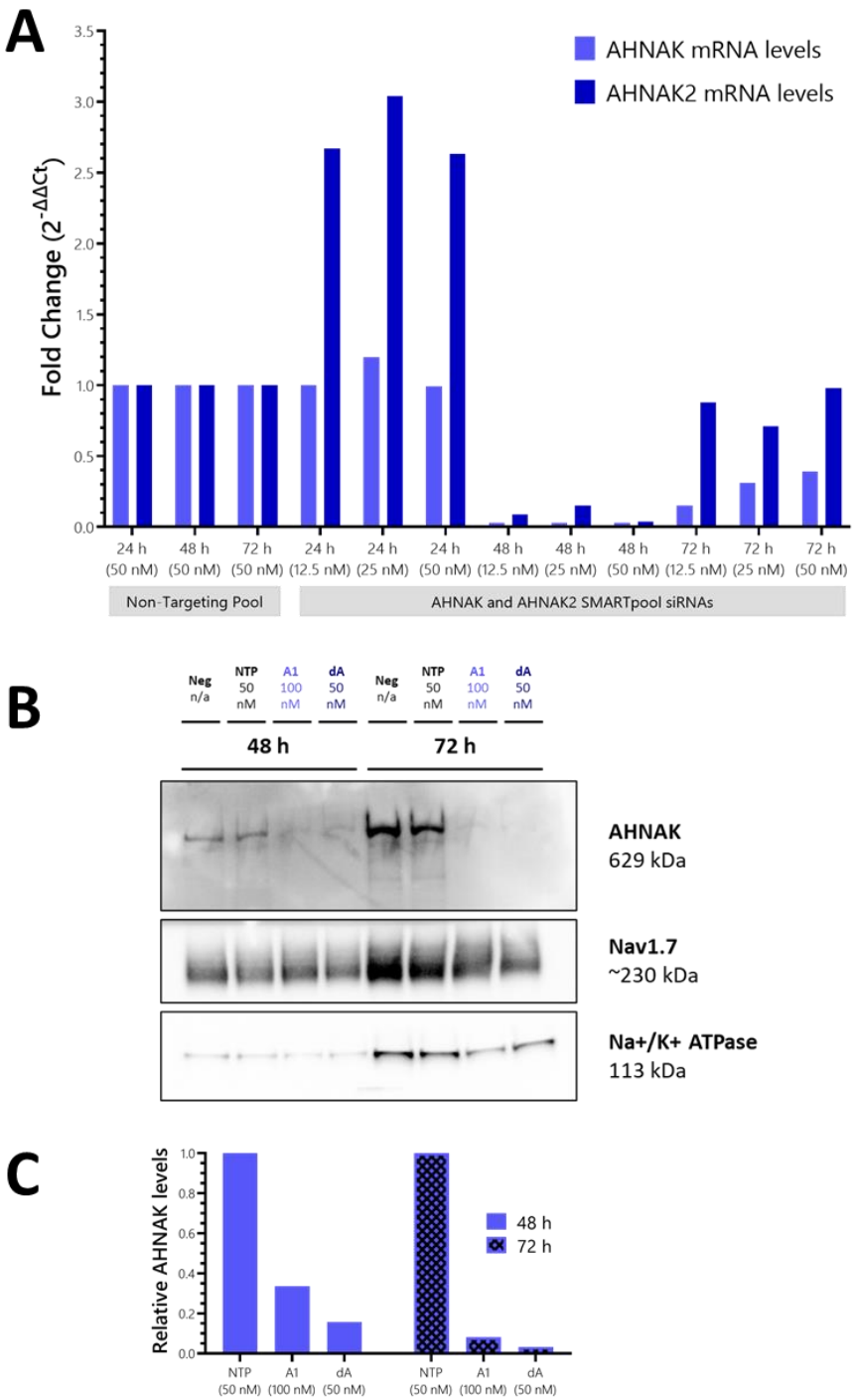

Figure 3.9: siRNA-mediated knockdown of AHNAK and AHNAK2
(A) *AHNAK* and *AHNAK2* mRNA expression was measured 24-72-hours after treatment with SMARTpool siRNAs targeting each protein at 12.5, 25 and 50 nM doses. Quantification by RT-qPCR showed double AHNAK (dA) knockdown was most effective after 48 hours with 50 nM both siRNAs. (B) AHNAK protein knockdown was effective with 50 nM dA and 100 nM AHNAK (A1) siRNA treatments, as quantified by densitometry analysis in (C).

3.4.5 – Nav1.7 biophysical profiling after siRNA-mediated knockdown of AHNAKs

Following siRNA dose optimisation above, electrophysiological analysis was undertaken of WT Nav1.7 in the inducible stable cell line, after 72 hours treatment with 50 nM each AHNAK and AHNAK2 versus 50 nM NTP siRNAs. Peak currents measured from dA-siRNA-treated cells were slightly lower than the control condition, but this difference was not statistically significant (dA: 2.8 ± 0.7 nA versus NTP: 3.9 ± 1.3 nA; p= 0.4773). Voltage-dependence of activation was unaffected by siRNA treatment (dA V_{50}: -27.94 ± 4.17 mV, n=6 versus NTP V_{50}: -25.76 ± 4.02, n=6; p = 0.7138). A slight hyperpolarised shift in voltage-dependence of inactivation was observed but did not reach statistical significance (dA V_{50}: -72.51 ± 4.25 mV, n=5 versus NTP V_{50}: -67.28 ± 6.20, n=6; p = 0.5215). These results illustrated in Figure 3.10 indicate the presence of AHNAK and AHNAK2 cytoskeletal proteins is not essential for sodium conductance through Nav1.7.

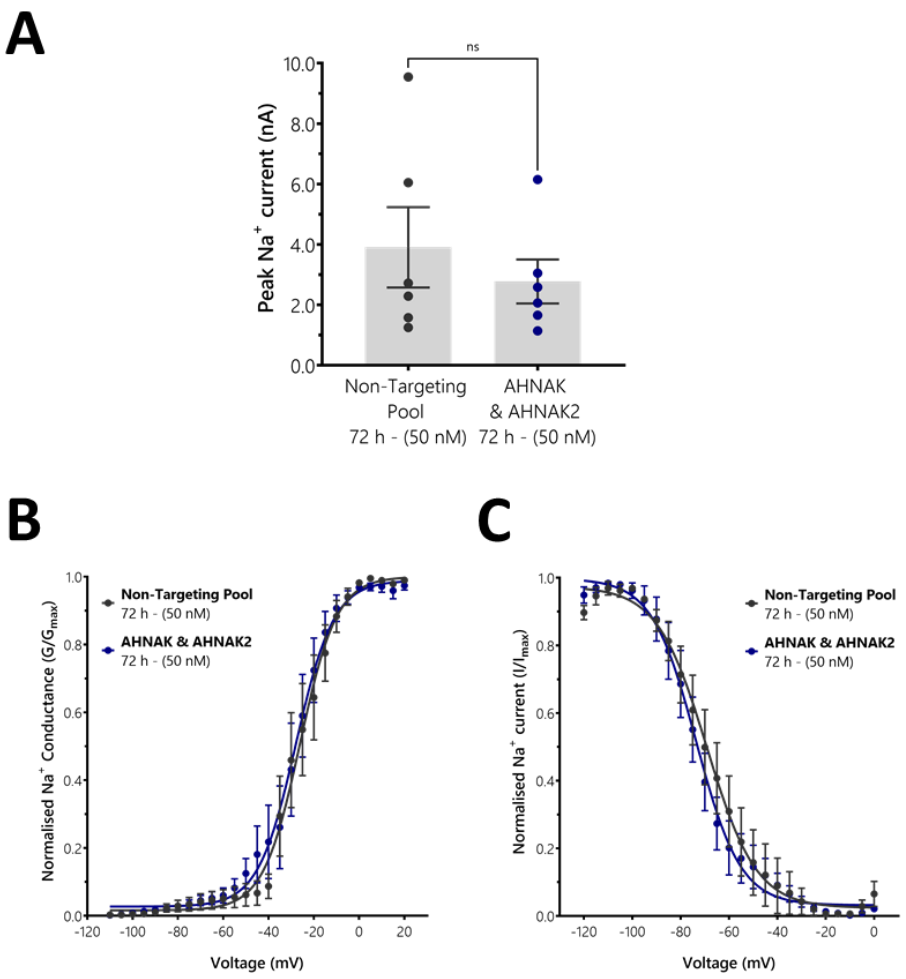

Figure 3.10: AHNAK & AHNAK2 knockdown had no effect on WT hNav1.7 biophysical properties
WT HEK JI TREX-Nav1.7-FLAG cells were treated with 50 nM AHNAK and AHNAK2 SMARTpool siRNAs for 72 hours before manual voltage-clamp recordings were performed. There was no significant difference in the peak currents (A), voltage-dependence of activation (B), or voltage dependence of fast inactivation (C) measured from cells after double AHNAK treatment compared to the negative control treatment with the non-targeting SMARTpool.

3.4.6 – Results of Label-Free Quantification Analysis

Formal analysis of the proteomic data was performed by Jack Houghton of the CIMR Core Proteomics Team, listed in Table 3.4 and presented in Figures 3.11A and 3.12A.

Comparing the WT(+) and 75(+) proteomes to WT(-) identified a small set of statistically significant proteins that pulldown with both WT and mutant Nav1.7: HERC2, NEURL4, PPP1R12A, PPP1CB, SPECC1L and UBA52. Analysis of mRNA expression using the mousebrain tool shows these genes are relatively abundant across the nervous system, although *SPECC1L* expression appears highest in sensory neurons. Functional enrichment analysis did not identify any known interactions between Nav1.7 and these proteins. However, functional links were found between HERC2, NEURL4 and UBA52 given their common involvement in ubiquitination, as well as between PPP1R12A and PPP1CB, with the former being a key regulator of the latter phosphatase enzyme.

In contrast, comparison of the WT(+) versus 75(+) proteomes identified 21 proteins that were enriched in WT Nav1.7 complexes, see Figure 3.12A. None of these proteins were known to interact with Nav1.7, and the vast majority were ribosomal proteins that were well connected in functional networks, as shown in Figure 3.12B. Of note, Filamin-A was also identified by Kanellopoulos et al. as a Nav1.7 interactor[309].

Table 3.4 – Significant Targets from IP-MS Experimental Replicates Based on LFQ Analysis

GENE	PROTEIN NAME	MOLECULAR WEIGHT (kDa)	EUPC LIST?	WT(+) v WT(-) LFQ p-value	75(+) v WT(-) LFQ p-value	WT(+) v 75(+) LFQ p-value
HERC2	E3 ubiquitin-protein ligase HERC2	527	☑	P < 0.0001	P < 0.0001	
PPP1R12A	Protein phosphatase 1 regulatory subunit 12A	115	☑	P < 0.0001	P < 0.001	
PPP1CB	Serine/threonine-protein phosphatase PP1-beta catalytic subunit	37	☒	P < 0.0001	P < 0.01	
SPECC1L	Cytospin-A	125	☒	P < 0.0001	P < 0.01	
NEURL4	Neuralized-like protein 4	167	☒	P < 0.001	P < 0.0001	
RPL11	60S ribosomal protein L11	20	☒	P < 0.01		P < 0.01
RPL12	60S ribosomal protein L12	18	☒	P < 0.01		P < 0.01
UBA52	Ubiquitin-60S ribosomal protein L40	15	☒	P < 0.01	P < 0.01	
EPPK1	Epiplakin	556	☑	P < 0.05		
HSPA8	Heat shock cognate 71 kDa protein	71	☑	P < 0.05		
RPL31	60S ribosomal protein L31	14	☒	P < 0.05		P < 0.05
RPL35	60S ribosomal protein L35	15	☒	P < 0.05		
ATP5B	ATP synthase subunit beta, mitochondrial	57	☒			P < 0.01
HNRNPA3	Heterogeneous nuclear ribonucleoprotein A3	40	☒			P < 0.01
HNRNPC	Heterogeneous nuclear ribonucleoproteins C1/C2	34	☒			P < 0.01
RPL6	60S ribosomal protein L6	33	☒			P < 0.01
RPL17-C18orf32	60S ribosomal protein L17	26	☒			P < 0.01
RPL27A	60S ribosomal protein L27a	17	☒			P < 0.01
RPL29	60S ribosomal protein L29	18	☒			P < 0.01
RPS3A	40S ribosomal protein S3a	30	☒			P < 0.01
FLNA	Filamin-A	281	☒			P < 0.05
HIST1H2BL	Histone H2B type 1-L	14	☒			P < 0.05
LMNA	Prelamin-A/C	74	☑			P < 0.05
RPL4	60S ribosomal protein L4	48	☒			P < 0.05
RPL13	60S ribosomal protein L13	24	☒			P < 0.05
RPL22	60S ribosomal protein L22	15	☒			P < 0.05
RPL28	60S ribosomal protein L28	16	☒			P < 0.05
RPS3	40S ribosomal protein S3	27	☒			P < 0.05
RPS11	40S ribosomal protein S11	18	☒			P < 0.05
RPS14	40S ribosomal protein S14	16	☒			P < 0.05

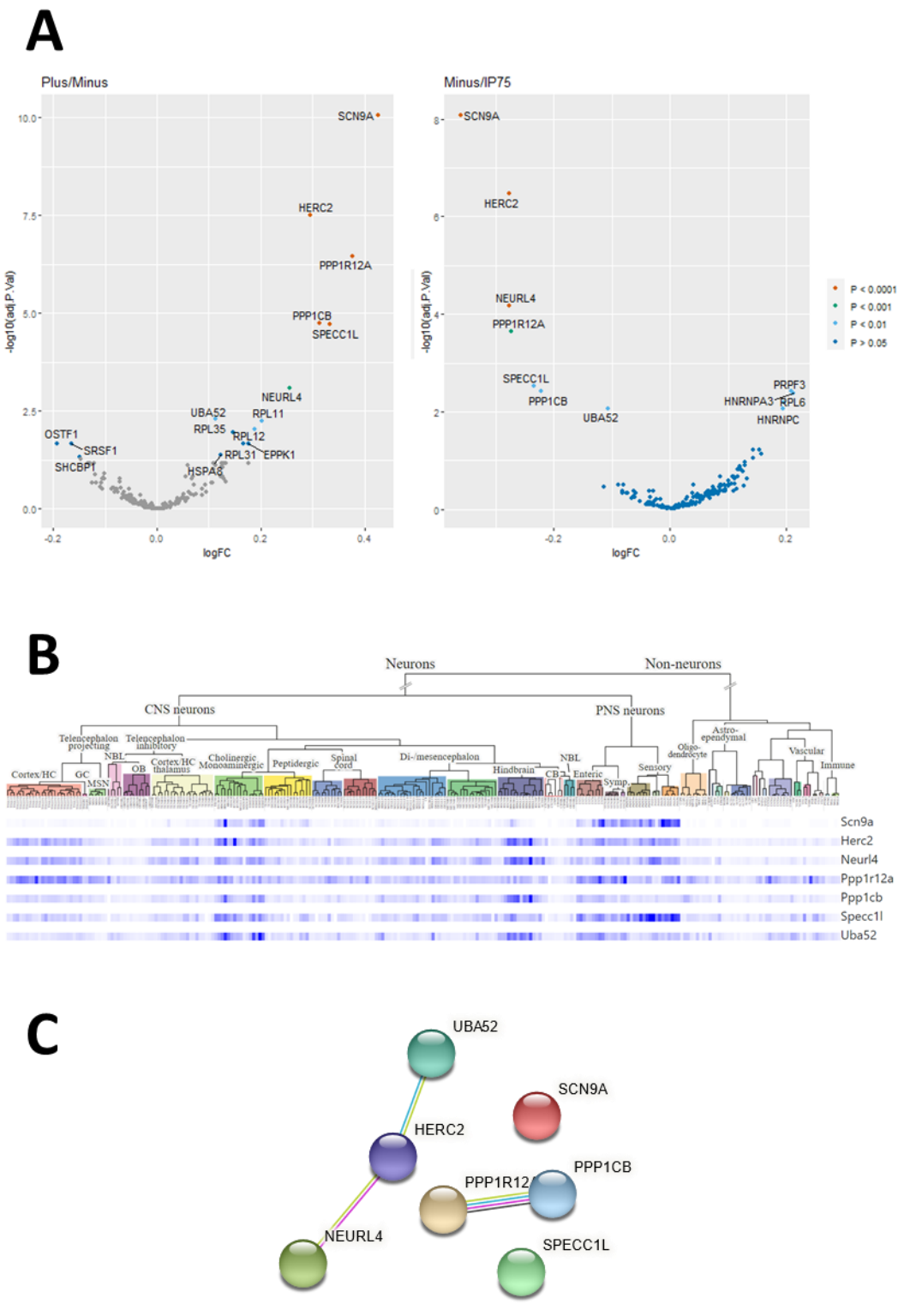

Figure 3.11: Proteins enriched upon induced expression of hNav1.7 in a HEK cell background
(A) Volcano plots of results from Label Free Quantification analysis of IP-MS experiments (n=5) were produced by Jack Houghton. (B) Comparisons of the WT(+) versus WT(-) and WT(-) versus 75(+) proteomes highlighted six proteins in common that were up-regulated in Nav1.7 complexes, but their mRNA expression was relatively abundant across the rodent nervous system. (C) Functional network analysis did not identify any known relationships between Nav1.7 and these proteins.

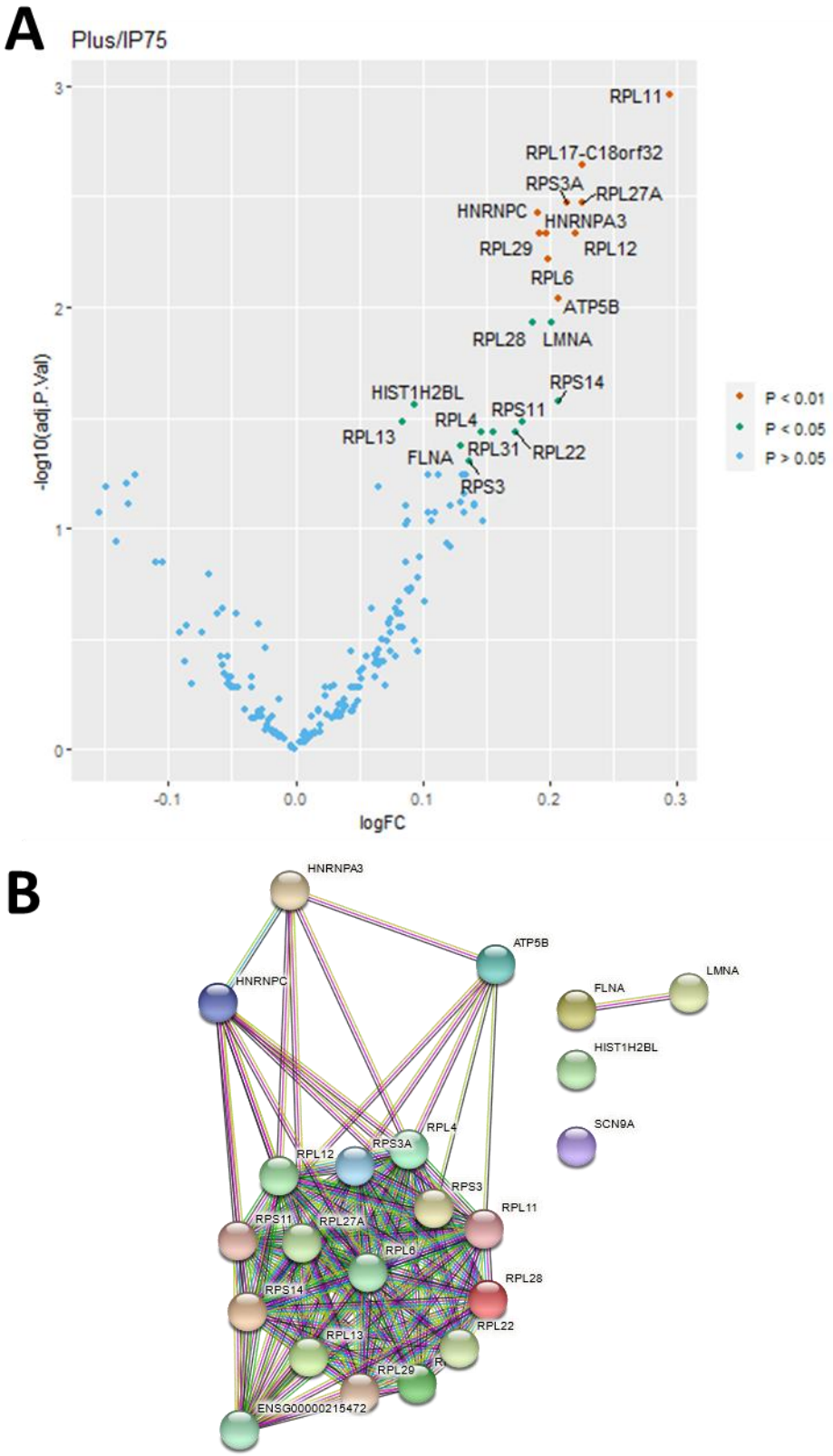

Figure 3.12: Proteins differentially enriched in WT vs L75P Nav1.7 interactomes
(A) Volcano plot comparing the WT(+) and 75(+) proteomes identified 31 proteins that were significantly enriched in WT Nav1.7 co-IPs. (B) Functional enrichment analysis did not identify any known relationships between Nav1.7 and these proteins; the vast majority of these proteins are part of the ribosome.

3.5 DISCUSSION

This chapter presents an interactome study of human Nav1.7, comparing the WT channel and LOF patient mutation Leu75Pro when stably expressed in the HEK JI TREX-Nav1.7-FLAG cell lines. Our primary aim was to explore these interactomes for PPIs that were disrupted by the mutation, and therefore potentially critical to channel function at the plasma membrane since this was the environment in which the Leu75Pro mutant was shown to be non-conducting. While this hypothesis was refuted by the selected candidates, our mass spectrometry data does lend support to some of the Nav1.7 protein complexes identified by Kanellopoulos et al. in their mouse Nav1.7 IP-MS study[309], which may benefit from further investigation.

The expression of WT or mutant Nav1.7 was induced in the HEK JI TREX cell lines with doxycycline, while a separate sampling of the WT Nav1.7 cell line without induction media was used as a negative control. This was to account for any adaptations in the proteome that may have emerged during stable cell line generation (e.g., antibiotic selection or Nav1.7 gene expression). As explained in Sections 2.3.4 and 2.3.9, the TetR protein is constitutively expressed in HEK JI TREX cell lines and binds to the CMV-TO promoter of the integrated gene construct to inhibit basal expression; adding doxycycline displaces TetR and allows the transcriptional machinery to access the promoter. However even in the absence of doxycycline, a low level of Nav1.7 was detected by western blot and mass spectrometry in the negative control condition, indicating incomplete repression of the *SCN9A* construct[360]. Unfortunately, this complicated the interpretation of some of the later western blot data, highlighting the HEK JI TREX parental cell line without integration of the *SCN9A* construct may have been a better choice of negative control.

Nevertheless, there was a robust up-regulation of Nav1.7 expression upon doxycycline exposure, which would be expected to coincide with a relative increase in the abundance of peptides from binding partners in the WT(+) compared to WT(-) samples, allowing the identification of these interactors. We used a label-free proteomics approach with the MaxQuant LFQ algorithm for measuring and normalizing spectral intensities and making protein identifications. However, since peptides are not always fragmented and detected with similar efficiency, the “match between runs” setting was enabled to increase confidence in protein assignments that might differ between runs[363]. Batch effects correction[364] was required due to sample replicates being run at different times and potential technical variation introduced from different lots of chromatography columns.

Due to technical and pandemic-related delays in analysing the replicate experiments, two candidates (AHNAK and NMIIa) were chosen from the pilot IP-MS experiment for further study as they met the selection criteria set out in Section 3.3.5 – (i) selectively abundant in WT Nav1.7 protein complexes; (ii) physiologically relevant expression in DRG sensory neurons; (iii) independent evidence of an interaction with Nav1.7. The AHNAK structural homologue, AHNAK2, was also chosen due to meeting criteria (i) and (ii).

An interaction between Nav1.7 and NMIIa (also known by its gene name *MYH9*) was demonstrated in rat DRG from NMIIa pulldown and the reciprocal co-IP. The functional consequences of this interaction were not studied, however overexpression of NMIIb (i.e., *MYH10*) and Nav1.8 increased peak current density 3-fold in the neuronal ND7/23 cell line, suggestive of an increase in plasma membrane expression similar to that mediated by non-muscle myosin binding partner KIF5B[196,310]. The authors noted that the robust endogenous expression of NMIIb may have obscured a larger effect on Nav1.8 function, such that knockdown of *MYH10* might reduce Nav1.8 current. Since both myosin proteins bound to Nav1.7[310], we hypothesised that NMIIa could regulate Nav1.7 in an analogous manner, and therefore disrupting this interaction by the Leu75Pro mutation may underlie its LOF.

AHNAK was identified as a Nav1.7 binding partner in mouse DRG by mass spectrometry, although the interaction was not validated at the whole protein level[309]. It is a giant scaffolding protein (5,890 amino acids long), comprised of 3 major segments separated by disordered linkers: a ~4,300 residue central rod formed of a 128-residue repetitive element, flanked by relatively shorter N- and C- terminal regions that bridge cytoskeletal and plasma membrane components[365]. It is recruited to sub-membranous zones via its C-terminal domain binding to adaptor proteins annexin A2 and S100A10 (also known as p11)[366]. The N-terminus stabilises L-type voltage-gated calcium channels at the plasma membrane of cortical neurons, and consequently, cell-surface expression and calcium currents via these channels were significantly reduced in AHNAK knockout mice[361].

Notably, p11 and annexin A2 are also involved in Nav1.8 membrane localisation[197,362,367]. The p11 binding site was refined to a 30 amino acid stretch of the Nav1.8 N-terminal tail, including the PLED motif in which our Nav1.7 Leu75Pro mutation occurs. However, the interaction between p11 and Nav1.7 was relatively weak, and the insensitivity to pain phenotype of p11 knockout mice was not mediated by a change in TTX-sensitive currents[197,367]. Taken together, these studies illustrate an important role for the AHNAK-AnnexinA2-p11 macromolecular complex in localising voltage-gated ion channels, although channel binding may be dependent on distinct adaptors. We hypothesised that

the Leu75Pro mutation might disturb Nav1.7 conductance by disrupting the Nav1.7-AHNAK interaction.

Western blot probing of HEK JI TREX whole cell lysates revealed both the AHNAKs and NMIIa were endogenously expressed at high levels. To validate their co-IP with Nav1.7, optimisation of membrane transfer conditions was conducted to maximise antigen detection; at this stage, AHNAK2 had to be excluded due to antibody batch issues. Despite the optimisation, AHNAK could not be detected in any of the co-IP conditions – this may be a true result or reflect an extremely low concentration of AHNAK in the co-IP fraction that is beyond the detection range of the antibody (see Figure 3.7A). In contrast, NMIIa was detected in the co-IPs of all three conditions. Given the independent evidence of an NMIIa-Nav1.7 interaction in DRG[310], it is unlikely this was a result of non-specific binding to the Dynabead-antibody matrix. The presence of NMIIa in the WT(-) co-IP may have been due to leaky Nav1.7 expression, although it is unclear why this band was stronger than in the WT(+) co-IP. The weak NMIIa band in the 75(+) co-IP suggests its interaction with Nav1.7 is not completely disrupted by the Leu75Pro mutation, but these results are uncertain given the current negative control.

To confirm the functional relevance of these interacting proteins, siRNA-mediated knockdown was applied to the WT HEK JI TREX-Nav1.7-FLAG cell line followed by electrophysiological profiling. Due to the caveat that siRNA transfection efficiency per cell would be unknown when choosing cells for patch clamping, recording conditions were chosen based on at least 75% protein-level knockdown per coverslip. For this reason, further study of NMIIa was dismissed as substantial levels of protein persisted at 72 hours, despite strong knockdown of *MYH9* mRNA. A reciprocal IP-MS experiment using the anti-NMIIa antibody (data not shown) verified its specificity for NMIIa (>250 exclusive unique peptides identified per sample) over NMIIb or NMIIc (<15 EUPCs per sample), suggesting cross-reactivity was not a major factor. In contrast, *AHNAK* and *AHNAK2* knockdowns were efficient at the mRNA level and AHNAK knockdown was over 80% at the protein level by 72 hours post-transfection. However, siRNA-mediated knockdown of both AHNAKs had no effect on WT Nav1.7 peak current or gating properties. Therefore, unless AHNAK2 protein persisted in a similar manner to NMIIa, the electrophysiology data infers that AHNAKs are non-essential to Nav1.7 function.

Later statistical analysis of replicate IP-MS experiments revealed the abundance of NMIIa and both AHNAKs was not significantly different between WT(+) and 75(+) samples, concluding they were not affected by the Leu75Pro mutation. However, nuclear membrane protein prelamin-A/C, cytoskeletal protein filamin-A, and a dense ribosomal network were all selectively enriched in WT Nav1.7

complexes. It is unlikely that the ribosomal proteins or prelamin-A/C are relevant to Nav1.7 function in plasma membrane excitability. Filamin-A on the other hand was also identified in the mouse Nav1.7 IP-MS study[309] and is known to anchor transmembrane proteins to the cytoskeleton. It colocalises with voltage-gated potassium channel Kv4.2 in the dendrites of cultured hippocampal neurons, and expression of Kv4.2 in a filamin-A-negative cell line led to a 2.7-fold reduction in current density[368]. Whether filamin-A plays a similar role for Nav1.7 in sensory neurons, and could be disrupted by the Leu75Pro mutation, remains to be seen.

Comparison of the WT(-) to the WT(+) and 75(+) interactomes revealed several proteins that were significantly up-regulated upon addition of doxycycline, and thus may be relevant to Nav1.7 expression and function. UBA52, HERC2 and NEURL4 are all involved in ubiquitin transfer. *UBA52* encodes a ubiquitin-conjugated version of the ribosomal protein RPL40. This modification is important in regulating ribosome function but also contributes to the free ubiquitin pool when deubiquitinated[369,370]. HERC2 is an E3 ubiquitin-protein ligase involved in a range of cellular processes including DNA damage repair, intracellular trafficking and synaptogenesis, the some of which involve an interaction with NEURL4[371–373]. NEURL4 acts as a platform for HERC2 substrates[373,374], and notably was also picked up as a Nav1.7 interactor by Kanellopoulos et al.[309]. Ubiquitination of Nav1.7 by NEDD4-2 targets the channel for membrane internalisation[358], but determining whether Nav1.7 itself is a substrate for the ubiquitination machinery found here or if they regulate other Nav1.7 binding partners requires further investigation[375].

Three other proteins up-regulated upon Nav1.7 expression were PPP1R12A and PPP1CB, which form substrate-targeting and catalytic subunits respectively of the myosin phosphatase holoenzyme PP1[376], and SPECC1L. SPECC1L is another cytoskeletal protein that forms a multitude of interactions including with NMIIa, NMIIb and PP1 subunits, although evidence is limited to mass spectrometry identification (see database entry “116960” at https://thebiogrid.org/)[377]. Interestingly, the targeting unit PPP1R9A (also known as neurabin-1) was detected in the mouse Nav1.7 IP-MS study[309]. PPP1R12A directs the PP1 holoenzyme to the regulatory light chain (RLC) of NMII isoforms, and the RLC phosphorylation state controls the conformation of NMII dimers. RLC dephosphorylation by PP1 induces the compact form of NMII so that it cannot assemble into bipolar myosin filaments that exert tension on actin filaments. However PP1 enzymatic activity is inhibited when the targeting subunit is phosphorylated[378]. Regulation of actomyosin filaments by PP1 occurs at the trans-Golgi network[379], within the neuronal membrane periodic skeleton[380,381] and during the maturation of dendritic

spines[382,383]. It would be interesting to examine whether these interactions are involved in vesicular budding and release during the secretory trafficking of Nav1.7.

Our study design had certain strengths as well as limitations that could be improved upon. To compare the interactomes of WT and mutant Nav1.7 channels, we benefitted from using the HEK JI TREX background, as the genome integration site was identical between the two conditions due to controlled recombination events (explained in Section 2.3.9), thus removing differences in bait copy number as a potential confounding factor. Yet despite being an inducible cell line, basal expression was not completely repressed, highlighting the importance of appropriate biological controls. Using the anti-Nav1.7 antibody combined with low stringency wash buffers helped to maximise bait-specific pulldown and to protect as many PPIs as possible. Nonetheless, the co-immunoprecipitation approach relies on relatively weak non-covalent bonds holding complexes together throughout cell lysis and several wash steps, during which time low abundance or low affinity interactions may be lost. Proximity labelling techniques such as APEX2 and TurboID that covalently tag proteins in a 1-10 nm radius of the bait construct, while the protein is located in its native environment, are more likely to reliably preserve such interactions for mass spectrometry analysis[384,385]. Finally, a label-free approach presented a simple practical workflow, required the least amount of sample material, and minimised instrument and analysis time. However, this was at the expense of superior accuracy and reproducibility in quantifying protein abundance between conditions afforded by metabolic or chemical proteome labelling approaches[386].

Given that the Leu75Pro mutant channel reached the cell membrane (see Section 2.4.7), it is possible that rather than a membrane tethering role, the mutation disturbs a binding partner that modulates an intramolecular interaction important for gating and/or ion permeation, as demonstrated for the VGSC CTD and the fast inactivation particle in Nav1.4 and Nav1.5[289,293]. The proximity of the N-terminal region to the domain I voltage sensor in the Na_vPas model[279], and the presence of multiple pathogenic mutations in this region that affect gating properties[258,259] hint that the N-terminus may also exert allosteric regulation on VGSC function. It is worth noting that the Na_vPas model excluded the first 46 amino acids which could change the local structure of the N-terminus from what was presented. Furthermore, there is minimal sequence conservation between the N-termini of Na_vPas and hNav channels so they may not share the same secondary structural organisation. Stabilising this region by chemical cross-linking could help to fill in some of these knowledge gaps, including the relative location and exposure of the Leu75Pro mutation.

CHAPTER 4: A Novel Sensory Disorder Arising from *PRDM12* Polyalanine Expansions

4.1 INTRODUCTION

4.1.1 – The PRDM Family

PRDM12 is one of 17 members of the human PRDI-BF1 and RIZ homology domain (PRDM) protein family[387] that regulate transcriptional programmes in a variety of developmental contexts[388]. Members of this family are characterised by the presence of a PR domain and multiple C2H2-type classical zinc fingers. The PR domain is structurally similar to the SET methyltransferase domain, which is required for the recognition and methylation of lysine substrates such as those within histone tails. In this context, depending on which lysine residue is methylated, chromatin structure is altered in a manner that facilitates activation or repression of transcriptional targets[389,390]. PR domains share 20-30% amino acid sequence identity with SET domains and can similarly accommodate the methyltransferase co-factor S-adenosyl-methionine (SAM) within its structure[391]. However, most PRDM proteins lack intrinsic enzymatic activity, instead recruiting methyltransferases as well as acetyltransferases and deacetylases to modify histone residues[392]. The zinc finger domains can play a part in engaging these enzymes but are more often involved in binding to DNA in a sequence-specific manner, either directly or through the formation of protein-protein transcriptional complexes[393].

The highly specific temporal and spatial expression of each PRDM protein during embryonic development is key to their roles in initiating transcriptional cascades that specify a particular cell fate, whereas the same PRDM protein expressed postnatally in different cell types can induce analogous cell-state transitions but through divergent gene expression programmes. For example, PRDM1 (also known as Blimp1) expression in the developing retina specifies a photoreceptor cell fate over maintaining the proliferation of multipotent precursors and their subsequent specification into bipolar cells[394]. In contrast, postnatal expression of PRDM1 is involved in the differentiation of naïve lymphocytes into effector rather than memory cell fates, including B-cells into antibody-secreting plasma cells, and CD8-positive T-cells into cytotoxic T lymphocytes[395].

As an added layer of complexity, PRDM proteins can form transcriptional complexes to assist in: (i) reaching their genetic targets, (ii) directly activating or repressing gene expression, and (iii) regulating transcriptional networks via feedback loops. As an example of the first characteristic, for Prdm8 to suppress expression of Cadherin-11, it is dependent on the presence of another transcriptional co-factor, Bhlhb5 (also known as Bhlhe22) to have bound to a consensus motif in intron 1 of the *Cdh11*

gene[396]. As described earlier, for the direct regulation of gene expression, interactions with histone-modifying enzymes are critical since most PRDM proteins are enzymatically inactive. With regards to regulatory feedback loops, Ptf1a is a non-PRDM transcription factor which can maintain its own expression by binding to the *Ptf1a* auto-regulatory enhancer sequence, in addition to its separate involvement in activating *Prdm13* transcription. Prdm13 protein in turn binds to the *Ptf1a* transcriptional enhancer complex to inhibit *Ptf1a* activation, thus ensuring temporally restricted expression of this upstream signal[397,398].

4.1.2 – Structure and Function of PRDM12

PRDM12 is the shortest member of the PRDM family, composed of a PR domain close to the middle of the protein, three C2H2-type zinc fingers further downstream, and a polyalanine tract that is eight residues away from the C-terminus. Yang and Shinkai[399] demonstrated that PRDM12 possesses some intrinsic methylation activity towards histone H3, however this was almost imperceptible when compared to methylation solely in the presence of EHMT2 (also known as G9a), a legitimate histone-lysine N-methyltransferases (HMT) that is recruited by PRDM1, 5 and 6. They established that PRDM12 also recruits G9a, but not other HMTs such as EHMT1 and SETDB1, to specifically methylate Lysine 9 on the N-terminal tail of Histone 3 (H3K9). Most notably, they showed that deletion of the whole PR domain had no effect on PRDM12's ability to co-immunoprecipitate (co-IP) with G9a or methylate histone 3; instead H3K9 methylation was dependent on G9a interacting with PRDM12 via the second zinc finger. H3K9 methylation in promoter regions is predominantly a repressive modification[390] and so deletion of all three zinc finger domains of the zebrafish orthologue prdm12b resulted in the loss of repressive activity, as measured by a luciferase reporter assay[400]. Curiously, the authors found G9a could still co-IP the prdm12b zinc finger-deletion construct, albeit slightly reduced when compared to the wild-type (WT) construct.

Monitoring the tissue-specific expression patterns of PRDM12 mRNA and protein in several model organisms has revealed clues about its role in developmental programmes. Whole mount *in situ hybridization* of mouse embryos showed *Prdm12* expression was present as early as embryonic day 9.5 (E9.5) which was strongest within the dorsal root ganglia (DRG) and cranial ganglia, as well as in the p1 domain of the ventral spinal cord. *Prdm12* expression was also detected at lower levels in the hypothalamus, which continued into the postnatal period, whereas embryonic expression in other restricted regions of the brain was relatively transient[401]. These tissue-specific patterns were confirmed at the protein level by immunostaining Prdm12 in cleared mouse embryos at E9.5 and E10.5[402]. Later work in zebrafish showed expression of both prdm12b and G9a is required for precise dorsoventral patterning of the neural tube p1 progenitor domain, which gives rise to V1 inhibitory interneurons in the spinal cord that are involved in co-ordinating locomotor activity[400,403]. Studies of Prdm12 expression in the mouse hypothalamus uncovered its role in specifying precursors into an anorexigenic pro-opiomelanocortin (POMC) cell fate, whose activity is involved in circuits regulating food intake and satiety[404,405].

Work by Matsukawa et al.[406] provided more detail on the relationship between Prdm12 and H3K9 methylation *in vivo* in *Xenopus* embryos, confirming what had been previously shown by *in vitro*

assays[399,400]. Microinjection of *Chd* and *Wnt8* mRNAs into animal cap cells, a pluripotent population commonly used for examining organogenesis, generates a neural crest cell (NCC)-like population which can be identified by the expression of markers such as *Foxd3*. Increasing ectopic doses of *Prdm12* mRNA into these treated cells led to a reduction of NCC markers which coincided with increasing tri-methylation of H3K9, but no change in methylation status of alternative histone 3 lysine residues such as activating marks on H3K4 or repressive marks on H3K27. ChIP-qPCR analyses showed Prdm12 occupied a conserved non-coding motif upstream of the *Foxd3* transcription start site and simultaneously led to an increase in H3K9 methylation within the same upstream region.

With regards to the vertebrate peripheral nervous system, these results suggested PRDM12 over-expression initiates a shift away from NCC precursor identity, likely via the repression of genes that maintain this multipotent cell state. Further transcriptomics analysis of *Xenopus* embryos identified a set of genes involved in the neurogenesis of sensory neurons that were upregulated by over-expression of Prdm12, and reduced by Prdm12-specific morpholinos but not mismatched controls[407]. As described in Section 1.2-1.3, peripheral sensory neurons of the DRG and TG are derived from NCCs. Nagy et al.'s investigations were beginning to reveal an essential role for PRDM12 in somatosensory development.

4.1.3 – Phenotypic Features of PRDM12-CIP in Humans

In 2015, biallelic loss-of-function mutations of *PRDM12* were discovered as a cause of congenital painlessness alongside other clinical features such as sensory neuropathy, minor autonomic dysfunction and increased susceptibility to *Staphylococcus aureus* infections[123]. The phenotype was highly reminiscent of those caused by *NTRK1* and *NGFB* LOF mutations which disrupt the normal development of nociceptive sensory neurons. Detailed clinical profiling of these patients plus five more adults[408] refined the set of features that distinguish *PRDM12*-CIP from that caused by more frequent *SCN9A* and *NTRK1* mutations. For example, *PRDM12*-CIP cases have a normal sense of smell whereas *SCN9A*-CIP cases have anosmia. In *NTRK1*-CIP, anhidrosis is a defining feature and intellectual disability is prevalent[109], whereas sweating and mental development are only occasionally reported as abnormal in *PRDM12*-CIP patients.

Pedigrees of the reported families indicated an autosomal recessive disorder, but no mutations were found in known CIP genes with this pattern of inheritance. Using SNP arrays on a large consanguineous family narrowed down a homozygous region on the chromosome arm 9q, and through a combination of exome and Sanger sequencing, biallelic *PRDM12* mutations were identified in 21 affected individuals from 11 families. Most mutations were missense, with native residues being completely conserved across vertebrate species and substitutions were predicted to be pathogenic by multiple bioinformatic tools. Furthermore, none of these mutations were present in public or institutional databases of common variants in healthy individuals[123]. Splice-site and frameshift mutations have also been identified[123,409], as well as homozygous expansions of the polyalanine tract from the normal range to 18 or 19 alanines. Of diagnostic importance, the DNA sequence encoding the polyalanine tract is extremely GC-rich so tends to have poor coverage when whole exome sequencing methods are used[410]; thus Sanger sequencing of exon five should be undertaken in suspected *PRDM12*-CIP cases.

Injuries that are self-inflicted or due to negligence (because of lacking pain sensation) reflect insensitivity to acute pain from noxious mechanical and thermal stimuli, and inflammatory pain that would arise from chronic, unhealed wounds. *PRDM12*-CIP injuries usually include mutilation of tongue, lips and fingers, as well as burns and limb fractures (see Figure 4.1A). However in contrast to other forms of CIP, pain insensitivity may not be global; one adult recounted only partial loss of pain sensation in one leg which they could discern from complete insensitivity in the other[408]. Proprioception and sensitivity to dimensions of light touch, such as pressure and vibration, are normal. Patients can recognise changes in temperature, although noxious hot and cold temperatures do not

register as painful and therefore dangerous. Corneal abrasions are ubiquitous, with the exception of one family (Family J – see P17 in Figure 4.1A)[123]. This type of injury occurs due to absent protective reflexes including blinking and tear production, which are normal responses that depend on local innervation by nociceptive fibres[109]. Wound infections that progress to osteomyelitis are another common feature, often leading to Charcot's joints or requiring amputation.

Quantitative assessment of myelinated fibres in sural nerve biopsies from two patients revealed selective loss of small diameter axons, representing lightly myelinated Aδ nociceptors. Immunostaining with PGP9.5 antibody of skin biopsies from two other patients showed intra-epidermal nerve fibres did not cross the basement membrane; this area is normally comprised of small fibre nociceptors[411], which can be observed in healthy controls[123]. Two further cases have since been reported by independent groups, with compatible clinical descriptions and *PRDM12* mutations identified[409,412]. In nerve conduction studies on these patients, motor potentials on both sides of the body were unaffected but sensory potentials were absent, supporting a sensory-specific deficit.

Figure 4.1: Typical injuries in *PRDM12*-CIP and *PRDM12*-MiTES patients
(A) CIP patients suffer from a range of injuries throughout their life including self-mutilation of the lips, tongue, digits as well as burns and corneal scarring. (B) MiTES patients present in early childhood with deep wounds across the nasal bridge and can extend towards the inner eyebrows and nasolabial folds. *Images taken from (2015) Chen et al., (2017) Srinivas et al., (2018) Moss et al., (2019) Inamadar et al., and (2020) Noguera-Morel et al.*

4.1.4 – Overview of Nociceptor Neurodevelopment

The molecular signature, connectivity and function of mature nociceptive neurons is determined during embryonic development. Following fertilisation and implantation of the blastocyst into the uterine wall, the early embryo enters a gastrulation phase to form the three germinal layers – surface ectoderm, mesoderm, and inner endoderm. The notochord is generated from the mesoderm soon after and releases Sonic hedgehog protein into the overlaying ectoderm layer. This initiates the neurulation stage (see Figure 4.2A) whereby the dorsal ectoderm thickens and differentiates into a segment of neuroepithelial cells, the neural plate, flanked by neural plate border (NPB) and pre-placodal ectoderm regions interfacing with the non-neural ectoderm. As the neural plate folds inwards, morphogenetic changes in the cells closest to the notochord and NPB form hinge points, driving the closure of the neural plate into the neural tube, with the NPB at the dorsal rim. By the end of primary neurulation, the surface ectoderm has separated from the neural tube to become the epidermis and other tissues on the outer surface of the body, while the neural tube will develop into the brain and spinal cord[413].

At this stage, cells of the pre-placodal ectoderm and NPB regions become more restricted in their developmental fate, forming multipotent cranial placodes in the head, and neural crest cells (NCCs) further down the rostrocaudal axis. NCCs are the earliest precursors of melanocyte, somatosensory and autonomic lineages, but BMP and WNT signals secreted by the ectoderm and dorsal neural tube act synergistically to suppress premature differentiation. Multipotent NCCs can be identified by expression of transcription factor SOX10, induced pre-migration by the balance of local BMP and WNT signals[414–416]. A developmental switch in cadherin subtype expression changes the adhesion properties of NCCs, allowing them to delaminate from the dorsal neural tube[417]. Depending on the route of migration (see Figure 4.2A), motile NCCs are exposed to distinct microenvironments where extrinsic cues and cell-cell interactions signal the pausing or advancement of travel until they reach their programmed destinations[418].

Of the undifferentiated NCCs, those that migrate laterally underneath the ectoderm and around the somites develop into melanocytes. Those migrating ventrally between the somites and neural tube encounter extracellular matrix proteins which regulate the expression of cell adhesion molecules within NCCs, prompting them to build the budding somatosensory or autonomic ganglia[419–421]. In the case of nociceptors, NCC-derived somatosensory progenitors coalesce into trigeminal ganglia (TG) and dorsal root ganglia (DRG), with the trigeminal placode providing an additional source of neural precursors to the TG[422,423]. Environmental cues exerted under strict spatiotemporal control also induce

early markers of differentiation. For example, high levels of BMP-4 and BMP-7 secreted together by the dorsal aorta induce the co-expression of MASH1 and PHOX2B in NCCs of the newly condensed sympathetic ganglia; these transcription factors specify neuronal and noradrenergic properties respectively[416,424,425]. PRDM12 is the earliest known marker of TrkA-positive nociceptors, observed in the neural folds of mice from embryonic day 9 (E9)[123]; it is non-essential to the induction of Neurogenin-1 expression, but is vital for its maintenance in nociceptor-fated progenitors[124,125]. The signals responsible for the induction of PRDM12 in this select lineage are currently unknown.

Genetic tracing and knockout studies in mice have revealed the progression of fate decisions that NCCs go through to achieve the functional diversity present in mature somatosensory ganglia, as shown in Figure 4.2B. The first stage is somatosensory neurogenesis, which occurs in three waves starting at E9, E9.5 and E10.5. During the first wave, a population of migrating SOX10-positive NCCs acquire neuronal fate by upregulating Neurogenin-2. Upon reaching the TG and DRG, pioneering cells switch off multipotency marker SOX10 and begin to express the sensory-biasing transcription factor, FOXS1[426,427]. These early progenitors exhibit limited proliferation, and by cell cycle exit express the sensory neuron-restricting transcription factors BRN3A and ISLET1[428] which protect somatosensory precursors from apoptosis[429] and regulate the expression of neurotrophin receptors TrkA-C[430,431]. This wave mainly gives rise to larger myelinated proprioceptors and low-threshold mechanoreceptor (LTMR) subtypes, later differentiated through the activity of RUNX3 transcription factor and early expression of GDNF-family ligand receptor RET[432,433]. A small proportion of myelinated nociceptors (Aδ fibres) are also produced during this first wave[434–436].

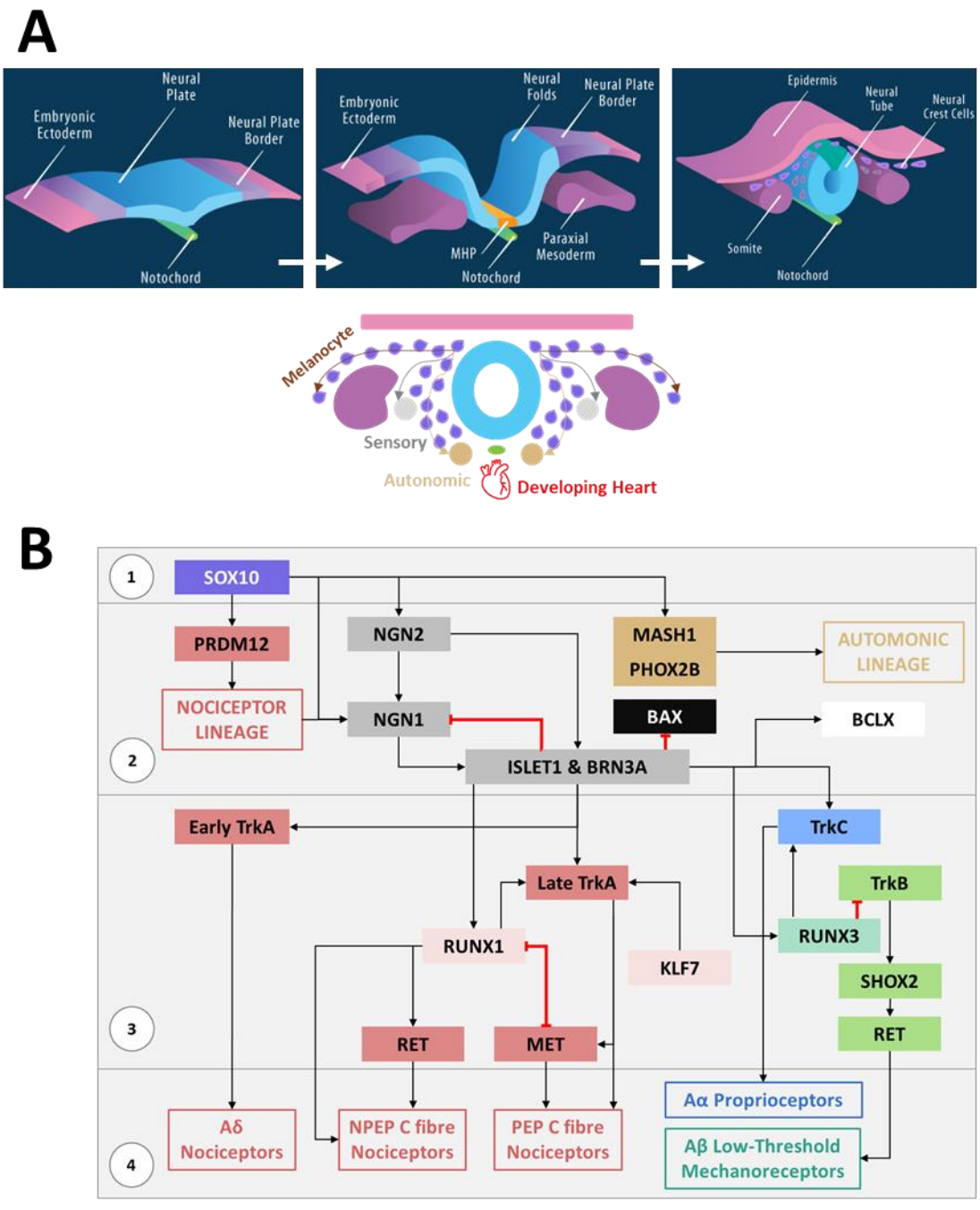

Figure 4.2: Neurodevelopment of somatosensory neurons
Morphogenesis and migration of neural crest cells specified for melanocyte, sensory and autonomic cell fates. *Figure adapted from* https://discovery.lifemapsc.com/library/images/neural-tube-formation-by-primary-neurulation*; Copyright LifeMap Sciences, Inc. - All Rights Reserved.*
(B) Transcriptional cascades determining the differentiation of (1) multipotent neural crest cells through (2) sensory neuron commitment and (3) subtype specification, to (4) mature functional classes in sensory ganglia. Black arrows indicate order of activation, while red lines indicate direction of repressive activity.

The second wave of neurogenesis is attributed to SOX10-positive NCCs that arrive later in the nascent DRG and only then upregulate Neurogenin-1 and FOXS1 expression, thought to bypass a requirement for Neurogenin-2[426,427,434]. This population undergoes an extended proliferative period to produce all unmyelinated nociceptors and a small proportion of proprioceptive or mechanoreceptive A fibres; in Neurogenin-1 knockout mice, this entire lineage is absent, contributing ~80% of all sensory neurons in the mature DRG[436]. However, it was recently shown that part of the postnatal Neurogenin-1-dependent population arises during the first wave, dependent on precursors co-expressing high levels of Neurogenin-2 and low levels of Neurogenin-1; in Neurogenin-2 knockout mice, these progenitors instead switch to a melanocyte fate or go through apoptosis. This developmental deficit is reflected in a loss of almost half the sensory neurons of the Neurogenin-1 lineage in postnatal DRG[436]. In the final wave of somatosensory neurogenesis, boundary cap NCCs travel the shortest distance, accumulating at the dorsal root entry zone (DREZ) of the spinal cord. From here they migrate along the nerve root into the DRG contributing a late population of TrkA-C neurons, as well as Schwann cells responsible for myelination[437,438].

Following the recent identification of mature somatosensory subtypes, single-cell RNA sequencing (scRNA-seq) analysis of mouse DRG across development has revealed the transcriptional path from multipotent NCCs through sensory neuron commitment and specialisation into mature proprioceptors, LTMRs and nociceptor subclasses[38]. At E11.5, the earliest timepoint at which DRG were isolated for scRNA-seq, three developmentally linked populations could be detected: (i) Multipotent NCCs marked by Sox10; (ii) sensory neuron progenitors marked by Neurogenins-1 and -2; and (iii) postmitotic cells marked by Advillin, a cytoskeletal regulator specific to DRG sensory neurons during embryonic stages[439,440]. Advillin-positive cells at E11.5 were considered transcriptionally unspecialised given the negligible expression of genes that distinguish sensory subtypes in adult ganglia. From E12.5 through to adulthood, the diversification of somatosensory precursors into mature subtypes required progressive transcription factor expression under tight regulation. These factors exert activating or repressive action depending on the cofactors available at different developmental stages[38,441].

Following neurogenesis, sensory-instructive transcription factors *BRN3A* and *ISLET1* are swiftly activated which initiate transcriptional programmes that generate the broadest classes of sensory neuron subtypes. They repress the expression of upstream neurogenic genes *NGN1*, *NEUROD1* and *NEUROD4*, and activate the expression of neurotrophin receptor genes (*NTRK1-3* for TrkA-C), promoting the differentiation of sensory neuron progenitors[428,442,443]. Progenitors born from the first

wave widely express TrkC, either alone or co-expressed with TrkA or TrkB; in the latter groups, downregulation of TrkC segregates nociceptor- and LTMR-fated cells from the proprioceptors, in which TrkC expression persists[431,434]. The Trk receptors mediate a neuron's capacity to respond to growth factor cues, guiding the peripheral axon to specific tissue targets for innervation. Upon extracellular ligand-binding and intracellular phosphorylation of Trk receptors, they are internalised and retrogradely transported to the nucleus to regulate genetic programmes involved in neuronal survival, axon growth and functional adaptation[444].

The emerging somatosensory system generates an excess of neural progenitors that undergo programmed cell death to avoid excessive peripheral innervation and inappropriate connectivity of sensory circuits. This maturation process also occurs in waves, with apoptosis of proprioceptors and LTMRs peaking first in mice at E12.5, while apoptosis of nociceptors is highest from E12.5 to E14.5[445]. Susceptibility to programmed cell death appears to be influenced by a combination of extrinsic and intrinsic agents. In the case of newborn proprioceptors, retinoic acid produced by the paraxial mesoderm determines the expression levels of transcription factor RUNX3, such that progenitors expressing very low levels of RUNX3 and TrkC mature more slowly and are less competitive by the time cell survival is dependent on target-derived growth factors[446,447]. BRN3A is critically important for progenitor survival during this period, as well as postnatally in the context of nerve injury, due to its role in activating antiapoptotic gene *BCLX* and antagonising activation of apoptotic gene *BAX*[429,448,449].

Subsequent to sensory neuron commitment by BRN3A and ISLET1, TrkA expression is one of the earliest markers of post-mitotic nociceptors, driven by BRN3A binding to the *NTRK1* enhancer region in both the Aδ and C fibre nociceptor lineages[450]. Transcription factors RUNX1 and KLF7 also support *NTRK1* activation during embryonic development of C fibres[451,452]. RUNX factors are prominent elements in sensory neuron diversification, with RUNX1 and RUNX3 being restricted to nociceptors and proprioceptors respectively by late embryonic stages[434]; this segregation is driven by the co-ordinated activity of ISLET1 and BRN3A, and occurs in parallel to TrkA and TrkC partitioning[428,432,442]. High levels of RUNX3 help to consolidate the TrkC-positive proprioceptor lineage in DRG, and TrkC-positive mechanoreceptors in TG, by maintaining TrkC expression and repressing TrkB in co-expressing progenitors[432,453,454]. Neurons expressing low levels of RUNX3 are permissive of *SHOX2* transcription factor activation, followed by early activation of *RET* and Aβ LTMR development[455,456].

RUNX1 splits the C fibre nociceptor lineage into two major groups – the non-peptidergic and peptidergic neurons. The peptidergic group arises from TrkA-positive sensory neurons that begin to

express receptor tyrosine kinase MET at E16.5 in mice. Synergistic activation of TrkA and MET (by nerve growth factor and hepatocyte growth factor ligands respectively) is required to repress RUNX1[457], and as a consequence, to de-repress the expression of neuropeptide CGRP[432,458]. In contrast, non-peptidergic neurons arise through the persistent expression of RUNX1 and a gradual switching of neurotrophin receptor expression from TrkA to RET from E15.5 onwards[441,459,460]. The magnitude and duration of RUNX1 expression is of particular importance in defining polymodal non-peptidergic nociceptors and compartmentalising pruriceptor subtypes[461]. The unmyelinated C-LTMR population may also arise from the non-peptidergic nociceptor lineage, as postnatally they are TrkA-negative and Ret-positive, and require RUNX1 plus transcription factor Zfp521 during embryonic development to express distinguishing markers tyrosine hydroxylase and vesicular glutamate transporter VGLUT3[462,463]. In contrast, Aδ nociceptors develop independently of RUNX1-driven transcriptional cascades in the first neurogenic wave; nevertheless, they seem to play a non-redundant role in sharp, pinprick mechanosensation[435,464].

Central axon navigation and termination on specific laminae is dependent on a wide range of growth cone receptors and diffusible guidance cues being expressed at the correct developmental timepoints. The transmembrane glycoprotein axonin-1 (also known as TAG-1 or Contactin2) was shown to be necessary first for the extension of central axons towards the spinal cord[465]. Upon reaching the DREZ, the central axon makes a turn and grows longitudinally for a short “waiting period” while spinal cord organisation is in progress; entry into the spinal cord is inhibited by SLIT1 and/or SLIT2 expressed in the dorsal horn acting on ROBO1 and ROBO2 receptors located on the growth cone[466]. Additional inhibitory signalling from the dorsal spinal cord via Netrin1 and its receptor UNC5C actively prevent premature entry[467]. During this waiting period, C-natriuretic peptide and its receptor natriuretic peptide receptor 2 are transiently upregulated in the dorsal spinal cord and on the central axon respectively, stimulating the growth of a daughter branch from the axon’s turning point[468]. Downregulation of Semaphorin3A, a repulsion cue in the dorsal horn, is necessary before central axon branches can enter, although its persistent expression in the ventral horn prevents nociceptive axons extending into this area[469,470]. In addition, cell adhesion molecules axonin-1, NgCAM and type III neuregulin-1 have been identified as positive regulators of axonal pathfinding, confining axon growth to laminae I and II[471,472], while the formation of terminal collateral branches that synapse with spinal microcircuits is regulated by microtubule-stabiliser MAP7[473].

4.1.5 – Pathogenicity of PRDM12-CIP Mutations – LOF at the Molecular Level

Molecular assays exploring pathogenicity of the human *PRDM12* mutations established a common LOF in PRDM12's ability to produce H3K9 methylation marks[123,407] (see Figure 4.3), although there were some discrepancies between the two papers. Tagged PRDM12 constructs were transiently transfected into HEK293 cells, to visualise the subcellular distribution of WT and mutant proteins by confocal microscopy in fixed cells. Both papers reported a nuclear-restricted, punctate or lace-like pattern of WT PRDM12. Chen et al.[123] observed the same pattern in cells transfected with the six missense mutants, whereas the 19 alanine (19A) expansion mutant formed bright nuclear and cytoplasmic aggregates.

In contrast, Nagy et al.[407] examined 4 of the 6 missense mutations and found Trp160Cys, Arg168Cys, and Glu172Asp mutants formed large, bright nuclear aggregates, while the Asp31Tyr mutant was mis-localised to the cytoplasm in a diffuse pattern. The reason behind these conflicting findings is unclear, as apart from some subtle differences in immunostaining protocols, the only obvious difference between the studies was the use of an N-terminal hemagglutinin tag versus a C-terminal FLAG tag in the PRDM12 constructs. However, both groups suggested that aggregation and mis-localisation reduced the availability of functional PRDM12 in the nucleus.

Further investigations by Chen et al. refined the mechanisms of pathogenicity behind the missense and expansion mutations[123]. Transfection of the 18A and 19A polyalanine expansion mutants into COS-7 cells indicated a 60% reduction in protein expression levels when compared to WT, but upon proteasome inhibition with MG132, expression levels of the mutants were commensurate with WT. The same assay conducted on the missense mutants revealed no significant differences in their relative expression compared to WT. These results suggest that in addition to aggregation, heightened degradation of the expansion mutants contributed to their LOF.

Turning to *in vivo* experiments in *Xenopus* embryos confirmed a robust increase in H3K9 di-methylation (H3K9me2) levels upon injection of WT *prdm12* mRNA into neutralized animal cap cells. Injection of *prdm12* mRNAs with corresponding human missense mutations resulted in approximately 80% reduction of H3K9me2 signal across all mutants compared to WT – a substantial disruption to PRDM12's histone-modifying function. Using a G9a co-IP protocol in COS-7 cells that were co-transfected with WT or mutant *PRDM12* revealed that the PRDM12-G9a interaction was only broken by the His289Leu mutation[123]; this was consistent with established knowledge of PRDM12 as His289Leu is located within the second zinc finger domain.

How the remaining 5 missense mutations (4 of which are located in the PR domain) disturb H3K9 methylation, when they were still able to pulldown G9a, is uncertain. *In vitro* assays of histone methylation had previously demonstrated that PR domain deletion constructs could still pulldown G9a and generated H3 methylation signal that was comparable to WT PRDM12[399]. It may be that in the *in vivo* context, the mutated residues in the PR domain mediate interactions with alternative HMT enzymes modulating H3K9 methylation status. Supporting the functional importance of this part of the protein was the discovery of two further PR domain missense mutations, Gly115Arg and Asn174Lys, in another *PRDM12*-CIP patient[412].

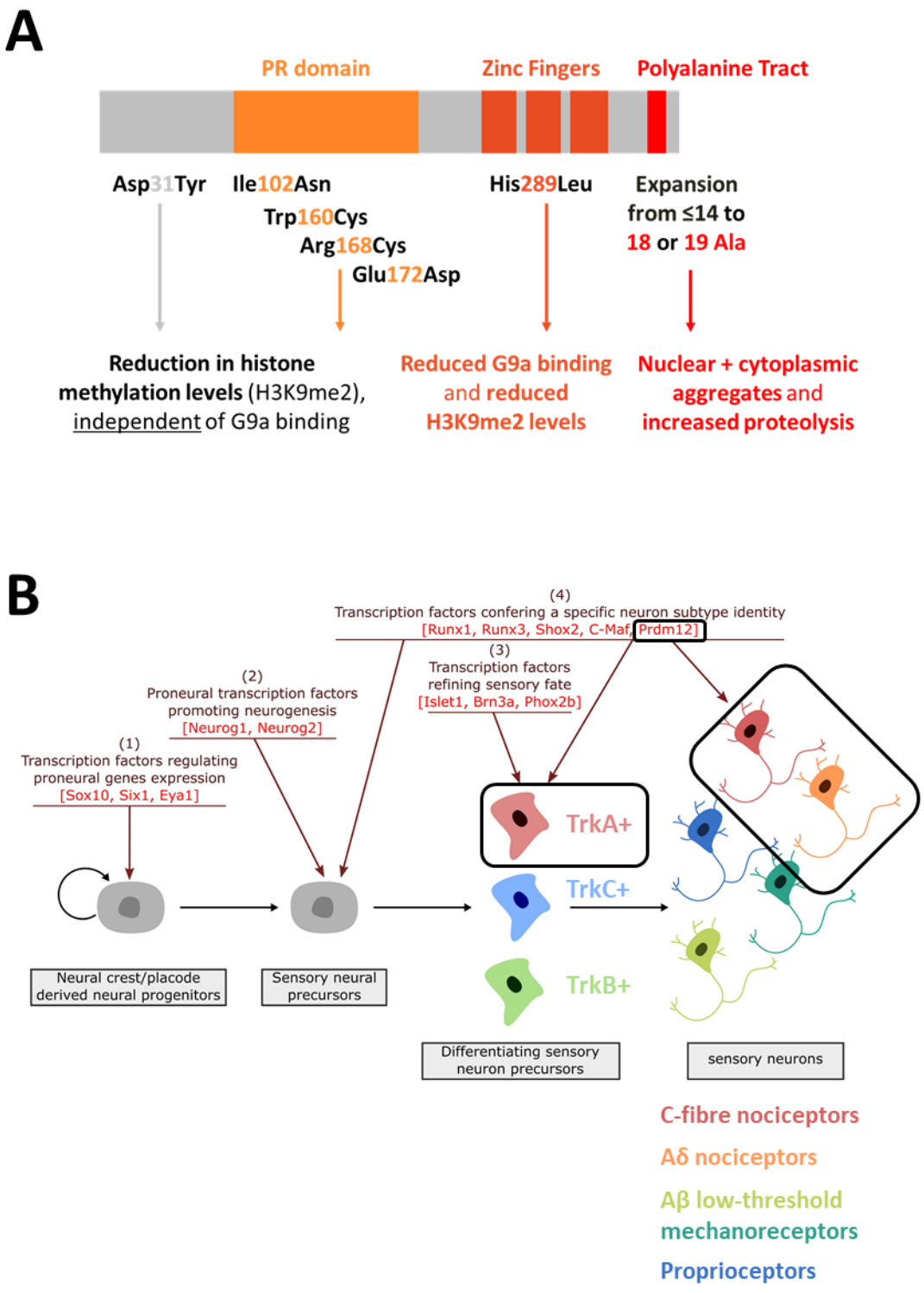

Figure 4.3: Impact of PRDM12 LOF in sensory neuron development
(A) Critical domains of the PRDM12 protein and functional consequences of missense or polyalanine tract expansion mutations identified from *PRDM12*-CIP patients. (B) Transcriptional cascades involved in the development of mature somatosensory neurons from multipotent precursors. *Adapted from (2020) Vermeiren et al.*

4.1.6 – Developmental and Physiological Roles of PRDM12

A number of model organisms have been used to understand the consequences of PRDM12 LOF or over-expression in the development of somatosensory neurons and pain-related behaviours. Further studies carried out in human stem cell-derived models and embryonic sections, as well as the adult phenotype of *PRDM12*-CIP patients, all point to a critical developmental role for this protein in generating the TrkA-positive lineage of nociceptive neurons (see Figure 4.3B).

Knockdown of *Prdm12* in *Xenopus* embryos led to reduced mRNA levels of *Ath3* and *Islet1*[406], early markers of neurons in the ectoderm-derived trigeminal placodes; these go on to contribute to the sensory neuron population in the trigeminal ganglia (TG), together with NCC-derived sensory neurons. In addition to lowering mRNA levels, the distribution of trigeminal placode markers appeared disorganised after *Prdm12* knockdown, whereas markers for other cranial placodes such as the otic placode which develops into the ear, were unaffected[123]. On the other hand, microinjection of human *PRDM12* mRNA into neuralized cap cells robustly induced mRNA expression of early markers of sensory neurons, *Islet1* and *Tlx3*, but this effect was diminished when several human missense mutant mRNAs were tested[407]. Together, these results indicated a requirement of functional PRDM12 for the early differentiation stages of NCCs into somatosensory neuron fate.

Similar temporal patterns of PRDM12 expression have been observed in mammalian systems. In mice, *Prdm12* mRNA was observed in the neural folds at E9.0, and by E10.5 was specifically enriched in the DRG and p1 progenitor domain in the spinal cord; purified tissue preparations and cell line controls established this expression was restricted to neurons rather than peripheral glial cells. *Prdm12* expression was stable and continued into adulthood as late as postnatal day 56 (P56)[123]. At the protein level, Prdm12 has been detected in DRG and TG from E9.5 onwards[125]. From E9.5-E10.5, this primarily consists of post-migratory cells that are committed to a sensory neuron fate, which begin to lose Sox10 expression (an early marker of multipotency in NCCs) and increasingly express Islet1, which is required for nociceptor specification[434,441,442]. The subsequent confined expression of tyrosine receptor kinase A (TrkA) from E10.5 onwards identifies all neurons that are fated to become either myelinated Aδ- or unmyelinated C-fibres, both involved in nociception, as opposed to the TrkB/C-positive low-threshold mechanoreceptive (LTMR) and proprioceptive neurons. Immunohistochemistry analysis confirmed the co-expression of PRDM12 with TrkA as early as E12.5 which continued postnatally even in adult mice, while the absence of Prdm12 co-expression in TrkB- and TrkC-positive neurons was observed from E11.5 onwards[124,125].

Homozygous knockout mice have been generated to study (1) the cellular mechanisms of Prdm12 LOF in the early stages of differentiation of NCCs into mature nociceptors, and (2) how well these molecular findings correlate with behavioural assays testing different modalities of sensation. In three different mouse models, *Prdm12* constitutive knockout mice died within a few hours of birth or could not be detected among newborn pups; the reason for perinatal lethality is not known, however embryonic mice up to E18.5 were viable[124,125,137,138]. Compared to Prdm12$^{+/+}$ control mice, a reduction in DRG size was observed around E11.5-E12.5, and by E12.5 there appeared to be a significant drop in the number of neurons marked by Islet1 or Peripherin. The number of TrkB and TrkC neurons was similar to WT at all timepoints, and Runx3 expression remained constant, suggesting Prdm12 does not regulate cascades specifying non-nociceptive fates nor does its absence lead to a compensatory up-regulation of these populations. In stark contrast, the TrkA nociceptive population was completely absent in DRG and TG from E11.5 onwards. Of note, TrkA is also required for the survival of developing neurons in the sympathetic ganglia[474] but its expression here was unaltered[124,125], indicating PRDM12 is not the universal regulator of *NTRK1* activation.

TrkA-C are the earliest markers used to define sensory neurons that form the nociceptor, LTMR and proprioceptor lineages. The latter two groups, as well as a subset of lightly myelinated Aδ-fibres which are TrkA+[435], are generated from an early wave of NCCs that express high levels of Neurogenin-2 and low levels of Neurogenin-1 at E9.5-E10.5. In a successive wave around E10.5-E13.5, NCCs expressing high levels of Neurogenin-1 alone produce the unmyelinated nociceptor class[441], hinting at a particular importance for PRDM12 in this phase. Supporting this hypothesis, cell populations marked solely by either Neurogenin-1 or Neurogenin-2 at E10.5 were equivalent in *Prdm12* germline KOs and WT mice, but at E12.5, the Neurogenin-1 population was substantially smaller in KO mice compared to WT. The mRNA levels of downstream genes important for neuronal differentiation (*Neurod1*)[475] and sensory neuron diversification (*Pou4f3*)[428,451] were also reduced in the *Prdm12* KOs. However, Neurogenin-1 or -2 KO had no effect on *Prdm12* expression. These results suggest *Prdm12* expression is activated in early sensory neurogenesis, independently of Neurogenin signalling, but is critical to the maintenance of Neurogenin-1 expression and subsequent nociceptor differentiation in the second wave[124,125].

Two hypotheses have been put forth as to how PRDM12 LOF leads to a loss of the TrkA+ lineage – reduced proliferation versus increased apoptosis of sensory neuron precursors. Both questions have been investigated in three different papers, all using germline *Prdm12* knockout mice. Desiderio et al. saw no difference between KO and WT mice in the number of phospho-histone H3 (pH3) positive cells (i.e., mitotic cells) at E10.5-E11.5, but they did observe more apoptotic cells at E12.5 in the mutant

mice, as marked by activated capsase-3[125]. Bartesaghi et al. looked specifically at the Sox10+ multipotent NCC population[416] in DRGs from E10.5-E12.5. Quantification of pH3+ cells revealed a 40-50% drop in proliferating NCCs in the *Prdm12* KOs at E11.5-E12.5 compared to WT mice, whereas they saw no difference between groups in apoptosis of NCCs from E10.5-E12.5[124]. To address this debate, Landy et al. measured activated caspase-3 positive cells as a readout for apoptosis, and cells positive for EdU-labelling (a thymidine analogue) as a readout for proliferation, from E11.5-E13.5. Their results indicated no significant difference in apoptotic rate between WT and *Prdm12* KOs, but rather a decrease in proliferation at E11.5, specifically of precursors destined to become TrkA+ nociceptors, while LTMR and proprioceptor populations continue to proliferate normally[137].

Downstream of TrkA, a number of markers for mature nociceptor subtypes were also affected by Prdm12 knockout. The expression of Ret, another neurotrophin receptor, can mark a variety of sensory neuron subtypes depending on the co-expression of other markers and the timepoint at which it is measured. At E12.5, a 60% reduction in the number of neurons expressing Ret was observed in KO mice and this was mirrored by a significant loss of Ret expressing neurons at P0[124,125]. Early Ret signalling from E10.5 onwards determines large-diameter, myelinated LTMRs and is maintained postnatally[441,476], thus the surviving Ret+ neurons likely reflect this class. However, Ret expression is also required during later embryonic timepoints and postnatally for the specification of unmyelinated C-LTMRs and non-peptidergic nociceptors. This was confirmed by a complete loss of tyrosine hydroxylase positive neurons by E18.5 which marks the C-LTMR class, as well as the Nav1.8-encoding gene *SCN10A* by E16.5, which is essential to maintaining electrical excitability of all nociceptor subtypes. Furthermore, Substance P and calcitonin-gene related peptide (CGRP) were completely absent at E18.5 indicating the peptidergic nociceptor population had also been lost[124,125]

Embryonic conditional knockout (cKO) of *Prdm12* in DRG neurons was achieved using the *Advillin* promoter in three mouse models, allowing for histological and behavioural analysis as these mice survived into adulthood[125,137,138]. Desiderio et al. showed Prdm12 expression was still detected from E13.5-E15.5 but was deleted by E16.5. Consistent with this pattern, fewer TrkA+ neurons were detected in the cKO mice than in controls from E13.5-E15.5, and were virtually absent in knockouts by E16.5[125]. Similar to the constitutive knockouts, both cKO models revealed a selective loss of small-diameter neurons, which included both peptidergic and non-peptidergic populations in adults. Other markers of maturing nociceptors were substantially reduced during embryonic development including *Runx1* and *Scn10a* at E15.5, and their encoded proteins by E18.5[125,137]. Kokotovic et al. also demonstrated a robust knockdown of *Prdm12* transcripts and protein in lumbar DRG in their cKO

model (*Prdm12*$^{fl/fl}$; *Avil-Cre*). These mice presented facial scars and corneal abrasions similar to human-CIP patients, as well as significantly reduced sensitivity to pain from intraplantar capsaicin injections when compared to WT littermate controls. The authors extended their analyses with single-cell electrophysiology and bulk RNA sequencing, demonstrating cultured DRG neurons from *Prdm12*$^{fl/fl}$; *Avil-Cre* were hypoexcitable in response to both ramp and block current stimulation protocols, which was associated with a depletion of several sodium and potassium channel transcripts important for nociceptor electrogenesis[138].

Human histological studies validated TrkA and PRDM12 co-expression in embryonic DRG at Carnegie stage 12[125]; approximately equivalent to E10.5 in mice[477]. Differentiation of human embryonic stem cells and inducible pluripotent stem cells (iPSCs) into nociceptor-like neurons also produced a sharp increase in *PRDM12* expression from day 7-11, coinciding with markers of neural crest specification. After 52 days *in vitro*, mature neurons expressed large transient TTX-resistant Na^+ currents, most likely from Nav1.8 channels as *SCN10A* mRNA was robustly detected in these cells[123]. In another iPSC line with *PRDM12* expression under tetracycline-inducible control, PRDM12 induction led to a strong increase of *NTRK1* levels as well as a decrease in *NTRK2* and *NTRK3* levels, suggesting that contrary to mouse studies, PRDM12 may repress TrkB and TrkC expression in this model[125].

Detailed behavioural analysis has been conducted in PRDM12 knockout flies and cKO mice. In *Drosophila*, latency in response to a heat probe set to 46°C was used as an assay of thermal nociception. Knockdown of *Hamlet*, the *Drosophila* orthologue of PRDM12, increased the response time to noxious stimuli compared to WT flies. These results were recapitulated when human *PRDM12* mRNA with patient mutations were ectopically expressed[407], mimicking the hyposensitivity seen in *PRDM12*-CIP patients who often suffer burn injuries. However, despite showing insensitivity to noxious mechanical and chemical stimuli in behavioural assays, studies of noxious heat sensitivity in embryonic cKO mouse models have produced conflicting results[137,138]. In Landy et al.'s model, WT and cKO mice demonstrated equivalent sensitivity to noxious thermal stimulation from 50-55°C[137]. In contrast, Kokotovic et al. investigated noxious heat sensitivity using single-cell electrophysiology where they observed 16 out of 42 cultured DRG neurons from WT mice produced temperature-evoked current, but only 1 of 42 cells from the cKO mice was heat-responsive in the same (noxious temperature range from ~35-45°C[138].

Both studies found a significant reduction in transcript expression of the noxious heat-sensitive channels *Trpa1* and *Trpv1*, while *Trpm3* transcripts were dysregulated in opposing directions in the

two cKO mouse lines[137,138]. Investigating the full complement of thermosensitive channels and comparing their regulation by PRDM12 may explain the discrepancies in nociceptive responses at the cellular and behavioural levels. Nevertheless, how these transcriptional differences arise is unclear as both groups ablated *Prdm12* expression within DRG using the Cre-LoxP system under the Advillin promoter – the only distinction being the loxP targeting to *Prdm12* exon 5 by Landy et al. versus exon 2 by Kokotovic et al. The former group did detect low-level expression of *Prdm12* transcripts with exons 1-4 present, encoding the PR domain and a portion of the flanking sequence before the zinc fingers, which may be partially functional[137].

Considering the robust postnatal expression of PRDM12 mRNA in adult mice and human DRG[123,125], and that enhancement of pain has been observed through G9a-mediated modulation of potassium channel expression[478,479] and endogenous opioid signalling[480,481] in nociceptors, it has been posited that PRDM12 could have a role in hypersensitisation. Tamoxifen-inducible cKO mice were generated to test the effects of adult-onset *Prdm12* ablation by two groups: Landy et al. continuing with DRG-restricted *Prdm12* deletion targeting exon 5, while Kokotovic et al. used the ubiquitously expressed promoter Rosa26 to target *Prdm12* exon 2 deletion globally. Using behavioural assays modelling acute and neuropathic pain, Landy et al. found no differences in sensitivity to any modality of noxious stimuli between WT and mutant mice; furthermore, despite dysregulation of ~150 genes upon *Prdm12* knockout, few could be obviously tied to nociceptor function[137].

In contrast, the adult-onset deletion mice studied by Kokotovic et al. exhibited a significant reduction in sensitivity to intraplantar capsaicin injection compared to control mice. Other pain behaviour assays were not conducted, but at the cellular level, they also found modest changes in nociceptor excitability and responsiveness to noxious thermal stimulation, as well as almost 70 genes differentially expressed upon *Prdm12* deletion – e.g., potassium channels Kcnv1 and Kcnb1, signal transducers Ntrk1 and Trpm8, neurotransmitter receptor subunits Grik1 and Chrna7[138]. Thus, the purpose of postnatal PRDM12 expression and its genetic targets require further corroboration.

One notable difference between human and mice PRDM12 knockouts is related to itch. In the original PRDM12-CIP study, affected cases from a single family with homozygous 18A polyalanine expansion mutations (Family J) displayed intense scratching of the face without the other archetypal severe CIP injuries such as burns and broken bones[123]. Two cKO mouse models (exon 2 and full protein deletion) exhibited similarly severe facial scratching without provocation, in addition to typical CIP injuries to the skin and corneal scarring[125,138]. However, in a separate cKO model (exon V deletion with reduced

but detectable expression of exon 1-4 transcripts), mutant mice spent markedly less time scratching than WT mice when chemically-evoked itch was tested by chloroquine or histamine injection[137]. These findings suggest a complex relationship in the specification of pain and itch sensing circuitry which may critically depend on different parts of the PRDM12 protein.

4.1.7 – Midface Toddler Excoriation Syndrome – a distinct *PRDM12* sensory disorder

From the original set of *PRDM12*-CIP patients, affected cases from two families were found to have homozygous expansions of the polyalanine tract – Family A originated from Pakistan and possessed 19A/19A alleles, while Family J originated from Ireland and had 18A/18A alleles. Unaffected parents were heterozygous for WT and mutant alleles. Genetic analysis of the polyalanine tract length in healthy Caucasian and Pakistani cohorts showed 12A or 13A alleles were most common but could range from 7 to 14 alanines.

A direct comparison of clinical phenotype between these two families highlighted several features in the 18A/18A cases that were atypical for *PRDM12*-CIP (see Table 4.1). The first sign of sensory abnormality in these individuals was severe scratching restricted to the face from 3-6 months of age, rather than the typical mutilation of lips, tongue and fingers. Corneal reflexes and sweating were intact, but all reported hypoesthesia (numbness) which had only been seen in one other *PRDM12*-CIP case. While abnormal sweating is not a definitive feature in *PRDM12*-CIP, it was observed in 9 individuals from 4 families, including Family A[123]. The presentation of patients in Family J was therefore considered a milder manifestation of *PRDM12*-CIP

Rare cases such as these had been recognised by dermatologists, because of the strikingly distinctive pattern and intensity of scratching across the midface (see Figure 4.1B), and the occurrence in families that hinted to a possible genetic aetiology. Family J had been presented at the British Society of Paediatric Dermatology on two occasions and when 2 independent affected Indian children were presented in 2015, members agreed they all shared the same phenotype. Together with colleagues in India, Professor Celia Moss reviewed the newer cases and suggested designating this disorder as a new clinical entity – Midface Toddler Excoriation Syndrome (MiTES).

They noted the severity of skin ulcers in children so young and in such a highly reproducible distribution across the face could not be explained by any other known causes of chronic pruritis. Lesions to the depth of muscle were observed across the bridge of the nose and extended in an X-like pattern to the eyebrows and beside the mouth. Occasionally scars were found on the forehead and behind the ears, but the chin and cheeks were largely spared. Common behaviours reported by parents and observed by physicians included nose-pulling, continual scratching and slapping the face, and disturbed sleep. An 11-year-old child could articulate “an irresistible urge to scratch the lesions”[482]. Interestingly, the patterns of facial lesions correlates strongly with sensory innervation by the V1 and V2 branches of the trigeminal nerve (see Figure 4.4).

After the *PRDM12* mutations of Family J were published, Professor Moss approached our group for genetic analysis of *PRDM12* in newly diagnosed MiTES cases. Astonishingly, we consistently found the homozygous 18A/18A expansion mutation in affected individuals, although compound heterozygous expansions to 16A/18A or 17A/18A have also been detected by other groups[483–486]. These results have been published and are described in more detail with a review of phenotypic profiles from 27 reported MiTES cases in Section 4.4.1. In two families, affected individuals were either negative for *PRDM12* mutations in any exon, or mutations were found in a different gene also associated with disorders of painlessness; these results suggest MiTES may be genetically heterogeneous like CIP.

Table 4.1: Comparing the clinical presentation of *PRDM12* polyalanine expansion families

Adapted from Chen et al., 2015. **M**: male; **F**: female; **m**: months; **y**: years; **+**: present; **-**: not present; **n.d.**: not determined

Family	Family A					Family J				
Ethnic Origin	Pakistan					Ireland				
Known parental consanguinity	+					-				
Base change	c.1056_1076dup					c.1059_1076dup				
Amino acid change	p.Ala353_Ala359dup					p.Ala354_Ala359dup				
Individual	P1	P2	P3	P4	P5	P16	P17	P18	P19	P20
Sex	M	M	M	F	M	M	M	M	F	F
Age at onset / last examination	6m/11y	12m/13y	6m/39y	6m/40y	6m/18y	3m/19y	3m/15y	3m/13y	6m/11y	6m/11y
First sign	No response to pain	Finger biting	Lip and tongue biting	Finger biting	No response to pain	Facial scratching	Facial scratching	Facial scratching	Facial scratching	Facial scratching
Disturbed pain perception	+	+	+	+	+	+	+	+	+	+
Disturbed temperature perception	+	+	+	+	+	+	+	+	+	+
Ulcers and mutilations	Fingers	Fingers	Tongue, lips and fingers	Tongue, lips	Fingers	Face	Face, feet	Face, feet	Face, feet	Face, feet
Corneal injuries	+	+	+	+	+	-	-	-	-	-
Skin / bone infections	+	+	+	+	+	+	-	-	-	-
Orthopaedic complications	+	+	+	+	+	+	+	+	+	-
Abnormal sweating	+ (reduced)	+ (reduced)	+ (reduced)	+ (reduced)	+ (reduced)	-	-	-	-	-
Hypo- / alacrimia	-	-	+	-	-	-	-	-	-	-
Hypoactive deep tendon reflexes	-	-	-	-	-	-	-	-	-	-
Disturbed vibration sense	-	-	-	-	-	-	-	-	-	-
Hypoesthesia	-	-	-	-	-	+	+	+	+	+
Disturbed proprioception	-	-	-	-	-	-	-	-	-	-
Life threatening hyperthermia	-	-	-	-	-	-	-	-	-	-
Abnormal blood pressure regulation	-	-	-	-	n.d	-	-	-	-	-
Intestinal dysmotility	-	-	-	-	-	-	-	-	-	-
Motor weakness	-	-	-	-	-	-	-	-	-	-
Sensorineural deafness	-	-	-	-	-	-	-	-	-	-
Hyposmia	-	-	-	-	-	-	-	-	-	-
Intellectual disability	-	-	-	-	-	-	-	-	-	-
Abnormal motor nerve conduction	n.d.	n.d.	n.d.	n.d.	n.d.	-	-	-	-	-
Abnormal sensory nerve conduction	n.d.	n.d.	n.d.	n.d.	n.d.	+	+	+	-	-
Pathologic sweat test	n.d.	n.d.	n.d.	n.d.	n.d.	n.d.	n.d.	n.d.	n.d.	n.d.
Abnormal histamine axonal flare test	n.d.	n.d.	+	n.d.	n.d.	n.d.	n.d.	n.d.	n.d.	n.d.

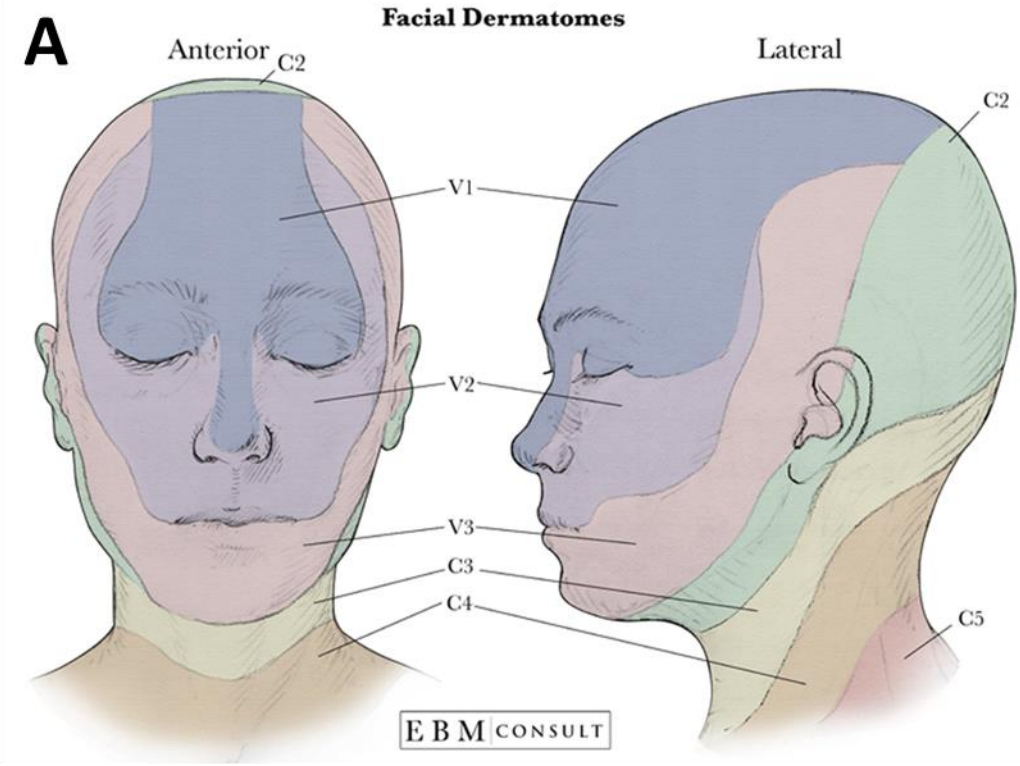

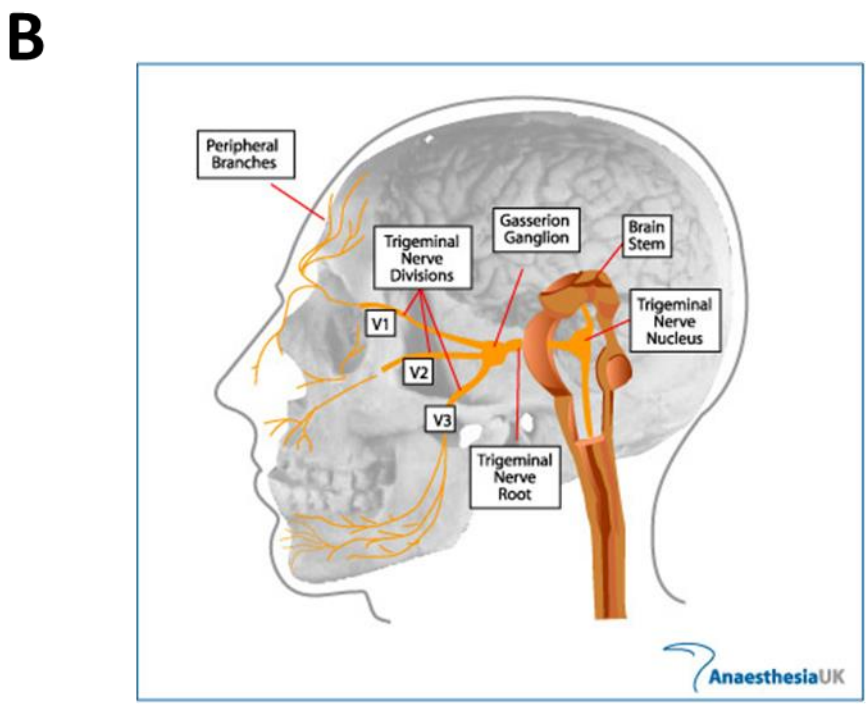

Figure 4.4: MiTES injuries correlate with innervation by V1 and V2 branches of the trigeminal nerve (A) Facial regions frequently affected in MiTES patients occur in the V1 and V2 dermatomes, (B) innervated by the ophthalmic (V1) and maxillary (V2) divisions of the trigeminal nerve. *Figure 4.4A provided by EBM Consult from https://www.ebmconsult.com/articles/anatomy-dermatomes-face. Figure 4.4B designed by AnaesthesiaUK, all rights reserved © 2021 – taken from https://www.frca.co.uk/article.aspx?articleid=100533.*

4.1.8 – Overview of Polyalanine Expansion Disorders

PRDM12 is not the only gene to cause disease due to pathogenic expansion of the polyalanine tract. Polyalanine (PA) expansions in eight other transcription factors and the mRNA-modifying protein PABPN1 (see Table 4.2) have been established as disease-causing mutations[487–489]. The transcription factor-associated diseases are all congenital, patients presenting with defects in physical and/or mental development from early childhood; they can also be caused by non-PA expansion mutations. In contrast, patients with *PABPN1* mutations are typically seen in their late 50s and are very rarely associated with missense mutations[490]. Despite most of these genes producing a single characteristic phenotype, the severity of major symptoms and penetrance can be variable, sometimes positively correlating with longer expansions[491–493]. However, none display such a strict genotype-phenotype correlation as seen with PRDM12 polyalanine tract length causing either MiTES or CIP.

PRDM12-CIP and -MiTES are the only autosomal recessive PA diseases, although biallelic mutations have been identified in *FOXL2* and *PHOX2B* in one family and a single child respectively[494,495]. The majority of PA expansion disorders are inherited in an autosomal dominant manner with the exception of X-linked mental retardation or X-linked hypopituitarism caused by mutations in *ARX* and *SOX3* respectively[489]. It is noteworthy that individuals who are heterozygous for WT/mutant *PRDM12*-CIP or -MiTES alleles are born healthy because this indicates the presence of one WT allele in enough for normal development to occur – i.e., the WT *PRDM12* allele is dominant over all mutant alleles identified so far, and disease phenotypes only arise from LOF in both *PRDM12* alleles rather than a dominant change or gain-of-function. In contrast, an autosomal dominant inheritance pattern would indicate that the polyalanine expansion results in either (A) a dominant negative variant that interferes with the function of the WT gene product, or (B) a LOF allele in a haploinsufficient gene, where the activity of one normal allele is not enough to produce a WT phenotype[488,496,497]. X-linked diseases usually arise through haploinsufficiency when a male only carries a single mutant allele on their X chromosome, while females must be homozygous to express the full disease phenotype[498].

Regardless of the route from PA expansion genotype to disease phenotype, *in vitro* studies have uncovered protein aggregation and mis-localisation to the cytoplasm as universal mechanisms of pathogenicity, compared to the diffuse, nuclear-restricted expression of WT transcription factors. In some cases, PA-expanded mutants were also shown to be more susceptible to degradation through the ubiquitin-proteasome system[499,500], as has been noted for both MiTES- and CIP-associated PRDM12 PA expansion mutants[123]. However, there is no evidence of aggregates *in vivo* in PA expansion mouse models of *HOXA13*, *SOX3* and *ARX* genes, suggesting this may be an artefact of overexpression

in cell culture. Instead, these studies revealed a decrease in steady-state abundance of expanded proteins compared to WT mice, without effects on mRNA processing or translation[501–504].

PRDM12-CIP and -MiTES clearly belong to this class of disorders based on clinical and genetic findings, as well as some evidence of shared molecular mechanisms of dysfunction with other members of this group. However, it is unclear how the discrete ranges of polyalanine length in PRDM12 produce such distinct sensory phenotypes. To address this puzzle, I used fluorescence microscopy to investigate potential differences in localisation between 18A (MiTES) and 19A (CIP) *PRDM12* constructs.

Table 4.2: Summary of polyalanine expansion diseases and molecular/cellular mechanisms of dysfunction

AD: autosomal dominant; **XR**: X-linked recessive; **AR**: autosomal recessive; **PA#**: Polyalanine tract number where multiple are present in the protein

GENE	DISEASE	INHERITANCE PATTERN	POLYALANINE TRACT LENGTH		MOLECULAR MECHANISMS OF DYSFUNCTION
			Wild-type	Disease	
HOXD13	Synpolydactyly type II	AD	15	22-29	**Aggregation**: (2004) Albrecht; (2007) Utsch; (2010) Villavicencio-Lorini **Mis-localisation**: (2004) Albrecht; (2007) Utsch; (2010) Villavicencio-Lorini **Increased Degradation**: (2004) Albrecht; (2007) Utsch **Altered Phase Separation**: (2020) Basu
HOXA13	Hand-foot-genital syndrome	AD	PA1: 14 PA2: 12 PA3: 18	PA1: 24 PA2: 18 PA3: 24-30	**Aggregation**: (2004) Albrecht; (2010) Villavicencio-Lorini **Mis-localisation**: (2004) Albrecht; (2010) Villavicencio-Lorini **Increased Degradation**: (2004) Innis; (2010) Villavicencio-Lorini **Altered Phase Separation**: (2020) Basu
ARX	X-linked mental retardation	XR	PA1: 16 PA2: 12	PA1: 18-23 PA2: 20	**Aggregation**: (2011) Fullston **Mis-localisation**: (2011) Fullston
PHOX2B	Congenital central hypoventilation syndrome (CCHS)	AD	20	25-33	**Aggregation**: (2012) Parodi; (2013) Di Lascio **Mis-localisation**: (2012) Parodi; (2013) Di Lascio; (2016) Di Lascio **Increased Degradation**: (2012) Parodi
SOX3	X-linked hypopituitarism	XR	15	22-26	**Aggregation**: (2004) Albrecht; (2007) Wong **Mis-localisation**: (2004) Albrecht; (2005) Woods; (2007) Wong
RUNX2	Cleidocranial dysplasia (CCD)	AD	17	27	**Aggregation**: (2004) Albrecht; (2014) Pelassa; (2016) Shibata **Mis-localisation**: (2004) Albrecht; (2014) Pelassa; (2016) Shibata **Altered Phase Separation**: (2020) Basu
FOXL2	Blepharophimosis-ptosis-epicanthus inversus syndrome (BPES)	AD	14	22-27	**Aggregation**: (2004) Caburet; (2008) Moumné **Mis-localisation**: (2004) Caburet; (2008) Moumné
PRDM12	Midface Toddler Excoriation Syndrome (MiTES) OR Congenital Insensitivity to Pain (CIP)	AR	7-15	MiTES: 16-18 CIP: 19	**Aggregation**: (2015) Chen **Mis-localisation**: (2015) Chen **Increased Degradation**: (2015) Chen
ZIC2	Holoprosencephaly	AD	15	25	Undetermined
PABPN1	Oculopharyngeal muscular dystrophy (OPMD)	AD	10	12-17	Not reviewed here

4.2 OBJECTIVES

The "milder" phenotype associated with a family initially diagnosed with *PRDM12*-CIP[123] was later recognised by paediatric dermatologists as the newly classified MiTES[482]. Clinical features of this family were distinct from the normal profile of *PRDM12*-CIP patients, and multiple MiTES cases were discovered with the same presentation:

i. Highly localised and deep excoriating wounds across the nasal bridge and nasolabial folds due to intense scratching, visible from the first year of life.
ii. Older patients have described an overwhelming itchy sensation, but lesions appear to settle with scarring by late teens – it is unclear if this is due to a change in sensation or behaviour.
iii. Signs of partial pain insensitivity may be present, such as in the hands and feet, but CIP-related defects in corneal reflexes and autonomic function are not observed.

In this project, I performed Sanger sequencing of *PRDM12* in newly diagnosed MiTES cases to determine if this was a separate congenital sensory disorder. This work has been published[483,484] and between our findings and those from independent groups[485,486], there is a clear genotype-phenotype correlation between *PRDM12* mutations and CIP versus MiTES (see Figure 4.5):

- *PRDM12*-CIP is caused by biallelic LOF mutations including missense, truncations or a homozygous expansion of the polyalanine tract to 19 alanines
- *PRDM12*-MiTES is so far only associated with homozygous expansions of the polyalanine tract in the range of 16-18 alanines

Following the genetic analysis, I conducted microscopy studies to compare the distribution and localisation of hemagglutinin (HA)-tagged PRDM12 constructs in the human HEK293 cell line. The main objective was to identify any differences between the MiTES and CIP polyalanine expansion mutants.

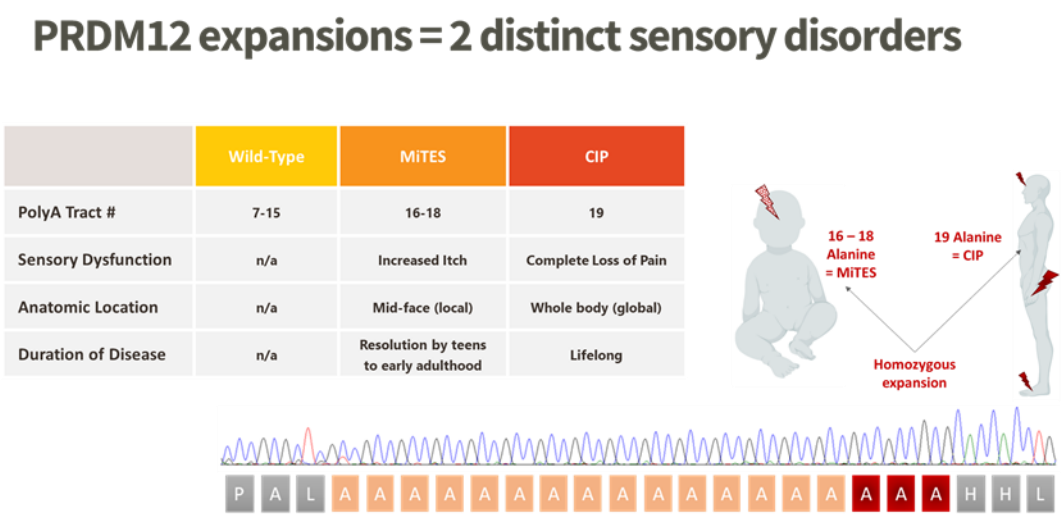

Figure 4.5: The PRDM12 polyalanine tract puzzle
Biallelic polyalanine expansion mutations in PRDM12, within discrete ranges, lead to either MiTES or CIP phenotypes. These disorders can be differentiated by clinical characteristics and genetic testing. How PRDM12 polyalanine tract length affects the development of somatosensory neuron identity and function in processing pain and itch sensations is unclear.

4.3 METHODS

4.3.1 – MiTES Case Ascertainment

Cases presented to local dermatological units with characteristic distribution of severe facial lesions, atrophic scars and/or post-inflammatory hyperpigmentation. Parents commonly reported sleep disturbance, self-inflicted scratching and nose-pulling in the affected children. As this is a newly described clinical entity, most diagnoses were confirmed by consultation with Professor Celia Moss at the University of Birmingham, before being referred to the Woods laboratory for *PRDM12* mutation screening. Full phenotype-genotype information and genetic pedigrees are described in the results.

4.3.2 – *PRDM12* Sanger Sequencing

Genomic DNA was isolated from suspected cases, parents and affected relatives where possible. Sequencing primers were designed using the reference transcript "NM_021619.2" – see Table 4.3. Exons 1-4 were amplified using the KOD Hot Start DNA Polymerase kit (Sigma-Aldrich), while exon 5 was amplified using FailSafe PCR 2X PreMix J (Lucigen) with OneTaq DNA Polymerase (NEB) – thermocycling conditions are described in Table 4.4. PCR products were purified by enzymatic treatment with Exonuclease I and Shrimp Alkaline Phosphatase (both from NEB).

For early cases, Sanger sequencing was conducted in-house using the BigDye Terminator v.3.1 Cycle Sequencing Kit and ABI PRISM 3730 DNA Analyzer (Applied Biosystems); for technical details see Section 2.3.6. Later cases were sequenced in commercial laboratories (Genewiz and/or Source BioScience). In all cases, patient sequences were compared to the reference transcript "NM_021619.2" using the alignment software, BioEdit[505]. Where variants were found in affected cases, parents were also screened to determine whether they were inherited or a result of de novo mutation.

Examination of hemizygosity in the father of cases C9, C10 and C11 was conducted by Mike Nahorski, and sequencing of case 27 (C27) was conducted by Yunisa Pamela, both members of the Woods laboratory.

Table 4.3: Sequencing primers for *PRDM12* exons

EXON	PRIMER ID	PRIMER SEQUENCE (5' – 3')
1	E1-FWD	TGCTCTGGTTCCTTCTCCAT
	E1-REV	CCATGGGGAAACTGAGGTG
2	E2-FWD	ACTTGGGTTTGGCTGGTCT
	E2-REV	CTTAGAGTCCCGGCTCAGG
3	E3-FWD	GGCTGTTGTGAGGATGGAGA
	E3-REV	TCTGTCCACTGTGGTTCCTG
4	E4-FWD	AATGGGACTGTGTGGCTTTC
	E4-REV	GAGCCTCTCTGCCTCTCTCA
5	E5-FWD	CTGTCCCTCCAGTCCGTCT
	E5-REV	GTGTCCTCATCTGCGACACG

Table 4.4: Input preparation for amplification of *PRDM12* exons

Amplification reaction components for *PRDM12* exons 1-4			
COMPONENT		**VOLUME (µl)**	
PCR grade water		32.5	
10X KOD Buffer		5.0	
dNTP mix (2mM)		5.0	
$MgSO_4$ (25 mM)		3.0	
FWD primer (10 µM)		1.5	
REV primer (10 µM)		1.5	
Genomic DNA template (100 ng/µl)		1.0	
KOD Hot Start DNA Polymerase (1.0 U/µl)		0.5	
Thermocycling Parameters			
STAGE	**TEMP (°C)**	**TIME**	**CYCLES**
Initiation	95	2 mins	---
Denaturation	95	30 secs	x35
Annealing	59	10 secs	
Extension	70	10 secs	
Final extension	70	10 secs	---
Hold	4	∞	---
Amplification reaction components for *PRDM12* exon 5			
COMPONENT		**VOLUME (µl)**	
PCR grade water		19.0	
FailSafe™ PCR 2X PreMix J		25.0	
FWD primer (10 µM)		2.0	
REV primer (10 µM)		2.0	
Genomic DNA template (100 ng/µl)		1.0	
OneTaq DNA Polymerase (5.0 U/µl)		1.0	
ABI Sanger Sequencing Reaction Parameters			
STAGE	**TEMP (°C)**	**TIME**	**CYCLES**
Initiation	95	4 mins	---
Denaturation	95	30 secs	x30
Annealing	60	30 secs	
Extension	72	45 secs	
Final extension	72	5 mins	---
Hold	4	∞	---

4.3.3 – *PRDM12* Plasmid Preparation

Wild-type and mutant PRDM12 plasmids were synthesised by Source BioScience. The coding sequence was based on the reference transcript "NM_021619.2", with an N-terminal fusion human influenza hemagglutinin (HA) tag, placed within the pcDNA3 mammalian expression vector. The polyalanine tract length was modified according to clinical phenotype and most common genotype: wild-type (12A), MiTES (18A) and CIP (19A).

Plasmid propagation was successful using both XL10-Gold Ultracompetent Cells (Agilent Technologies) and MAX Efficiency Stbl2 Competent cells (Invitrogen) – see Section 2.3.5 for protocol details. For PRDM12 plasmids, all bacterial growth stages were conducted in LB-Ampicillin cultures at 37°C. Double restriction enzyme digests with KpnI-HF and XhoI (NEB) were conducted for 2 hours at 37°C, and comparison against the Hyperladder 1 kb molecular weight marker (Bioline) and GelPilot 100 bp Plus Ladder (Qiagen) produced two bands corresponding to the PRDM12 insert and plasmid backbone. All plasmid preps were sequence verified by Source BioScience with dGTP chemistry to ensure clear reading of the GC-rich sequence, using common primers CMV-F and BGH-rev.

4.3.4 – HEK293 Cell Maintenance

HEK293 cells were maintained in high-glucose DMEM with pyruvate and GlutaMAX Supplement (Gibco), supplemented with 10% dialysed fetal bovine serum (Sigma). Cells were grown in 75 cm^2 tissue culture treated flasks, incubated at 37°C and 5% CO_2, and split at a 1:10 ratio twice a week.

4.3.5 – PRDM12 Localisation Studies Using Confocal Microscopy

Coverslips were sterilised and coated with poly-L-lysine solution (Sigma) before plating HEK293 cells at an appropriate density to ensure well separated cells in confocal microscopy images. Transfection complexes were prepared the next day, as recommended in the FuGENE HD Protocol Database [https://www.promega.com/techserv/tools/FugeneHdTool/] – at a 3:1 ratio FuGENE HD transfection reagent (Promega) to PRDM12 plasmid DNA, diluted in reduced serum Opti-MEM media (Gibco). The immunocytochemistry protocol was conducted 24 hours post-transfection.

Cell culture medium was removed and cells were washed in PBS, followed by fixation using freshly prepared 4% PFA in PBS for 10 minutes at room temperature. Cells were then washed twice with PBS, followed by permeabilization in 0.1% PBS-Tx for 10 minutes at room temperature. Permeabilization buffer was removed before directly adding blocking buffer comprised of 5% BSA and 10% NDS in PBS-Tx, which was incubated with cells for 1 hour at room temperature. After blocking buffer removal, primary antibody combinations were diluted in blocking buffer and incubated with cells at 4°C overnight.

The next day cells were washed thrice with PBS. Fluorescently conjugated secondary antibodies were diluted in blocking buffer and incubated with cells for 1 hour at room temperature. Following three more PBS washes, coverslips were mounted ProLong Diamond Antifade Mountant with DAPI (Invitrogen), and stored at 4°C until imaging.

PRDM12 distribution was initially detected using the Biolegend mouse anti-HA primary antibody. In co-localisation studies, the CST rabbit anti-HA primary antibody allowed for co-staining with marker antibodies generated in mouse. Preliminary co-localisation studies used combinations of secondary antibodies with Alexa Fluor Dyes AF488 and AF546. These were subsequently confirmed with AF488 and AF647 to ensure sufficient separation of excitation and emission spectra, therefore minimising signal bleed-through. Full antibody information is detailed in Table 4.5.

Representative single plane images were acquired on an LSM880 confocal microscope, using the Airyscan detector system and a 63x magnification, planar-apochromatic, 1.4NA oil immersion lens. Laser wavelengths were set at 405, 488, 561 and 633 nm to excite DAPI stain, AF488, AF546 and AF647 dyes respectively. Airyscan image processing and pseudo-colouring was done in ZEN Black and ZEN Blue software (Carl Zeiss).

Table 4.5: Antibodies used for PRDM12 co-localisation studies by immunocytochemistry

Primary Antibodies				
#	**TARGET**	**CAT #, MANUFACTURER**	**SPECIES & CLONALITY**	**DILUTION**
1	Anti-HA	901501, BioLegend	Mouse mAb	1 in 500
2	Anti-HA	C2954, CST	Rabbit mAb	1 in 500
3	Anti-G9a	PP-A8620A-00, R&D Systems	Mouse mAb	1 in 500
4	Anti-SC35	ab11826, Abcam	Mouse mAb	1 in 500
5	Anti-Nucleolin	ab22758, Abcam	Rabbit pAb	1 in 2000
6	Anti-KDEL	ab176333, Abcam	Rabbit mAb	1 in 500
Secondary Antibodies				
#	**TARGET**	**CAT #, MANUFACTURER**	**SPECIES & CLONALITY**	**DILUTION**
7	Anti-Mouse IgG AF488	A-21202, Invitrogen	Donkey pAb	1 in 1000
8	Anti-Rabbit IgG AF488	A-21206, Invitrogen	Donkey pAb	1 in 1000
9	Anti-Mouse IgG AF546	A10036, Invitrogen	Donkey pAb	1 in 1000
10	Anti-Rabbit IgG AF546	A10040, Invitrogen	Donkey pAb	1 in 1000
11	Anti-Mouse IgG AF647	A-31571, Invitrogen	Donkey pAb	1 in 1000
12	Anti-Rabbit IgG AF647	A-31573, Invitrogen	Donkey pAb	1 in 1000

4.3.6 – PRDM12 Localisation Studies Using High-Content Widefield Imaging

HEK293 cells were transfected by reverse transfection in PDL-coated, 96-well imaging plates (Thermo Scientific). Transfection complexes were prepared as above in Section 4.3.5, although the recommended protocol from the FuGENE HD Protocol Database was adapted and confirmed to have sufficient transfection efficiency in pilot studies – 100 ng DNA for 5,000 cells per well. The immunocytochemistry protocol followed as above in Section 4.3.5 up to the primary antibody stage.

The rabbit anti-HA primary antibody (CST) was incubated with cells at 4°C overnight. The next day, cells were washed thrice with PBS and incubated sequentially with fluorescent stains, each step at room temperature and protected from light, with three PBS washes between staining incubations. The first fluorescent incubation was with anti-rabbit AF488 for 1 hour. The second incubation was with HCS CellMask Deep Red Stain (Invitrogen) for 30 minutes, freshly prepared at 2 μg/ml in PBS. The final incubation was with Hoechst 33342 nucleic acid stain (Invitrogen) for 15 minutes, also freshly prepared at 2 μg/ml in PBS. After three final PBS washes, PBS was added to all wells and plates were stored covered in foil at 4°C until imaging. Plates were brought to room temperature at least 30 minutes before imaging.

For unbiased, high-throughput image acquisition, the ImageXpress Micro XLS Widefield High-Content Analysis System (Molecular Devices) was used. Site images were acquired using a planar-apochromatic objective at 60x magnification, with DAPI, FITC and Cy5 imaging channels set to detect Hoechst stain, AF488 and CellMask Deep Red Stain respectively.

Using the Multiwavelength Scoring Module in MetaXpress image analysis software (Molecular Devices), fluorescence and area thresholds were adjusted to create segmentation masks of different cell compartments; Hoechst for the nucleus and CellMask for the whole cell, but from which the cytoplasm could be isolated by subtraction. In every image, each cell was individually counted using the nuclear mask and then marked as positive or negative for transfection using the “Cell Positive: W3” setting which measures whole cell fluorescence in the FITC channel (i.e., from AF488 secondary antibody). The total pixel intensity in the FITC channel was then measured within the masked areas for the nucleus versus cytoplasm.

Raw data was exported to Microsoft Excel for further processing; all site images were reviewed manually to remove out of focus sites which produced segmentation artefacts, and then individual cells were sorted based on their “Cell Positive: W3” score so that untransfected cells were excluded.

For each transfected cell, AF488 fluorescence in the cytoplasm was divided by that in the nucleus to generate a C:N ratio. Statistical analysis was conducted in GraphPad Prism where mean average C:N ratios per genotype were compared using a one-way ANOVA. Statistical significance between groups was assessed by the Kruskal-Wallis test with alpha threshold set to $P < 0.05$ and corrected for multiple comparisons using Dunn's test.

4.4 RESULTS

4.4.1 – MiTES cases and results of *PRDM12* sequencing

Several patients with a formal diagnosis of MiTES were referred to our lab for Sanger sequencing of *PRDM12*. Pedigrees of families tested are illustrated in Figure 4.6 and clinical features are described for each case in Table 4.6. In almost all cases, affected individuals were homozygous for a polyalanine tract expansion to 18 alanines (18A/18A), with one mutant allele inherited from each heterozygous parent. C22 was an affected paternal uncle of index case C21, both of whom were homozygous 18A/18A, but DNA from earlier generations was not available for testing. C14 was the only exception in whom no *PRDM12* mutations were found in any exon and their polyalanine tract was homozygous 12A/12A which is within the normal range.

Initial inspection of the chromatograms for the C10-C11 sib-pair looked as if they were homozygous for 18 alanines as there was no apparent frameshift which is observed when the two alleles differ in length – this type of frameshift is demonstrated in Figure 4.7A, preceding the red dashed line in the heterozygous parents. Upon sequencing the parents, the mother was found to be heterozygous 13A/18A as expected but the father was seemingly homozygous for 7 alanines. After confirming that sample mix-up and non-paternity did not explain the result, this suggested that either the second 18A allele occurred as a de novo expansion in both children independently, or that there was a deletion in a portion of the paternal *PRDM12* allele which both children had inherited.

Sequencing of a microsatellite repeat in intron 3 by Mike Nahorski revealed normal segregation of alleles at least up to this position, but further analysis to prove the presence of a deletion and the location of the breakpoint was impossible due to the GC-rich content of exon 5[483]. Nevertheless, the most likely conclusion was the father being hemizygous in part of *PRDM12* between intron 3 and the end of the gene, and this partial gene deletion was the allele inherited by both children. This would mean the only full-length PRDM12 protein they expressed contained the 18A polyalanine tract expansion, which is consistent with an autosomal recessive pattern of inheritance in *PRDM12*-MiTES.

A notable finding from these sequencing studies was the refinement of the polyalanine boundary between normal and pathogenic. The unaffected mother of sib-pair C19 and C20 was heterozygous 15A/18A, which is the longest polyalanine tract length in a healthy individual observed to date Figure 4.7B. Careful physical examination and review of her medical history affirmed she had never experienced any symptoms associated with MiTES, and due to the clear segregation of *PRDM12* expansion mutations within this family and others, we concluded 15 alanines was not pathogenic.

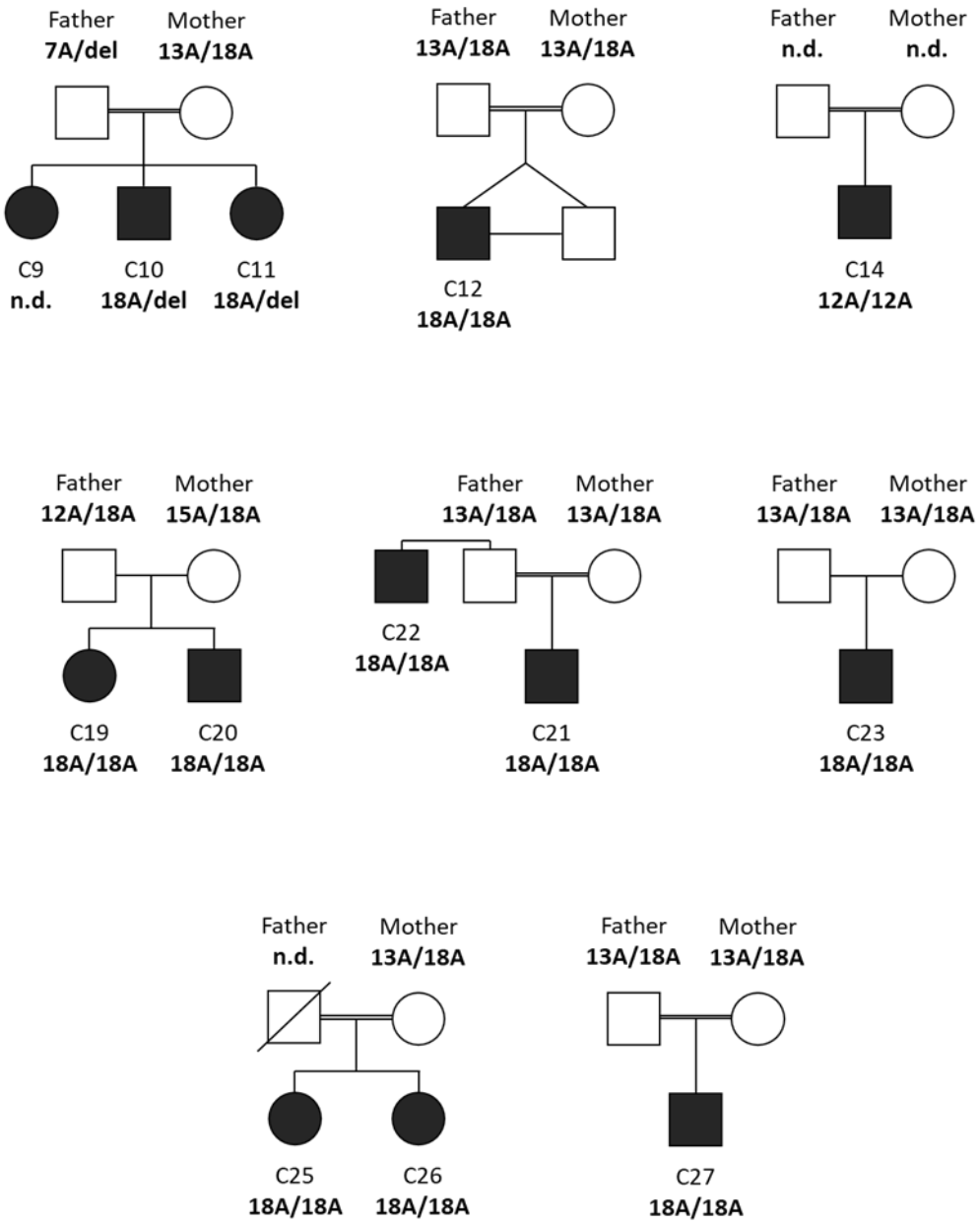

Figure 4.6: MiTES case pedigrees screened for *PRDM12* mutations in the Woods laboratory
DNA was obtained from affected cases with a formal diagnosis of MiTES to be screened for mutations in the *PRDM12* gene. Genetic pedigrees are illustrated above with detailed family histories and results published for C9-C14 in (2018) Moss et al. and for C19-C23 in (2019) Inamadar et al.; C25-C27 are unpublished.

Table 4.6: Reported MiTES cases with phenotype-genotype information

n.a.: not applicable; **n.d.:** not determined; **#A:** total number of alanine residues in exon 5 polyalanine tract

PUBLICATION	CASE	FAMILIAL RELATIONS	COUNTRY OF ORIGIN	AGE AT ONSET	OTHER NOTABLE FEATURES	PARENTAL CONSANGUINITY	CASE: PRDM12 GENOTYPE	MATERNAL: PRDM12 GENOTYPE	PATERNAL: PRDM12 GENOTYPE
(2014) Watson	1	Siblings: 1 & 2 Father: 3	Ireland	Infancy	• Absent tendon reflex	Unknown	n.a. SCN11A missense mutation	n.a.	n.a.
	2			Infancy	• Absent tendon reflex • Pressure sore				
	3			Childhood	• Charcot joints • Pain insensitivity	Unknown			
(2015) Chen	4	Siblings: 4, 5, 6, 7, 8	Ireland	3 months	• Pain insensitivity (all) • Foot ulcers (all) • Hypoesthesia (all) • Abnormal sensory nerve conduction (cases 4, 5, 6)	No	18A / 18A	18A / WT	18A / WT
	5			3 months			18A / 18A		
	6			3 months			18A / 18A		
	7			6 months			18A / 18A		
	8			6 months			18A / 18A		
(2018) Moss	9	Siblings: 9, 10, 11	India	9 months	None	Yes	18A / deletion	13A / 18A	7A / deletion
	10			4 months			18A / deletion		
	11			3 months			n.d.		
	12	Cousins: 12 & 13	India	9 months	None	Yes	18A / 18A	13A / 18A	13A / 18A
	13			Childhood	None	Unknown	n.d.	n.d.	n.d.
	14	Single case	India	1 year	• Developmental delay • Pain insensitivity	Yes	12A / 12A	n.d.	n.d.
	15	Single case	Ireland	1 year	• Delayed speech • Pain insensitivity	No	17A / 18A	n.d.	n.d.
	16	Single case	India	1 year	• Developmental delay	No	n.d.	n.d.	n.d.
	17	Single case	India	6 months	None	Yes	n.d.		
	18	Single case	Pakistan	9 months	None	Yes	n.d.	n.d.	n.d.
(2019) Inamadar	19	Siblings	India	6 months	None	No	18A / 18A	15A / 18A	12A / 18A
	20			6 months			18A / 18A		
	21	Nephew: 21 Uncle: 22	India	7 months	None	Yes	18A / 18A	13A / 18A	13A / 18A
	22			Early childhood	None	Yes	18A / 18A	n.d.	n.d.
	23	Single case	UK	10 months	• High pain threshold	No	18A / 18A	13A / 18A	13A / 18A
(2020) Noguera-Morel	24	Single case	Spain	9 months	• High pain threshold	No	16A / 18A	n.d.	n.d.
Unpublished	25	Siblings: 25 & 26	India	Early childhood	• Pain insensitivity in hands (both siblings)	Yes	18A / 18A	13A / 18A	deceased
	26			Early childhood			18A / 18A		
	27	Single case	India	1 year	None	Yes	18A / 18A	13A / 18A	13A / 18A
(2021) Kumar	28	Single case	India	11 months	None	No	n.d.	n.d.	n.d.

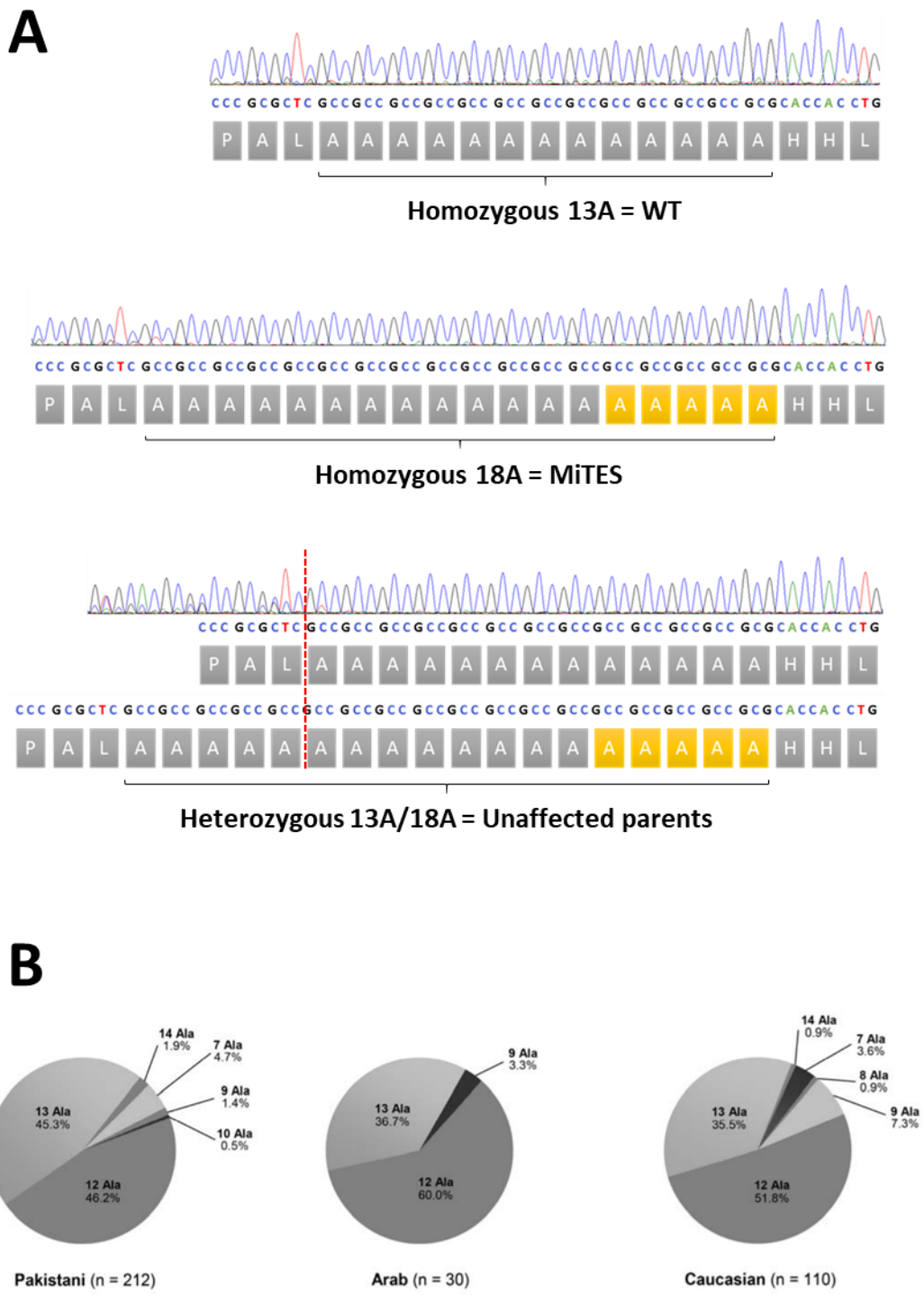

Figure 4.7: *PRDM12*-MiTES exhibits a clear correlation with polyalanine tract expansion
(A) Example chromatogram traces illustrate the GC-rich content of the polyalanine tract in exon 5. Reading the genetic sequence is relatively easy when polyalanine tract length is homozygous, however where a frameshift occurs due to polyalanine tract length differing between two alleles (e.g., in heterozygous parents of an affected child), careful assignment of nucleotides at each site is required. (B) The length of the PRDM12 polyalanine tract in healthy individuals from different ethnic populations ranges from 7 to 14 alanines – taken from (2015) Chen et al..

4.4.2 – Subcellular expression patterns of PRDM12 in HEK293 cells

HA-tagged PRDM12 fusion constructs were transiently transfected into HEK293 cells to investigate differences in subcellular localisation between wild-type (12A), MiTES (18A) and CIP (19A) forms of PRDM12 protein. In all three genotypes, low-expressing cells produced a low intensity, homogeneous staining of the nucleus, as displayed in Figure 4.8. This was the predominant cellular phenotype in the WT condition, occasionally combined with very low-level diffuse staining in the cytoplasm. Remarkably, in a small proportion of WT-expressing cells, PRDM12 appeared to condense into non-DAPI stained regions of the nucleus as seen in Figure 4.8C-D.

Expression of the 18A and 19A constructs produced a spectrum of cellular phenotypes, including prominent bright nuclear aggregates of increasing size and cytoplasmic mis-localisation. Neither of these phenotypes were ever seen in WT-transfected cells. In contrast to WT PRDM12 condensates, the fluorescence intensity of 18A and 19A nuclear aggregates were stronger and did not specifically localise to non-DAPI stained spaces, as shown in Figure 4.9A-B and 4.10A-B. This pattern was broadly similar between both mutant constructs, however where nuclear spots of similar size were expressed, 19A-transfected cells appeared to have less diffuse expression of PRDM12 in the nucleoplasm, as though more protein had been drawn up into these aggregates (see Figure 4.10A-D). Mutant PRDM12 localised in the cytoplasm formed fibril-like patterns extending from the nuclear envelope to the cell perimeter with small clumps as shown in (Figure 4.9C and 4.10C). In more dramatic cases, mutant PRDM12 protein formed larger plaques in the nucleus and cytoplasm, see (Figure 4.9D and 4.10D).

The proportion of abnormal cellular phenotypes in 18A versus 19A expressed PRDM12 was not obviously different between the two mutations, and a tile-scan of a larger field of view in 18A-transfected HEK293 cells (see Figure 4.11) shows these are not rare artefacts. Rather than scoring cell phenotypes by eye and comparing their prevalence between genotypes, an image segmentation analysis approach was taken to make unbiased measurements of cytoplasmic mis-localisation.

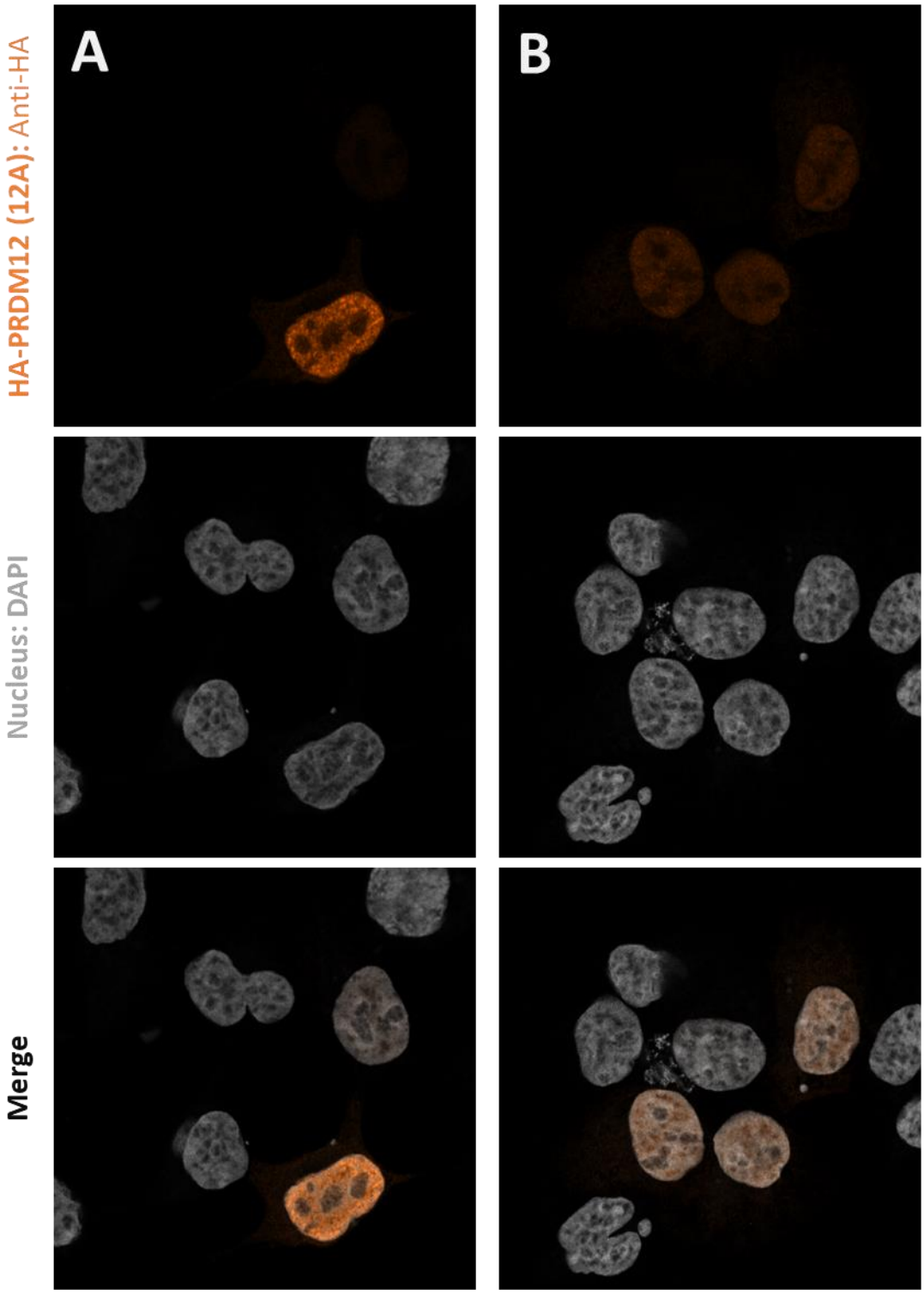

Figure 4.8: PRDM12-12A was predominantly expressed in the nucleus with possible condensates
(A – B) WT PRDM12 was expressed diffusely in the nucleus, with very low-level staining visible in the cytoplasm of transfected cells. (C – D, on next page) In some cells, WT PRDM12 condensed into nuclear cavities that were not stained by DAPI (i.e., DNA-poor regions).

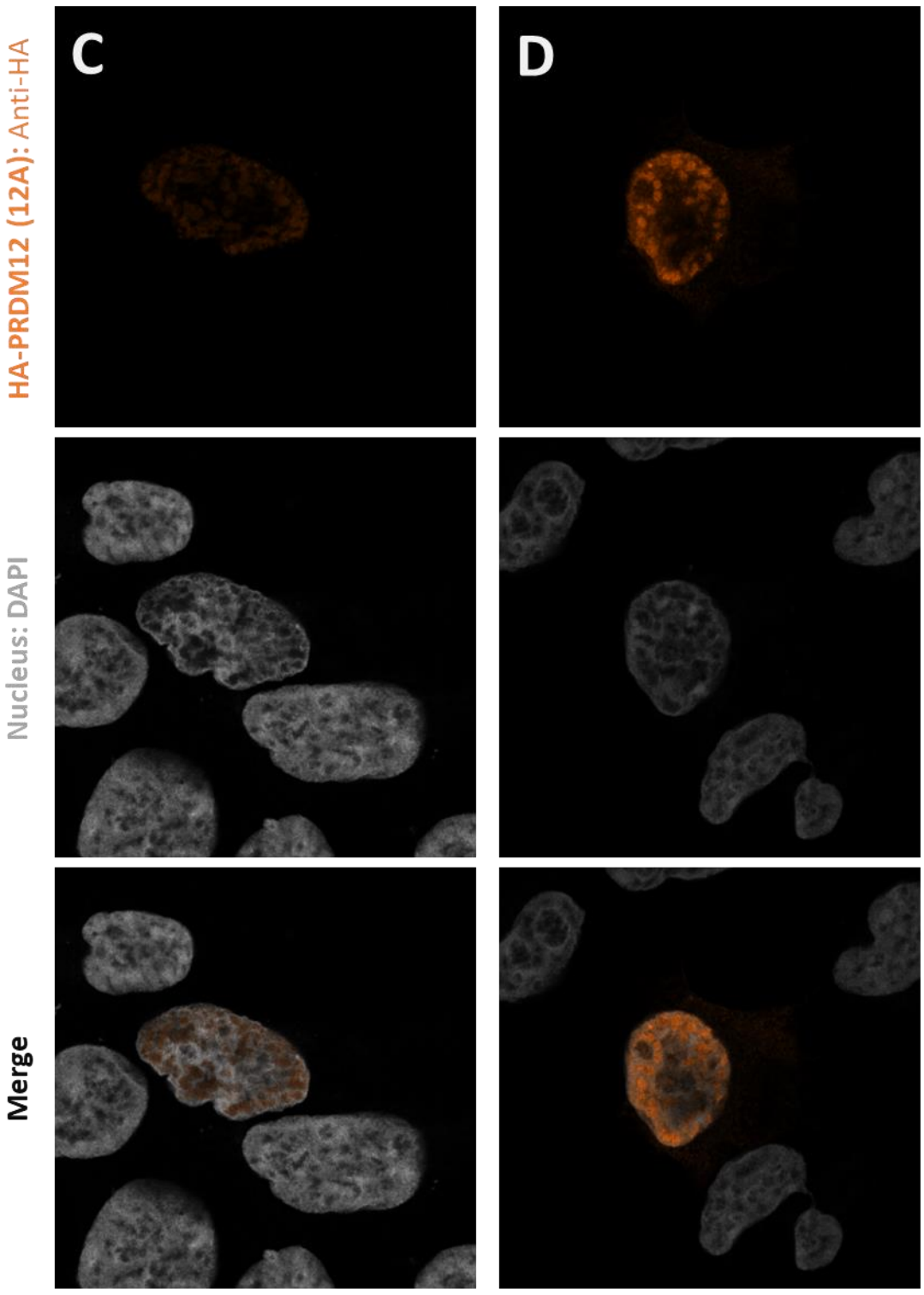

Figure 4.8: PRDM12-12A was predominantly expressed in the nucleus with possible condensates (A – B, on previous page) WT PRDM12 was expressed diffusely in the nucleus, with very low-level staining visible in the cytoplasm of transfected cells. (C – D) In some cells, WT PRDM12 condensed into nuclear cavities that were not stained by DAPI (i.e., DNA-poor regions).

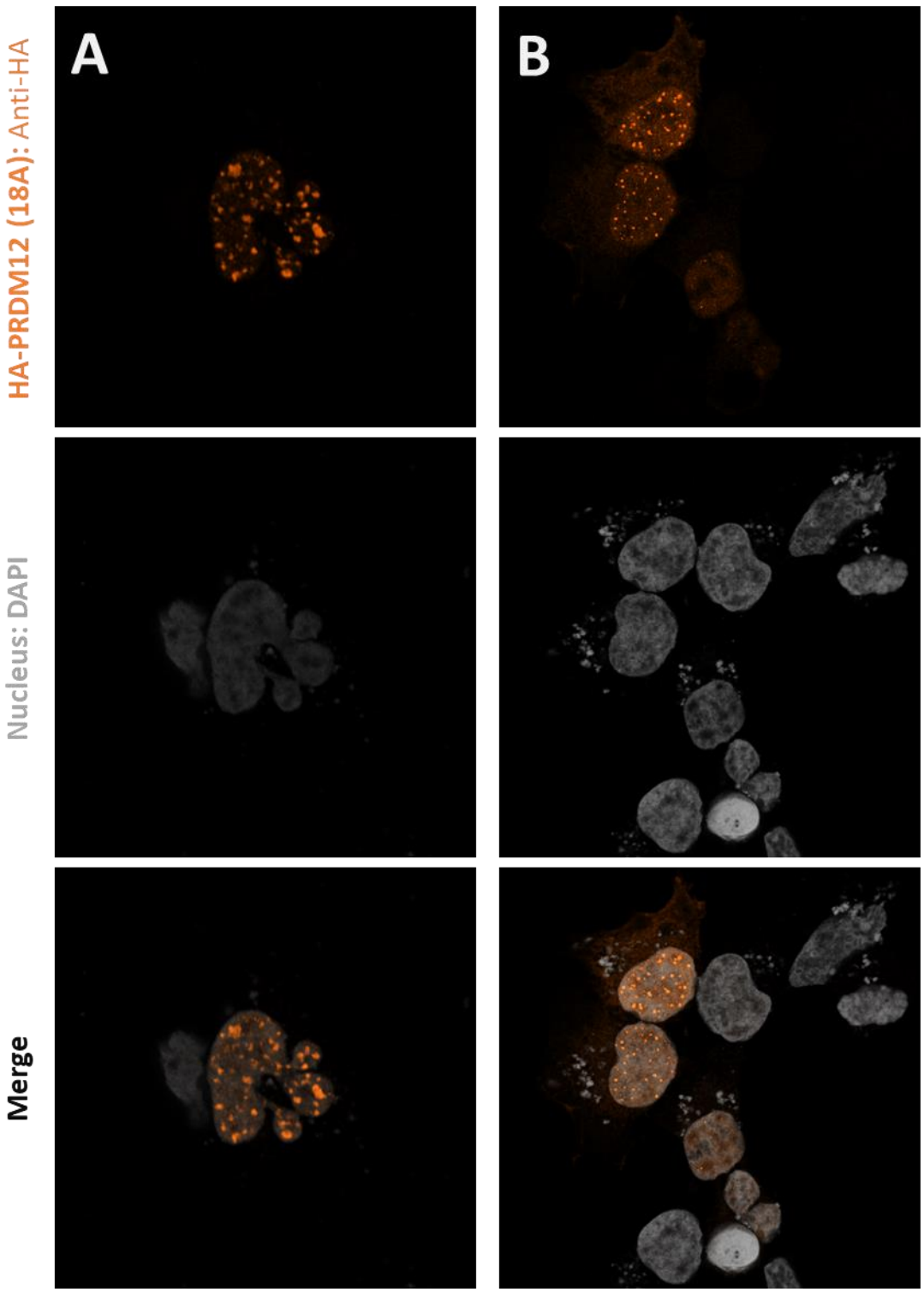

Figure 4.9: PRDM12-18A localisation ranged from bright nuclear spots to cytoplasmic plaques
(A – B) The PRDM12-18A construct, representing the MiTES condition, produced small but bright nuclear aggregates in addition to diffuse nuclear staining. (C – D, on next page) Larger aggregates were seen in the nucleus and cytoplasm of other cells, as well as cytoplasmic fibrils and plaques.

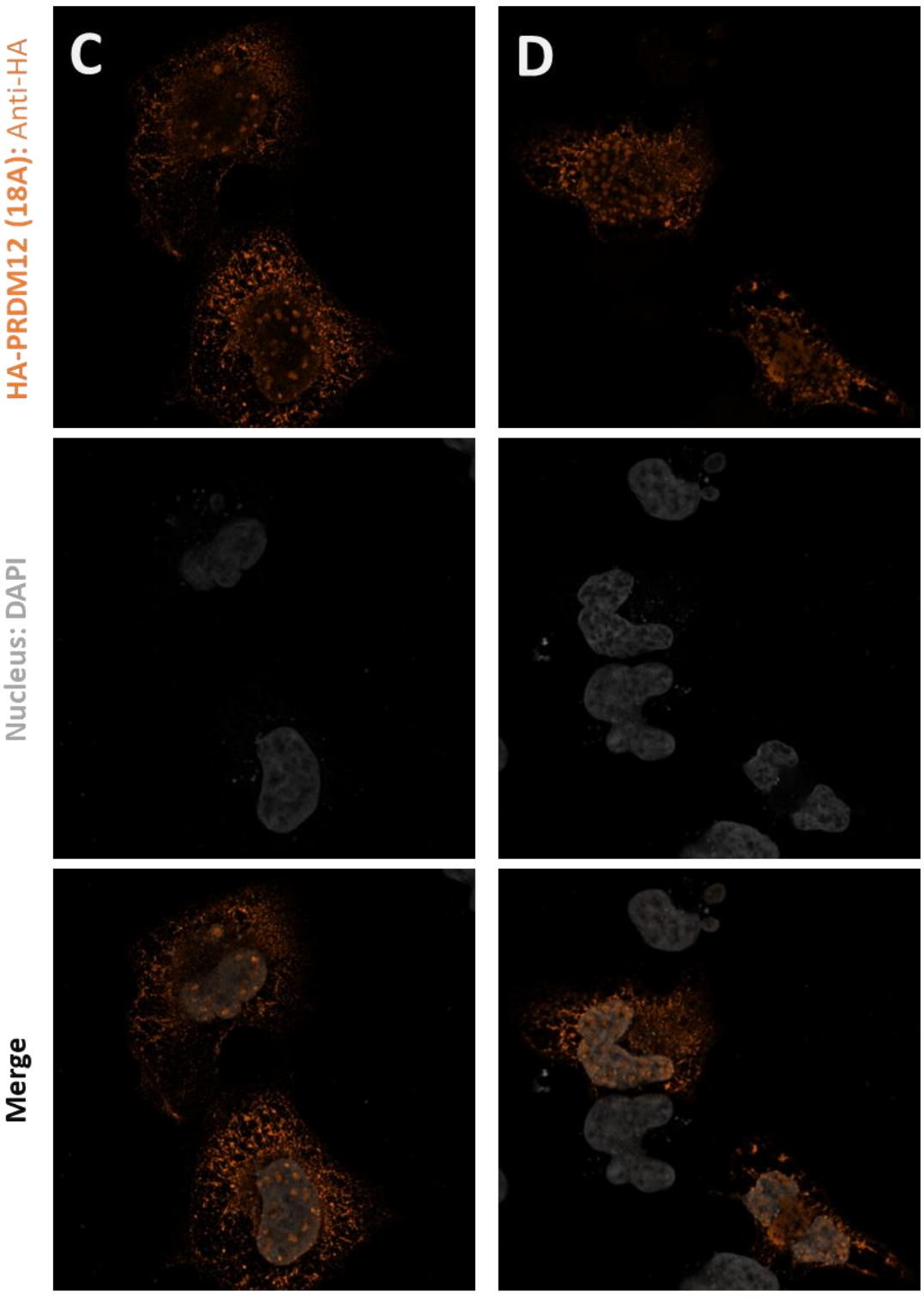

Figure 4.9: PRDM12-18A localisation ranged from bright nuclear spots to cytoplasmic plaques
(A – B, on previous page) The PRDM12-18A construct, representing the MiTES condition, produced small but bright nuclear aggregates in addition to diffuse nuclear staining. (C – D) Larger aggregates were seen in the nucleus and cytoplasm of other cells, as well as cytoplasmic fibrils and plaques.

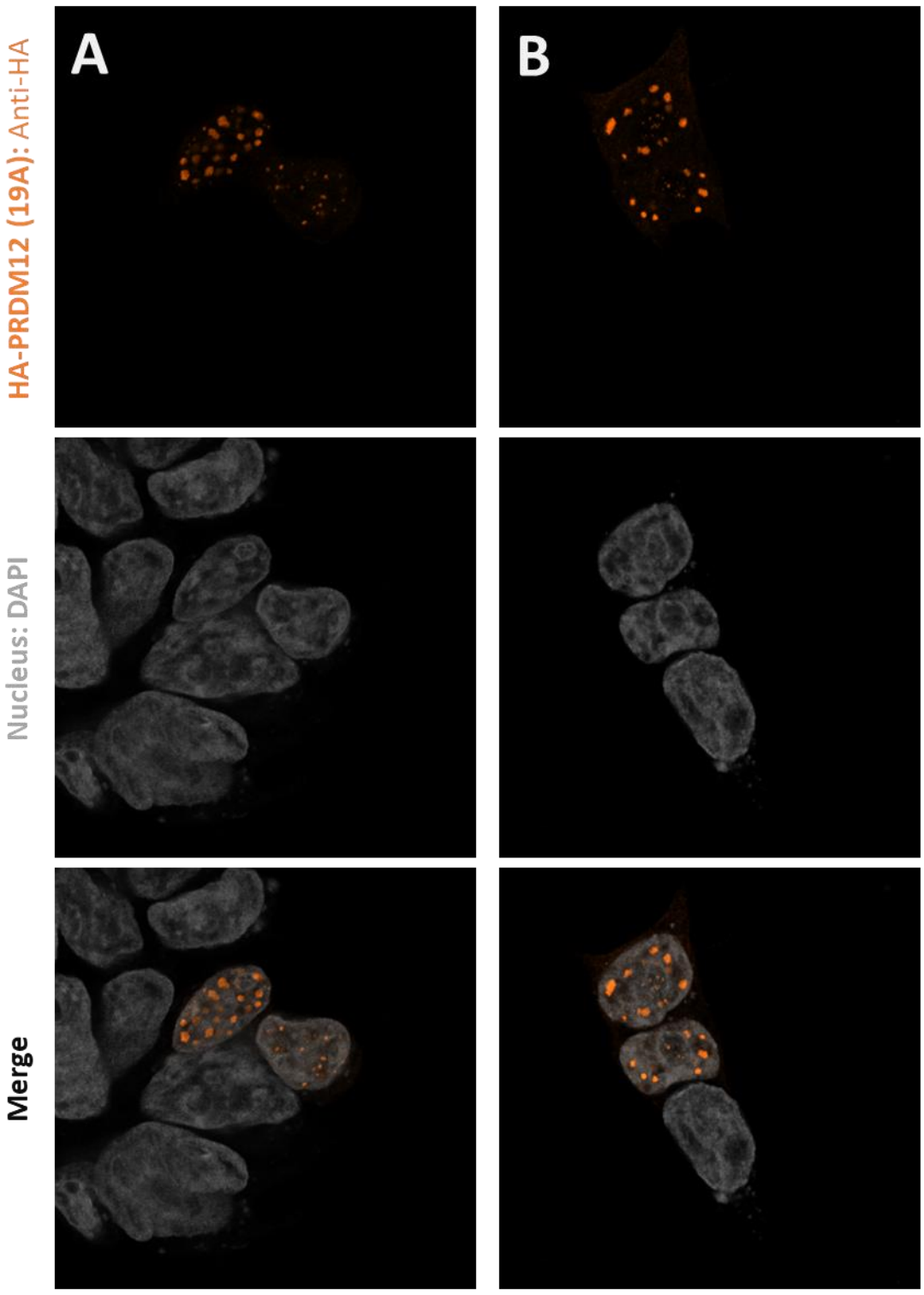

Figure 4.10: PRDM12-19A subcellular expression was similar to PRDM12-18A
(A – B) The PRDM12-19A construct, representing the CIP condition, produced similarly bright nuclear aggregates as observed with the 18A construct, as well as cytoplasmic fibrils and plaques (C – D, on next page). The intensity of non-aggregated PRDM12 in the nucleoplasm was lower here than in 18A-transfected cells, suggesting more protein was taken up into the aggregates.

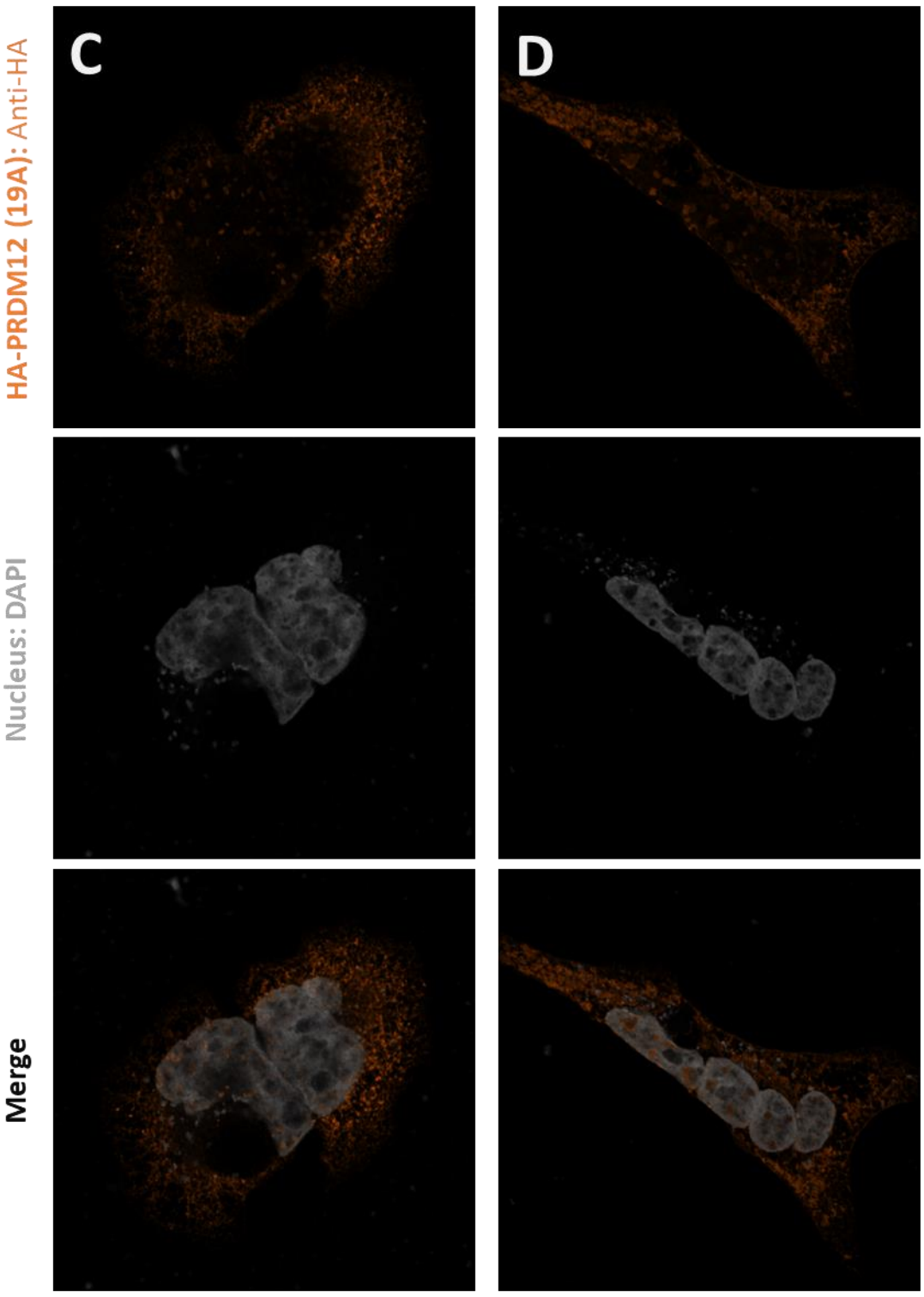

Figure 4.10: PRDM12-19A subcellular expression was similar to PRDM12-18A
(A – B, on previous page) The PRDM12-19A construct, representing the CIP condition, produced similarly bright nuclear aggregates as observed with the 18A construct, as well as cytoplasmic fibrils and plaques (C – D). The intensity of non-aggregated PRDM12 in the nucleoplasm was lower here than in 18A-transfected cells, suggesting more protein was taken up into the aggregates.

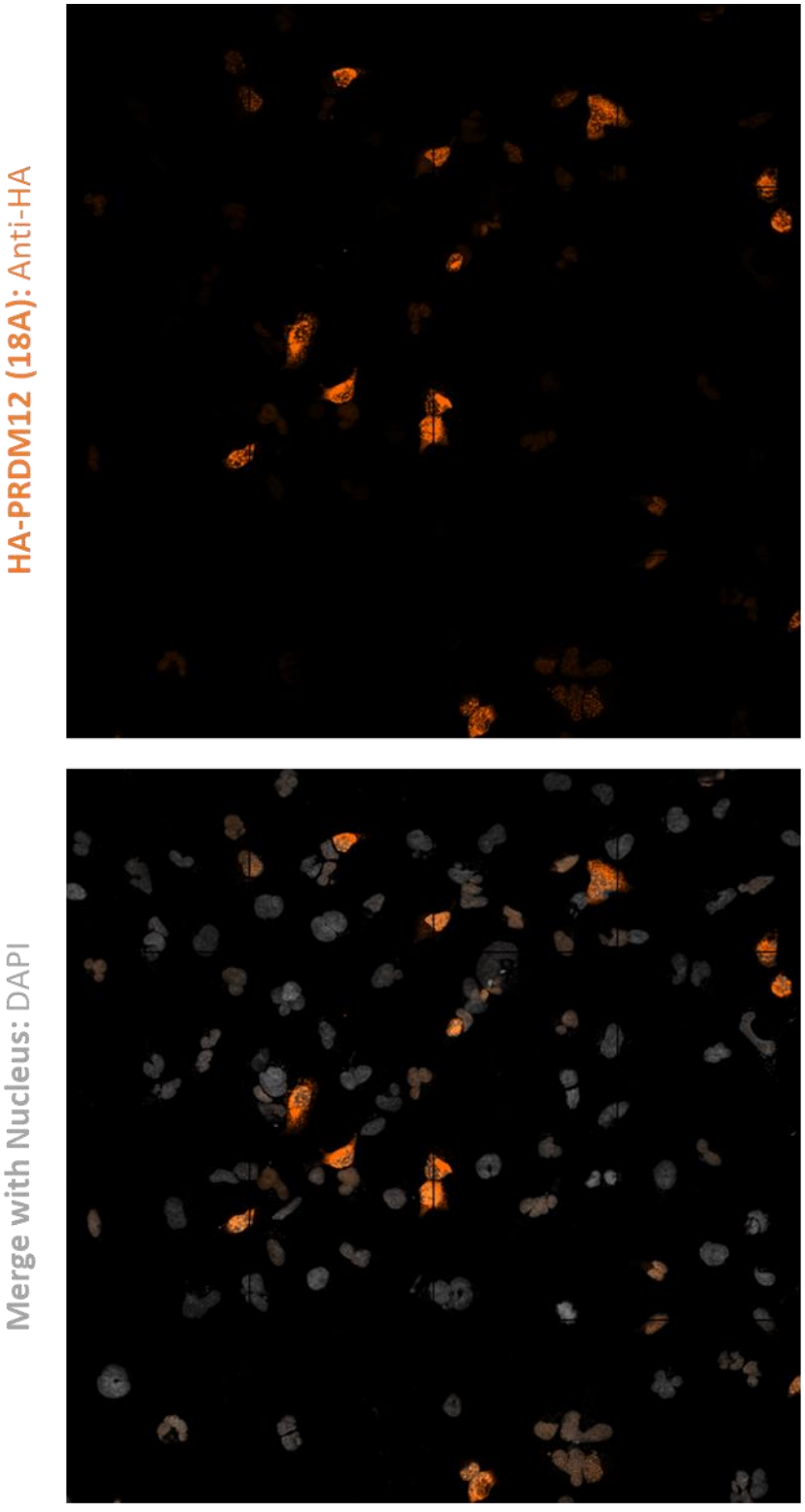

Figure 4.11: Spectrum of cellular phenotypes exhibited by PRDM12-18A
A confocal tile scan of transiently transfected PRDM12-18A in HEK293 cells confirmed the spectrum of cellular phenotypes from homogeneous nuclear staining with or without small nuclear spots, to dramatic cytoplasmic fibrils. Neither of these phenotypes were rare artefacts.

4.4.3 – Quantification of PRDM12 cytoplasmic mis-localisation

Automated image acquisition and analysis was undertaken to assess the magnitude of PRDM12 mis-localisation between WT and mutant genotypes. Figure 4.12A illustrates the image segmentation principles that defined the nucleus from the cytoplasm, allowing separate measurements of PRDM12 intensity in each compartment per cell. The average cytoplasmic to nuclear (C:N) signal intensity ratio was calculated for each transfection condition and presented in Figure 4.12B – 12A: 1.14 ± 0.04, n=378 versus 18A: 1.49 ± 0.08, n=282 versus 19A: 1.59 ± 0.06, n=336. Comparisons of C:N ratios between WT and each mutant were highly significant (p = < 0.001), but the difference between 18A and 19A C:N ratios was not statistically significant (p = 0.101). This assay supported previous observations by providing quantitative evidence of cytoplasmic mis-localisation when pathogenic PRDM12 mutants were expressed in HEK293 cells.

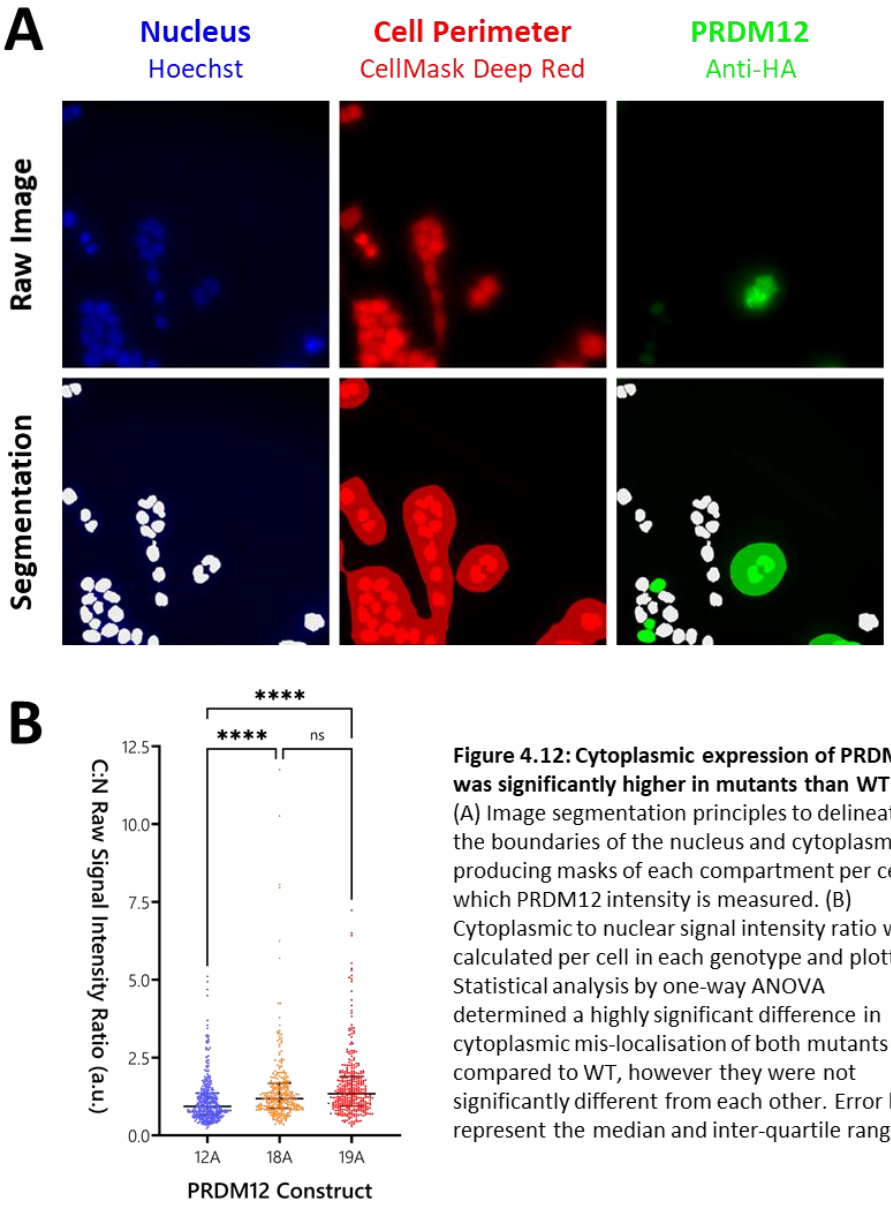

Figure 4.12: Cytoplasmic expression of PRDM12 was significantly higher in mutants than WT
(A) Image segmentation principles to delineate the boundaries of the nucleus and cytoplasm, producing masks of each compartment per cell in which PRDM12 intensity is measured. (B) Cytoplasmic to nuclear signal intensity ratio was calculated per cell in each genotype and plotted. Statistical analysis by one-way ANOVA determined a highly significant difference in cytoplasmic mis-localisation of both mutants compared to WT, however they were not significantly different from each other. Error bars represent the median and inter-quartile range.

4.4.4 – Co-localisation studies with ER and nuclear proteins

The final set of microscopy studies sought to rule in or out a number of hypotheses that could hint at different mechanisms of pathogenicity behind the two polyalanine expansion mutations. PRDM12 recruits the histone methyltransferase G9a to exert its regulatory effects on histones and gene expression[399]. Interaction between the two proteins is dependent on the PRDM12 zinc finger domains upstream of the polyalanine tract, and has been shown to be disturbed by a missense mutation in this domain, resulting in lowered histone methylation levels in the developing *Xenopus* neurula[123]. As these assays were not tested on the polyalanine expansion mutations, co-staining of G9a and PRDM12 in transfected cells was performed as a simple test to see if mutant PRDM12 expression was accompanied by a change in G9a distribution that might be different between the 18A and 19A mutants. Figure 4.13 shows endogenous G9a levels were low in untransfected HEK293 cells, but fluorescence intensity increased with exogenous expression of PRDM12. G9a staining was always homogeneous and slightly granular in the nucleus, but was never concentrated into WT PRDM12 condensates or mutant PRDM12 aggregates. These results indicate aggregation of PRDM12 polyalanine expansion mutants does not affect G9a localisation.

The nucleus can be further organised into membrane-less subnuclear bodies that compartmentalize factors involved in different cell functions, e.g., splicing factor storage in nuclear speckles and ribosome biogenesis in nucleoli[506]. Expansions of polyalanine tracts in nuclear-targeted proteins have been shown to cause abnormal co-localisation or de-localisation with splicing speckles, as observed with RBM4[507] and PABPN1[508] respectively. PRDM12-transfected HEK293 cells were thus co-stained with markers of nuclear speckles (SC35) and nucleoli (nucleolin), to see if WT and mutant PRDM12 differentially associated with these compartments. It is well known that nucleoli are not stained with DAPI or Hoechst due to low DNA-density, and so this region was of particular interest in localising WT PRDM12 condensates. Figures 4.14-15 reveal that all forms of PRDM12 were spatially separate to nuclear speckles and nucleoli, and this lack of association was not altered by any genotype. Therefore, selective disturbance of these functions in nociceptive neurons is unlikely to be a pathogenic mechanism behind PRDM12 polyalanine expansion mutations.

The cytoplasmic mis-localisation was previously observed for the 19A expansion mutant in HEK293T cells, and both 18A and 19A PRDM12 mutants were shown to be less stable than WT PRDM12 when expressed in COS-7 cells, the difference being recovered upon proteasome inhibition[123]. In support of this hypothesis, Figure 4.16 shows the intracellular staining of mutant PRDM12 is distinct from the ER marker KDEL, indicating mutant PRDM12 is not retained in the ER due to misfolding.

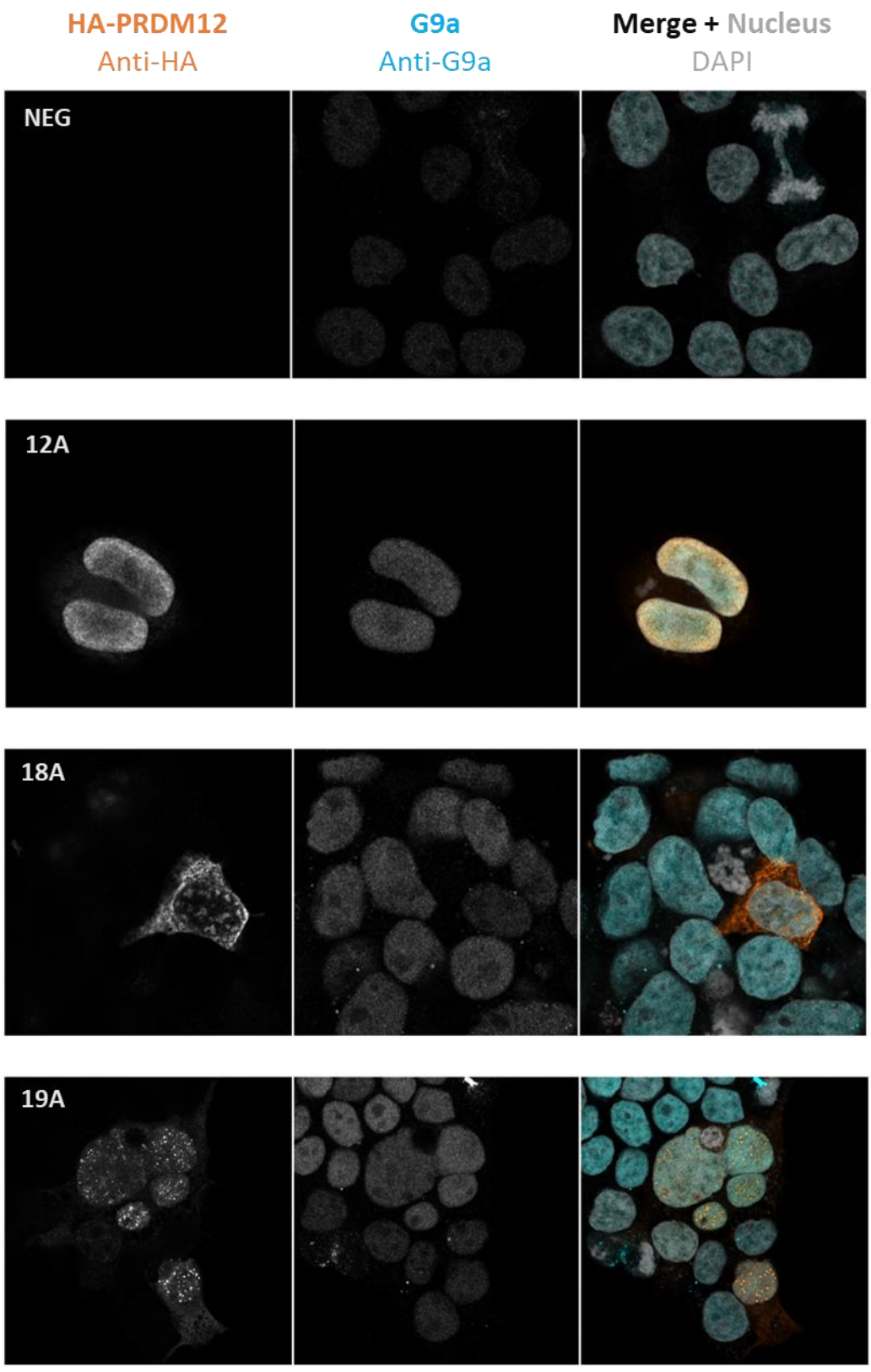

Figure 4.13: PRDM12 aggregates did not affect the distribution of endogenous G9a
Endogenous G9a expression was low in untransfected HEK293 cells but appeared to be up-regulated after transfection of PRDM12 constructs. In all cases, G9a maintained a homogeneous, slightly granular distribution in the nucleus which was not disturbed in the presence of PRDM12 aggregates.

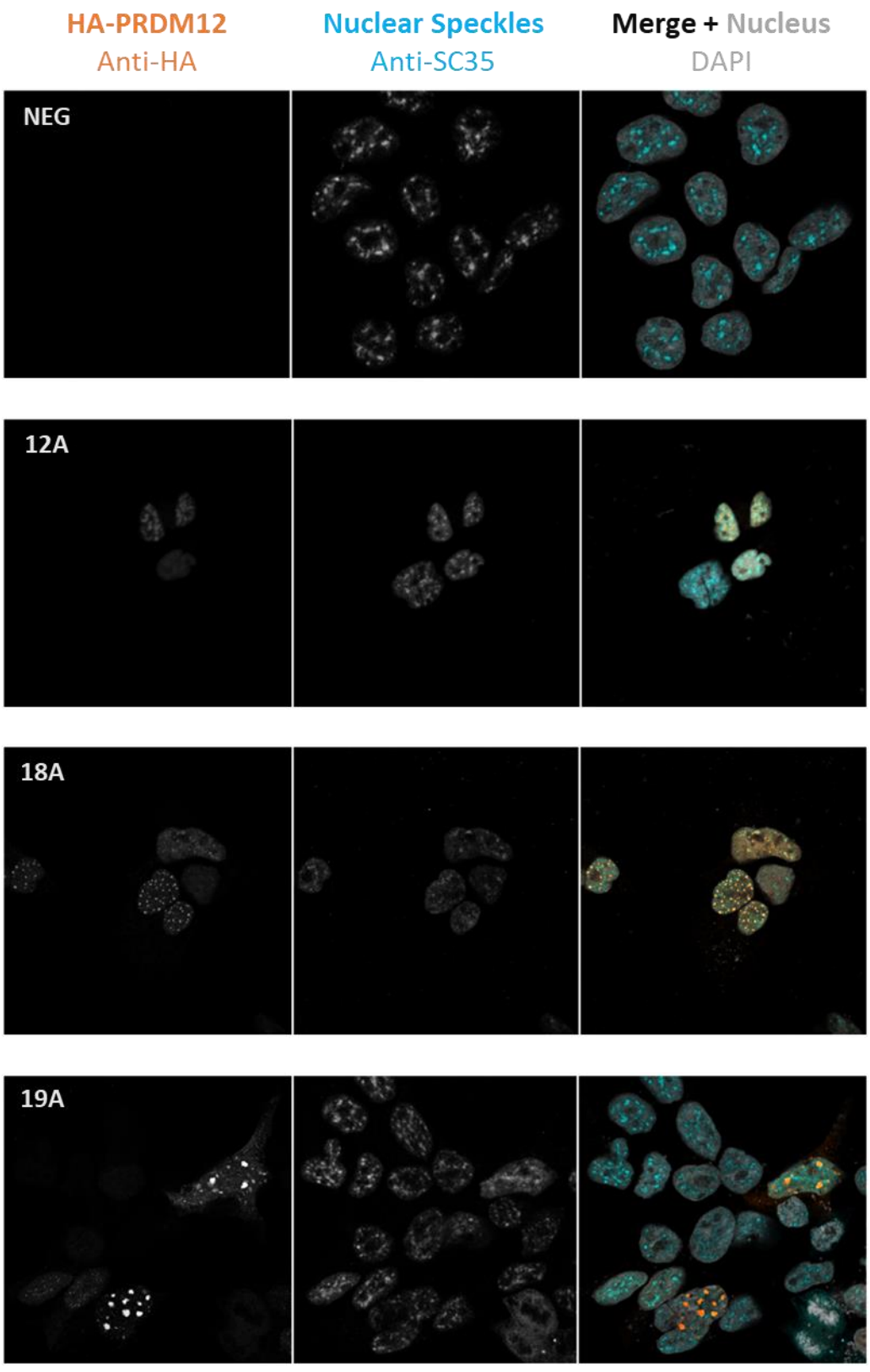

Figure 4.14: WT and mutant PRDM12 foci did not associate with nuclear speckles
Both WT PRDM12 condensates and mutant PRDM12 aggregates remained spatially separated from SC35, a marker protein of nuclear speckles.

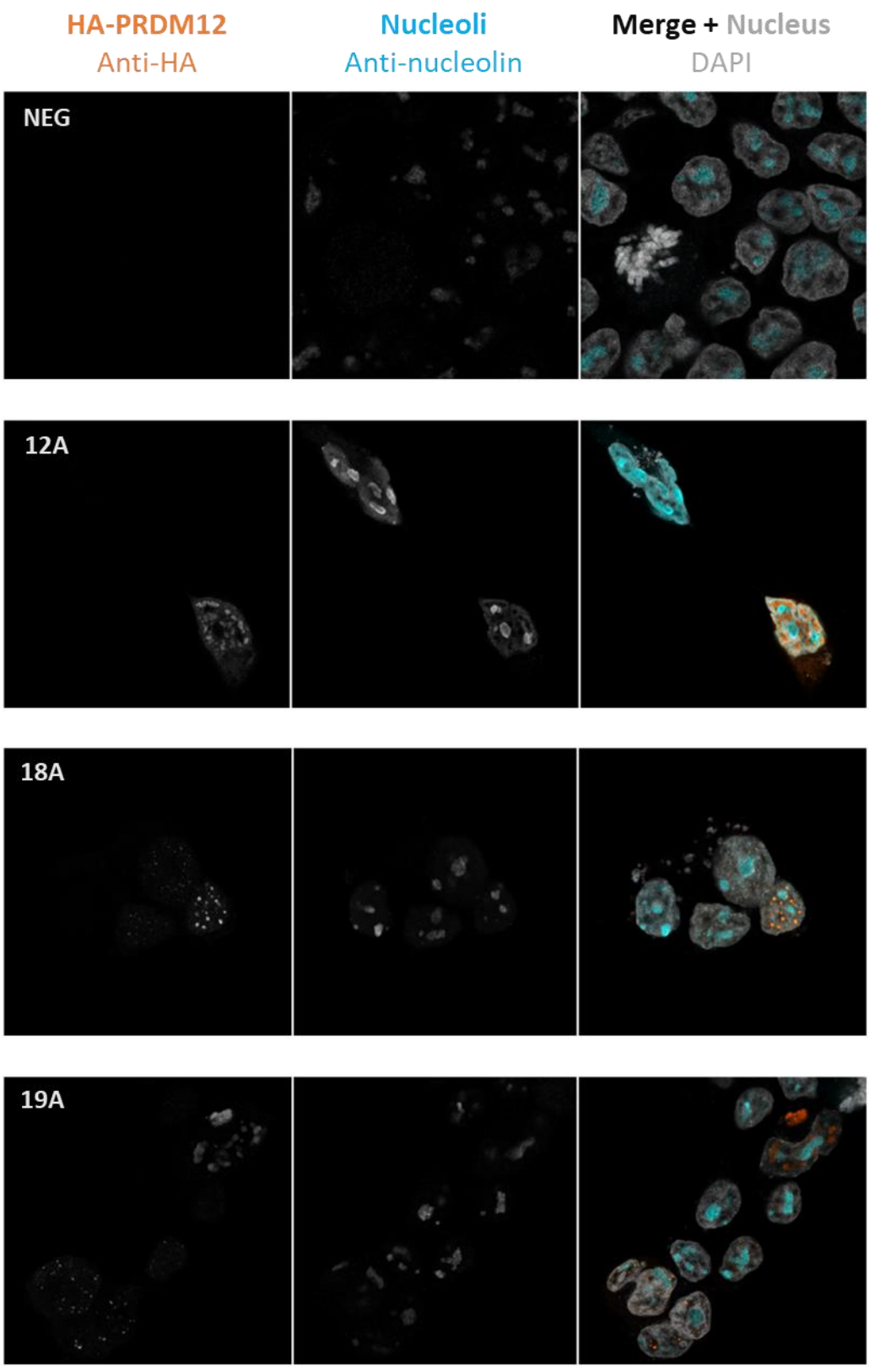

Figure 4.15: WT and mutant PRDM12 foci did not localise within the nucleolus
Both WT PRDM12 condensates and mutant PRDM12 aggregates were spatially separate from nucleolin, a marker protein of nucleoli.

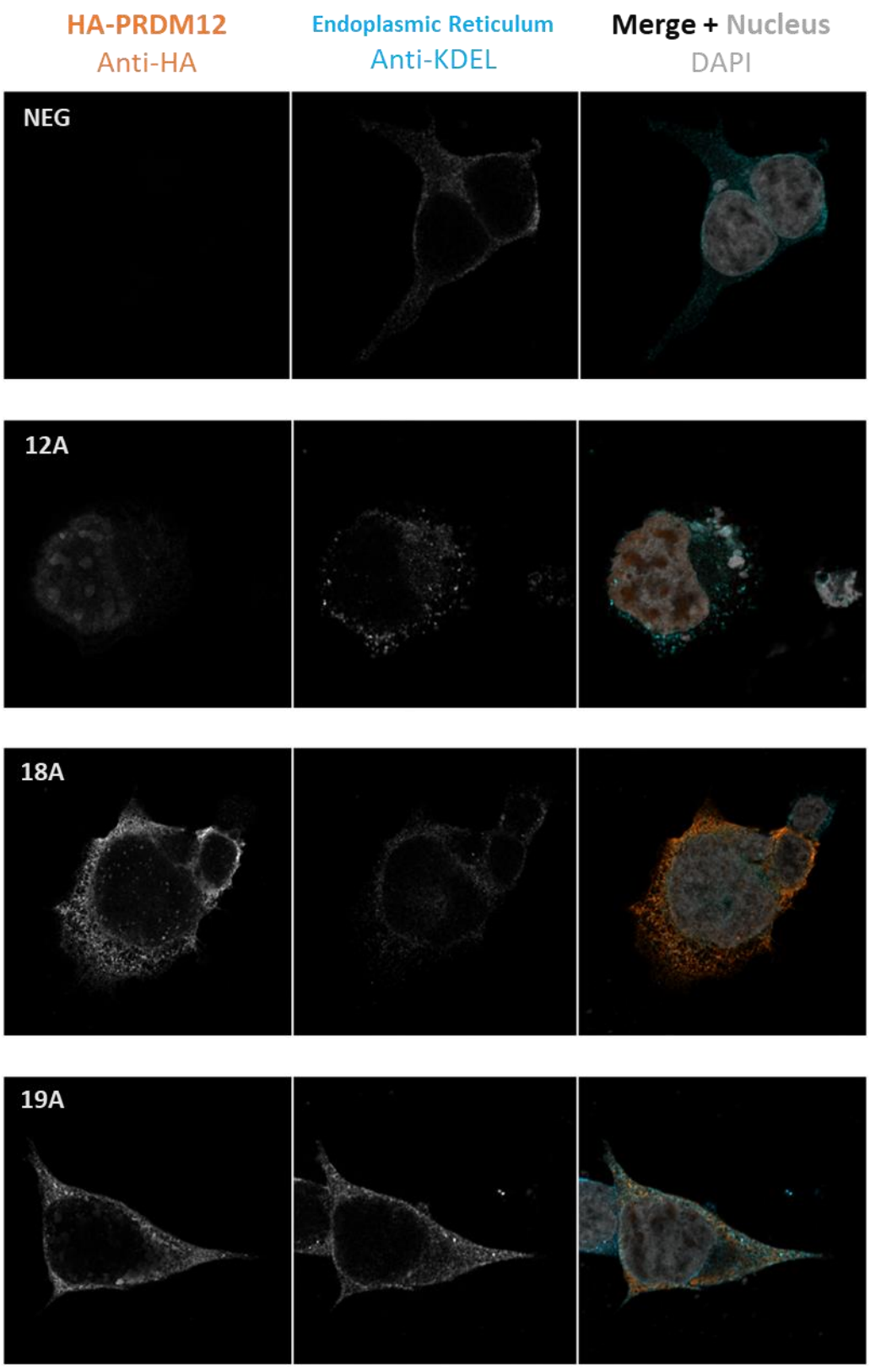

Figure 4.16: Cytoplasmic mutant PRDM12 was not retained in the ER
Where 18A and 19A PRDM12 constructs mis-localized to the cytoplasm, they displayed similar granular staining as KDEL, an ER marker. However, merging these two images revealed the puncta were discriminate from each other suggesting PRDM12 aggregates were not misfolded in the ER.

4.5 DISCUSSION

Through this project we found a consistent genotype-phenotype correlation between MiTES and homozygous expansions in the polyalanine tract of PRDM12 within the range of 16-18 alanines. These results confirm MiTES is a distinct congenital sensory disorder which can be distinguished from other neurological or infectious causes of chronic itch, or from fabricated illness, based on clinical presentation and genetic testing for this specific type of *PRDM12* mutation. However, MiTES may be a genetically heterogenous disease as some patients were negative for this or any *PRDM12* mutation. At the cellular level, we found PRDM12 constructs representing the MiTES (18A) and CIP (19A) expansion proteins both formed aggregates and mis-localised to the cytoplasm when expressed in HEK293 cells, compared to the homogeneous, nuclear-restricted expression of the WT (12A) protein. This result matches the *in vitro* findings from other transcription factors whose polyalanine expansions are associated with disease, indicating both *PRDM12*-CIP and *PRDM12*-MiTES should be considered bona fide polyalanine expansion disorders. However, we could not detect any significant differences between the MiTES and CIP constructs in our molecular studies.

In 2017, Srinivas et al.[482] outlined the unique characteristics of MiTES that set it apart from other dermatological conditions where chronic facial lesions are observed, emphasising these injuries are particularly rare in young children. Patient history and clinical investigations can help to rule out other causes of repetitive, self-mutilating behaviour such as trigeminal-trophic syndrome, erythropoietic protoporphyria or Lesch-Nyhan syndrome[482,483,486]. Recognition that this presentation represented a real disease has meant more cases could be formally diagnosed and supported with appropriate treatment, which at this time is limited to topical emollients as a protective layer and antibiotics to reduce the chance of infection. Psychological support is also recommended to patients to cope with the sensory, behavioural and emotional elements of MiTES.

Reviewing the reported MiTES cases from the literature (Table 4.6) confirmed disease onset occurs within the first year of life in 75% of cases and thus a valid distinguishing feature of MiTES. As illustrated in Figures 4.1 & 4.3, the distribution of lesions across the mid-face is highly reproducible and correlate with the ophthalmic (V1) and maxillary (V2) branches of the trigeminal sensory nerve. Given the association between *PRDM12* mutations and CIP, it may be that MiTES mutations cause localised analgesia accompanied by intensified itch in these particular nerve branches, such that facial scratching in response to itch is able to get so severe because it is not inhibited by painful sensations. Pain insensitivity or high pain threshold in other areas of the body have been reported in several patients, sometimes evidenced by injuries associated with CIP such as foot ulcers and Charcot joints.

When making these assessments, clinicians should provide details of the exams undertaken and/or injuries identified, as explained by Schon et al.[109]; this would allow for patterns in sensory dysfunction to be clearly defined, which may be of particular importance in MiTES where excessive itch is highly localised.

Due to language barriers and the age of most cases sequenced, it has been difficult to pin down the exact sensations that patients are experiencing. However, an 18-year-old sister (case 11) of a sib-pair we tested, and a 26-year-old affected man (case 22), had both suffered from similar facial lesions during their childhood which had settled with scarring by their teens. Case 11 still complains of itchy sensations. Developing a pictorial-based questionnaire with simple descriptors of itch and other relevant sensory dimensions (e.g., tingling, prickling, cooling etc.)[509] could be helpful to understand what dysesthesias are experienced in the onset of and during an episode; if there are any external triggers; and what motivates the scratching, slapping and nose-pulling behaviours.

Genetic analysis driven by our group and others has revealed *PRDM12* polyalanine expansion mutations in 18 of 28 reported cases; of the remaining cases, 4 were negative for *PRDM12* mutations, and 6 have not been tested. The consistency of this association, as well as the segregation of disease with homozygous expansion mutations specifically in the range of 16-18 alanines (which are absent in the general population), provides strong evidence that this type of variant is a causative mutation[510,511]. Although MiTES is not a progressive disease, the severity of injuries and sensory disturbances are clearly troublesome for affected children and their parents. Obtaining a precise molecular diagnosis can alleviate the uncertainty as to the cause of disease and where possible, genetic counselling should be offered to help parents understand the impact of the results for themselves and other family members. MiTES is incredibly rare and so the ability to follow up patients sharing the same condition allows clinicians to identify treatments and disease management programmes that may be of mutual benefit.

Expanding on the population data collected by Chen et al.[123], genetic analysis of MiTES families has refined the boundary between functional and pathogenic polyalanine tract length in PRDM12[483–485]. The unaffected mother of MiTES sib-pair C19 & C20 was found to be heterozygous 15A/18A and had no history of disease-related symptoms. Previously, the longest known PRDM12 polyalanine tract in healthy individuals was 14 alanines; our data implies PRDM12 with 15 alanines produces fully functional WT protein. Independent sequencing of C15 and C24 revealed they were heterozygous 17A/18A and 16A/18A respectively, suggesting PRDM12 with 16 alanines is the threshold at which

function is altered. However, genetic testing of the unaffected parents would help to corroborate this claim and strengthen the evidence that 16A and 17A alleles are pathogenic variants.

Molecular studies of the PRDM12 polyalanine expansion mutations has been limited to observations of the 19A mutant by confocal microscopy in fixed HEK293 cells and examining steady-state abundance of 18A and 19A mutants in COS-7 cells[123]. The immunocytochemistry studies in this chapter aimed to identify subtle differences between the two expansion mutants. The Airyscan LSM880 microscope used in this work generated higher resolution images than previously shown and confirmed WT PRDM12 was strictly localised to the nucleus in a slightly granular but homogeneous pattern, whereas both expansion mutants produced bright aggregates in the nucleus and cytoplasm. Interestingly, we observed condensation of WT PRDM12 in nuclear cavities that did not stain with DAPI (i.e., areas of low DNA density), but were not nucleolar sites. This was markedly different to the mutant nuclear aggregates which were much brighter, amorphous and randomly distributed. WT or mutant PRDM12 were not associated with nuclear speckles either, a membraneless sub-compartment involved in splicing whose function is disrupted by PABPN1 polyalanine expansions[512]. The one noticeable difference between the two expansion mutants was depletion of diffuse PRDM12 in the nucleoplasm, to a greater extent in the 19A-transfected cells.

Several transcription factors from the polyalanine expansion group of disorders – HOXD13, HOXA13 and RUNX2 – were recently shown to display liquid-liquid phase separation behaviour[513]. The WT proteins were expressed diffusely in the nucleus but could be reversibly induced to form droplets through an optogenetic assay. In contrast, disease-associated polyalanine expansion alleles formed spontaneous foci in the nucleus and cytoplasm, which were more concentrated and exhibited gel-like properties. It is tempting to consider if WT PRDM12 also possesses the capacity to phase separate in order to accumulate co-factors involved in the activation of various transcriptional targets, and perhaps this process is differentially disrupted by MiTES- versus CIP-associated expansion mutations.

As neither polyalanine expansion mutant had been tested in G9a pulldown assays in the original *PRDM12*-CIP paper[123], I co-stained G9a to rule out the possibility that the MiTES and/or CIP-associated aggregates differentially altered its distribution. As anticipated, G9a maintained nuclear-restricted expression in all conditions and was not absorbed into mutant aggregates. A more striking observation was the cytoplasmic, fibril-like pattern in mutant-transfected cells, compared to larger cytoplasmic plaques observed in other polyalanine expanded proteins. Co-staining with endoplasmic reticulum marker anti-KDEL revealed minimal overlap, suggesting the transient transfection of these proteins

overloaded quality control mechanisms in the ER, with escaped proteins forming cytoplasmic aggregates[514]. Testing for ubiquitin-positive inclusions would answer if these proteins had been recognised as terminally misfolded but had overcome the capacity for proteasomal degradation due to high levels of ectopic expression.

In the study of polyalanine expansion disorders, comparisons between WT and mutant proteins have been made by defining abnormal cell phenotypes (e.g., aggregates present/absent; protein localised to nucleus only/cytoplasm only/both compartments) and asking blinded observers to score prepared images[515,516]. Given the spectrum of aggregate size, brightness and location seen in cells transfected by the PRDM12 expansion mutants, I focused our quantification efforts on an automated image acquisition and analysis method. These results clearly illustrated the significant cytoplasmic expression of expansion mutants which would lead to a LOF in transcriptional regulation. Together with previously collected data on reduced steady-state abundance in COS-7 cells[123], it seems polyalanine expansions associated with MiTES or CIP both cause PRDM12 LOF through reduced availability of functional protein.

The *PRDM12*-KO mouse models generated so far recapitulate the CIP phenotype, and it is probable that a homozygous 19A/19A mouse model would similarly show a loss of the TrkA+ nociceptor lineage through neurodevelopmental defects, rather than neurodegeneration caused by toxic aggregates as observed in mouse models of polyglutamine expansion disorders[517,518]. Albrecht et al. also observed aggregates of HOXD13 polyalanine expansion mutants when over-expressed *in vitro*, but when transfection was controlled to a single gene copy per cell, they found mutants were rapidly degraded by the proteasome while WT HOXD13 was expressed normally. Parallel studies in the HOXD13 expansion mouse model confirmed the primary defect *in vivo* was reduced protein expression and mis-localisation to the cytoplasm[499]. It will likely take a combination of neuronal cell line and transgenic animal model studies to be able to distinguish the differences in cellular and physiological defects arising from MiTES versus CIP expansion mutations.

The puzzle of how *PRDM12* polyalanine tract length causes CIP versus MiTES phenotypes can be divided into 3 key aspects:

(1) A loss of pain sensation in CIP compared to enhanced, seemingly spontaneous itch in MiTES.
(2) Global dysfunction of nociception across all somatosensory ganglia in CIP compared to localised change in function in the trigeminal ganglia in MiTES.

(3) A lifelong lack of nociception and thus vulnerability to injury in CIP, compared to ongoing itch sensations in MiTES that may become manageable by early adulthood.

Given the restricted expression and role of PRDM12 in specifying peripheral sensory neurons, it is likely that this is the affected component within sensory circuits that produces the MiTES phenotype. The existence of any sensation at all and mostly intact nociception in MiTES cases indicates the presence of some nociceptor classes, compared to the complete absence of the TrkA+ lineage in *PRDM12*-CIP mice and humans. The lack of a discernible trigger in MiTES suggests that these neurons could be hypersensitive or hyperexcitable within itch pathways. Together these features imply that PRDM12 with MiTES mutations may be partially functional, changing the intrinsic identity of certain somatosensory neurons so that they are biased to signalling itch rather than pain. This may be via the expression of signal transducing molecules or peptides involved in neurotransmission, or by changing the targeting of central axons within dorsal horn circuits.

Several spinal interneuron populations have been implicated in itch processing and produced chronic itch phenotypes when they were ablated or their inputs from peripheral sensory neurons were disrupted. The loss of Bhlhb5-dependent inhibitory interneurons was shown to produce chronic itch in mice as well as hypersensitivity to chemical pruritic stimuli such as histamine and chloroquine, but without any defects in thermal, chemical or mechanical pain[519]. The loss of Ptf1a-dependent interneurons results in disinhibition within itch circuits that normally filter out self-generated mechanosensory stimuli, thus leading to chronic and spontaneous scratching behaviour[520,521]. Other interneurons mediating mechanical itch are located within spinal circuits with inputs from Aβ-LTMRs[476,522–524]. If PRDM12-dependent somatosensory neurons are present postnatally in MiTES, investigating their morphology and the identity of their synaptic targets in the dorsal horn could be informative in understanding how itch and pain sensations from polymodal nociceptive neurons are processed at the spinal level.

The most curious features of MiTES are the strict localisation of scratching and the potential resolution of symptoms in adult patients. As MiTES cases have only begun to be formally diagnosed in the last 3 years and most are still children, monitoring their sensory perceptions and physical injuries as they grow older will shed light on this aspect. Why somatosensory neurons of the trigeminal ganglia seem to be vulnerable to MiTES mutations is intriguing. Single-cell RNA sequencing studies comparing DRG and TG concluded they share a similar breadth of functionally distinct classes to be able to identify mechanical, thermal and pruritic stimuli[525]. However, examining mRNAs that are actively translated

revealed some genes may be differentially expressed at the protein level between ganglia, suggesting a heightened sensitivity to certain stimuli – e.g., pruritogen receptor *MrgprD* is translated with high efficiency in trigeminal nociceptors, but barely detected in DRG nociceptors[526]. Alternatively, the organisation of circuitry in the spinal trigeminal nucleus caudalis (i.e., the medullary dorsal horn) may differ to the dorsal horn of the spinal cord, but sensory wiring at this site is relatively understudied[527]. Finally, while DRG neurons arise solely from neural crest cells, TG neurons are additionally derived from the trigeminal cranial placodes[17]. Whether PRDM12 regulates different transcription programmes in this source population, as has been shown for its downstream signal Brn3a[528], remains to be seen.

In summary, this chapter introduces a novel congenital sensory disorder arising from *PRDM12* mutations, and the tight genotype-phenotype correlation that distinguishes the unique clinical profile of MiTES from *PRDM12*-CIP. This disorder reiterates the complexity of somatosensory development and highlights the importance of both neural architecture and functional connectivity when it comes to understanding sensory processing, particularly the relationship between itch and pain.

CHAPTER 5: Thesis Summary & Research Implications

5.1 – Summary of Thesis Findings

This dissertation demonstrates the strength of leveraging genetic data from patients with rare disorders to enhance our understanding of human physiology; specifically, how the disruption of certain molecular components alters the nociceptive system and causes congenital insensitivity to pain (CIP). Chapter 2 provided bioinformatic analyses and experimental data to confirm missense mutations from patients with *SCN9A*-CIP resulted in loss-of-function (LOF). Chapter 3 presented an interactome study of the null Nav1.7 N-terminal mutation and alternative hypotheses to explain the molecular contribution of this region. Chapter 4 extended early work on *PRDM12*-CIP, revealing a previously presumed milder phenotype was actually a distinct condition arising from a particular set of *PRDM12* mutations, and highlighted the connection between neurons mediating pain and itch.

The genotype-phenotype relationship between Nav1.7 dysfunction and pain is well established; bi-allelic mutations that abolish or cause >50% reduction in Nav1.7 current magnitude are associated with congenital painlessness, while dominant mutations that increase the open-state probability of Nav1.7 lead to disorders of excessive pain[235]. The clinical picture and disease segregation of our *SCN9A* variants were strongly indicative of *SCN9A*-CIP[109], and the novel missense variants were absent in cohorts of healthy controls. Furthermore, the Polyphen-2 tool predicted these missense variants were probably damaging based on extremely high sequence conservation and algorithms scoring the impact of substituted residues on local structural features[249]. However, using population frequency and bioinformatic predictions to infer pathogenicity has significant drawbacks that have been noted more generally and for Nav channels involved in pain[235,510,529]. Thus, our functional assays provided valuable experimental data to confirm these variants were the causative mutations. An examination of recently resolved eukaryotic Nav structures also shed light on vital biochemical and physical features at these locations. In addition, this project demonstrated how engineered cell systems and automated patch clamp technology can increase the efficiency of variant interpretation – an approach that has been successfully employed for ion channel genes with cardiac implications[530,531].

Although many variants in the N-terminal tail of Nav channels are associated with disease[147] and a few have been functionally assessed[209,258,259], this region does not have an obvious role in controlling gating or conductance. The Leu75Pro mutation in Nav1.7 was thus the most difficult to comprehend, given that it reached the cell surface but was non-conducting. Because the N-terminus has been suggested to tether membrane-localised channels to the cytoskeleton, we conducted an interactome study to test whether a disrupted protein-protein interaction (PPI) could explain the LOF observed in the cell

line system. While our results did not necessarily support this hypothesis, it is possible that by using a label-free method, a transient, low affinity or less abundant PPI was missed. Proximity-labelling approaches could overcome these issues[384], and combined with metabolic or chemical labelling *in vitro*, would increase the reliability of quantitative comparisons. Alternatively, when performed in label-free conditions *in vivo*, proximity labelling is a powerful approach to study native PPIs in a physiologically relevant context[532]. Nevertheless, we were able to identify a handful of Nav1.7 binding partners (e.g. NEURL4, PPP1R12A, filamin-A) present in both our human, non-neuronal interactomes and the mouse, neuronal dataset produced by Kanellopoulos et al.[309]. Future investigation of these candidates are needed to understand their involvement in Nav1.7 function.

In contrast to nociceptor dysfunction in *SCN9A*-CIP, *PRDM12*-CIP is caused by a neurodevelopmental defect. Bi-allelic mutations in *PRDM12* disrupt histone methylation of key genetic targets during embryogenesis, resulting in complete absence of TrkA-positive sensory neurons from birth. In the original case series[123], missense mutations seemed to disturb the function of PRDM12-G9a transcriptional complexes whereas polyalanine tract expansions reduced the availability of PRDM12 due to aggregation and enhanced degradation. While molecular studies indicated these defects were comparable between the 18-alanine (18A) and 19-alanine (19A) PRDM12 mutants, the clinical phenotypes of these families were quite distinct. Dermatologists recognised the “milder” phenotype of homozygous 18A patients as a rare familial itch presentation, designated ‘Mid-face Toddler Excoriation Syndrome’ (MiTES)[482]. This report aided the diagnosis of more patients, careful clinical characterisation to delineate the unique features of this condition, and confirmation that the majority of MiTES cases are associated with homozygous *PRDM12* polyalanine expansion mutations to 18 alanines. Our work and independent case studies have further defined the boundaries of PRDM12 polyalanine tract length that are non-pathogenic (7-15A), MiTES-associated (16-18A) or CIP-associated (19A)[483–485]. Furthermore, the identification of cases without *PRDM12* mutations suggests MiTES is genetically heterogeneous like CIP[483].

Similar to previous work in the monkey COS-7 cell line[123], we could not identify an obvious difference between the 18A and 19A PRDM12 mutants in the human HEK293 cell line. Both mutants formed nuclear aggregates of various sizes and exhibited significant cytoplasmic mis-localisation, although nucleoplasmic expression appeared to be diminished to a higher degree in 19A-transfected cells. These studies hint at a subtle difference between expansion mutants in their bioavailability during nociceptor development, which likely requires a neuronal model to be accurately captured. Comparing the clinical profiles of *PRDM12*-CIP (lifelong, global painlessness) to *PRDM12*-MiTES

(facially-localised intense itch that resolves by early adulthood) suggests sensory neurons may develop physically in the latter condition but undergo a delay in nociceptor maturation, transitioning through an intermediate cellular identity. Moreover, the absence of typical facial injuries to the eyes, lips and tongues in MiTES patients imply that some trigeminal nociceptors function normally. Skin biopsies from scarred areas, plus unaffected areas of the face and trunk, would clarify whether cutaneous innervation by small fibre nociceptors is affected differently than in *PRDM12*-CIP.

Mouse models with polyalanine expansion alleles knocked in have been generated for other human disease genes[489], even recapitulating genotype-phenotype patterns[533]. Translating disease-associated alleles between species may be more complex for *PRDM12* than other genes, due to the shorter polyalanine tract length in mouse PRDM12, and the tight range that separates MiTES from wild-type or CIP phenotypes. However, these mice would be valuable tools for physiological comparisons of MiTES and CIP, as well as validating findings from *PRDM12* knockout mice modelling *PRDM12*-CIP[124,125,137]. If TrkA-positive sensory neurons are present in MiTES, it would be helpful to know whether these *PRDM12* mutations affect transcriptional cascades in sensory neurons and/or synaptic contacts with spinal circuitry, as well as how these factors change during postnatal development.

5.2 – Analgesic Potential of Nav1.7 and PRDM12

As a novel analgesic drug target, Nav1.7 remains the most attractive of the CIP genes due to strong human genetic validation, limited side effect profile and involvement in both inflammatory and neuropathic pain states[111,534]. Dosing of approved VGSC blockers such as lidocaine or carbamazepine are constrained by off-target effects on central and cardiac channels, which led to increased efforts to optimise subtype-selectivity. These adaptations have been more successful for gating modifiers than pore blocking drugs, due to higher sequence and structural variation at the external surface of voltage sensor modules where gating modifiers bind. A range of therapeutic modalities have been developed to inhibit Nav1.7 activity such as the sulfonamide class of small-molecules and synthetic peptides adapted from natural toxins, as well as repurposing the anticonvulsant lacosamide for certain chronic pain indications[534,535].

Several compounds have shown robust antagonism of Nav1.7 and subtype-selectivity in pre-clinical stages, as well as passing phase I clinical trials to determine drug safety, tolerability and pharmacokinetics. However, most compounds failed at the phase II stage due to poor efficacy or lack of differentiation from the standard of care in the patient populations tested[534–536]. These failures

could stem from the complexity of human biology including native beta subunit expression obscuring the voltage sensor binding interface, rapid turnover of peptides, or insufficient target engagement at the crucial cellular location[536,537]. Inclusion of beta subunit combinations during *in vitro* profiling, modifications to enhance peptide stability, and intrathecal delivery have been proposed to address these issues[534,537]; the latter recommendation may have the most impact given the recent demonstration of Nav1.7's critical role in neurotransmitter release at the central synapse[113].

Novel strategies to inhibit Nav1.7 activity involve modulating intracellular pathways. One example is the long-term repression of *SCN9A* via a catalytically inactive form of the DNA-binding Cas9 protein, fused to the KRAB repressor domain, and co-delivered with *SCN9A*-guide RNAs via adeno-associated virus[538]. Alternatively, the Khanna laboratory has generated a cell-penetrant peptide that prevents Ubc9-mediated SUMOylation of CRMP2, thus biasing its action towards endocytosis of Nav1.7[329]. These projects highlight the importance of basic research into the biology of drug targets, as those that seem less amenable to modulation can become more attractive with technical innovations. If a disrupted PPI underlies the LOF mechanism behind the Nav1.7 Leu75Pro mutation, intracellular delivery of a peptide mimetic of the mutant motif may produce similar effects on channel conductance and pain perception; a similar approach was taken to disturb $Ca_V2.2$-CRMP2, Nav1.8-Magi1 and GluN2A-SHP1 interactions and successfully attenuated pain in behavioural models[539–541].

PRDM12 may have analgesic potential as an epigenetic modifier, but requires in-depth study to tease out its genetic binding sites and effectors. During embryogenesis, the interaction between PRDM12 and histone methyltransferase G9a is required for the initiation and maintenance of TrkA expression to define the nociceptor lineage. Notably, the methylation marks imparted by G9a are typically considered repressive[390], implying PRDM12 regulates *NTRK1* activation indirectly in this context. Given the persistent postnatal expression of PRDM12[123,125], it may modulate TrkA expression and potentially attenuate pain analogous to *NTRK1*-CIP patients or TrkA antagonists[122,132]. Adult-onset deletion of *PRDM12* in a transgenic mouse did result in a 47% reduction of *NTRK1* expression in DRG in native conditions; however, sensitivity to pain in a variety of behavioural models was comparable to wild-type mice, even 4 weeks after *PRDM12* knockout was induced[137]. *NTRK1* mRNA and TrkA protein levels were not measured at this stage, but could be stimulated by the action of multiple transcriptional activators or enhancers[542] that out-compete the unknown repressor. While this study suggests reducing PRDM12 activity in adults is insufficient as an analgesic strategy, isolating its genetic targets by chromatin immunoprecipitation sequencing would reveal downstream effectors whose optimisation could provide stronger pain relief.

5.3 – Implications for the Interpretation of Missense Variants in Nav Channels

In Mendelian disorders, a genetic diagnosis can positively impact the patient experience. It signals an end to investigative procedures and the psychological burden of the diagnostic odyssey, as well as giving patients access to disease-specific support groups and genetic counselling. In the medical setting, collating data from patients who share a genetic diagnosis can lead to more accurate predictions of prognosis and help clinicians make more rational treatment choices[543,544]. As next generation sequencing technologies have become less costly, there has been a shift from targeted sequencing of genes that have established relationships with disease, to whole exome or genome sequencing which can restrict results to a gene panel or be expanded to search for novel genetic causes[545]. However, this accelerated acquisition of genetic data has led to the detection of thousands of variants that require careful interpretation before they can be causally associated with disease[510,546].

At the genetic level[510], a novel variant must co-segregate with affected individuals and unaffected relatives in a manner that is consistent with the proposed pattern of inheritance; mismatches at this stage allow the exclusion of benign variants. If the variant under investigation is absent or rare in healthy control populations (e.g., 1000 Genomes Project and gnomAD databases[547,548]), this can also hint at potential disease associations, although this analysis is more suited to congenital or early-onset diseases. Another important caveat is allele frequency data is limited to the populations sampled which can confound variant interpretation. For example, the missense *SCN9A* variant Asn641Tyr was previously implicated with monogenic epilepsy due to co-segregation with disease in a large American pedigree and allele frequency of 0.001% in the gnomAD database[549]. However, the same variant was later found in 18 unaffected individuals of an extended Amish family, contradicting its designation as a pathogenic mutation[550]. These findings reinforce observations from other labs that the rarity of Nav channel variants does not always correlate with pathogenicity[235].

Bioinformatic annotation based on sequence conservation across protein families and local changes to structural features can be used to increase confidence in variants of interest[510,529]; this is the basis of scoring algorithms used by pathogenicity prediction tools such as PolyPhen-2 and SIFT[239,551]. A machine learning model was recently trained on patient mutations across the voltage-gated sodium channel (VGSC) family to predict pathogenicity as well as the direction of altered function caused by missense variants[552]. Other computational models have been developed to predict painful, gain-of-function missense variants in Nav1.7 based on intramolecular interactions and hydropathicity[553,554]. These *in silico* approaches should be integrated into variant analysis with caution for a few reasons;

(i) substitutions of functionally critical residues may not necessarily be pathogenic[235], (ii) homologous mutations do not always have the same effect in VGSC paralogues[99,555,556], and (iii) their predictive power is limited for variants in intracellular tails and linkers, whose functions are less understood[235].

Functional characterisation by voltage-clamp provides the strongest evidence that a variant causes a change in function at the molecular level[235,552]. These experiments are typically conducted in HEK293 cells due to the lack of interfering currents from endogenous VGSCs, sufficient cellular machinery to express wild-type human channels, and ease of use in parallel biochemical assays. Such studies usually focus on a handful of variants as manual patch clamp electrophysiology is a time-consuming process, which can be prolonged by transient transfection complications or if stable cell lines need to be generated. While Nav1.7 pain-related disorders are extremely rare, understanding the exact gating changes caused by a mutation can inform which pharmacotherapies are most likely to be effective in certain patients[99,557,558]. Combining the HEK JI TREX cell line and QPatch system in this project drastically sped up the profiling of Nav1.7 mutations – an approach that could also be applied to more common VGSC-associated disorders such as life-threatening cardiac conditions, or infantile-onset epilepsy, where early treatment decisions can dramatically improve disease prognosis and quality of life[559,560].

CHAPTER 6: References

1. Raja, S. N. *et al.* The revised International Association for the Study of Pain definition of pain: concepts, challenges, and compromises. *Pain* **161**, 1976–1982 (2020).

2. Smith, E. S. J. & Lewin, G. R. Nociceptors: a phylogenetic view. *Journal of comparative physiology. A, Neuroethology, sensory, neural, and behavioral physiology* vol. 195 1089–1106 (2009).

3. Sneddon, L. U. Comparative physiology of nociception and pain. *Physiology* vol. 33 63–73 (2018).

4. Melzack, R. & Katz, J. Pain. *Wiley Interdiscip. Rev. Cogn. Sci.* **4**, 1–15 (2013).

5. Treede, R.-D. D. *et al. Chronic pain as a symptom or a disease: the IASP Classification of Chronic Pain for the International Classification of Diseases (ICD-11)*. *Pain* vol. 160 19–27 (Lippincott Williams and Wilkins, 2019).

6. Breivik, H., Collett, B., Ventafridda, V., Cohen, R. & Gallacher, D. Survey of chronic pain in Europe: Prevalence, impact on daily life, and treatment. *Eur. J. Pain* **10**, 287 (2006).

7. McGhie, J. & Grady, K. Where now for UK chronic pain management services? *British Journal of Anaesthesia* vol. 116 159–162 (2016).

8. Gatchel, R. J., Peng, Y. B., Peters, M. L., Fuchs, P. N. & Turk, D. C. The Biopsychosocial Approach to Chronic Pain: Scientific Advances and Future Directions. *Psychol. Bull.* **133**, 581–624 (2007).

9. Moseley, G. L. & Butler, D. S. Fifteen Years of Explaining Pain: The Past, Present, and Future. *Journal of Pain* vol. 16 807–813 (2015).

10. Smith, B. H. *et al.* The IASP classification of chronic pain for ICD-11: Applicability in primary care. *Pain* vol. 160 83–87 (2019).

11. Devor, M. Unexplained peculiarities of the dorsal root ganglion. *Pain* **82**, (1999).

12. Nascimento, A. I., Mar, F. M. & Sousa, M. M. The intriguing nature of dorsal root ganglion neurons: Linking structure with polarity and function. *Progress in Neurobiology* vol. 168 86–103 (2018).

13. Haberberger, R. V., Barry, C., Dominguez, N. & Matusica, D. Human dorsal root ganglia. *Frontiers in Cellular Neuroscience* vol. 13 (2019).

14. WHITWAM, J. G. Classification of peripheral nerve fibres: An historical perspective. *Anaesthesia* vol. 31 494–503 (1976).

15. Raja, S. N., Meyer, R. A. & Campbell, J. N. Peripheral mechanisms of somatic pain. *Anesthesiology* vol. 68 571–590 (1988).

16. Snider, W. D. Dorsal root ganglion neurons require functional neurotrophin receptors for survival during development. *Philos. Trans. R. Soc. B Biol. Sci.* **351**, 395–403 (1996).

17. Vermeiren, S., Bellefroid, E. J. & Desiderio, S. Vertebrate Sensory Ganglia: Common and Divergent Features of the Transcriptional Programs Generating Their Functional Specialization. *Frontiers in Cell and Developmental Biology* vol. 8 (2020).

18. Grundy, L., Erickson, A. & Brierley, S. M. Visceral Pain. *Annual Review of Physiology* vol. 81 261–284 (2019).

19. Abraira, V. E. & Ginty, D. D. The sensory neurons of touch. *Neuron* vol. 79 618–639 (2013).

20. Tuthill, J. C. & Azim, E. Proprioception. *Current Biology* vol. 28 R194–R203 (2018).

21. Basbaum, A. I., Bautista, D. M., Scherrer, G. & Julius, D. Cellular and Molecular Mechanisms of Pain. *Cell* vol. 139 267–284 (2009).

22. Todd, A. J. Neuronal circuitry for pain processing in the dorsal horn. *Nat. Rev. Neurosci.* **11**, 823–836 (2010).

23. Côté, M. P., Murray, L. M. & Knikou, M. Spinal control of locomotion: Individual neurons, their circuits and functions. *Frontiers in Physiology* vol. 9 (2018).

24. Sathyamurthy, A. *et al.* Massively Parallel Single Nucleus Transcriptional Profiling Defines Spinal Cord Neurons and Their Activity during Behavior. *Cell Rep.* **22**, 2216–2225 (2018).

25. Häring, M. *et al.* Neuronal atlas of the dorsal horn defines its architecture and links sensory input to transcriptional cell types. *Nat. Neurosci.* **21**, 869–880 (2018).

26. Kuner, R. & Kuner, T. Cellular circuits in the brain and their modulation in acute and chronic pain. *Physiol. Rev.* **101**, 213–258 (2021).

27. Corder, G. *et al.* An amygdalar neural ensemble that encodes the unpleasantness of pain. *Science (80-.).* **363**, 276–281 (2019).

28. Seymour, B. Pain: A Precision Signal for Reinforcement Learning and Control. *Neuron* vol. 101 1029–1041 (2019).

29. Colin, S. & Kruger, L. Peptidergic nociceptive axon visualization in whole-mount preparations of cornea and tympanic membrane in rat. *Brain Res.* **398**, 199–203 (1986).

30. Silverman, J. D. & Kruger, L. Lectin and neuropeptide labeling of separate populations of dorsal root ganglion neurons and associated 'nociceptor' thin axons in rat testis and cornea whole-mount preparations. *Somatosens. Mot. Res.* **5**, 259–267 (1988).

31. Taylor, A. M. W., Peleshok, J. C. & Ribeiro-Da-Silva, A. Distribution of P2X3-immunoreactive fibers in hairy and glabrous skin of the rat. *J. Comp. Neurol.* **514**, 555–566 (2009).

32. Franck, M. C. M. *et al.* Essential role of Ret for defining non-peptidergic nociceptor phenotypes and functions in the adult mouse. *Eur. J. Neurosci.* **33**, 1385–1400 (2011).

33. Brumovsky, P. R. Dorsal root ganglion neurons and tyrosine hydroxylase - An intriguing association with implications for sensation and pain. *Pain* vol. 157 314–320 (2016).

34. Price, T. J. & Flores, C. M. Critical Evaluation of the Colocalization Between Calcitonin Gene-Related Peptide, Substance P, Transient Receptor Potential Vanilloid Subfamily Type 1 Immunoreactivities, and Isolectin B4 Binding in Primary Afferent Neurons of the Rat and Mouse. *J. Pain* **8**, 263–272 (2007).

35. Shiers, S. I. *et al.* Convergence of peptidergic and non-peptidergic protein markers in the human dorsal root ganglion and spinal dorsal horn. *J. Comp. Neurol.* **529**, 2771–2788 (2021).

36. Usoskin, D. *et al.* Unbiased classification of sensory neuron types by large-scale single-cell RNA sequencing. *Nat. Neurosci.* **18**, 145–153 (2015).

37. Li, C. L. *et al.* Somatosensory neuron types identified by high-coverage single-cell RNA-sequencing and functional heterogeneity. *Cell Res.* **26**, 83–102 (2016).

38. Sharma, N. *et al.* The emergence of transcriptional identity in somatosensory neurons. *Nature* **577**, 392–398 (2020).

39. Kupari, J. *et al.* Single cell transcriptomics of primate sensory neurons identifies cell types associated with chronic pain. *Nat. Commun.* **12**, (2021).

40. Hoffstaetter, L. J., Bagriantsev, S. N. & Gracheva, E. O. TRPs et al.: a molecular toolkit for thermosensory adaptations. *Pflugers Archiv European Journal of Physiology* vol. 470 745–759 (2018).

41. LaMotte, R. H., Shain, C. N., Simone, D. A. & Tsai, E. F. P. Neurogenic hyperalgesia: Psychophysical studies of underlying mechanisms. *J. Neurophysiol.* **66**, 190–211 (1991).

42. LaMotte, R. H., Lundberg, L. E. & Torebjörk, H. E. Pain, hyperalgesia and activity in nociceptive C units in humans after intradermal injection of capsaicin. *J. Physiol.* **448**, 749–764 (1992).

43. Wasner, G., Schattschneider, J., Binder, A. & Baron, R. Topical menthol - A human model for cold pain by activation and sensitization of C nociceptors. *Brain* vol. 127 1159–1171 (2004).

44. Campero, M., Baumann, T. K., Bostock, H. & Ochoa, J. L. Human cutaneous C fibres activated by cooling, heating and menthol. *J. Physiol.* **587**, 5633–5652 (2009).

45. Caterina, M. J. *et al.* The capsaicin receptor: A heat-activated ion channel in the pain pathway. *Nature* **389**, 816–824 (1997).

46. McKemy, D. D., Neuhausser, W. M. & Julius, D. Identification of a cold receptor reveals a general role for TRP channels in thermosensation. *Nature* **416**, 52–58 (2002).

47. Kwan, K. Y. *et al.* TRPA1 Contributes to Cold, Mechanical, and Chemical Nociception but Is Not Essential for Hair-Cell Transduction. *Neuron* **50**, 277–289 (2006).

48. Nencini, S. & Ivanusic, J. Mechanically sensitive Aδ nociceptors that innervate bone marrow respond to changes in intra-osseous pressure. *J. Physiol.* **595**, 4399–4415 (2017).

49. Fernández-Trillo, J. *et al.* Piezo2 mediates low-threshold mechanically evoked pain in the cornea. *J. Neurosci.* **40**, 8976–8993 (2020).

50. Alloui, A. *et al.* TREK-1, a K+ channel involved in polymodal pain perception. *EMBO J.* **25**, 2368–2376 (2006).

51. Pereira, V. *et al.* Role of the TREK2 potassium channel in cold and warm thermosensation and in pain perception. *Pain* **155**, 2534–2544 (2014).

52. Castellanos, A. *et al.* TRESK background K+ channel deletion selectively uncovers enhanced mechanical and cold sensitivity. *J. Physiol.* **598**, 1017–1038 (2020).

53. Lamotte, R. H., Dong, X. & Ringkamp, M. Sensory neurons and circuits mediating itch. *Nature Reviews Neuroscience* vol. 15 19–31 (2014).

54. Dong, X. X. & Dong, X. X. Peripheral and Central Mechanisms of Itch. *Neuron* vol. 98 482–494 (2018).

55. Waxman, S. G. Sodium channels, the electrogenisome and the electrogenistat: Lessons and questions from the clinic. *Journal of Physiology* vol. 590 2601–2612 (2012).

56. Dib-Hajj, S. D., Black, J. A. & Waxman, S. G. Na v 1.9: A sodium channel linked to human pain. *Nat. Rev. Neurosci.* **16**, 511–519 (2015).

57. Waxman, S. G. Nav1.7, its mutations, and the syndromes that they cause. *Neurology* vol. 69 505–507 (2007).

58. Renganathan, M., Cummins, T. R. & Waxman, S. G. Contribution of Nav 1.8 sodium channels to action potential electrogenesis in DRG neurons. *J. Neurophysiol.* **86**, 629–640 (2001).

59. Blair, N. T. & Bean, B. P. Roles of tetrodotoxin (TTX)-sensitive Na+ current, TTX-resistant Na+ current, and Ca2+ current in the action potentials of nociceptive sensory neurons. *J. Neurosci.* **22**, 10277–10290 (2002).

60. Bennett, D. L., Clark, X. A. J., Huang, J., Waxman, S. G. & Dib-Hajj, S. D. The role of voltage-gated sodium channels in pain signaling. *Physiol. Rev.* **99**, 1079–1151 (2019).

61. Goodwin, G. & McMahon, S. B. The physiological function of different voltage-gated sodium channels in pain. *Nature Reviews Neuroscience* vol. 22 (2021).

62. Bourinet, E. *et al.* Calcium-permeable ion channels in pain signaling. *Physiol. Rev.* **94**, 81–140 (2014).

63. Pereira, V. & Goudet, C. Emerging trends in pain modulation by metabotropic glutamate receptors. *Frontiers in Molecular Neuroscience* vol. 11 (2019).

64. D'Mello, R. & Dickenson, A. H. Spinal cord mechanisms of pain. *British Journal of Anaesthesia* vol. 101 8–16 (2008).

65. Baluk, P. Neurogenic inflammation in skin and airways. in *Journal of Investigative Dermatology Symposium Proceedings* vol. 2 76–81 (Nature Publishing Group, 1997).

66. Sharif, B., Ase, A. R., Ribeiro-da-Silva, A. & Séguéla, P. Differential Coding of Itch and Pain by a Subpopulation of Primary Afferent Neurons. *Neuron* **106**, 940-951.e4 (2020).

67. Cervero, F. Chapter 24. Spinal cord mechanisms of hyperalgesia and allodynia: Role of peripheral input from nociceptors. *Prog. Brain Res.* **113**, 413–422 (1996).

68. IASP Task Force on Taxonomy. Part III: Pain Terms, A Current List with Definitions and Notes on Usage. in *Classification of Chronic Pain* (eds. Merskey, H. & Bogduk, N.) 209–214 (IASP Press, 1994).

69. Jensen, T. S. & Finnerup, N. B. Allodynia and hyperalgesia in neuropathic pain: Clinical manifestations and mechanisms. *The Lancet Neurology* vol. 13 924–935 (2014).

70. Landerholm, Å. H. & Hansson, P. T. Mechanisms of dynamic mechanical allodynia and dysesthesia in patients with peripheral and central neuropathic pain. *Eur. J. Pain* **15**, 498–503 (2011).

71. Dhandapani, R. *et al.* Control of mechanical pain hypersensitivity in mice through ligand-targeted photoablation of TrkB-positive sensory neurons. *Nat. Commun. 2018 91* **9**, 1–14 (2018).

72. Gangadharan, V. & Kuner, R. Pain hypersensitivity mechanisms at a glance. *Dis. Model. Mech.* **6**, 889–895 (2013).

73. Ji, R. R. R., Nackley, A., Huh, Y., Terrando, N. & Maixner, W. Neuroinflammation and Central Sensitization in Chronic and Widespread Pain. *Anesthesiology* **129**, 343–366 (2018).

74. Dansereau, M. *et al.* Mechanistic insights into the role of the chemokine CCL2/CCR2 axis in dorsal root ganglia to peripheral inflammation and pain hypersensitivity. *J. Neuroinflammation* **18**, (2021).

75. Von Hehn, C. A., Baron, R. & Woolf, C. J. Review Deconstructing the Neuropathic Pain Phenotype to Reveal Neural Mechanisms. *Neuron* **73**, 638–652 (2012).

76. Tao, Y. AMPA receptor trafficking in inflammation-induced dorsal horn central sensitization. *Neurosci. Bull.* **28**, 111–120 (2012).

77. Kwon, M., Altin, M., Duenas, H. & Alev, L. The role of descending inhibitory pathways on chronic pain modulation and clinical implications. *Pain Pract.* **14**, 656–667 (2014).

78. Zhang, Z., Wang, X., Wang, W., Lu, Y. & Pan, Z. Brain-derived neurotrophic factor-mediated downregulation of brainstem K+-Cl- cotransporter and cell-type-specific GABA impairment for activation of descending pain facilitation. *Mol. Pharmacol.* **84**, 511–520 (2013).

79. Li, C. *et al.* The etiological contribution of GABAergic plasticity to the pathogenesis of neuropathic pain. *Mol. Pain* **15**, (2019).

80. Gaudet, A., Popovich, P. & Ramer, M. Wallerian degeneration: gaining perspective on inflammatory events after peripheral nerve injury. *J. Neuroinflammation* **8**, (2011).

81. Hung, A., Lim, M. & Doshi, T. Targeting cytokines for treatment of neuropathic pain. *Scand. J. pain* **17**, 287–293 (2017).

82. Finnerup, N., Kuner, R. & Jensen, T. Neuropathic Pain: From Mechanisms to Treatment. *Physiol. Rev.* **101**, 259–301 (2021).

83. Moore, A., Derry, S., Eccleston, C. & Kalso, E. Expect analgesic failure; pursue analgesic success. *BMJ* **346**, (2013).

84. British Medical Association. *Chronic pain: supporting safer prescribing of analgesics*. https://www.bma.org.uk/media/2100/analgesics-chronic-pain.pdf (2017).

85. People living with Pain. *British Pain Society* https://www.britishpainsociety.org/people-with-pain/.

86. Neuropathic pain in adults: pharmacological management in non-specialist settings [CG173]. *National Institute for Health and Care Excellence (NICE)* https://www.nice.org.uk/guidance/cg173 (2013).

87. Kalso, E., Aldington, D. J. & Moore, R. A. Drugs for neuropathic pain. *BMJ* **347**, (2013).

88. Guy, S. *et al.* The CanPain SCI Clinical Practice Guidelines for Rehabilitation Management of Neuropathic Pain after Spinal Cord: Recommendations for treatment. *Spinal Cord* **54 Suppl 1**, S14-23 (2016).

89. Bates, D. *et al.* A Comprehensive Algorithm for Management of Neuropathic Pain. *Pain Med.* **20**, S2–S12 (2019).

90. Brune, K. & Patrignani, P. New insights into the use of currently available non-steroidal anti-inflammatory drugs. *J. Pain Res.* **8**, 105–118 (2015).

91. Högestätt, E. *et al.* Conversion of acetaminophen to the bioactive N-acylphenolamine AM404 via fatty acid amide hydrolase-dependent arachidonic acid conjugation in the nervous system. *J. Biol. Chem.* **280**, 31405–31412 (2005).

92. Barrière, D. A. *et al.* Paracetamol is a centrally acting analgesic using mechanisms located in the periaqueductal grey. *Br. J. Pharmacol.* **177**, 1773–1792 (2020).

93. Saliba, S. W. *et al.* AM404, paracetamol metabolite, prevents prostaglandin synthesis in activated microglia by inhibiting COX activity. *J. Neuroinflammation 2017 141* **14**, 1–11 (2017).

94. Ohashi, N. *et al.* Acetaminophen Metabolite N-Acylphenolamine Induces Analgesia via Transient Receptor Potential Vanilloid 1 Receptors Expressed on the Primary Afferent Terminals of C-fibers in the Spinal Dorsal Horn. *Anesthesiology* **127**, 355–371 (2017).

95. Finnerup, N. B. *et al.* Pharmacotherapy for neuropathic pain in adults: a systematic review and meta-analysis. *Lancet Neurol.* **14**, 162–173 (2015).

96. Kremer, M., Salvat, E., Muller, A., Yalcin, I. & Barrot, M. Antidepressants and gabapentinoids in neuropathic pain: Mechanistic insights. *Neuroscience* **338**, 183–206 (2016).

97. Chincholkar, M. Analgesic mechanisms of gabapentinoids and effects in experimental pain models: a narrative review. *Br. J. Anaesth.* **120**, 1315–1334 (2018).

98. Yang, Y. *et al.* Structural modelling and mutant cycle analysis predict pharmacoresponsiveness of a Na v 1.7 mutant channel. *Nat. Commun. 2012 31* **3**, 1–12 (2012).

99. Han, C. *et al.* The Novel Activity of Carbamazepine as an Activation Modulator Extends from NaV1.7 Mutations to the NaV1.8-S242T Mutant Channel from a Patient with Painful Diabetic Neuropathy. *Mol. Pharmacol.* **94**, 1256–1269 (2018).

100. Hermanns, H. *et al.* Molecular mechanisms of action of systemic lidocaine in acute and chronic pain: a narrative review. *Br. J. Anaesth.* **123**, 335–349 (2019).

101. Corder, G., Castro, D. C., Bruchas, M. R. & Scherrer, G. Endogenous and exogenous opioids in pain. *Annual Review of Neuroscience* vol. 41 453–473 (2018).

102. DeWeerdt, S. Tracing the US opioid crisis to its roots. *Nature* **573**, S10–S12 (2019).

103. Ballantyne, J. C., Kalso, E. & Stannard, C. WHO analgesic ladder: a good concept gone astray. *BMJ* **352**, (2016).

104. Busse, J. W. *et al.* Opioids for Chronic Noncancer Pain: A Systematic Review and Meta-analysis. *JAMA* **320**, 2448–2460 (2018).

105. Opioids Aware. *Faculty of Pain Medicine* https://fpm.ac.uk/opioids-aware.

106. Covington, E. C. *et al.* Ensuring Patient Protections When Tapering Opioids: Consensus Panel Recommendations. *Mayo Clin. Proc.* **95**, 2155–2171 (2020).

107. Public Health England. *Chronic pain in adults 2017; Health Survey for England [GW-1758]*. (2017).

108. Maniadakis, N. & Gray, A. The economic burden of back pain in the UK. *Pain* **84**, 95–103 (2000).

109. Schon, K., Parker, A. & Woods, C. G. *Congenital Insensitivity to Pain Overview*. *GeneReviews®*

(University of Washington, Seattle, 2020).

110. Nahorski, M. S., Chen, Y. C. & Woods, C. G. New Mendelian Disorders of Painlessness. *Trends in Neurosciences* vol. 38 712–724 (2015).

111. Drissi, I., Woods, W. A. & Woods, C. G. Understanding the genetic basis of congenital insensitivity to pain. *Br. Med. Bull.* **133**, 65–78 (2020).

112. Habib, A. M. *et al.* Microdeletion in a FAAH pseudogene identified in a patient with high anandamide concentrations and pain insensitivity. *Br. J. Anaesth.* **123**, e249–e253 (2019).

113. MacDonald, D. I. *et al.* A central mechanism of analgesia in mice and humans lacking the sodium channel NaV1.7. *Neuron* (2021) doi:10.1016/j.neuron.2021.03.012.

114. McDermott, L. A. *et al.* Defining the Functional Role of Na V 1.7 in Human Nociception. *Neuron* **101**, 905-919.e8 (2019).

115. Alexandrou, A. J. *et al.* Subtype-selective small molecule inhibitors reveal a fundamental role for Nav1.7 in nociceptor electrogenesis, axonal conduction and presynaptic release. *PLoS One* **11**, (2016).

116. Leipold, E. *et al.* A de novo gain-of-function mutation in SCN11A causes loss of pain perception. *Nature Genetics* vol. 45 1399–1407 (2013).

117. Habib, A. M. *et al.* A novel human pain insensitivity disorder caused by a point mutation in ZFHX2. *Brain* **141**, 365–376 (2018).

118. Huang, J. *et al.* Sodium channel NaV1.9 mutations associated with insensitivity to pain dampen neuronal excitability. *J. Clin. Invest.* **127**, 2805–2814 (2017).

119. Petruska, J. C. & Mendell, L. M. The many functions of nerve growth factor: multiple actions on nociceptors. *Neurosci. Lett.* **361**, 168–171 (2004).

120. Carvalho, O. P. *et al.* A novel NGF mutation clarifies the molecular mechanism and extends the phenotypic spectrum of the HSAN5 neuropathy. *J. Med. Genet.* **48**, 131–135 (2011).

121. Capsoni, S. From genes to pain: Nerve growth factor and hereditary sensory and autonomic neuropathy type V. *Eur. J. Neurosci.* **39**, 392–400 (2014).

122. Shaikh, S. S. *et al.* A Comprehensive Functional Analysis of NTRK1 Missense Mutations Causing Hereditary Sensory and Autonomic Neuropathy Type IV (HSAN IV). *Hum. Mutat.* **38**, 55–63 (2017).

123. Chen, Y. C. *et al.* Transcriptional regulator PRDM12 is essential for human pain perception. *Nat. Genet.* **47**, 803–808 (2015).

124. Bartesaghi, L. *et al.* PRDM12 Is Required for Initiation of the Nociceptive Neuron Lineage during Neurogenesis. *Cell Rep.* **26**, 3484-3492.e4 (2019).

125. Desiderio, S. *et al.* Prdm12 Directs Nociceptive Sensory Neuron Development by Regulating the Expression of the NGF Receptor TrkA. *Cell Rep.* **26**, 3522-3536.e5 (2019).

126. Nahorski, M. S. *et al.* A novel disorder reveals clathrin heavy chain-22 is essential for human pain and touch development. *Brain* **138**, 2147–2160 (2015).

127. Nahorski, M. S. *et al.* Clathrin heavy chain 22 contributes to the control of neuropeptide degradation and secretion during neuronal development. *Sci. Rep.* **8**, (2018).

128. Indo, Y. NGF-dependent neurons and neurobiology of emotions and feelings: Lessons from congenital insensitivity to pain with anhidrosis. *Neurosci. Biobehav. Rev.* **87**, 1–16 (2018).

129. Hepburn, L. *et al.* A Spaetzle-like role for nerve growth factor β in vertebrate immunity to Staphylococcus aureus. *Science (80-.).* **346**, 641–646 (2014).

130. Marlin, M. & Li, G. Biogenesis and function of the NGF/TrkA signaling endosome. *Int. Rev. Cell Mol. Biol.* **314**, 239–257 (2015).

131. Barker, P., Mantyh, P., Arendt-Nielsen, L., Viktrup, L. & Tive, L. Nerve Growth Factor Signaling and Its Contribution to Pain. *J. Pain Res.* **13**, 1223–1241 (2020).

132. Wise, B., Seidel, M. & Lane, N. The evolution of nerve growth factor inhibition in clinical medicine. *Nat. Rev. Rheumatol.* **17**, 34–46 (2021).

133. Lever, I. *et al.* Brain-derived neurotrophic factor is released in the dorsal horn by distinctive patterns of afferent fiber stimulation. *J. Neurosci.* **21**, 4469–4477 (2001).

134. Cappoli, N., Tabolacci, E., Aceto, P. & Dello Russo, C. The emerging role of the BDNF-TrkB signaling pathway in the modulation of pain perception. *J. Neuroimmunol.* **349**, 577406 (2020).

135. Joint FDA Advisory Committee Votes on Application for Tanezumab for the Treatment of Osteoarthritis Pain. *Business Wire* https://www.businesswire.com/news/home/20210325005905/en/ (2021).

136. Vassilopoulos, S. *et al.* A Role for the CHC22 Clathrin Heavy-Chain Isoform in Human Glucose Metabolism. *Science (80-.).* **324**, 1192–1196 (2009).

137. Landy, M. A., Goyal, M., Casey, K. M., Liu, C. & Lai, H. C. Loss of Prdm12 during development, but not in mature nociceptors, causes defects in pain sensation. *Cell Rep.* **34**, (2021).

138. Kokotović, T. *et al.* PRDM12 Is Transcriptionally Active and Required for Nociceptor Function Throughout Life. *Front. Mol. Neurosci.* **14**, 192 (2021).

139. Cajanus, K. *et al.* Effect of endocannabinoid degradation on pain: role of FAAH polymorphisms in experimental and postoperative pain in women treated for breast cancer. *Pain* **157**, 361–369 (2016).

140. Peciña, M. *et al.* FAAH selectively influences placebo effects. *Mol. Psychiatry* **19**, 385–391 (2014).

141. Chiang, K., Gerber, A., Sipe, J. & Cravatt, B. Reduced cellular expression and activity of the P129T mutant of human fatty acid amide hydrolase: evidence for a link between defects in the endocannabinoid system and problem drug use. *Hum. Mol. Genet.* **13**, 2113–2119 (2004).

142. Zimmer, A. Genetic Manipulation of the Endocannabinoid System. *Handb. Exp. Pharmacol.* **231**, 129–183 (2015).

143. Lodola, A., Castelli, R., Mor, M. & Rivara, S. Fatty acid amide hydrolase inhibitors: a patent review (2009-2014). *Expert Opin. Ther. Pat.* **25**, 1247–1266 (2015).

144. Catterall, W. A., Wisedchaisri, G. & Zheng, N. The chemical basis for electrical signaling. *Nature Chemical Biology* vol. 13 455–463 (2017).

145. Hull, J. M. & Isom, L. L. Voltage-gated sodium channel β subunits: The power outside the pore in brain development and disease. *Neuropharmacology* vol. 132 43–57 (2018).

146. Catterall, W. A. Voltage-gated sodium channels at 60: Structure, function and pathophysiology. *Journal of Physiology* vol. 590 2577–2589 (2012).

147. Huang, W., Liu, M., Yan, S. F. & Yan, N. Structure-based assessment of disease-related mutations in human voltage-gated sodium channels. *Protein and Cell* vol. 8 401–438 (2017).

148. Meisler, M. H., Hill, S. F. & Yu, W. Sodium channelopathies in neurodevelopmental disorders. *Nature Reviews Neuroscience* vol. 22 152–166 (2021).

149. Matthews, E., Balestrini, S., Sisodiya, S. M. & Hanna, M. G. Muscle and brain sodium channelopathies: genetic causes, clinical phenotypes, and management approaches. *The Lancet Child and Adolescent Health* vol. 4 536–547 (2020).

150. Savio-Galimberti, E., Argenziano, M. & Antzelevitch, C. Cardiac arrhythmias related to sodium channel dysfunction. in *Handbook of Experimental Pharmacology* vol. 246 331–354 (Springer New York LLC, 2018).

151. Dib-Hajj, S. D. & Waxman, S. G. Sodium Channels in Human Pain Disorders: Genetics and Pharmacogenomics. *Annu. Rev. Neurosci.* **42**, 87–106 (2019).

152. Brouwer, B. A. *et al.* Painful neuropathies: The emerging role of sodium channelopathies. in *Journal of the Peripheral Nervous System* vol. 19 53–65 (Blackwell Publishing Inc., 2014).

153. Cox, J. J. *et al.* An SCN9A channelopathy causes congenital inability to experience pain. *Nature* **444**, 894–898 (2006).

154. Brown, A. M. *A companion guide to the Hodgkin-Huxley papers*. (The Physiological Society, 2020).

155. CM, A. & B, H. Voltage-gated ion channels and electrical excitability. *Neuron* **20**, 371–380 (1998).

156. Noda, M. *et al.* Primary structure of Electrophorus electricus sodium channel deduced from cDNA sequence. *Nature* **312**, 121–127 (1984).

157. Noda, M. *et al.* Expression of functional sodium channels from cloned cDNA. *Nature* **322**, 826–828 (1986).

158. Noreng, S., Li, T. & Payandeh, J. Structural Pharmacology of Voltage-Gated Sodium Channels. *Journal of Molecular Biology* 166967 (2021) doi:10.1016/j.jmb.2021.166967.

159. B, H. The permeability of the sodium channel to metal cations in myelinated nerve. *J. Gen. Physiol.* **59**, 637–658 (1972).

160. Sun, Y. M., Favre, I., Schild, L. & Moczydlowski, E. On the structural basis for size-selective permeation of organic cations through the voltage-gated sodium channel: Effect of alanine mutations at the DEKA locus on selectivity, inhibition by Ca2+ and H+, and molecular sieving. *J. Gen. Physiol.* **110**, 693–715 (1997).

161. Favre, I., Moczydlowski, E. & Schild, L. On the structural basis for ionic selectivity among Na+, K+, and Ca2+ in the voltage-gated sodium channel. *Biophys. J.* **71**, 3110–3125 (1996).

162. Heinemann, S. H., Terlau, H., Stühmer, W., Imoto, K. & Numa, S. Calcium channel characteristics conferred on the sodium channel by single mutations. *Nature* **356**, 441–443 (1992).

163. Catterall, W. A., Wisedchaisri, G. & Zheng, N. The conformational cycle of a prototypical voltage-gated sodium channel. *Nat. Chem. Biol.* **16**, 1314–1320 (2020).

164. Lampert, A. *et al.* A pore-blocking hydrophobic motif at the cytoplasmic aperture of the closed-state Nav1.7 channel is disrupted by the erythromelalgia- associated F1449V mutation. *J. Biol. Chem.* **283**, 24118–24127 (2008).

165. Yang, Y., Estacion, M., Dib-Hajj, S. D. & Waxman, S. G. Molecular Architecture of a Sodium Channel S6 Helix RADIAL TUNING OF THE VOLTAGE-GATED SODIUM CHANNEL 1.7 ACTIVATION GATE *. *J. Biol. Chem.* (2013) doi:10.1074/jbc.M113.462366.

166. Klugbauer, N., Lacinova, L., Flockerzi, V. & Hofmann, F. Structure and functional expression of a new member of the tetrodotoxin-sensitive voltage-activated sodium channel family from human neuroendocrine cells. *EMBO J.* **14**, 1084–1090 (1995).

167. Rühlmann, A. H. *et al.* Uncoupling sodium channel dimers restores the phenotype of a pain-linked Nav1.7 channel mutation. *Br. J. Pharmacol.* **177**, 4481–4496 (2020).

168. Armstrong, C. M. & Hollingworth, S. Na+ and K+ channels: history and structure. *Biophysical Journal* vol. 120 756–763 (2021).

169. Chatterjee, S. *et al.* The voltage-gated sodium channel pore exhibits conformational flexibility during slow inactivation. *J. Gen. Physiol.* **150**, 1333–1347 (2018).

170. Silva, J. R. & Goldstein, S. A. N. Voltage-sensor movements describe slow inactivation of voltage-gated sodium channels I: Wild-type skeletal muscle NaV1.4. *J. Gen. Physiol.* **141**, 309–321 (2013).

171. Clatot, J. *et al.* Voltage-gated sodium channels assemble and gate as dimers. *Nat. Commun. 2017 81* **8**, 1–14 (2017).

172. Raymond, C. K. *et al.* Expression of alternatively spliced sodium channel α-subunit genes. Unique

splicing patterns are observed in dorsal root ganglia. *J. Biol. Chem.* **279**, 46234–46241 (2004).

173. Chatelier, A., Dahllund, L., Eriksson, A., Krupp, J. & Chahine, M. Biophysical properties of human Nav1.7 splice variants and their regulation by protein kinase A. *J. Neurophysiol.* **99**, 2241–2250 (2008).

174. Copley, R. R. Evolutionary convergence of alternative splicing in ion channels. *Trends Genet.* **20**, 171–176 (2004).

175. Liavas, A., Lignani, G. & Schorge, S. Conservation of alternative splicing in sodium channels reveals evolutionary focus on release from inactivation and structural insights into gating. *J. Physiol.* **595**, 5671–5685 (2017).

176. Jarecki, B. W., Sheets, P. L., Xiao, Y., Jackson, J. O. & Cummins, T. R. Alternative splicing of NaV1.7 exon 5 increases the impact of the painful PEPD mutant channel I1461T. *Channels (Austin)* **3**, (2009).

177. Choi, J. S. *et al.* Alternative splicing may contribute to time-dependent manifestation of inherited erythromelalgia. *Brain* **133**, 1823–1835 (2010).

178. Thimmapaya, R. *et al.* Distribution and functional characterization of human Nav1.3 splice variants. *Eur. J. Neurosci.* **22**, 1–9 (2005).

179. Farmer, C. *et al.* Splice variants of Nav1.7 sodium channels have distinct β subunit-dependent biophysical properties. *PLoS One* **7**, (2012).

180. Cheng, X., Choi, J. S., Waxman, S. G. & Dib-Hajj, S. D. *Mini-review - Sodium channels and beyond in peripheral nerve disease: Modulation by cytokines and their effector protein kinases*. *Neuroscience Letters* vol. 741 135446 (Elsevier, 2021).

181. Toledo-Aral, J. J. *et al.* Identification of PN1, a predominant voltage-dependent sodium channel expressed principally in peripheral neurons. *Proc. Natl. Acad. Sci.* **94**, 1527–1532 (1997).

182. Fukuoka, T. & Noguchi, K. Comparative study of voltage-gated sodium channel α-subunits in non-overlapping four neuronal populations in the rat dorsal root ganglion. *Neurosci. Res.* **70**, 164–171 (2011).

183. Ho, C. & O'Leary, M. E. Single-cell analysis of sodium channel expression in dorsal root ganglion neurons. *Mol. Cell. Neurosci.* **46**, 159–166 (2011).

184. Chiu, I. M. *et al.* Transcriptional profiling at whole population and single cell levels reveals somatosensory neuron molecular diversity. *Elife* **3**, (2014).

185. Zeisel, A. *et al.* Molecular Architecture of the Mouse Nervous System. *Cell* **174**, 999-1014.e22 (2018).

186. Black, J. A., Frézel, N., Dib-Hajj, S. D. & Waxman, S. G. Expression of Nav1.7 in DRG neurons extends from peripheral terminals in the skin to central preterminal branches and terminals in the dorsal horn. *Mol. Pain* **8**, (2012).

187. Akin, E. J. *et al.* Building sensory axons: Delivery and distribution of NaV1.7 channels and effects of inflammatory mediators. *Sci. Adv.* **5**, eaax4755 (2019).

188. Alles, S. R. *et al.* Sensory neuron-derived Na V 1.7 contributes to dorsal horn neuron excitability. *Sci. Adv* **6**, 4568 (2020).

189. Kang, S. J. *et al.* Unified neural pathways that gate affective pain and multisensory innate threat signals to the amygdala. *bioRxiv* 2020.11.17.385104 (2020) doi:10.1101/2020.11.17.385104.

190. Chang, W. *et al.* Expression and Role of Voltage-Gated Sodium Channels in Human Dorsal Root Ganglion Neurons with Special Focus on Nav1.7, Species Differences, and Regulation by Paclitaxel. *Neurosci. Bull.* **34**, 4–12 (2018).

191. Shiers, S., Klein, R. M. & Price, T. J. Quantitative differences in neuronal subpopulations between mouse and human dorsal root ganglia demonstrated with RNAscope in situ hybridization. *Pain* **161**, 2410–2424 (2020).

192. Rice, F. L. *et al.* Sodium Channel Nav1.7 in Vascular Myocytes, Endothelium, and Innervating Axons in Human Skin: *Mol. Pain* **11**, (2015).

193. Mercier, A., Bois, P. & Chatelier, A. Sodium Channel Trafficking. in *Voltage-gated Sodium Channels: Structure, Function and Channelopathies. Handbook of Experimental Pharmacology, vol 246.* (ed. Chahine, M.) vol. 246 125–145 (Springer, Cham, 2017).

194. Lasiecka, Z. M. & Winckler, B. Mechanisms of polarized membrane trafficking in neurons — Focusing in on endosomes. *Mol. Cell. Neurosci.* **48**, 278–287 (2011).

195. Bao, L. Trafficking Regulates the Subcellular Distribution of Voltage-Gated Sodium Channels in Primary Sensory Neurons: *Mol. Pain* **11**, 61 (2015).

196. Su, Y.-Y. *et al.* KIF5B Promotes the Forward Transport and Axonal Function of the Voltage-Gated Sodium Channel Nav1.8. *J. Neurosci.* **33**, 17884–17896 (2013).

197. Poon, W.-Y. L., Malik-Hall, M., Wood, J. N. & Okuse, K. Identification of binding domains in the sodium channel Na $_V$ 1.8 intracellular N-terminal region and annexin II light chain p11. *FEBS Lett.* **558**, 114–118 (2004).

198. Laedermann, C. J., Syam, N., Pertin, M., Decosterd, I. & Abriel, H. β1- and β3- voltage-gated sodium channel subunits modulate cell surface expression and glycosylation of Nav1.7 in HEK293 cells. *Front. Cell. Neurosci.* **7**, (2013).

199. Chew, L. A. & Khanna, R. CRMP2 and voltage-gated ion channels: potential roles in neuropathic pain. *Neuronal Signal.* **2**, 20170220 (2018).

200. Gomez, K., Ran, D., Madura, C. L., Moutal, A. & Khanna, R. Non-SUMOylated CRMP2 decreases Na V 1.7 currents via the endocytic proteins Numb, Nedd4-2 and Eps15. *Mol. Brain 2021 141* **14**, 1–11 (2021).

201. Yang, Y. *et al.* Mutations in SCN9A, encoding a sodium channel alpha subunit, in patients with primary erythermalgia. *J. Med. Genet.* **41**, 171–174 (2004).

202. Fertleman, C. R. *et al.* SCN9A Mutations in Paroxysmal Extreme Pain Disorder: Allelic Variants Underlie Distinct Channel Defects and Phenotypes. *Neuron* **52**, 767–774 (2006).

203. Goldberg, Y. P. *et al.* Loss-of-function mutations in the Nav1.7 gene underlie congenital indifference to pain in multiple human populations. *Clin. Genet.* **71**, 311–319 (2007).

204. Nilsen, K. B. *et al.* Two novel SCN9A mutations causing insensitivity to pain. *Pain* **143**, 155–158 (2009).

205. Shaikh, S. S., Nahorski, M. S., Rai, H. & Woods, C. G. Before progressing from “exomes” to “genomes”… don’t forget splicing variants. *Eur. J. Hum. Genet.* **26**, 1559–1562 (2018).

206. Marchi, M. *et al.* A novel SCN9A splicing mutation in a compound heterozygous girl with congenital insensitivity to pain, hyposmia and hypogeusia. *J. Peripher. Nerv. Syst.* **23**, 202–206 (2018).

207. Cox, J. J. *et al.* Congenital insensitivity to pain: Novel SCN9A missense and in-frame deletion mutations. *Hum. Mutat.* **31**, (2010).

208. Emery, E. C. *et al.* Novel SCN9A mutations underlying extreme pain phenotypes: Unexpected electrophysiological and clinical phenotype correlations. *J. Neurosci.* **35**, 7674–7681 (2015).

209. Sun, J. *et al.* Novel SCN9A missense mutations contribute to congenital insensitivity to pain: Unexpected correlation between electrophysiological characterization and clinical phenotype. *Mol. Pain* **16**, (2020).

210. Duzkale, H. *et al.* A systematic approach to assessing the clinical significance of genetic variants. *Clin. Genet.* **84**, 453–463 (2013).

211. Ahmad, S. *et al.* A stop codon mutation in SCN9A causes lack of pain sensation. *Hum. Mol. Genet.* **16**, 2114–2121 (2007).

212. He, W. *et al.* Functional confirmation that the R1488* variant in SCN9A results in complete loss-of-function of Na v 1.7. *BMC Med. Genet.* **19**, (2018).

213. Staud, R. *et al.* Two novel mutations of SCN9A (Nav1.7) are associated with partial congenital insensitivity to pain. *Eur. J. Pain* **15**, 223–230 (2011).

214. Shorer, Z., Wajsbrot, E., Liran, T. H., Levy, J. & Parvari, R. A novel mutation in SCN9A in a child with congenital insensitivity to pain. *Pediatr. Neurol.* **50**, 73–76 (2014).

215. Palma, J.-A. *et al.* Expanding the Genotypic Spectrum of Congenital Sensory and Autonomic Neuropathies Using Whole-Exome Sequencing. *Neurol. Genet.* **7**, e568 (2021).

216. Ramirez, J. D. *et al.* Null mutation in scn9a in which noxious stimuli can be detected in the absence of pain. *Neurology* vol. 83 1577–1580 (2014).

217. Wheeler, D. W., Lee, M. C. H., Harrison, E. K., Menon, D. K. & Woods, C. G. Case Report: Neuropathic pain in a patient with congenital insensitivity to pain. *F1000Research* **3**, (2015).

218. Minett, M. S. *et al.* Endogenous opioids contribute to insensitivity to pain in humans and mice lacking sodium channel Nav1.7. *Nat. Commun.* **6**, (2015).

219. OMIM Entry - # 256800 - INSENSITIVITY TO PAIN, CONGENITAL, WITH ANHIDROSIS; CIPA. https://www.omim.org/entry/256800.

220. OMIM Entry - # 608654 - NEUROPATHY, HEREDITARY SENSORY AND AUTONOMIC, TYPE V; HSAN5. https://www.omim.org/entry/608654.

221. Gasparotti, R., Padua, L., Briani, C. & Lauria, G. New technologies for the assessment of neuropathies. *Nat. Rev. Neurol.* **13**, 203–216 (2017).

222. Gingras, J. *et al.* Global Nav1.7 knockout mice recapitulate the phenotype of human congenital indifference to pain. *PLoS One* **9**, (2014).

223. Weiss, J. *et al.* Loss-of-function mutations in sodium channel Na v 1.7 cause anosmia. *Nature* **472**, 186–192 (2011).

224. Wangzhou, A. *et al.* Pharmacological target-focused transcriptomic analysis of native vs cultured human and mouse dorsal root ganglia. *Pain* **161**, 1497–1517 (2020).

225. Nassar, M. A. *et al.* Nociceptor-specific gene deletion reveals a major role for Nav 1.7 (PN1) in acute and inflammatory pain. *Proc. Natl. Acad. Sci. U. S. A.* **101**, 12706–12711 (2004).

226. Nassar, M. A., Levato, A., Stirling, L. C. & Wood, J. N. Neuropathic pain develops normally in mice lacking both Nav 1.7 and Nav 1.8. *Mol. Pain* **1**, (2005).

227. Minett, M. S. *et al.* Distinct Nav1.7-dependent pain sensations require different sets of sensory and sympathetic neurons. *Nat. Commun.* **3**, (2012).

228. Shields, S. D. *et al.* Sodium channel NA v1.7 is essential for lowering heat pain threshold after burn injury. *J. Neurosci.* **32**, 10819–10832 (2012).

229. de Greef, B. T. A. *et al.* Lacosamide in patients with Nav1.7 mutations-related small fibre neuropathy: a randomized controlled trial. *Brain* **142**, 263–275 (2019).

230. Blesneac, I. *et al.* Rare NaV1.7 variants associated with painful diabetic peripheral neuropathy. *Pain* **159**, 469–480 (2018).

231. Li, Y. *et al.* DRG Voltage-Gated Sodium Channel 1.7 Is Upregulated in Paclitaxel-Induced Neuropathy in Rats and in Humans with Neuropathic Pain. *J. Neurosci.* **38**, 1124–1136 (2018).

232. Hoffmann, T. *et al.* NaV1.7 and pain: contribution of peripheral nerves. *Pain* **159**, 496–506 (2018).

233. Isensee, J. *et al.* Synergistic regulation of serotonin and opioid signaling contribute to pain insensitivity in Nav1.7 knockout mice. *Sci. Signal.* **10**, (2017).

234. Pereira, V. *et al.* Analgesia linked to nav1.7 loss of function requires μ-and δ-opioid receptors [version 1; referees: 2 approved]. *Wellcome Open Res.* **3**, (2018).

235. Waxman, S. G. *et al.* Sodium channel genes in pain-related disorders: Phenotype-genotype associations and recommendations for clinical use. *The Lancet Neurology* vol. 13 1152–1160 (2014).

236. Bateman, A. *et al.* UniProt: The universal protein knowledgebase in 2021. *Nucleic Acids Res.* **49**, D480–D489 (2021).

237. Sievers, F. *et al.* Fast, scalable generation of high-quality protein multiple sequence alignments using Clustal Omega. *Mol. Syst. Biol.* **7**, (2011).

238. Waterhouse, A. M., Procter, J. B., Martin, D. M. A. A., Clamp, M. & Barton, G. J. Jalview Version 2--a multiple sequence alignment editor and analysis workbench. *Bioinformatics* **25**, 1189–1191 (2009).

239. Adzhubei, I. A. *et al.* A method and server for predicting damaging missense mutations. *Nature Methods* vol. 7 248–249 (2010).

240. Shen, H., Liu, D., Wu, K., Lei, J. & Yan, N. Structures of human Na v 1.7 channel in complex with auxiliary subunits and animal toxins. *Science (80-.).* **363**, 1303–1308 (2019).

241. Pettersen, E. F. *et al.* UCSF Chimera - A visualization system for exploratory research and analysis. *J. Comput. Chem.* **25**, 1605–1612 (2004).

242. Shapovalov, M. V. & Dunbrack, R. L. A smoothed backbone-dependent rotamer library for proteins derived from adaptive kernel density estimates and regressions. *Structure* **19**, 844–858 (2011).

243. Hillen, W. & Berens, C. Mechanisms underlying expression of Tn10 encoded tetracycline resistance. *Annual Review of Microbiology* vol. 48 345–369 (1994).

244. Feldman, D. H. & Lossin, C. The Nav channel bench series: Plasmid preparation. *MethodsX* **1**, 6–11 (2014).

245. Lieu, P. T. *et al.* Generation of site-specific retargeting platform cell lines for drug discovery using phiC31 and R4 integrases. *J. Biomol. Screen.* **14**, 1207–1215 (2009).

246. Huff, J. The Airyscan detector from ZEISS: confocal imaging with improved signal-to-noise ratio and super-resolution. *Nat. Methods* **12**, i–ii (2015).

247. Hamill, O. P., Marty, A., Neher, E., Sakmann, B. & Sigworth, F. J. Improved patch-clamp techniques for high-resolution current recording from cells and cell-free membrane patches. *Pflügers Arch. Eur. J. Physiol.* **391**, 85–100 (1981).

248. Ogden, D. & Stanfield, P. Patch clamp techniques for single channel and whole-cell recording. in *Microelectrode techniques. The Plymouth Workshop Handbook.* 53–78 (The Company of Biologists Ltd, Cambridge, 1994).

249. Adzhubei, I., Jordan, D. M. & Sunyaev, S. R. Predicting Functional Effect of Human Missense Mutations Using PolyPhen-2. *Protoc. Hum. Genet* **76**, (2013).

250. Dustrude, E. T., Wilson, S. M., Ju, W., Xiao, Y. & Khanna, R. CRMP2 protein SUMOylation modulates NaV1.7 channel trafficking. *J. Biol. Chem.* **288**, 24316–24331 (2013).

251. VC, J. *et al.* LV-pIN-KDEL: a novel lentiviral vector demonstrates the morphology, dynamics and continuity of the endoplasmic reticulum in live neurones. *BMC Neurosci.* **9**, 1–12 (2008).

252. Hall, A. R. *et al.* Visualizing Mutation-Specific Differences in the Trafficking-Deficient Phenotype of Kv11.1 Proteins Linked to Long QT Syndrome Type 2. *Front. Physiol.* **0**, 584 (2018).

253. Goldenthal, K. L., Hedman, K., Chen, J. W., August, J. T. & Willingham, M. C. Postfixation detergent treatment for immunofluorescence suppresses localization of some integral membrane proteins.: *J. Histochem. Cytochem.* **33**, 813–820 (1985).

254. Jonkman, J., Brown, C. M., Wright, G. D., Anderson, K. I. & North, A. J. Tutorial: guidance for

quantitative confocal microscopy. *Nat. Protoc. 2020 155* **15**, 1585–1611 (2020).

255. Butler, R. *et al.* Use of the Site-Specific Retargeting Jump-In Platform Cell Line to Support Biologic Drug Discovery: *J. Biomol. Screen.* **20**, 528–535 (2014).

256. Gui, J. *et al.* Multiple Loss-of-Function Mechanisms Contribute to SCN5A-Related Familial Sick Sinus Syndrome. *PLoS One* **5**, e10985 (2010).

257. Blasi, R. Di, Marbiah, M. M., Siciliano, V., Polizzi, K. & Ceroni, F. A call for caution in analysing mammalian co-transfection experiments and implications of resource competition in data misinterpretation. *Nat. Commun. 2021 121* **12**, 1–6 (2021).

258. Han, C. *et al.* Early- and late-onset inherited erythromelalgia: genotype–phenotype correlation. *Brain* **132**, 1711–1722 (2009).

259. Ben-Shalom, R. *et al.* Opposing Effects on NaV1.2 Function Underlie Differences Between SCN2A Variants Observed in Individuals With Autism Spectrum Disorder or Infantile Seizures. *Biol. Psychiatry* **82**, 224–232 (2017).

260. Manganas, L. N. *et al.* Episodic Ataxia Type-1 Mutations in the Kv1.1 Potassium Channel Display Distinct Folding and Intracellular Trafficking Properties *. *J. Biol. Chem.* **276**, 49427–49434 (2001).

261. Marangoni, S. *et al.* A Brugada syndrome mutation (p.S216L) and its modulation by p.H558R polymorphism: standard and dynamic characterization. *Cardiovasc. Res.* **91**, 606–616 (2011).

262. Schlief, T., Schönherr, R., Imoto, K. & Heinemann, S. H. Pore properties of rat brain II sodium channels mutated in the selectivity filter domain. *Eur. Biophys. J.* **25**, 75–91 (1996).

263. Naylor, C. E. *et al.* Molecular basis of ion permeability in a voltage-gated sodium channel. *EMBO J.* **35**, 820–830 (2016).

264. Wang, J. W. *et al.* Prevalence of SCN1A mutations in children with suspected Dravet syndrome and intractable childhood epilepsy. *Epilepsy Res.* **102**, 195–200 (2012).

265. Betts, M. & Russell, R. Amino-acid properties and consequences of subsitutions. in *Bioinformatics for Geneticists* (ed. Barnes, M.) (Wiley, 2007).

266. Requião, R. D. *et al.* Protein charge distribution in proteomes and its impact on translation. *PLOS Comput. Biol.* **13**, e1005549 (2017).

267. Casey, J. R., Grinstein, S. & Orlowski, J. Sensors and regulators of intracellular pH. *Nat. Rev. Mol. Cell Biol. 2009 111* **11**, 50–61 (2009).

268. Liao, W.-P. *et al.* Partial epilepsy with antecedent febrile seizures and seizure aggravation by antiepileptic drugs: Associated with loss of function of Nav1.1. *Epilepsia* **51**, 1669–1678 (2010).

269. Volkers, L. *et al.* Na v1.1 dysfunction in genetic epilepsy with febrile seizures-plus or Dravet syndrome. *Eur. J. Neurosci.* **34**, 1268–1275 (2011).

270. Kapplinger, J. D. *et al.* An international compendium of mutations in the SCN5A-encoded cardiac sodium channel in patients referred for Brugada syndrome genetic testing. *Hear. Rhythm* **7**, 33–46 (2010).

271. Zhang, Y. *et al.* Correlations between clinical and physiological consequences of the novel mutation R878C in a highly conserved pore residue in the cardiac Na+ channel. *Acta Physiol.* **194**, 311–323 (2008).

272. Pfahnl, A. E. *et al.* A Sodium Channel Pore Mutation Causing Brugada Syndrome. *Hear. Rhythm* **4**, 46 (2007).

273. Zuberi, S. M. *et al.* Genotype–phenotype associations in SCN1A-related epilepsies. *Neurology* **76**, 594 LP – 600 (2011).

274. Núñez, L. *et al.* p.D1690N Nav1.5 rescues p.G1748D mutation gating defects in a compound

heterozygous Brugada syndrome patient. *Hear. Rhythm* **10**, 264–272 (2013).

275. Mancardi, M. M. *et al.* Familial Occurrence of Febrile Seizures and Epilepsy in Severe Myoclonic Epilepsy of Infancy (SMEI) Patients with SCN1A Mutations. *Epilepsia* **47**, 1629–1635 (2006).

276. Pan, X. *et al.* Structure of the human voltage-gated sodium channel Nav1.4 in complex with β1. *Science (80-.).* **362**, (2018).

277. Pan, X. *et al.* Molecular basis for pore blockade of human Na+ channel Nav1.2 by the μ-conotoxin KIIIA. *Science (80-.).* **363**, 1309–1313 (2019).

278. Pan, X. *et al.* Comparative structural analysis of human Nav1.1 and Nav1.5 reveals mutational hotspots for sodium channelopathies. *Proc. Natl. Acad. Sci.* **118**, (2021).

279. Shen, H. *et al.* Structure of a eukaryotic voltage-gated sodium channel at near-atomic resolution. *Science (80-.).* **355**, (2017).

280. Fux, J. E., Mehta, A., Moffat, J. & Spafford, J. D. Eukaryotic Voltage-Gated Sodium Channels: On Their Origins, Asymmetries, Losses, Diversification and Adaptations. *Front. Physiol.* **0**, 1406 (2018).

281. Lee, A. & Goldin, A. L. Role of the terminal domains in sodium channel localization. *Channels (Austin)* **3**, (2009).

282. Garrido, J. J. *et al.* Identification of an axonal determinant in the C-terminus of the sodium channel Nav1.2. *EMBO J.* **20**, 5950–5961 (2001).

283. Matamoros, M. *et al.* Nav1.5 N-terminal domain binding to α1-syntrophin increases membrane density of human Kir2.1, Kir2.2 and Nav1.5 channels. *Cardiovasc. Res.* **110**, 279–290 (2016).

284. Mantegazza, M., Yu, F. H., Catterall, W. A. & Scheuer, T. Role of the C-terminal domain in inactivation of brain and cardiac sodium channels. *Proc. Natl. Acad. Sci.* **98**, 15348–15353 (2001).

285. Lee, A. & Goldin, A. L. Role of the amino and carboxy termini in isoform-specific sodium channel variation. *J. Physiol.* **586**, 3917–3926 (2008).

286. Nguyen, H. M. & Goldin, A. L. Sodium Channel Carboxyl-terminal Residue Regulates Fast Inactivation *. *J. Biol. Chem.* **285**, 9077–9089 (2010).

287. Rivolta, I. *et al.* Inherited Brugada and Long QT-3 Syndrome Mutations of a Single Residue of the Cardiac Sodium Channel Confer Distinct Channel and Clinical Phenotypes *. *J. Biol. Chem.* **276**, 30623–30630 (2001).

288. Wu, F., Gordon, E., Hoffman, E. P. & Cannon, S. C. A C-terminal skeletal muscle sodium channel mutation associated with myotonia disrupts fast inactivation. *J. Physiol.* **565**, 371–380 (2005).

289. Gade, A. R., Marx, S. O. & Pitt, G. S. An interaction between the III-IV linker and CTD in NaV1.5 confers regulation of inactivation by CaM and FHF. *J. Gen. Physiol.* **152**, (2020).

290. Yan, H., Wang, C., Marx, S. & Pitt, G. Calmodulin limits pathogenic Na+ channel persistent current. *J. Gen. Physiol.* **149**, 277–293 (2017).

291. Isbell, H. M., Kilpatrick, A. M., Lin, Z., Mahling, R. & Shea, M. A. Backbone resonance assignments of complexes of apo human calmodulin bound to IQ motif peptides of voltage-dependent sodium channels NaV1.1, NaV1.4 and NaV1.7. *Biomol. NMR Assignments 2018 122* **12**, 283–289 (2018).

292. Yoder, J. B. *et al.* Ca2+-dependent regulation of sodium channels NaV1.4 and NaV1.5 is controlled by the post-IQ motif. *Nat. Commun. 2019 101* **10**, 1–12 (2019).

293. Nathan, S. *et al.* Structural basis of cytoplasmic NaV1.5 and NaV1.4 regulation. *J. Gen. Physiol.* **153**, (2021).

294. Herzog, R. I., Liu, C., Waxman, S. G. & Cummins, T. R. Calmodulin Binds to the C Terminus of Sodium Channels Nav1.4 and Nav1.6 and Differentially Modulates Their Functional Properties. *J. Neurosci.* **23**, 8261–8270 (2003).

295. Vijayaragavan, K., Acharfi, S. & Chahine, M. The C-terminal region as a modulator of rNav1.7 and rNav1.8 expression levels. *FEBS Lett.* **559**, 39–44 (2004).

296. Zhou, X. *et al.* A Chimeric NaV1.8 Channel Expression System Based on HEK293T Cell Line. *Front. Pharmacol.* **0**, 337 (2018).

297. Sizova, D. V. *et al.* A 49-residue sequence motif in the C terminus of Nav1.9 regulates trafficking of the channel to the plasma membrane. *J. Biol. Chem.* **295**, 1077–1090 (2020).

298. Effraim, P. R. *et al.* Fibroblast growth factor homologous factor 2 (FGF-13) associates with Nav1.7 in DRG neurons and alters its current properties in an isoform-dependent manner. *Neurobiol. Pain* **6**, 100029 (2019).

299. Dong, C., Wang, Y., Ma, A. & Wang, T. Life Cycle of the Cardiac Voltage-Gated Sodium Channel NaV1.5. *Front. Physiol.* **0**, 1581 (2020).

300. Solé, L. & Tamkun, M. M. Trafficking mechanisms underlying Nav channel subcellular localization in neurons. *Channels (Austin)* **14**, 1–17 (2019).

301. Tyrrell, L., Renganathan, M., Dib-Hajj, S. D. & Waxman, S. G. Glycosylation Alters Steady-State Inactivation of Sodium Channel Nav1.9/NaN in Dorsal Root Ganglion Neurons and Is Developmentally Regulated. *J. Neurosci.* **21**, 9629–9637 (2001).

302. Bennett, E. S. Isoform-specific effects of sialic acid on voltage-dependent Na+ channel gating: functional sialic acids are localized to the S5-S6 loop of domain I. *J. Physiol.* **538**, 675–690 (2002).

303. Mercier, A. *et al.* Nav1.5 channels can reach the plasma membrane through distinct N-glycosylation states. *Biochim. Biophys. Acta - Gen. Subj.* **1850**, 1215–1223 (2015).

304. Ednie, A. R., Harper, J. M. & Bennett, E. S. Sialic acids attached to N- and O-glycans within the Nav1.4 D1S5–S6 linker contribute to channel gating. *Biochim. Biophys. Acta - Gen. Subj.* **1850**, 307–317 (2015).

305. Zhang, Z.-N. *et al.* The voltage-gated Na+ channel Nav1.8 contains an ER-retention/retrieval signal antagonized by the β3 subunit. *J. Cell Sci.* **121**, 3243–3252 (2008).

306. Biskup, C., Zimmer, T. & Benndorf, K. FRET between cardiac Na+ channel subunits measured with a confocal microscope and a streak camera. *Nat. Biotechnol. 2004 222* **22**, 220–224 (2004).

307. Wandinger-Ness, A. & Zerial, M. Rab Proteins and the Compartmentalization of the Endosomal System. *Cold Spring Harb. Perspect. Biol.* **6**, a022616 (2014).

308. Zhang, X.-L. *et al.* Palmitoylation of δ-catenin promotes kinesin-mediated membrane trafficking of Nav1.6 in sensory neurons to promote neuropathic pain. *Sci. Signal.* **11**, (2018).

309. Kanellopoulos, A. H. *et al.* Mapping protein interactions of sodium channel Na V 1.7 using epitope-tagged gene-targeted mice. *EMBO J.* **37**, 427–445 (2018).

310. Dash, B., Han, C., Waxman, S. G. & Dib-Hajj, S. D. Nonmuscle myosin II isoforms interact with sodium channel alpha subunits. *Mol. Pain* **14**, (2018).

311. Barry, J. *et al.* Ankyrin-G Directly Binds to Kinesin-1 to Transport Voltage-Gated Na+ Channels into Axons. *Dev. Cell* **28**, 117–131 (2014).

312. Kretschmer, T. *et al.* Painful human neuromas: a potential role for a structural transmembrane protein, ankyrin G. *J. Neurosurg.* **97**, 1424–1431 (2002).

313. Black, J. A., Nikolajsen, L., Kroner, K., Jensen, T. S. & Waxman, S. G. Multiple sodium channel isoforms and mitogen-activated protein kinases are present in painful human neuromas. *Ann. Neurol.* **64**, 644–653 (2008).

314. Lemaillet, G., Walker, B. & Lambert, S. Identification of a Conserved Ankyrin-binding Motif in the Family of Sodium Channel α Subunits *. *J. Biol. Chem.* **278**, 27333–27339 (2003).

315. Miserey-Lenkei, S. *et al.* Rab and actomyosin-dependent fission of transport vesicles at the Golgi

complex. *Nat. Cell Biol. 2010 127* **12**, 645–654 (2010).

316. Awabdh, S. Al *et al.* A New Vesicular Scaffolding Complex Mediates the G-Protein-Coupled 5-HT1A Receptor Targeting to Neuronal Dendrites. *J. Neurosci.* **32**, 14227–14241 (2012).

317. Serra-Marques, A. *et al.* Concerted action of kinesins kif5b and kif13b promotes efficient secretory vesicle transport to microtubule plus ends. *Elife* **9**, 1–37 (2020).

318. Jensen, C. S. *et al.* Specific Sorting and Post-Golgi Trafficking of Dendritic Potassium Channels in Living Neurons *. *J. Biol. Chem.* **289**, 10566–10581 (2014).

319. Xu, K., Zhong, G. & Zhuang, X. Actin, Spectrin, and Associated Proteins Form a Periodic Cytoskeletal Structure in Axons. *Science (80-.).* **339**, 452–456 (2013).

320. D'Este, E. *et al.* Subcortical cytoskeleton periodicity throughout the nervous system. *Sci. Reports 2016 61* **6**, 1–8 (2016).

321. Leterrier, C. Putting the axonal periodic scaffold in order. *Curr. Opin. Neurobiol.* **69**, 33–40 (2021).

322. Costa, A. R. & Sousa, M. M. The role of the membrane-associated periodic skeleton in axons. *Cell. Mol. Life Sci. 2021 7813* **78**, 5371–5379 (2021).

323. Ratcliffe, C. F., Westenbroek, R. E., Curtis, R. & Catterall, W. A. Sodium channel β1 and β3 subunits associate with neurofascin through their extracellular immunoglobulin-like domain. *J. Cell Biol.* **154**, 427–434 (2001).

324. Koticha, D. *et al.* Neurofascin interactions play a critical role in clustering sodium channels, ankyrinG and βIV spectrin at peripheral nodes of Ranvier. *Dev. Biol.* **293**, 1–12 (2006).

325. Desmazieres, A. *et al.* Differential Stability of PNS and CNS Nodal Complexes When Neuronal Neurofascin Is Lost. *J. Neurosci.* **34**, 5083–5088 (2014).

326. Zollinger, D. R., Baalman, K. L. & Rasband, M. N. The Ins and Outs of Polarized Axonal Domains. *Annu. Rev. Cell Dev. Biol.* **31**, 647–667 (2015).

327. Laedermann, C. J. *et al.* Dysregulation of voltage-gated sodium channels by ubiquitin ligase NEDD4-2 in neuropathic pain. *J. Clin. Invest.* **123**, 3002–3013 (2013).

328. Dustrude, E. T. *et al.* Hierarchical CRMP2 posttranslational modifications control NaV1.7 function. *Proc. Natl. Acad. Sci.* **113**, E8443–E8452 (2016).

329. Francois-Moutal, L. *et al.* Inhibition of the Ubc9 E2 SUMO-conjugating enzyme-CRMP2 interaction decreases NaV1.7 currents and reverses experimental neuropathic pain. *Pain* **159**, 2115–2127 (2018).

330. Moutal, A. *et al.* CRMP2–Neurofibromin Interface Drives NF1-related Pain. *Neuroscience* **381**, 79–90 (2018).

331. de Macedo, F. H. P. *et al.* TNF-α mediated upregulation of Na V 1.7 currents in rat dorsal root ganglion neurons is independent of CRMP2 SUMOylation. *Mol. Brain 2019 121* **12**, 1–14 (2019).

332. Moutal, A., Ji, Y., Bellampalli, S. S. & Khanna, R. Differential expression of Cdk5-phosphorylated CRMP2 following a spared nerve injury. *Mol. Brain 2020 131* **13**, 1–13 (2020).

333. Moutal, A. *et al.* Studies on CRMP2 SUMOylation-deficient transgenic mice identify sex-specific Nav1.7 regulation in the pathogenesis of chronic neuropathic pain. *Pain* **161**, 2629–2651 (2020).

334. François-Moutal, L. *et al.* Chemical shift perturbation mapping of the Ubc9-CRMP2 interface identifies a pocket in CRMP2 amenable for allosteric modulation of Nav1.7 channels. *Channels (Austin)* **12**, 219–227 (2018).

335. Burel, S. *et al.* C-terminal phosphorylation of NaV1.5 impairs FGF13-dependent regulation of channel inactivation. *J. Biol. Chem.* **292**, 17431–17448 (2017).

336. Sokolov, M. V. *et al.* Co-expression of β Subunits with the Voltage-Gated Sodium Channel NaV1.7: the

Importance of Subunit Association and Phosphorylation and Their Effects on Channel Pharmacology and Biophysics. *J. Mol. Neurosci. 2018 652* **65**, 154–166 (2018).

337. Persson, A. K., Gasser, A., Black, J. A. & Waxman, S. G. NaV1.7 accumulates and co-localizes with phosphorylated ERK1/2 within transected axons in early experimental neuromas. *Exp. Neurol.* **230**, 273–279 (2011).

338. Stamboulian, S. *et al.* ERK1/2 Mitogen-Activated Protein Kinase Phosphorylates Sodium Channel Nav1.7 and Alters Its Gating Properties. *J. Neurosci.* **30**, 1637–1647 (2010).

339. Yan, J., Melemedjian, O. K., Price, T. J. & Dussor, G. Sensitization of Dural Afferents Underlies Migraine-Related Behavior following Meningeal Application of Interleukin-6 (IL-6): *Mol. Pain* **8**, (2012).

340. Chattopadhyay, M., Mata, M. & Fink, D. J. Continuous δ-Opioid Receptor Activation Reduces Neuronal Voltage-Gated Sodium Channel (NaV1.7) Levels through Activation of Protein Kinase C in Painful Diabetic Neuropathy. *J. Neurosci.* **28**, 6652–6658 (2008).

341. Ji, R. R., Gereau IV, R. W., Malcangio, M. & Strichartz, G. R. MAP kinase and pain. *Brain Res. Rev.* **60**, 135–148 (2009).

342. Vijayaragavan, K., Boutjdir, M. & Chahine, M. Modulation of Nav1.7 and Nav1.8 Peripheral Nerve Sodium Channels by Protein Kinase A and Protein Kinase C. *J. Neurophysiol.* **91**, 1556–1569 (2004).

343. Few, W. P., Scheuer, T. & Catterall, W. A. Dopamine modulation of neuronal Na+ channels requires binding of A kinase-anchoring protein 15and PKA by a modified leucine zipper motif. *Proc. Natl. Acad. Sci.* **104**, 5187–5192 (2007).

344. Tan, Z.-Y. *et al.* Protein kinase C enhances human sodium channel hNav1.7 resurgent currents via a serine residue in the domain III–IV linker. *FEBS Lett.* **588**, 3964–3969 (2014).

345. Kerth, C. M., Hautvast, P., Körner, J., Lampert, A. & Meents, J. E. Phosphorylation of a chronic pain mutation in the voltage-gated sodium channel Nav1.7 increases voltage sensitivity. *J. Biol. Chem.* **296**, 100227 (2021).

346. Li, Y. *et al.* Nav1.7 is phosphorylated by Fyn tyrosine kinase which modulates channel expression and gating in a cell type-dependent manner: *Mol. Pain* **14**, (2018).

347. Iqbal, S. M., Aufy, M., Shabbir, W. & Lemmens-Gruber, R. Identification of phosphorylation sites and binding pockets for modulation of NaV1.5 channel by Fyn tyrosine kinase. *FEBS J.* **285**, 2520–2530 (2018).

348. Beacham, D., Ahn, M., Catterall, W. A. & Scheuer, T. Sites and Molecular Mechanisms of Modulation of NaV1.2 Channels by Fyn Tyrosine Kinase. *J. Neurosci.* **27**, 11543–11551 (2007).

349. Ahern, C. A., Zhang, J.-F., Wookalis, M. J. & Horn, R. Modulation of the Cardiac Sodium Channel NaV1.5 by Fyn, a Src Family Tyrosine Kinase. *Circ. Res.* **96**, 991–998 (2005).

350. Yang, L. *et al.* FGF13 Selectively Regulates Heat Nociception by Interacting with Nav1.7. *Neuron* **93**, 806-821.e9 (2017).

351. Vijayaragavan, K., O'Leary, M. E. & Chahine, M. Gating Properties of Nav1.7 and Nav1.8 Peripheral Nerve Sodium Channels. *J. Neurosci.* **21**, 7909–7918 (2001).

352. Ho, C., Zhao, J., Malinowski, S., Chahine, M. & O'Leary, M. E. Differential Expression of Sodium Channel β Subunits in Dorsal Root Ganglion Sensory Neurons *. *J. Biol. Chem.* **287**, 15044–15053 (2012).

353. Theile, J. W., Jarecki, B. W., Piekarz, A. D. & Cummins, T. R. Nav1.7 mutations associated with paroxysmal extreme pain disorder, but not erythromelalgia, enhance Navβ4 peptide-mediated resurgent sodium currents. *J. Physiol.* **589**, 597–608 (2011).

354. Alsaloum, M. *et al.* A gain-of-function sodium channel β2-subunit mutation in painful diabetic neuropathy: *Mol. Pain* **15**, 1–14 (2019).

355. Alsaloum, M. *et al.* A novel gain-of-function sodium channel β2 subunit mutation in idiopathic small fiber neuropathy. *J. Neurophysiol.* (2021) doi:10.1152/JN.00184.2021.

356. Malik-Hall, M., Poon, W. Y. L., Baker, M. D., Wood, J. N. & Okuse, K. Sensory neuron proteins interact with the intracellular domains of sodium channel NaV1.8. *Mol. Brain Res.* **110**, 298–304 (2003).

357. Wildburger, N. C. *et al.* Quantitative Proteomics Reveals Protein–Protein Interactions with Fibroblast Growth Factor 12 as a Component of the Voltage-Gated Sodium Channel 1.2 (Nav1.2) Macromolecular Complex in Mammalian Brain*. *Mol. Cell. Proteomics* **14**, 1288–1300 (2015).

358. Chew, L. A., Bellampalli, S. S., Dustrude, E. T. & Khanna, R. Mining the Nav1.7 interactome: Opportunities for chronic pain therapeutics. *Biochem. Pharmacol.* **163**, 9–20 (2019).

359. Kreimer, S. *et al.* Advanced Precursor Ion Selection Algorithms for Increased Depth of Bottom-Up Proteomic Profiling. *J. Proteome Res.* **15**, 3563–3573 (2016).

360. Costello, A. *et al.* Leaky Expression of the TET-On System Hinders Control of Endogenous miRNA Abundance. *Biotechnol. J.* **14**, (2019).

361. Jin, J. *et al.* Ahnak scaffolds p11/Anxa2 complex and L-type voltage-gated calcium channel and modulates depressive behavior. *Mol. Psychiatry* **25**, 1035–1049 (2019).

362. Okuse, K. *et al.* Annexin II light chain regulates sensory neuron-specific sodium channel expression. *Nature* **417**, 653–656 (2002).

363. Cox, J. *et al.* Accurate Proteome-wide Label-free Quantification by Delayed Normalization and Maximal Peptide Ratio Extraction, Termed MaxLFQ *. *Mol. Cell. Proteomics* **13**, 2513–2526 (2014).

364. Čuklina, J., Pedrioli, P. G. A. & Aebersold, R. Review of Batch Effects Prevention, Diagnostics, and Correction Approaches. *Methods Mol. Biol.* **2051**, 373–387 (2020).

365. Davis, T. A., Loos, B. & Engelbrecht, A. M. AHNAK: The giant jack of all trades. *Cell. Signal.* **26**, 2683–2693 (2014).

366. Dempsey, B. R. *et al.* Structure of an Asymmetric Ternary Protein Complex Provides Insight for Membrane Interaction. *Structure* **20**, 1737–1745 (2012).

367. Foulkes, T. *et al.* Deletion of Annexin 2 Light Chain p11 in Nociceptors Causes Deficits in Somatosensory Coding and Pain Behavior. *J. Neurosci.* **26**, 10499–10507 (2006).

368. Petrecca, K., Miller, D. M. & Shrier, A. Localization and Enhanced Current Density of the Kv4.2 Potassium Channel by Interaction with the Actin-Binding Protein Filamin. *J. Neurosci.* **20**, 8736–8744 (2000).

369. Grou, C. P., Pinto, M. P., Mendes, A. V., Domingues, P. & Azevedo, J. E. The de novo synthesis of ubiquitin: identification of deubiquitinases acting on ubiquitin precursors. *Sci. Reports 2015 51* **5**, 1–16 (2015).

370. Kobayashi, M. *et al.* The ubiquitin hybrid gene UBA52 regulates ubiquitination of ribosome and sustains embryonic development. *Sci. Reports 2016 61* **6**, 1–11 (2016).

371. García-Cano, J., Martinez-Martinez, A., Sala-Gaston, J., Pedrazza, L. & Rosa, J. L. HERCing: Structural and Functional Relevance of the Large HERC Ubiquitin Ligases. *Front. Physiol.* **0**, 1014 (2019).

372. Galligan, J. T. *et al.* Proteomic Analysis and Identification of Cellular Interactors of the Giant Ubiquitin Ligase HERC2. *J. Proteome Res.* **14**, 953–966 (2014).

373. Valnegri, P. *et al.* RNF8/UBC13 ubiquitin signaling suppresses synapse formation in the mammalian brain. *Nat. Commun. 2017 81* **8**, 1–15 (2017).

374. Al-Hakim, A. K., Bashkurov, M., Gingras, A.-C., Durocher, D. & Pelletier, L. Interaction Proteomics Identify NEURL4 and the HECT E3 Ligase HERC2 as Novel Modulators of Centrosome Architecture *. *Mol. Cell. Proteomics* **11**, M111.014233 (2012).

375. Kliza, K. & Husnjak, K. Resolving the Complexity of Ubiquitin Networks. *Front. Mol. Biosci.* **0**, 21 (2020).

376. Kiss, A., Erdődi, F. & Lontay, B. Myosin phosphatase: Unexpected functions of a long-known enzyme. *Biochim. Biophys. Acta - Mol. Cell Res.* **1866**, 2–15 (2019).

377. Oughtred, R. *et al.* The BioGRID database: A comprehensive biomedical resource of curated protein, genetic, and chemical interactions. *Protein Sci.* **30**, 187–200 (2021).

378. Vicente-Manzanares, M., Ma, X., Adelstein, R. S. & Horwitz, A. R. Non-muscle myosin II takes centre stage in cell adhesion and migration. *Nat. Rev. Mol. Cell Biol. 2009 1011* **10**, 778–790 (2009).

379. Stephens, D. J. & Banting, G. Direct Interaction of the trans-Golgi Network Membrane Protein, TGN38, with the F-actin Binding Protein, Neurabin. *J. Biol. Chem.* **274**, 30080–30086 (1999).

380. Berger, S. L. *et al.* Localized Myosin II Activity Regulates Assembly and Plasticity of the Axon Initial Segment. *Neuron* **97**, 555-570.e6 (2018).

381. Costa, A. R. *et al.* The membrane periodic skeleton is an actomyosin network that regulates axonal diameter and conduction. *Elife* **9**, (2020).

382. Terry-Lorenzo, R. T. *et al.* Neurabin/Protein Phosphatase-1 Complex Regulates Dendritic Spine Morphogenesis and Maturation. *Mol. Biol. Cell* **16**, 2349–2362 (2005).

383. Hu, X., Huang, Q., Yang, X. & Xia, H. Differential Regulation of AMPA Receptor Trafficking by Neurabin-Targeted Synaptic Protein Phosphatase-1 in Synaptic Transmission and Long-Term Depression in Hippocampus. *J. Neurosci.* **27**, 4674–4686 (2007).

384. Cho, K. F. *et al.* Proximity labeling in mammalian cells with TurboID and split-TurboID. *Nat. Protoc. 2020 1512* **15**, 3971–3999 (2020).

385. Qin, W., Cho, K. F., Cavanagh, P. E. & Ting, A. Y. Deciphering molecular interactions by proximity labeling. *Nat. Methods 2021 182* **18**, 133–143 (2021).

386. Bantscheff, M., Schirle, M., Sweetman, G., Rick, J. & Kuster, B. Quantitative mass spectrometry in proteomics: a critical review. *Anal. Bioanal. Chem. 2007 3894* **389**, 1017–1031 (2007).

387. Fumasoni, I. *et al.* Family expansion and gene rearrangements contributed to the functional specialization of PRDM genes in vertebrates. *BMC Evol. Biol.* **7**, (2007).

388. Fog, C. K., Galli, G. G. & Lund, A. H. PRDM proteins: Important players in differentiation and disease. *BioEssays* vol. 34 50–60 (2012).

389. Herz, H. M., Garruss, A. & Shilatifard, A. SET for life: Biochemical activities and biological functions of SET domain-containing proteins. *Trends in Biochemical Sciences* vol. 38 621–639 (2013).

390. Kouzarides, T. Chromatin Modifications and Their Function. *Cell* vol. 128 693–705 (2007).

391. Wu, H. *et al.* Structural biology of human H3K9 methyltransferases. *PLoS One* **5**, (2010).

392. Hohenauer, T. & Moore, A. W. The Prdm family: Expanding roles in stem cells and development. *Development (Cambridge)* vol. 139 2267–2282 (2012).

393. Zannino, D. A. & Sagerström, C. G. An emerging role for prdm family genes in dorsoventral patterning of the vertebrate nervous system. *Neural Development* vol. 10 (2015).

394. Brzezinski IV, J. A., Lamba, D. A. & Reh, T. A. Blimp1 controls photoreceptor versus bipolar cell fate choice during retinal development. *Development* **137**, 619–629 (2010).

395. Crotty, S., Johnston, R. J. & Schoenberger, S. P. Effectors and memories: Bcl-6 and Blimp-1 in T and B lymphocyte differentiation. *Nature Immunology* vol. 11 114–120 (2010).

396. Ross, S. E. *et al.* Bhlhb5 and Prdm8 Form a Repressor Complex Involved in Neuronal Circuit Assembly. *Neuron* **73**, 292–303 (2012).

397. Hanotel, J. *et al.* The Prdm13 histone methyltransferase encoding gene is a Ptf1a-Rbpj downstream target that suppresses glutamatergic and promotes GABAergic neuronal fate in the dorsal neural tube. *Dev. Biol.* **386**, 340–357 (2014).

398. Mona, B. *et al.* Repression by PRDM13 is critical for generating precision in neuronal identity. *Elife* **6**, (2017).

399. Yang, C. M. & Shinkai, Y. Prdm12 is induced by retinoic acid and exhibits anti-proliferative properties through the cell cycle modulation of P19 embryonic carcinoma cells. *Cell Struct. Funct.* **38**, 195–204 (2013).

400. Yildiz, O., Downes, G. B. & Sagerström, C. G. Zebrafish prdm12b acts independently of nkx6.1 repression to promote eng1b expression in the neural tube p1 domain. *Neural Dev.* **14**, (2019).

401. Kinameri, E. *et al.* Prdm proto-oncogene transcription factor family expression and interaction with the Notch-Hes pathway in mouse neurogenesis. *PLoS One* **3**, (2008).

402. Woo, J., Kang, H., Lee, E. Y., Park, S. & Cho, Y. E. Investigation of PRDM7 and PRDM12 expression pattern during mouse embryonic development by using a modified passive clearing technique. *Biochem. Biophys. Res. Commun.* **524**, 346–353 (2020).

403. Zannino, D. A., Downes, G. B. & Sagerström, C. G. Prdm12b specifies the p1 progenitor domain and reveals a role for V1 interneurons in swim movements. *Dev. Biol.* **390**, 247–260 (2014).

404. Hael, C. E., Rojo, D., Orquera, D. P., Low, M. J. & Rubinstein, M. The transcriptional regulator PRDM12 is critical for Pomc expression in the mouse hypothalamus and controlling food intake, adiposity, and body weight. *Mol. Metab.* **34**, 43–53 (2020).

405. Chen, X. *et al.* Comparative transcriptomic analyses of developing melanocortin neurons reveal new regulators for the anorexigenic neuron identity. *J. Neurosci.* **40**, 3165–3177 (2020).

406. Matsukawa, S., Miwata, K., Asashima, M. & Michiue, T. The requirement of histone modification by PRDM12 and Kdm4a for the development of pre-placodal ectoderm and neural crest in Xenopus. *Dev. Biol.* **399**, 164–176 (2015).

407. Nagy, V. *et al.* The evolutionarily conserved transcription factor PRDM12 controls sensory neuron development and pain perception. *Cell Cycle* **14**, 1799–1808 (2015).

408. Zhang, S. *et al.* Clinical features for diagnosis and management of patients with PRDM12 congenital insensitivity to pain. *J. Med. Genet.* **53**, 533–535 (2016).

409. Saini, A. G. *et al.* Hereditary Sensory Polyneuropathy, Pain Insensitivity and Global Developmental Delay due to Novel Mutation in PRDM12 Gene. *Indian Journal of Pediatrics* vol. 84 332–333 (2017).

410. Meienberg, J. *et al.* New insights into the performance of human whole-exome capture platforms. *Nucleic Acids Res.* **43**, (2015).

411. Lauria, G. *et al.* EFNS guidelines on the use of skin biopsy in the diagnosis of peripheral neuropathy. *European Journal of Neurology* vol. 12 747–758 (2005).

412. Kaur, J., Singanamalla, B., Suresh, R. G. & Saini, A. G. Insensitivity to Pain, Self-mutilation, and Neuropathy Associated With PRDM12. *Pediatr. Neurol.* **110**, 95–96 (2020).

413. Gilbert, S. F. Formation of the Neural Tube. in *Developmental Biology* (Sinauer Associates, 2000).

414. Lee, H. Y. *et al.* Instructive Role of Wnt/β-Catenin in Sensory Fate Specification in Neural Crest Stem Cells. *Science (80-.).* **303**, 1020–1023 (2004).

415. Kléber, M. *et al.* Neural crest stem cell maintenance by combinatorial Wnt and BMP signaling. *J. Cell Biol.* **169**, 309–320 (2005).

416. Kim, J., Lo, L., Dormand, E. & Anderson, D. J. SOX10 maintains multipotency and inhibits neuronal differentiation of neural crest stem cells. *Neuron* **38**, 17–31 (2003).

417. Taneyhill, L. A. & Schiffmacher, A. T. Should I stay or should I go? Cadherin function and regulation in the neural crest. *Genesis* vol. 55 (2017).

418. Clay, M. R. & Halloran, M. C. Control of neural crest cell behavior and migration: Insights from live imaging. *Cell Adhesion and Migration* vol. 4 586–594 (2010).

419. Kasemeir-Kulesa, J. C., Kulesa, P. M. & Lefcort, F. Imaging neural crest cell dynamics during formation of dorsal root ganglia and sympathetic ganglia. *Development* **132**, 235–245 (2005).

420. Honjo, Y., Kniss, J. & Eisen, J. S. Neuregulin-mediated ErbB3 signaling is required for formation of zebrafish dorsal root ganglion neurons. *Development* **135**, 2615–2625 (2008).

421. Bononi, J., Cole, A., Tewson, P., Schumacher, A. & Bradley, R. Chicken protocadherin-1 functions to localize neural crest cells to the dorsal root ganglia during PNS formation. *Mech. Dev.* **125**, 1033–1047 (2008).

422. Pla, P. & Monsoro-Burq, A. H. The neural border: Induction, specification and maturation of the territory that generates neural crest cells. *Developmental Biology* vol. 444 S36–S46 (2018).

423. Thawani, A. & Groves, A. K. Building the Border: Development of the Chordate Neural Plate Border Region and Its Derivatives. *Frontiers in Physiology* vol. 11 (2020).

424. Pattyn, A., Morin, X., Cremer, H., Goridis, C. & Brunet, J. F. The homeobox gene Phox2b is essential for the development of autonomic neural crest derivatives. *Nature* **399**, 366–370 (1999).

425. Stanke, M., Stubbusch, J. & Rohrer, H. Interaction of Mash1 and Phox2b in sympathetic neuron development. *Mol. Cell. Neurosci.* **25**, 374–382 (2004).

426. Ma, Q., Fode, C., Guillemot, F. & Anderson, D. J. NEUROGENIN1 and NEUROGENIN2 control two distinct waves of neurogenesis in developing dorsal root ganglia. *Genes Dev.* **13**, 1717–1728 (1999).

427. Montelius, A. *et al.* Emergence of the sensory nervous system as defined by Foxs1 expression. *Differentiation* **75**, 404–417 (2007).

428. Dykes, I. M., Tempest, L., Lee, S. I. & Turner, E. E. Brn3a and Islet1 act epistatically to regulate the gene expression program of sensory differentiation. *J. Neurosci.* **31**, 9789–9799 (2011).

429. Smith, M. D. *et al.* Brn-3a activates the expression of Bcl-xL and promotes neuronal survival in vivo as well as in vitro. *Mol. Cell. Neurosci.* **17**, 460–470 (2001).

430. Huang, E. J. *et al.* POU domain factor Brn-3a controls the differentiation and survival of trigeminal neurons by regulating Trk receptor expression. *Development* **126**, 2869–2882 (1999).

431. Rifkin, J. T., Todd, V. J., Anderson, L. W. & Lefcort, F. Dynamic expression of neurotrophin receptors during sensory neuron genesis and differentiation. *Dev. Biol.* **227**, 465–480 (2000).

432. Kramer, I. *et al.* A role for Runx transcription factor signaling in dorsal root ganglion sensory neuron diversification. *Neuron* **49**, 379–393 (2006).

433. Luo, W., Enomoto, H., Rice, F. L., Milbrandt, J. & Ginty, D. D. Molecular Identification of Rapidly Adapting Mechanoreceptors and Their Developmental Dependence on Ret Signaling. *Neuron* **64**, 841–856 (2009).

434. Marmigère, F. & Ernfors, P. Specification and connectivity of neuronal subtypes in the sensory lineage. *Nature Reviews Neuroscience* vol. 8 114–127 (2007).

435. Bachy, I. *et al.* The transcription factor Cux2 marks development of an A-delta sublineage of TrkA sensory neurons. *Dev. Biol.* **360**, 77–86 (2011).

436. Ventéo, S. *et al.* Neurog2 Deficiency Uncovers a Critical Period of Cell Fate Plasticity and Vulnerability among Neural-Crest-Derived Somatosensory Progenitors. *Cell Rep.* **29**, 2953-2960.e2 (2019).

437. Maro, G. S. *et al.* Neural crest boundary cap cells constitute a source of neuronal and glial cells of the PNS. *Nat. Neurosci.* **7**, 930–938 (2004).

438. Gresset, A. *et al.* Boundary Caps Give Rise to Neurogenic Stem Cells and Terminal Glia in the Skin. *Stem Cell Reports* **5**, 278–290 (2015).

439. Hasegawa, H., Abbott, S., Han, B. X., Qi, Y. & Wang, F. Analyzing somatosensory axon projections with the sensory neuron-specific Advillin gene. *J. Neurosci.* **27**, 14404–14414 (2007).

440. Hunter, D. V. *et al.* Advillin is expressed in all adult neural crest-derived neurons. *eNeuro* **5**, (2018).

441. Lallemend, F. & Ernfors, P. Molecular interactions underlying the specification of sensory neurons. *Trends in Neurosciences* vol. 35 373–381 (2012).

442. Sun, Y. *et al.* A central role for Islet1 in sensory neuron development linking sensory and spinal gene regulatory programs. *Nat. Neurosci.* **11**, 1283–1293 (2008).

443. Lanier, J., Dykes, I. M., Nissen, S., Eng, S. R. & Turner, E. E. Brn3a regulates the transition from neurogenesis to terminal differentiation and represses non-neural gene expression in the trigeminal ganglion. *Dev. Dyn.* **238**, 3065–3079 (2009).

444. Scott-Solomon, E. & Kuruvilla, R. Mechanisms of neurotrophin trafficking via Trk receptors. *Molecular and Cellular Neuroscience* vol. 91 25–33 (2018).

445. Cheng, I., Jin, L., Rose, L. C. & Deppmann, C. D. Temporally restricted death and the role of p75NTR as a survival receptor in the developing sensory nervous system. *Dev. Neurobiol.* **78**, 701–717 (2018).

446. Ménard, M. *et al.* The dependence receptor TrkC regulates the number of sensory neurons during DRG development. *Dev. Biol.* **442**, 249–261 (2018).

447. Wang, Y. *et al.* A cell fitness selection model for neuronal survival during development. *Nat. Commun.* **10**, (2019).

448. Wiggins, A. K. *et al.* Interaction of Brn3a and HIPK2 mediates transcriptional repression of sensory neuron survival. *J. Cell Biol.* **167**, 257–267 (2004).

449. Hudson, C. D., Morris, P. J., Latchman, D. S. & Budhram-Mahadeo, V. S. Brn-3a transcription factor blocks p53-mediated activation of proapoptotic target genes Noxa and Bax in vitro and in vivo to determine cell fate. *J. Biol. Chem.* **280**, 11851–11858 (2005).

450. Ma, L., Lei, L., Eng, S. R., Turner, E. & Parada, L. F. Brn3a regulation of TrkA/NGF receptor expression in developing sensory neurons. *Development* **130**, 3525–3534 (2003).

451. Lei, L., Zhou, J., Lin, L. & Parada, L. F. Brn3a and Klf7 cooperate to control TrkA expression in sensory neurons. *Dev. Biol.* **300**, 758–769 (2006).

452. Marmigère, F. *et al.* The Runx1/AML1 transcription factor selectively regulates development and survival of TrkA nociceptive sensory neurons. *Nat. Neurosci.* **9**, 180–187 (2006).

453. Inoue, K. I. *et al.* The transcription factor Runx3 represses the neurotrophin receptor TrkB during lineage commitment of dorsal root ganglion neurons. *J. Biol. Chem.* **282**, 24175–24184 (2007).

454. Senzaki, K., Ozaki, S., Yoshikawa, M., Ito, Y. & Shiga, T. Runx3 is required for the specification of TrkC-expressing mechanoreceptive trigeminal ganglion neurons. *Mol. Cell. Neurosci.* **43**, 296–307 (2010).

455. Scott, A. *et al.* Transcription factor short stature homeobox 2 is required for proper development of tropomyosin-related kinase B-expressing mechanosensory neurons. *J. Neurosci.* **31**, 6741–6749 (2011).

456. Abdo, H. *et al.* Dependence on the transcription factor Shox2 for specification of sensory neurons conveying discriminative touch. *Eur. J. Neurosci.* **34**, 1529–1541 (2011).

457. Gascon, E. *et al.* Hepatocyte growth factor-met signaling is required for Runx1 extinction and peptidergic differentiation in primary nociceptive neurons. *J. Neurosci.* **30**, 12414–12423 (2010).

458. Yoshikawa, M. *et al.* Runx1 selectively regulates cell fate specification and axonal projections of dorsal root ganglion neurons. *Dev. Biol.* **303**, 663–674 (2007).

459. Molliver, D. C. *et al.* IB4-binding DRG neurons switch from NGF to GDNF dependence in early postnatal life. *Neuron* **19**, 849–861 (1997).

460. Luo, W. *et al.* A Hierarchical NGF Signaling Cascade Controls Ret-Dependent and Ret-Independent Events during Development of Nonpeptidergic DRG Neurons. *Neuron* **54**, 739–754 (2007).

461. Qi, L. *et al.* Hierarchical specification of pruriceptors by runt-domain transcription factor runx1. *J. Neurosci.* **37**, 5549–5561 (2017).

462. Lou, S., Duan, B., Vong, L., Lowell, B. B. & Ma, Q. Runx1 controls terminal morphology and mechanosensitivity of VGLUT3-expressing C-Mechanoreceptors. *J. Neurosci.* **33**, 870–882 (2013).

463. Lou, S. *et al.* Incoherent feed-forward regulatory loops control segregation of C-mechanoreceptors, nociceptors, and pruriceptors. *J. Neurosci.* **35**, 5317–5329 (2015).

464. Qi, L. *et al.* Nuclear Factor I/A Controls A-fiber Nociceptor Development. *Neurosci. Bull.* **36**, 685–695 (2020).

465. Liu, Y. & Halloran, M. C. Central and peripheral axon branches from one neuron are guided differentially by semaphorin3D and transient axonal glycoprotein-1. *J. Neurosci.* **25**, 10556–10563 (2005).

466. Ma, L. & Tessier-Lavigne, M. Dual branch-promoting and branch-repelling actions of Slit/Robo signaling on peripheral and central branches of developing sensory axons. *J. Neurosci.* **27**, 6843–6851 (2007).

467. Watanabe, K. *et al.* Dorsally derived netrin 1 provides an inhibitory cue and elaborates the 'waiting period' for primary sensory axons in the developing spinal cord. *Development* **133**, 1379–1387 (2006).

468. Zhao, Z. & Ma, L. Regulation of axonal development by natriuretic peptide hormones. *Proc. Natl. Acad. Sci. U. S. A.* **106**, 18016–18021 (2009).

469. Kolodkin, A. L. *et al.* Neuropilin is a semaphorin III receptor. *Cell* **90**, 753–762 (1997).

470. Fu, S. Y., Sharma, K., Luo, Y., Raper, J. A. & Frank, E. *SEMA3A Regulates Developing Sensory Projections in the Chicken Spinal Cord*. *J Neurobiol* vol. 45 (2000).

471. Perrin, F. E., Rathjen, F. G. & Stoeckli, E. T. Distinct subpopulations of sensory afferents require F11 or axonin-1 for growth to their target layers within the spinal cord of the chick. *Neuron* **30**, 707–723 (2001).

472. Hancock, M. L., Nowakowski, D. W., Role, L. W., Talmage, D. A. & Flanagan, J. G. Type III neuregulin 1 regulates pathfinding of sensory axons in the developing spinal cord and periphery. *Development* **138**, 4887–4898 (2011).

473. Tymanskyj, S. R., Yang, B., Falnikar, A., Lepore, A. C. & Ma, L. MAP7 regulates axon collateral branch development in dorsal root ganglion neurons. *J. Neurosci.* **37**, 1648–1661 (2017).

474. Smeyne, R. J. *et al.* Severe sensory and sympathetic neuropathies in mice carrying a disrupted Trk/NGF receptor gene. *Nature* **368**, 246–249 (1994).

475. Hu, Z. L. *et al.* The role of the transcription factor Rbpj in the development of dorsal root ganglia. *Neural Dev.* **6**, (2011).

476. Bourane, S. *et al.* Low-Threshold Mechanoreceptor Subtypes Selectively Express MafA and Are Specified by Ret Signaling. *Neuron* **64**, 857–870 (2009).

477. Hill, M. Carnegie Stage Comparison. *Embryology* https://embryology.med.unsw.edu.au/embryology/index.php/Carnegie_Stage_Comparison (2021).

478. Laumet, G. *et al.* G9a is essential for epigenetic silencing of K+ channel genes in acute-to-chronic pain transition. *Nat. Neurosci.* **18**, 1746–1755 (2015).

479. Liang, L. *et al.* G9a participates in nerve injury-induced Kcna2 downregulation in primary sensory neurons. *Sci. Rep.* **6**, (2016).

480. Liang, L. *et al.* G9a inhibits CREB-triggered expression of mu opioid receptor in primary sensory neurons following peripheral nerve injury. *Mol. Pain* **12**, (2016).

481. Zhang, Y., Chen, S. R., Laumet, G., Chen, H. & Pan, H. L. Nerve injury diminishes opioid analgesia through lysine methyltransferase-mediated transcriptional repression of μ-opioid receptors in primary sensory neurons. *J. Biol. Chem.* **291**, 8475–8485 (2016).

482. Srinivas, S. M., Gowda, V. K., Owen, C. M., Moss, C. & Hiremagalore, R. Mid-face toddler excoriation syndrome (MiTES): a new paediatric diagnosis. *Clin. Exp. Dermatol.* **42**, 68–71 (2017).

483. Moss, C. *et al.* Midface toddler excoriation syndrome (MiTES) can be caused by autosomal recessive biallelic mutations in a gene for congenital insensitivity to pain, PRDM12. *Br. J. Dermatol.* **179**, 1135–1140 (2018).

484. Inamadar, A. C. A. C. *et al.* Extending the phenotype of midface toddler excoriation syndrome (MiTES): Five new cases in three families with PR domain containing protein 12 (PRDM12) mutations. *J. Am. Acad. Dermatol.* **81**, 1415–1417 (2019).

485. Noguera-Morel, L., Ortiz-Cabrera, N. V., Campos, M., Hernández-Martín, Á. & Torrelo, A. A case of mid-face toddler excoriation syndrome (MiTES). *Pediatr. Dermatol.* **37**, 345–346 (2020).

486. Kumar, P. & Das, A. Midface toddler excoriation syndrome. *Indian J. Dermatol. Venereol. Leprol.* **0**, 0 (2021).

487. Albrecht, A. & Mundlos, S. The other trinucleotide repeat: Polyalanine expansion disorders. *Current Opinion in Genetics and Development* vol. 15 285–293 (2005).

488. Messaed, C. & Rouleau, G. A. Molecular mechanisms underlying polyalanine diseases. *Neurobiology of Disease* vol. 34 397–405 (2009).

489. Hughes, J. N. & Thomas, P. Q. Molecular pathology of polyalanine expansion disorders: New perspectives from mouse models. *Methods Mol. Biol.* **1017**, 135–151 (2013).

490. Robinson, D. O. *et al.* Two cases of oculopharyngeal muscular dystrophy (OPMD) with the rare PABPN1 c.35G>C; p.Gly12Ala point mutation. *Neuromuscul. Disord.* **21**, 809–811 (2011).

491. Goodman, F. R. *et al.* Synpolydactyly phenotypes correlate with size of expansions in hoxd13 polyalanine tract. *Proc. Natl. Acad. Sci. U. S. A.* **94**, 7458–7463 (1997).

492. Matera, I. *et al.* PHOX2B mutations and polyalanine expansions correlate with the severity of the respiratory phenotype and associated symptoms in both congenital and late onset Central Hypoventilation syndrome. *J. Med. Genet.* **41**, 373–380 (2004).

493. Shoubridge, C., Fullston, T. & Gécz, J. ARX spectrum disorders: Making inroads into the molecular pathology. *Human Mutation* vol. 31 889–900 (2010).

494. Nallathambi, J. *et al.* A novel polyalanine expansion in FOXL2: The first evidence for a recessive form of the blepharophimosis syndrome (BPES) associated with ovarian dysfunction. *Hum. Genet.* **121**, 107–112 (2007).

495. Sivan, Y. *et al.* Congenital central hypoventilation syndrome: Severe disease caused by co-occurrence of two PHOX2B variants inherited separately from asymptomatic family members. *Am. J. Med. Genet. Part A* **179**, 503–506 (2019).

496. Veitia, R. A., Caburet, S. & Birchler, J. A. Mechanisms of Mendelian dominance. *Clinical Genetics* vol. 93 419–428 (2018).

497. Johnson, A. F., Nguyen, H. T. & Veitia, R. A. Causes and effects of haploinsufficiency. *Biol. Rev.* **94**, 1774–1785 (2019).

498. Migeon, B. R. X-linked diseases: susceptible females. *Genetics in Medicine* vol. 22 1156–1174 (2020).

499. Albrecht, A. N. *et al.* A molecular pathogenesis for transcription factor associated poly-alanine tract

expansions. *Hum. Mol. Genet.* **13**, 2351–2359 (2004).

500. Parodi, S. *et al.* The E3 ubiquitin ligase TRIM11 mediates the degradation of congenital central hypoventilation syndrome-associated polyalanine-expanded PHOX2B. *J. Mol. Med.* **90**, 1025–1035 (2012).

501. Innis, J. W. *et al.* Polyalanine expansion in HOXA13: Three new affected families and the molecular consequences in a mouse model. *Hum. Mol. Genet.* **13**, 2841–2851 (2004).

502. Villavicencio-Lorini, P. *et al.* Homeobox genes d11-d13 and a13 control mouse autopod cortical bone and joint formation. *J. Clin. Invest.* **120**, 1994–2004 (2010).

503. Hughes, J. *et al.* Mechanistic Insight into the Pathology of Polyalanine Expansion Disorders Revealed by a Mouse Model for X Linked Hypopituitarism. *PLoS Genet.* **9**, (2013).

504. Lee, K., Mattiske, T., Kitamura, K., Gecz, J. & Shoubridge, C. Reduced polyalanine-expanded arx mutant protein in developing mouse subpallium alters lmo1 transcriptional regulation. *Hum. Mol. Genet.* **23**, 1084–1094 (2014).

505. Tippmann, H. F. Analysis for free: comparing programs for sequence analysis. *Brief. Bioinform.* **5**, 82–87 (2004).

506. Nunes, V. S. & Moretti, N. S. Nuclear subcompartments: an overview. *Cell Biology International* vol. 41 2–7 (2017).

507. Chang, S. H., Chang, W. L., Lu, C. C. & Tarn, W. Y. Alanine repeats influence protein localization in splicing speckles and paraspeckles. *Nucleic Acids Res.* **42**, 13788–13798 (2014).

508. Klein, P. *et al.* Nuclear poly(A)-binding protein aggregates misplace a pre-mRNA outside of SC35 speckle causing its abnormal splicing. *Nucleic Acids Res.* **44**, 10929–10945 (2016).

509. Dominick, F., van Laarhoven, A. I. M., Evers, A. W. M. & Weisshaar, E. A systematic review of questionnaires on itch by the Special Interest Group “Questionnaires” of the International Forum for the Study of Itch (IFSI). *Itch* **4**, e26–e26 (2019).

510. Macarthur, D. G. *et al.* Guidelines for investigating causality of sequence variants in human disease. *Nat. 2014 5087497* **508**, 469–476 (2014).

511. Strande, N. T. *et al.* Evaluating the Clinical Validity of Gene-Disease Associations: An Evidence-Based Framework Developed by the Clinical Genome Resource. *Am. J. Hum. Genet.* **100**, 895–906 (2017).

512. Bengoechea, R. *et al.* Nuclear speckles are involved in nuclear aggregation of PABPN1 and in the pathophysiology of oculopharyngeal muscular dystrophy. *Neurobiol. Dis.* **46**, 118–129 (2012).

513. Basu, S. *et al.* Unblending of Transcriptional Condensates in Human Repeat Expansion Disease. *Cell* **181**, 1062-1079.e30 (2020).

514. Dobson, C. M. Principles of protein folding, misfolding and aggregation. in *Seminars in Cell and Developmental Biology* vol. 15 3–16 (Elsevier Ltd, 2004).

515. Caburet, S. *et al.* A recurrent polyalanine expansion in the transcription factor FOXL2 induces extensive nuclear and cytoplasmic protein aggregation. *J. Med. Genet.* **41**, 932–936 (2004).

516. Fullston, T. *et al.* Screening and cell-based assessment of mutations in the Aristaless-related homeobox (ARX) gene. *Clin. Genet.* **80**, 510–522 (2011).

517. Ramani, B. *et al.* A knockin mouse model of spinocerebellar ataxia type 3 exhibits prominent aggregate pathology and aberrant splicing of the disease gene transcript. *Hum. Mol. Genet.* **24**, 1211–1224 (2015).

518. Lebon, C., Behar-Cohen, F. & Torriglia, A. Cell Death Mechanisms in a Mouse Model of Retinal Degeneration in Spinocerebellar Ataxia 7. *Neuroscience* **400**, 72–84 (2019).

519. Ross, S. E. *et al.* Loss of Inhibitory Interneurons in the Dorsal Spinal Cord and Elevated Itch in Bhlhb5

Mutant Mice. *Neuron* **65**, 886–898 (2010).

520. Mona, B. *et al.* Positive autofeedback regulation of Ptf1a transcription generates the levels of PTF1A required to generate itch circuit neurons. *Genes Dev.* **34**, 621–636 (2020).

521. Escalante, A. & Klein, R. Spinal Inhibitory Ptf1a-Derived Neurons Prevent Self-Generated Itch. *Cell Rep.* **33**, (2020).

522. Acton, D. *et al.* Spinal Neuropeptide Y1 Receptor-Expressing Neurons Form an Essential Excitatory Pathway for Mechanical Itch. *Cell Rep.* **28**, 625-639.e6 (2019).

523. Pan, H. *et al.* Identification of a Spinal Circuit for Mechanical and Persistent Spontaneous Itch. *Neuron* **103**, 1135-1149.e6 (2019).

524. Chen, S. *et al.* A spinal neural circuitry for converting touch to itch sensation. *Nat. Commun.* **11**, (2020).

525. Nguyen, M. Q., Wu, Y., Bonilla, L. S., von Buchholtz, L. J. & Ryba, N. J. P. Diversity amongst trigeminal neurons revealed by high throughput single cell sequencing. *PLoS One* **12**, (2017).

526. Megat, S. *et al.* Differences between Dorsal Root and Trigeminal Ganglion Nociceptors in Mice Revealed by Translational Profiling. *J. Neurosci.* **39**, 6829–6847 (2019).

527. Luz, L. L. *et al.* Trigeminal Aδ- and C-afferent supply of lamina I neurons in the trigeminocervical complex. *Pain* **160**, 2612–2623 (2019).

528. Raisa Eng, S., Dykes, I. M., Lanier, J., Fedtsova, N. & Turner, E. E. POU-domain factor Brn3a regulates both distinct and common programs of gene expression in the spinal and trigeminal sensory ganglia. *Neural Dev.* **2**, (2007).

529. Eilbeck, K., Quinlan, A. & Yandell, M. Settling the score: variant prioritization and Mendelian disease. *Nat. Rev. Genet. 2017 1810* **18**, 599–612 (2017).

530. Glazer, A. M. *et al.* High-Throughput Reclassification of SCN5A Variants. *Am. J. Hum. Genet.* **107**, 111–123 (2020).

531. Ng, C.-A. *et al.* Heterozygous KCNH2 variant phenotyping using Flp-In HEK293 and high-throughput automated patch clamp electrophysiology. *Biol. Methods Protoc.* **6**, (2021).

532. Uezu, A. *et al.* Identification of an elaborate complex mediating postsynaptic inhibition. *Science (80-.).* **353**, 1123–1129 (2016).

533. Jackson, M. R. *et al.* Extensive phenotyping of two ARX polyalanine expansion mutation mouse models that span clinical spectrum of intellectual disability and epilepsy. *Neurobiol. Dis.* **105**, 245–256 (2017).

534. Alsaloum, M., Higerd, G. P., Effraim, P. R. & Waxman, S. G. Status of peripheral sodium channel blockers for non-addictive pain treatment. *Nat. Rev. Neurol. 2020 1612* **16**, 689–705 (2020).

535. Wulff, H., Christophersen, P., Colussi, P., Chandy, K. G. & Yarov-Yarovoy, V. Antibodies and venom peptides: new modalities for ion channels. *Nat. Rev. Drug Discov. 2019 185* **18**, 339–357 (2019).

536. Kingwell, K. Nav1.7 withholds its pain potential. *Nat. Rev. Drug Discov.* (2019) doi:10.1038/D41573-019-00065-0.

537. Eagles, D. A., Chow, C. Y. & King, G. F. Fifteen years of NaV1.7 channels as an analgesic target: Why has excellent in vitro pharmacology not translated into in vivo analgesic efficacy? *Br. J. Pharmacol.* (2020) doi:10.1111/BPH.15327.

538. Moreno, A. M. *et al.* Long-lasting analgesia via targeted in situ repression of NaV1.7 in mice. *Sci. Transl. Med.* **13**, 9056 (2021).

539. Yu, H. *et al.* AAV-encoded CaV2.2 peptide aptamer CBD3A6K for primary sensory neuron-targeted treatment of established neuropathic pain. *Gene Ther. 2019 267* **26**, 308–323 (2019).

540. Pryce, K. D. *et al.* Magi-1 scaffolds Nav1-8 and Slack KNa channels in dorsal root ganglion neurons

regulating excitability and pain. *FASEB J.* **33**, 7315–7330 (2019).

541. He, Y. T. *et al.* A synthetic peptide disturbing GluN2A/SHP1 interaction in dorsal root ganglion attenuated pathological pain. *Eur. J. Pharmacol.* **854**, 62–69 (2019).

542. Ma, L., Merenmies, J. & Parada, L. F. Molecular characterization of the TrkA/NGF receptor minimal enhancer reveals regulation by multiple cis elements to drive embryonic neuron expression. *Development* **127**, 3777–3788 (2000).

543. Exe, N., Ferguson, H., Krokosky, A., Sawyer, S. & Terry, S. *Genetic Testing Stories*. *Genetic Testing Stories* (Genetic Alliance, 2006).

544. Burke, W., Zimmern, R. L. & Kroese, M. Defining purpose: a key step in genetic test evaluation. *Genet. Med. 2007 910* **9**, 675–681 (2007).

545. Katsanis, S. H. & Katsanis, N. Molecular genetic testing and the future of clinical genomics. *Nat. Rev. Genet. 2013 146* **14**, 415–426 (2013).

546. Weck, K. E. Interpretation of genomic sequencing: variants should be considered uncertain until proven guilty. *Genet. Med. 2018 203* **20**, 291–293 (2018).

547. Clarke, L. *et al.* The international Genome sample resource (IGSR): A worldwide collection of genome variation incorporating the 1000 Genomes Project data. *Nucleic Acids Res.* **45**, D854–D859 (2017).

548. Karczewski, K. J. *et al.* The mutational constraint spectrum quantified from variation in 141,456 humans. *Nat. 2020 5817809* **581**, 434–443 (2020).

549. Singh, N. A. *et al.* A Role of SCN9A in Human Epilepsies, As a Cause of Febrile Seizures and As a Potential Modifier of Dravet Syndrome. *PLOS Genet.* **5**, e1000649 (2009).

550. Fasham, J. *et al.* No association between SCN9A and monogenic human epilepsy disorders. *PLOS Genet.* **16**, e1009161 (2020).

551. Kumar, P., Henikoff, S. & Ng, P. C. Predicting the effects of coding non-synonymous variants on protein function using the SIFT algorithm. *Nat. Protoc. 2009 47* **4**, 1073–1081 (2009).

552. Heyne, H. O. *et al.* Predicting functional effects of missense variants in voltage-gated sodium and calcium channels. *Sci. Transl. Med.* **12**, 6848 (2020).

553. Kapetis, D. *et al.* Network topology of NaV1.7 mutations in sodium channel-related painful disorders. *BMC Syst. Biol. 2017 111* **11**, 1–16 (2017).

554. Xenakis, M. N. *et al.* Hydropathicity-based prediction of pain-causing NaV1.7 variants. *BMC Bioinforma. 2021 221* **22**, 1–24 (2021).

555. Chen, Y.-J. *et al.* Electrophysiological Differences between the Same Pore Region Mutation in SCN1A and SCN3A. *Mol. Neurobiol. 2014 513* **51**, 1263–1270 (2014).

556. Amarouch, M.-Y. & Abriel, H. Cellular hyper-excitability caused by mutations that alter the activation process of voltage-gated sodium channels. *Front. Physiol.* **0**, 45 (2015).

557. Yang, Y. *et al.* Reverse pharmacogenomics: carbamazepine normalizes activation and attenuates thermal hyperexcitability of sensory neurons due to Nav1.7 mutation I234T. *Br. J. Pharmacol.* **175**, 2261–2271 (2018).

558. Labau, J. I. R. *et al.* Differential effect of lacosamide on Nav1.7 variants from responsive and non-responsive patients with small fibre neuropathy. *Brain* **143**, 771–782 (2020).

559. Musto, E., Gardella, E. & Møller, R. S. Recent advances in treatment of epilepsy-related sodium channelopathies. *Eur. J. Paediatr. Neurol.* **24**, 123–128 (2020).

560. Balestrini, S. *et al.* Real-life survey of pitfalls and successes of precision medicine in genetic epilepsies. *J. Neurol. Neurosurg. Psychiatry* **0**, 1–9 (2021).

CHAPTER 7: Appendix

Appendix A: Reported biophysical properties of WT Nav1.7 expressed in HEK293 cells

ICS: intracellular solution; **CsF:** caesium fluoride; **CsAsp:** caesium aspartate; **CsCl:** caesium chloride; **n.d.:** not determined

BETA SUBUNITS PRESENT?	ICS MAJOR CATION	V_{50} ACTIVATION (mV)	V_{50} FAST INACTIVATION (mV)	PMID
none	135 mM CsAsp	-26.2 ± 1.6	-80.9 ± 1.4	18945915
none	110 mM CsCl	-14.0 ± 1.0	-64.0 ± 1.0	23836888
none	150 mM CsCl	-10.0 ± 0.7	-81.5 ± 1.3	22911851
β1 only	150 mM CsCl	-15.8 ± 1.8	-76.8 ± 2.2	22911851
β1 & β2	140 mM CsCl	-8.3 ± 0.5	-51.2 ± 0.6	23292638
β1 & β2	140 mM CsCl	-2.6 ± 1.3	-59.3 ± 3.1	24866741
none	140 mM CsF	-29.9 ± 1.3	-86.6 ± 1.4	29176367
none	140 mM CsF	-21.5 ± 1.7	-75.4 ± 1.3	23376079
none	140 mM CsF	-18.5 ± 1.1	-79.0 ± 0.5	25575597
none	140 mM CsF	-9.5 ± 1.1	-64.6 ± 1.3	29335280
β1 & β2	107 mM CsF	-28.0 ± 1.0	-71.0 ± 1.0	17167479
β1 & β2	140 mM CsF	-28.9 ± 0.2	-77.6 ± 0.1	18599537
β1 & β2	140 mM CsF	-24.6 ± 1.1	-73.6 ± 1.1	15385606
β1 & β2	140 mM CsF	-17.2 ± 1.1	-80.2 ± 1.4	28381558
β1 & β2	140 mM CsF	n.d.	-77.5 ± 1.4	21232038

Appendix B: Sequencing Primers for *SCN9A* constructs

NB: At the time of design, we were still using manual ABI sequencing machine. Trace quality was decreasing, hence the number of primers to ensure ample coverage of the whole insert.

PRIMER PAIR	FORWARD PRIMER	REVERSE PRIMER
1	CACGCTGTTTTGACCTCCAT	GCGTAGTAGGGGTCCAGATC
2	AGCTGCCCTTCATCTACGG	TGGTCATGAAGATGCAGTTGG
3	GCTGATCATGTGCACCATCC	TGATGGTTTTCAGGGCCCG
4	CTGGACTTCGTGGTGATCGT	ATGCTTTCCAGGGTCTCGTT
5	CACAAGTGCTTCCGGAACAG	TCTCAGGGTCTGCTGGTACA
6	TACACCAGCTTCGACACCTT	GGCCTCTTCCTGCTCTTTCT
7	CCAACATCGAGGAAGCCAAG	CTGATGCTGTCCTCGCTCT
8	GGCGGAAGAAGAAGAACCAG	GAAGATGCTGTGCTCGTCG
9	TTCAGCTTCAAGGGCAGAGG	GTGGATCTGATTGGTGGTGC
10	GAGCAGCAACATCAGCCAG	TCAGAAACTTGTGGGCGAAC
11	GAAGAGTCCCGGCAGAAATG	TAAGGGTCCATGGCGATCAG
12	AGAACGTGCTGGCCATCG	GCACCAGGGTCAGATTGC
13	GTGTTCAAGCTGGCCAAGAG	CTTCCATGCAGTCCCACATG
14	GCTGTGTGGCGAGTGGAT	GGCTGATCTTGGGCTTCTTG
15	CCCGGATCAAGAAAGGCATC	GGTTGTGGATGAAGCTCTGG
16	CGTGGACAAGCACCTGATG	GCTGTTCATGGGCTCGGC
17	GACTCCGAGTACAGCAAAGTG	CAGCAGCATTTCCAGGATGA
18	ACTCCTGGTTCGAGAGCTTT	ACGTTCATGATGGAGGGGAT
19	CAACACCCTGGGCTACTCC	AAAGCACTCGGACCGGTT
20	GGCAAGTTCTACGAGTGCAT	CCCGAAGATGATGAACACCAC
21	GGATAAGCAGCCCAAGTACG	ATGGAGATGTCGAAGGCCTG
22	ACAACGCCATGAAGAAGCTG	CAAAGATATTCCACCCCACGG
23	GAGTGCGTGCTGAAACTGAT	CATCACCAGAAACAGCAGCA
24	CTGTTCGCCCTGATGATGAG	GAAGTAGAAGATGCCCACGC
25	CATCCTGAACAGCAAGCCC	ATCGGACAGCTTGGAGAACT
26	CACCGAGCCTCTGAGCGA	TGAACCGCTCTTCCATCTGG
27	GACATCCTGTTCGCCTTCAC	GTTATCGAAGGCCATGTCCT
28	ACGACGACCTGCTGAACAAA	TAAACGGGCCCTCTAGACTC

Appendix C: MSA of Nav1.7 paralogues hNav family

```
hNav1.1      ---MEQTVLVPPGPDSFNFFTRESLAAIERRIAEEKAKNPKPD---KK-DDDENGPKPNS   53
hNav1.2      ---MAQSVLVPPGPDSFRFFTRESLAAIEQRIAEEKAKRPKQE---RKDEDDENGPKPNS   54
hNav1.3      ---MAQALLVPPGPESFRLFTRESLAAIEKRAAEEKAKKPKKE---Q-DNDDENKPKPNS   53
hNav1.4      MARPSLCTLVPLGPECLRPFTRESLAAIEQRAVEEEARLQRNK----QMEIEEPERKPRS   56
hNav1.5      ----MANFLLPRGTSSFRRFTRESLAAIEKRMAEKQARGSTTLQESREGLPEEEAPRPQL   56
hNav1.6      ---MAARLLAPPGPDSFKPFTPESLANIERRIAESKLKKPPKADGSHREDDEDSKPKPNS   57
hNav1.7      -----MAMLPPPGPQSFVHFTKQSLALIEQRIAERKSKEPKEE---KK-DDDEEAPKPSS   51
hNav1.8      ----MEFPIGSLETNNFRRFTPESLVEIEKQIAAKQGTKKARE-KHREQKDQEEKPRPQL   55
hNav1.9      -MDDRCYPVIFPDERNFRPFTSDSLAAIEKRIAIQKEKKKSKD-----QTGEVPQPRPQL   54
                    :       :  ** :**. **:: .  :               :    :*

hNav1.1      DLEAGKNLPFIYGDIPPEMVSEPLEDLDPYYINKKTFIVLNKGKAIFRFSATSALYILTP   113
hNav1.2      DLEAGKSLPFIYGDIPPEMVSVPLEDLDPYYINKKTFIVLNKGKAISRFSATPALYILTP   114
hNav1.3      DLEAGKNLPFIYGDIPPEMVSEPLEDLDPYYINKKTFIVMNKGKAIFRFSATSALYILTP   113
hNav1.4      DLEAGKNLPMIYGDPPPEVIGIPLEDLDPYYSNKKTFIVLNKGKAIFRFSATPALYLLSP   116
hNav1.5      DLQASKKLPDLYGNPPQELIGEPLEDLDPFYSTQKTFIVLNKGKTIFRFSATNALYVLSP   116
hNav1.6      DLEAGKSLPFIYGDIPQGLVAVPLEDFDPYYLTQKTFVVLNRGKTLFRFSATPALYILSP   117
hNav1.7      DLEAGKQLPFIYGDIPPGMVSEPLEDLDPYYADKKTFIVLNKGKTIFRFNATPALYMLSP   111
hNav1.8      DLKACNQLPKFYGELPAELIGEPLEDLDPFYSTHRTFMVLNKGRTISRFSATRALWLFSP   115
hNav1.9      DLKASRKLPKLYGDIPRELIGKPLEDLDPFYRNHKTFMVLNRKRTIYRFSAKHALFIFGP   114
             **:* ..** :**: *  ::. ****:**:*  ::**:*:*: ::: **.*. **::: *

hNav1.1      FNPLRKIAIKILVHSLFSMLIMCTILTNCVFMTMSNPP----DWTKNVEYTFTGIYTFES   169
hNav1.2      FNPIRKLAIKILVHSLFNMLIMCTILTNCVFMTMSNPP----DWTKNVEYTFTGIYTFES   170
hNav1.3      LNPVRKIAIKILVHSLFSMLIMCTILTNCVFMTLSNPP----DWTKNVEYTFTGIYTFES   169
hNav1.4      FSVVRRGAIKVLIHALFSMFIMITILTNCVFMTMSDPP----PWSKNVEYTFTGIYTFES   172
hNav1.5      FHPIRRAAVKILVHSLFNMLIMCTILTNCVFMAQHDPP----PWTKYVEYTFTAIYTFES   172
hNav1.6      FNLIRRIAIKILIHSVFSMIIMCTILTNCVFMTFSNPP----DWSKNVEYTFTGIYTFES   173
hNav1.7      FSPLRRISIKILVHSLFSMLIMCTILTNCIFMTMNNPP----DWTKNVEYTFTGIYTFES   167
hNav1.8      FNLIRRTAIKVSVHSWFSLFITVTILVNCVCMTRTDLP-------EKIEYVFTVIYTFEA   168
hNav1.9      FNSIRSLAIRVSVHSLFSMFIIGTVIINCVFMATGPAKNSNSNNTDIAECVFTGIYIFEA   174
             :  :*  :::: :*: *.::*  *:: **: *:           .  * .** ** **:

hNav1.1      LIKIIARGFCLEDFTFLRDPWNWLDFTVITFAYVTEFVDL-GNVSALRTFRVLRALKTIS   228
hNav1.2      LIKILARGFCLEDFTFLRDPWNWLDFTVITFAYVTEFVDL-GNVSALRTFRVLRALKTIS   229
hNav1.3      LIKILARGFCLEDFTFLRDPWNWLDFSVIVMAYVTEFVSL-GNVSALRTFRVLRALKTIS   228
hNav1.4      LIKILARGFCVDDFTFLRDPWNWLDFSVIMMAYLTEFVDL-GNISALRTFRVLRALKTIT   231
hNav1.5      LVKILARGFCLHAFTFLRDPWNWLDFSVIIMAYTTEFVDL-GNVSALRTFRVLRALKTIS   231
hNav1.6      LVKIIARGFCIDGFTFLRDPWNWLDFSVIMMAYITEFVNL-GNVSALRTFRVLRALKTIS   232
hNav1.7      LVKILARGFCVGEFTFLRDPWNWLDFVVIVFAYLTEFVNL-GNVSALRTFRVLRALKTIS   226
hNav1.8      LIKILARGFCLNEFTYLRDPWNWLDFSVITLAYVGTAIDL-RGISGLRTFRVLRALKTVS   227
hNav1.9      LIKILARGFILDEFSFLRDPWNWLDSIVIGIAIVSYIPGITIKLLPLRTFRVFRALKAIS   234
             *:**:**** :  *::*********  ** :*      .:   :  ******:****:::

hNav1.1      VIPGLKTIVGALIQSVKKLSDVMILTVFCLSVFALIGLQLFMGNLRNKCIQWPPTNASLE   288
hNav1.2      VIPGLKTIVGALIQSVKKLSDVMILTVFCLSVFALIGLQLFMGNLRNKCLQWPPDNSSFE   289
hNav1.3      VIPGLKTIVGALIQSVKKLSDVMILTVFCLSVFALIGLQLFMGNLRNKCLQWPPSDSAFE   288
hNav1.4      VIPGLKTIVGALIQSVKKLSDVMILTVFCLSVFALVGLQLFMGNLRQKCVRWPPPFNDTN   291
hNav1.5      VISGLKTIVGALIQSVKKLADVMVLTVFCLSVFALIGLQLFMGNLRHKCVRNFTALNGTN   291
hNav1.6      VIPGLKTIVGALIQSVKKLSDVMILTVFCLSVFALIGLQLFMGNLRNKCVVWPINFNE--   290
hNav1.7      VIPGLKTIVGALIQSVKKLSDVMILTVFCLSVFALIGLQLFMGNLKHKCFRNSLENNETL   286
hNav1.8      VIPGLKVIVGALIHSVKKLADVTILTIFCLSVFALVGLQLFKGNLKNKCVKNDMAVNETT   287
hNav1.9      VVSRLKVIVGALLRSVKKLVNVIILTFFCLSIFALVGQQLFMGSLNLKCISRDCKNISNP   294
             *:  **.*****::***** :* :**.****:***:* *** *.*. **.

hNav1.1      EHSIE-KNITVNYNG----------------------TLINETVFEFDWKSYIQDSRYHY   325
hNav1.2      INITSFFNNSLDGNG----------------------TTFNRTVSIFNWDEYIEDKSHFY   327
hNav1.3      TNTTSYFNGTMDSNG----------------------TFVNVTMSTFNWKDYIGDDSHFY   326
hNav1.4      TTW--YSNDTWYGNDTWYGNEMWYGNDSWYANDTWNSHASWATNDTFDWDAYISDEGNFY   349
hNav1.5      GSV--------EADG---------------------------LVWESLDLYLSDPENYL   315
hNav1.6      ------------------------------------SYLENGTKGFDWEEYINNKTNFY   313
hNav1.7      ESIM---------------------------------NT------LESEEDFRKYFY   304
hNav1.8      NYS-------------------------------------------SHRKPDIYI   299
hNav1.9      EAY-----------------------------------------------DHCFE   302
                                                                   .
```

```
hNav1.1      FLEGFLDALLCGNSSDAGQCPEGYMCVKAGRNPNYGYTSFDTFSWAFLSLFRLMTQDFWE   385
hNav1.2      FLEGQNDALLCGNSSDAGQCPEGYICVKAGRNPNYGYTSFDTFSWAFLSLFRLMTQDFWE   387
hNav1.3      VLDGQKDPLLCGNGSDAGQCPEGYICVKAGRNPNYGYTSFDTFSWAFLSLFRLMTQDYWE   386
hNav1.4      FLEGSNDALLCGNSSDAGHCPEGYECIKTGRNPNYGYTSYDTFSWAFLALFRLMTQDYWE   409
hNav1.5      LKNGTSDVLLCGNSSDAGTCPEGYRCLKAGENPDHGYTSFDSFAWAFLALFRLMTQDCWE   375
hNav1.6      TVPGMLEPLLCGNSSDAGQCPEGYQCMKAGRNPNYGYTSFDTFSWAFLALFRLMTQDYWE   373
hNav1.7      YLEGSKDALLCGFSTDSGQCPEGYTCVKIGRNPDYGYTSFDTFSWAFLALFRLMTQDYWE   364
hNav1.8      NKRGTSDPLLCGNGSDSGHCPDGYICLKTSDNPDFNYTSFDSFAWAFLSLFRLMTQDSWE   359
hNav1.9      KKENSPEFKMCGIWMGNSACSIQYECKHTKINPDYNYTNFDNFGWSFLAMFRLMTQDSWE   362
                .  :  :**   . . *   * * :   **:..**.:*.*.*:**::******* **

hNav1.1      NLYQLTLRAAGKTYMIFFVLVIFLGSFYLINLILAVVAMAYEEQNQATLEEAEQKEAEFQ   445
hNav1.2      NLYQLTLRAAGKTYMIFFVLVIFLGSFYLINLILAVVAMAYEEQNQATLEEAEQKEAEFQ   447
hNav1.3      NLYQLTLRAAGKTYMIFFVLVIFLGSFYLVNLILAVVAMAYEEQNQATLEEAEQKEAEFQ   446
hNav1.4      NLFQLTLRAAGKTYMIFFVVIIFLGSFYLINLILAVVAMAYAEQNEATLAEDKEKEEEFQ   469
hNav1.5      RLYQQTLRSAGKIYMIFFMLVIFLGSFYLVNLILAVVAMAYEEQNQATIAETEEKEKRFQ   435
hNav1.6      NLYQLTLRAAGKTYMIFFVLVIFVGSFYLVNLILAVVAMAYEEQNQATLEEAEQKEAEFK   433
hNav1.7      NLYQQTLRAAGKTYMIFFVVVIFLGSFYLINLILAVVAMAYEEQNQANIEEAKQKELEFQ   424
hNav1.8      RLYQQTLRTSGKIYMIFFVLVIFLGSFYLVNLILAVVTMAYEEQNQATTDEIEAKEKKFQ   419
hNav1.9      KLYQQTLRTTGLYSVFFFIVVIFLGSFYLINLTLAVVTMAYEEQNKNVAAEIEAKEKMFQ   422
             .*:* ***::*   ::**:::**:*****:** ****:*** ***:    * : **  *:

hNav1.1      QMIEQLKKQQEAAQQAATATASE--HS----REPSAAGRLSDSSSEASKLSSKSAKERRN   499
hNav1.2      QMLEQLKKQQEEAQAAAAAAASAESRDF----SGAGGIGVFSESSSVASKLSSKSEKELKN   503
hNav1.3      QMLEQLKKQQEEAQAVA-AASAASRDF----SGIGGLGELLESSSEASKLSSKSAKEWRN   501
hNav1.4      QMLEKFKKHQEELEKAKAAQALE-------------------------------------   492
hNav1.5      EAMEMLKKEHEALTIRGV------------------DTVSRSSLEMSPLAPVNSHERRS   476
hNav1.6      AMLEQLKKQQEEAQAAAMATSAGTVSEDAIEEEGEEGGGSPRSSSEISKLSSKSAKERRN   493
hNav1.7      QMLDRLKKEQEEAEAIAAAAAEY--TS----IRRSRIMGLSESSSETSKLSSKSAKERRN   478
hNav1.8      EALEMLRKEQEVLAALGIDTT------------------SLHSHNGSPLTSKNASERRH   460
hNav1.9      EAQQLLKEEKEALVAMGIDRSSL------------------TSLETSYFTPKKRKLFGN   463
                : :::.:*

hNav1.1      RRKKRKQKEQSGGEEKD-EDEFQKSESEDSIRRKGFRFSIEGNRLTYEKRYSSPHQSLLS   558
hNav1.2      RRKKKKQKEQSGEE--EKNDRVRKSESEDSIRRKGFRFSLEGSRLTYEKRFSSPHQSLLS   561
hNav1.3      RRKKRRQREHLEGNNKGERDSFPKSESEDSVKRSSFLFSMDGNRLTSDKKFCSPHQSLLS   561
hNav1.4      -----------GGEADGDPAH-------------------------------------   502
hNav1.5      KR----RKRMSSGTEECGEDRLPKSDSEDGPRAMNHLSLTRG--------LSRT------   518
hNav1.6      RRKKRKQKELSEGEEKGDPEKVFKSESEDGMRRKAFRLPDNR----IGRKFSIMNQSLLS   549
hNav1.7      RRKKKNQKKLSSGEEKGDAEKLSKSESEDSIRRKSFHLGVEGHRRAHEKRLSTPNQSPLS   538
hNav1.8      RIKPRVS----EGSTED--NKSPRSD--------------------------PYNQRRMS   488
hNav1.9      KKR-----------------------------------------------------------   466

hNav1.1      IRGSLFSPRRNSRTSLFSFRGR--AKDVGSENDFADDEHSTFEDNESRRDSLFVPRRHGE   616
hNav1.2      IRGSLFSPRRNSRASLFSFRGR--AKDIGSENDFADDEHSTFEDNDSRRDSLFVPHRHGE   619
hNav1.3      IRGSLFSPRRNSKTSIFSFRGR--AKDVGSENDFADDEHSTFEDSESRRDSLFVPHRHGE   619
hNav1.4      -----------------------------------------------------------   502
hNav1.5      -----SMKPRSSRGSIFTFR----RRDLGSEADFADDENSTAGESESHHTSLLVPWPLRR   569
hNav1.6      IPGSPFLSRHNSKSSIFSFRGPGRFRDPGSENEFADDEHSTVEESEGRRDSLFIPIRARE   609
hNav1.7      IRGSLFSARRSSRTSLFSFKGR--GRDIGSETEFADDEHSIFGDNESRRGSLFVPHRPQE   596
hNav1.8      FLGLASGKRRASHGSVFHFRSPGRDISL--PEGV-TDDGVFPGDHESHRGSLLLGGGAGQ   545
hNav1.9      --------------KSFFLRESGKDQPPGSDS----------------------------   484

hNav1.1      RRNS-----NLSQTSRSSRMLAVFPANGKMHSTVDCNGVVSLVGGP-SVPTSPVGQLLPE   670
hNav1.2      RRHS-----NVSQASRASRVLPILPMNGKMHSAVDCNGVVSLVGGP-STLTS-AGQLLPE   672
hNav1.3      RRNS-----NVSQASMSSRMVPGLPANGKMHSTVDCNGVVSLVGGP-SALTSPTGQLPPE   673
hNav1.4      ----------------------------------GKDCNGSLDTSQGE-KG-----------   518
hNav1.5      TSAQ--GQ------PSPGTSAPGHALHGKKNSTVDCNGVVSLLGAGDPEATSPGSHLLRP   621
hNav1.6      RRSSYSGYSGYSQGSRSSRIFPSLRRSVKRNSTVDCNGVVSLIGGP-GSHI--GGRLLPE   666
hNav1.7      RRSS-----NISQASRSP---PMLPVNGKMHSAVDCNGVVSLVDGR-SALMLPNGQLLPE   647
hNav1.8      QGPL----------PRSPLPQPSNPD---------------SRHGEDEHQPPPTSELAPG   580
hNav1.9      ---------------------------------DEDCQKKPQLLEQT--------------   498

hNav1.1      VIIDKPATDDNGTTTETEMRKRRSSSFHVSMDFLEDPSQRQRAMSIASILTNT-VEELEE   729
hNav1.2      -----------GTTTETEIRKRRSSSYHVSMDLLEDPTSRQRAMSIASILTNT-MEELEE   720
hNav1.3      -----------GTTTETEVRKRRLSSYQISMEMLEDSSGRQRAVSIASILTNT-MEELEE   721
hNav1.4      ------------APRQ--------------------------SSSGDSGISDAMEELEE   539
hNav1.5      VMLEHPPDTT--TPSEEPGGPQMLTSQAPCVDGFEEPGARQRALSAVSVLTSA-LEELEE   678
hNav1.6      ------------ATTEVEIKKKGPGSLLVSMDQLASYGRKDRINSIMSVVTNTLVEELEE   714
hNav1.7      VIIDKATSDDSGTTNQI-HKKRRCSSYLLSEDMLNDPNLRQRAMSRASILTNT-VEELEE   705
hNav1.8      A-------------VDVSAFDAGQKKTFLSAEYLDEPFRAQRAMSVVSIITSV-LEELEE   626
hNav1.9      -------------------KRLSQNLSLDHFDEHGDPLQRQRALSAVSILTIT-MKEQEK   538
                                                       *  .      ::* *:
```

```
hNav1.1      SRQKCPPCWYKFSNIFLIWDCSPYWLKVKHVVNLVVMDPFVDLAITICIVLNTLFMAMEH   789
hNav1.2      SRQKCPPCWYKFANMCLIWDCCKPWLKVKHLVNLVVMDPFVDLAITICIVLNTLFMAMEH   780
hNav1.3      SRQKCPPCWYRFANVFLIWDCCDAWLKVKHLVNLIVMDPFVDLAITICIVLNTLFMAMEH   781
hNav1.4      AHQKCPPWWYKCAHKVLIWNCCAPWLKFKNIIHLIVMDPFVDLGITICIVLNTLFMAMEH   599
hNav1.5      SRHKCPPCWNRLAQRYLIWECCPLWMSIKQGVKLVVMDPFTDLTITMCIVLNTLFMALEH   738
hNav1.6      SQRKCPPCWYKFANTFLIWECHPYWIKLKEIVNLIVMDPFVDLAITICIVLNTLFMAMEH   774
hNav1.7      SRQKCPPWWYRFAHKFLIWNCSPYWIKFKKCIYFIVMDPFVDLAITICIVLNTLFMAMEH   765
hNav1.8      SEQKCPPCLTSLSQKYLIWDCCPMWVKLKTILFGLVTDPFAELTITLCIVVNTIFMAMEH   686
hNav1.9      SQEPCLPCGENLASKYLVWNCCPQWLCVKKVLRTVMTDPFTELAITICIIINTVFLAMEH   598
             :.. * *     :   *:*:*   *: .*  :  :: ***.:* **:**::**:*:*:**

hNav1.1      YPMTDHFNNVLTVGNLVFTGIFTAEMFLKIIAMDPYYYFQEGWNIFDGFIVTLSLVELG-   848
hNav1.2      YPMTEQFSSVLSVGNLVFTGIFTAEMFLKIIAMDPYYYFQEGWNIFDGFIVSLSLMELG-   839
hNav1.3      YPMTEQFSSVLTVGNLVFTGIFTAEMVLKIIAMDPYYYFQEGWNIFDGIIVSLSLMELG-   840
hNav1.4      YPMTEHFDNVLTVGNLVFTGIFTAEMVLKLIAMDPYEYFQQGWNIFDSIIVTLSLVELG-   658
hNav1.5      YNMTSEFEEMLQVGNLVFTGIFTAEMTFKIIALDPYYYFQQGWNIFDSIIVILSLMELG-   797
hNav1.6      HPMTPQFEHVLAVGNLVFTGIFTAEMFLKLIAMDPYYYFQEGWNIFDGFIVSLSLMELS-   833
hNav1.7      HPMTEEFKNVLAIGNLVFTGIFAAEMVLKLIAMDPYEYFQVGWNIFDSLIVTLSLVELF-   824
hNav1.8      HGMSPTFEAMLQIGNIVFTIFFTAEMVFKIIAFDPYYYFQKKWNIFDCIIVTVSLLELG-   745
hNav1.9      HKMEASFEKMLNIGNLVFTSIFIAEMCLKIIALDPYHYFRRGWNIFDSIVALLSFADVMN   658
             : *   *. :* :**:*** :* *** :*:**:*** **:  ***** ::. :*: ::

hNav1.1      -LANVEGLSVLRSFRLLRVFKLAKSWPTLNMLIKIIGNSVGALGNLTLVLAIIVFIFAVV   907
hNav1.2      -LANVEGLSVLRSFRLLRVFKLAKSWPTLNMLIKIIGNSVGALGNLTLVLAIIVFIFAVV   898
hNav1.3      -LSNVEGLSVLRSFRLLRVFKLAKSWPTLNMLIKIIGNSVGALGNLTLVLAIIVFIFAVV   899
hNav1.4      -LANVQGLSVLRSFRLLRVFKLAKSWPTLNMLIKIIGNSVGALGNLTLVLAIIVFIFAVV   717
hNav1.5      -LSRMSNLSVLRSFRLLRVFKLAKSWPTLNTLIKIIGNSVGALGNLTLVLAIIVFIFAVV   856
hNav1.6      -LADVEGLSVLRSFRLLRVFKLAKSWPTLNMLIKIIGNSVGALGNLTLVLAIIVFIFAVV   892
hNav1.7      -LADVEGLSVLRSFRLLRVFKLAKSWPTLNMLIKIIGNSVGALGNLTLVLAIIVFIFAVV   883
hNav1.8      -VAKKGSLSVLRSFRLLRVFKLAKSWPTLNTLIKIIGNSVGALGNLTIILAIIVFVFALV   804
hNav1.9      CVLQKRSWPFLRSFRVLRVFKLAKSWPTLNTLIKIIGNSVGALGSLTVVLVIVIFIFSVV   718
              :    .  .*****:************** *************.**::*.*::*:*::*

hNav1.1      GMQLFGKSYKDCV----CKIAS--DCQLPRWHMNDFFHSFLIVFRVLCGEWIETMWDCME   961
hNav1.2      GMQLFGKSYKECV----CKISN--DCELPRWHMHDFFHSFLIVFRVLCGEWIETMWDCME   952
hNav1.3      GMQLFGKSYKECV----CKIND--DCTLPRWHMNDFFHSFLIVFRVLCGEWIETMWDCME   953
hNav1.4      GMQLFGKSYKECV----CKIAL--DCNLPRWHMHDFFHSFLIVFRILCGEWIETMWDCME   771
hNav1.5      GMQLFGKNYSELR------DSD--SGLLPRWHMMDFFHAFLIIFRILCGEWIETMWDCME   908
hNav1.6      GMQLFGKSYKECV----CKINQ--DCELPRWHMHDFFHSFLIVFRVLCGEWIETMWDCME   946
hNav1.7      GMQLFGKSYKECV----CKIND--DCTLPRWHMNDFFHSFLIVFRVLCGEWIETMWDCME   937
hNav1.8      GKQLLGENYRNNR----KNISAP-HEDWPRWHMHDFFHSFLIVFRILCGEWIENMWACME   859
hNav1.9      GMQLFGRSFNSQKSPKLCNPTGPTVSCLRHWHMGDFWHSFLVVFRILCGEWIENMWECMQ   778
             * **:*..: .                  :*** **:*:**::**:*******.** **:

hNav1.1      VA--GQAMCLTVFMMVMVIGNLVVLNLFLALLLSSFSADNLAAT-DDDNEMNNLQIAVDR  1018
hNav1.2      VA--GQTMCLTVFMMVMVIGNLVVLNLFLALLLSSFSSDNLAAT-DDDNEMNNLQIAVGR  1009
hNav1.3      VA--GQTMCLIVFMLVMVIGNLVVLNLFLALLLSSFSSDNLAAT-DDDNEMNNLQIAVGR  1010
hNav1.4      VA--GQAMCLTVFLMVMVIGNLVVLNLFLALLLSSFSADSLAAS-DEDGEMNNLQIAIGR  828
hNav1.5      VS--GQSLCLLVFLLVMVIGNLVVLNLFLALLLSSFSADNLTAP-DEDREMNNLQLALAR  965
hNav1.6      VA--GQAMCLIVFMMVMVIGNLVVLNLFLALLLSSFSADNLAAT-DDDGEMNNLQISVIR  1003
hNav1.7      VA--GQAMCLIVYMMVMVIGNLVVLNLFLALLLSSFSSDNLTAI-EEDPDANNLQIAVTR  994
hNav1.8      VG--QKSICLILFLTVMVLGNLVVLNLFIALLLNSFSADNLTAP-EDDGEVNNLQVALAR  916
hNav1.9      EANASSSLCVIVFILITVIGKLVVLNLFIALLLNSFSNEERNGNLEGEARKTKVQLALDR  838
              .   .::*: ::: : *:*:*******:****.*** :.  .  : :   .::*::: *

hNav1.1      MHKGVAYVKRKIYEFIQQSFIRKQK--ILDEIKPLDDLNNKKDSCMSNHT-A------EI  1069
hNav1.2      MQKGIDFVKRKIREFIQKAFVRKQK--ALDEIKPLEDLNNKKDSCISNHTTI------EI  1061
hNav1.3      MQKGIDYVKNKMRECFQKAFFRKPK--VIEI-----HEGNKIDSCMSNNTGI------EI  1057
hNav1.4      IKLGIGFAKAFLLGLLHGKILSPKD--IMLSLGEADGAGEAGEAGETAPEDE------KK  880
hNav1.5      IQRGLRFVKRTTWDFCCGLLRQRPQ--KPAALAAQ----GQLPSCIATPYSPPPPETEKV  1019
hNav1.6      IKKGVAWTKLKVHAFMQAHFK--QR--EADEVKPLDELYEKKANCIANHTGA------DI  1053
hNav1.7      IKKGINYVKQTLREFILKAFSKKPK--ISREIRQAEDLNTKKENYISNHTLA------EM  1046
hNav1.8      IQVFGHRTKQALCSFFSRSCPFPQPKAEPELVVKLPLSSSKAENHI--------------  962
hNav1.9      FRRAFCFVRHTLEHFCHKWCRKQNLPQQ----------KEVAGGCAAQSK--------DI  880
             ::     .:

hNav1.1      GKDLDYLKDVNGTTSGIGTGSSVEKYIIDESDYMSFINNPSLTVTVPIAVGESDFENLNT  1129
hNav1.2      GKDLNYLKDGNGTTSGI--GSSVEKYVVDESDYMSFINNPSLTVTVPIAVGESDFENLNT  1119
hNav1.3      SKELNYLRDGNGTTSGVGTGSSVEKYVIDENDYMSFINNPSLTVTVPIAVGESDFENLNT  1117
hNav1.4      EPPEEDLKKDNHILNHMGLAD--GPPSSLELDHLNFINNPYLTIQVPIASEESDLEMPTE  938
hNav1.5      PPTRKETRFEEGEQPGQGTPG------------------DPEPVCVPIAVAESDTDDQEE  1061
hNav1.6      HRNGDFQKNGNGTTSGI--GSSVEKYIIDE-DHMSFINNPNLTVRVPIAVGESDFENLNT  1110
hNav1.7      SKGHNFLKEKDKI---SGFGSSVDKHLMEDSDGQSFIHNPSLTVTVPIAPGESDLENMNA  1103
hNav1.8      -----------AANTARGSSGGLQAPRGPRDEHSDFIANPTVWVSVPIAEGESDLDDLED  1011
hNav1.9      IPLVMEMKRGSETQEELGILTSVPKTLGVRHDW---------TWLAPLAEEEDDVEFSGE  931
                                                        .*:*  *.* :
```

```
hNav1.1      EDFSSESDLEES---KEK-------------------------------------------   1144
hNav1.2      EEFSSESDMEES---KEK-------------------------------------------   1134
hNav1.3      EEFSSESELEES---KEK-------------------------------------------   1132
hNav1.4      EETDTFSEPEDS---KKP-------------------------------------------   953
hNav1.5      DEENSLGTEEES---SKQQE--SQPVSGGPEAPPDSRTWSQVSATASSEAEASASQADWR   1116
hNav1.6      EDVSSESDPEGS---KDK-------------------------------------------   1125
hNav1.7      EELSSDSDSEYS---KVR-------------------------------------------   1118
hNav1.8      DGGEDAQSFQQEVIPKGQQEQLQQVERCGDHLTPRSP-----GTGTSSEDLAPSLGETWK   1066
hNav1.9      DNAQRITQPEPE----QQAYELH-----QENKKPTSQRVQSVEIDMFSEDEP--------   974
             :  .     : .

hNav1.1      -----------LNE--SSSSSEGSTVDIGAPVE-E-QPVVEPEETLEPEACFTEGCVQRF   1189
hNav1.2      -----------LNA--TS-SSEGSTVDIGAPAEGE-QPEVEPEESLEPEACFTEDCVRKF   1179
hNav1.3      -----------LNA--TS-SSEGSTVDVVLPREGE-QAETEPEEDLKPEACFTEGCIKKF   1177
hNav1.4      -----------PQPLYDGNSSVCSTADYKPPEEDPEEQAEENPEGEQPEECFTEACVQRW   1002
hNav1.5      QQWKAEPQAPGCGETPEDSCSEGSTADMTNTAELLEQIPDLGQDVKDPEDCFTEGCVRRC   1176
hNav1.6      -----------LDD--TS-SSEGSTIDIKPEV-EE-VPVEQPEEYLDPDACFTEGCVQRF   1169
hNav1.7      -----------LNR--SS-SSECSTVDNPLPGEGE-EAEAEPMNSDEPEACFTDGCVWRF   1163
hNav1.8      DESVPQVPAEGV---DDTSSSEGSTVDCLDPEEILRKIPELADDLEEPDDCFTEGCIRHC   1123
hNav1.9      ---HLTIQDPRKKSDVTSILSECSTIDLQDGFGWL----PEMVPKKQPERCLPKGFGCCF   1027
                              *  ** *                   .*: *: .

hNav1.1      KCCQINVEEGRGKQWWNLRRTCFRIVEHNWFETFIVFMILLSSGALAFEDIYIDQRKTIK   1249
hNav1.2      KCCQISIEEGKGKLWWNLRKTCYKIVEHNWFETFIVFMILLSSGALAFEDIYIEQRKTIK   1239
hNav1.3      PFCQVSTEEGKGKIWWNLRKTCYSIVEHNWFETFIVFMILLSSGALAFEDIYIEQRKTIK   1237
hNav1.4      PCLYVDISQGRGKKWWTLRRACFKIVEHNWFETFIVFMILLSSGALAFEDIYIEQRRVIR   1062
hNav1.5      PCCAVDTTQAPGKVWWRLRKTCYHIVEHSWFETFIIFMILLSSGALAFEDIYLEERKTIK   1236
hNav1.6      KCCQVNIEEGLGKSWWILRKTCFLIVEHNWFETFIIFMILLSSGALAFEDIYIEQRKTIR   1229
hNav1.7      SCCQVNIESGKGKIWWNIRKTCYKIVEHSWFESFIVLMILLSSGALAFEDIYIERKKTIK   1223
hNav1.8      PCCKLDTTKSPWDVGWQVRKTCYRIVEHSWFESFIIFMILLSSGSLAFEDYYLDQKPTVK   1183
hNav1.9      PCCSVDKRKPPWVIWWNLRKTCYQIVKHSWFESFIIFVILLSSGALIFEDVHLENQPKIQ   1087
                 :.  .      * :*::*: **:*.***:**:::******:* *** :::.:  ::

hNav1.1      TMLEYADKVFTYIFILEMLLKWVAYGYQTYFTNAWCWLDFLIVDVSLVSLTANALGYSEL   1309
hNav1.2      TMLEYADKVFTYIFILEMLLKWVAYGFQVYFTNAWCWLDFLIVDVSLVSLTANALGYSEL   1299
hNav1.3      TMLEYADKVFTYIFILEMLLKWVAYGFQTYFTNAWCWLDFLIVDVSLVSLVANALGYSEL   1297
hNav1.4      TILEYADKVFTYIFIMEMLLKWVAYGFKVYFTNAWCWLDFLIVDVSIISLVANWLGYSEL   1122
hNav1.5      VLLEYADKMFTYVFVLEMLLKWVAYGFKKYFTNAWCWLDFLIVDVSLVSLVANTLGFAEM   1296
hNav1.6      TILEYADKVFTYIFILEMLLKWTAYGFVKFFTNAWCWLDFLIVAVSLVSLIANALGYSEL   1289
hNav1.7      IILEYADKIFTYIFILEMLLKWIAYGYKTYFTNAWCWLDFLIVDVSLVTLVANTLGYSDL   1283
hNav1.8      ALLEYTDRVFTFIFVFEMLLKWVAYGFKKYFTNAWCWLDFLIVNISLISLTAKILEYSEV   1243
hNav1.9      ELLNCTDIIFTHIFILEMVLKWVAFGFGKYFTSAWCCLDFIIVIVSVTTLI-------NL   1140
              :*: :* :**.:*::**:*** *:*:  :**.*** ***:** :*: :*        ::

hNav1.1      GAIKSLRTLRALRPLRALSRFEGMRVVVNALLGAIPSIMNVLLVCLIFWLIFSIMGVNLF   1369
hNav1.2      GAIKSLRTLRALRPLRALSRFEGMRVVVNALLGAIPSIMNVLLVCLIFWLIFSIMGVNLF   1359
hNav1.3      GAIKSLRTLRALRPLRALSRFEGMRVVVNALVGAIPSIMNVLLVCLIFWLIFSIMGVNLF   1357
hNav1.4      GPIKSLRTLRALRPLRALSRFEGMRVVVNALLGAIPSIMNVLLVCLIFWLIFSIMGVNLF   1182
hNav1.5      GPIKSLRTLRALRPLRALSRFEGMRVVVNALVGAIPSIMNVLLVCLIFWLIFSIMGVNLF   1356
hNav1.6      GAIKSLRTLRALRPLRALSRFEGMRVVVNALVGAIPSIMNVLLVCLIFWLIFSIMGVNLF   1349
hNav1.7      GPIKSLRTLRALRPLRALSRFEGMRVVVNALIGAIPSIMNVLLVCLIFWLIFSIMGVNLF   1343
hNav1.8      APIKALRTLRALRPLRALSRFEGMRVVVDALVGAIPSIMNVLLVCLIFWLIFSIMGVNLF   1303
hNav1.9      MELKSFRTLRALRPLRALSQFEGMKVVVNALIGAIPAILNVLLVCLIFWLVFCILGVYFF   1200
               :*::**************:****:***:**:****:*:***********:*.*:** :*

hNav1.1      AGKFYHCINTTTGDR--FDIEDVNNHTDCLKLIERN-ETARWKNVKVNFDNVGFGYLSLL   1426
hNav1.2      AGKFYHCINYTTGEM--FDVSVVNNYSECKALIESN-QTARWKNVKVNFDNVGLGYLSLL   1416
hNav1.3      AGKFYHCVNMTTGNM--FDISDVNNLSDCQALG----KQARWKNVKVNFDNVGAGYLALL   1411
hNav1.4      AGKFYYCINTTTSER--FDISEVNNKSECESLMHT--GQVRWLNVKVNYDNVGLGYLSLL   1238
hNav1.5      AGKFGRCINQTEGDLP-LNYTIVNNKSQCESLNLT--GELYWTKVKVNFDNVGAGYLALL   1413
hNav1.6      AGKYHYCFNETSEIR--FEIEDVNNKTECEKLMEGNNTEIRWKNVKINFDNVGAGYLALL   1407
hNav1.7      AGKFYECINTTDGSR--FPASQVPNRSECFALMNVS-QNVRWKNLKVNFDNVGLGYLSLL   1400
hNav1.8      AGKFWRCINYTDGEFSLVPLSIVNNKSDCKIQNST--GSFFWVNVKVNFDNVAMGYLALL   1361
hNav1.9      SGKFGKCINGTDSV---INYTIITNKSQCES------GNFSWINQKVNFDNVGNAYLALL   1251
             :**:  *.* *      .    : * ::*           * : *:*:***. .**:**

hNav1.1      QVATFKGWMDIMYAAVDSRNVELQPKYEESLYMYLYFVIFIIFGSFFTLNLFIGVIIDNF   1486
hNav1.2      QVATFKGWMDIMYAAVDSRNVELQPKYEDNLYMYLYFVIFIIFGSFFTLNLFIGVIIDNF   1476
hNav1.3      QVATFKGWMDIMYAAVDSRDVKLQPVYEENLYMYLYFVIFIIFGSFFTLNLFIGVIIDNF   1471
hNav1.4      QVATFKGWMDIMYAAVDSREKEEQPQYEVNLYMYLYFVIFIIFGSFFTLNLFIGVIIDNF   1298
hNav1.5      QVATFKGWMDIMYAAVDSRGYEEQPQWEYNLYMYIYFVIFIIFGSFFTLNLFIGVIIDNF   1473
hNav1.6      QVATFKGWMDIMYAAVDSRKPDEQPKYEDNIYMYIYFVIFIIFGSFFTLNLFIGVIIDNF   1467
hNav1.7      QVATFKGWTIIMYAAVDSVNVDKQPKYEYSLYMYIYFVVFIIFGSFFTLNLFIGVIIDNF   1460
hNav1.8      QVATFKGWMDIMYAAVDSREVNMQPKWEDNVYMYLYFVIFIIFGGFFTLNLFVGVIIDNF   1421
hNav1.9      QVATFKGWMDIIYAAVDSTEKEQQPEFESNSLGYIYFVVFIIFGSFFTLNLFIGVIIDNF   1311
             ********  *:******   . ** :* .   *:***:*****.*******:*******
```

```
hNav1.1      NQQKKKFGGQDIFMTEEQKKYYNAMKKLGSKKPQKPIPRPGNKFQGMVFDFVTRQVFDIS   1546
hNav1.2      NQQKKKFGGQDIFMTEEQKKYYNAMKKLGSKKPQKPIPRPANKFQGMVFDFVTKQVFDIS   1536
hNav1.3      NQQKKKFGGQDIFMTEEQKKYYNAMKKLGSKKPQKPIPRPANKFQGMVFDFVTRQVFDIS   1531
hNav1.4      NQQKKKLGGKDIFMTEEQKKYYNAMKKLGSKKPQKPIPRPQNKIQGMVYDLVTKQAFDIT   1358
hNav1.5      NQQKKKLGGQDIFMTEEQKKYYNAMKKLGSKKPQKPIPRPLNKYQGFIFDIVTKQAFDVT   1533
hNav1.6      NQQKKKFGGQDIFMTEEQKKYYNAMKKLGSKKPQKPIPRPLNKIQGIVFDFVTQQAFDIV   1527
hNav1.7      NQQKKKLGGQDIFMTEEQKKYYNAMKKLGSKKPQKPIPRPGNKIQGCIFDLVTNQAFDIS   1520
hNav1.8      NQQKKKLGGQDIFMTEEQKKYYNAMKKLGSKKPQKPIPRPLNKFQGFVFDIVTRQAFDIT   1481
hNav1.9      NQQQKKLGGQDIFMTEEQKKYYNAMKKLGSKKPQKPIPRPLNKCQGLVFDIVTSQIFDII   1371
             ***:**:**:****************************** ** ** ::*:** * **:

hNav1.1      IMILICLNMVTMMVETDDQSEYVTTILSRINLVFIVLFTGECVLKLISLRHYYFTIGWNI   1606
hNav1.2      IMILICLNMVTMMVETDDQSQEMTNILYWINLVFIVLFTGECVLKLISLRYYYFTIGWNI   1596
hNav1.3      IMILICLNMVTMMVETDDQGKYMTLVLSRINLVFIVLFTGEFVLKLVSLRHYYFTIGWNI   1591
hNav1.4      IMILICLNMVTMMVETDNQSQLKVDILYNINMIFIIIFTGECVLKMLALRQYYFTVGWNI   1418
hNav1.5      IMFLICLNMVTMMVETDDQSPEKINILAKINLLFVAIFTGECIVKLAALRHYYFTNSWNI   1593
hNav1.6      IMMLICLNMVTMMVETDTQSKQMENILYWINLVFVIFFTCECVLKMFALRHYYFTIGWNI   1587
hNav1.7      IMVLICLNMVTMMVEKEGQSQHMTEVLYWINVVFIILFTGECVLKLISLRHYYFTVGWNI   1580
hNav1.8      IMVLICLNMITMMVETDDQSEEKTKILGKINQFFVAVFTGECVMKMFALRQYYFTNGWNV   1541
hNav1.9      IISLIILNMISMMAESYNQPKAMKSILDHLNWVFVVIFTLECLIKIFALRQYYFTNGWNL   1431
             *: ** ***::**.*.  *      :*  :* .*: .** * ::*: :** **** .**:

hNav1.1      FDFVVVILSIVGMFLAELIEK--YFVSPTLFRVIRLARIGRILRLIKGAKGIRTLLFALM   1664
hNav1.2      FDFVVVILSIVGMFLAELIEK--YFVSPTLFRVIRLARIGRILRLIKGAKGIRTLLFALM   1654
hNav1.3      FDFVVVILSIVGMFLAEMIEK--YFVSPTLFRVIRLARIGRILRLIKGAKGIRTLLFALM   1649
hNav1.4      FDFVVVILSIVGLALSDLIQK--YFVSPTLFRVIRLARIGRVLRLIRGAKGIRTLLFALM   1476
hNav1.5      FDFVVVILSIVGTVLSDIIQK--YFFSPTLFRVIRLARIGRILRLIRGAKGIRTLLFALM   1651
hNav1.6      FDFVVVILSIVGMFLADIIEK--YFVSPTLFRVIRLARIGRILRLIKGAKGIRTLLFALM   1645
hNav1.7      FDFVVVIISIVGMFLADLIET--YFVSPTLFRVIRLARIGRILRLVKGAKGIRTLLFALM   1638
hNav1.8      FDFIVVVLSIASLIFSAILKSLQSYFSPTLFRVIRLARIGRILRLIRAAKGIRTLLFALM   1601
hNav1.9      FDCVVVLLSIVSTMISTLENQEHIPFPPTLFRIVRLARIGRILRLVRAARGIRTLLFALM   1491
             ** :**::**..  :: : :     . *****::*******:***::.*:**********

hNav1.1      MSLPALFNIGLLLFLVMFIYAIFGMSNFAYVKREVGIDDMFNFETFGNSMICLFQITTSA   1724
hNav1.2      MSLPALFNIGLLLFLVMFIYAIFGMSNFAYVKREVGIDDMFNFETFGNSMICLFQITTSA   1714
hNav1.3      MSLPALFNIGLLLFLVMFIYAIFGMSNFAYVKKEAGIDDMFNFETFGNSMICLFQITTSA   1709
hNav1.4      MSLPALFNIGLLLFLVMFIYSIFGMSNFAYVKKESGIDDMFNFETFGNSIICLFEITTSA   1536
hNav1.5      MSLPALFNIGLLLFLVMFIYSIFGMANFAYVKWEAGIDDMFNFQTFANSMLCLFQITTSA   1711
hNav1.6      MSLPALFNIGLLLFLVMFIFSIFGMSNFAYVKHEAGIDDMFNFETFGNSMICLFQITTSA   1705
hNav1.7      MSLPALFNIGLLLFLVMFIYAIFGMSNFAYVKKEDGINDMFNFETFGNSMICLFQITTSA   1698
hNav1.8      MSLPALFNIGLLLFLVMFIYSIFGMSSFPHVRWEAGIDDMFNFQTFANSMLCLFQITTSA   1661
hNav1.9      MSLPSLFNIGLLLFLIMFIYAILGMNWFSKVNPESGIDDIFNFKTFASSMLCLFQISTSA   1551
             ****:**********:***::*:**  *  *. * **:*:***:**..*::***:*:***

hNav1.1      GWDGLLAPILNSKPPDCDPNKVNPGSSVKGDCGNPSVGIFFFVSYIIISFLVVVNMYIAV   1784
hNav1.2      GWDGLLAPILNSGPPDCDPDKDHPGSSVKGDCGNPSVGIFFFVSYIIISFLVVVNMYIAV   1774
hNav1.3      GWDGLLAPILNSAPPDCDPDTIHPGSSVKGDCGNPSVGIFFFVSYIIISFLVVVNMYIAV   1769
hNav1.4      GWDGLLNPILNSGPPDCDPNLENPGTSVKGDCGNPSIGICFFCSYIIISFLIVVNMYIAI   1596
hNav1.5      GWDGLLSPILNTGPPYCDPTLPNS-NGSRGDCGSPAVGILFFTTYIIISFLIVVNMYIAI   1770
hNav1.6      GWDGLLLPILN-RPPDCSLDKEHPGSGFKGDCGNPSVGIFFFVSYIIISFLIVVNMYIAI   1764
hNav1.7      GWDGLLAPILNSKPPDCDPKKVHPGSSVEGDCGNPSVGIFYFVSYIIISFLVVVNMYIAV   1758
hNav1.8      GWDGLLSPILNTGPPYCDPNLPNS-NGTRGDCGSPAVGIIFFTTYIIISFLIMVNMYIAV   1720
hNav1.9      GWDSLLSPMLRSKES-C--------NSSSENCHLPGIATSYFVSYIIISFLIVVNMYIAV   1602
             ***.** *:*.     *        ..   :*  *.:.  :* :*******::******:

hNav1.1      ILENFSVATEESAEPLSEDDFEMFYEVWEKFDPDATQFMEFEKLSQFAAALEPPLNLPQP   1844
hNav1.2      ILENFSVATEESAEPLSEDDFEMFYEVWEKFDPDATQFIEFAKLSDFADALDPPLLIAKP   1834
hNav1.3      ILENFSVATEESAEPLSEDDFEMFYEVWEKFDPDATQFIEFSKLSDFAAALDPPLLIAKP   1829
hNav1.4      ILENFNVATEESSEPLGEDDFEMFYETWEKFDPDATQFIAYSRLSDFVDTLQEPLRIAKP   1656
hNav1.5      ILENFSVATEESTEPLSEDDFDMFYEIWEKFDPEATQFIEYSVLSDFADALSEPLRIAKP   1830
hNav1.6      ILENFSVATEESADPLSEDDFETFYEIWEKFDPDATQFIEYCKLADFADALEHPLRVPKP   1824
hNav1.7      ILENFSVATEESTEPLSEDDFEMFYEVWEKFDPDATQFIEFSKLSDFAAALDPPLLIAKP   1818
hNav1.8      ILENFNVATEESTEPLSEDDFDMFYETWEKFDPEATQFITFSALSDFADTLSGPLRIPKP   1780
hNav1.9      ILENFNTATEESEDPLGEDDFDIFYEVWEKFDPEATQFIKYSALSDFADALPEPLRVAKP   1662
             *****..***** :**.****: *** ******:****: :  *::*. :*  ** : :*

hNav1.1      NKLQLIAMDLPMVSGDRIHCLDILFAFTKRVLGESGEMDALRIQMEERFMASNPSKVSYQ   1904
hNav1.2      NKVQLIAMDLPMVSGDRIHCLDILFAFTKRVLGESGEMDALRIQMEERFMASNPSKVSYE   1894
hNav1.3      NKVQLIAMDLPMVSGDRIHCLDILFAFTKRVLGESGEMDALRIQMEDRFMASNPSKVSYE   1889
hNav1.4      NKIKLITLDLPMVPGDKIHCLDILFALTKEVLGDSGEMDALKQTMEEKFMAANPSKVSYE   1716
hNav1.5      NQISLINMDLPMVSGDRIHCMDILFAFTKRVLGESGEMDALKIQMEEKFMAANPSKISYE   1890
hNav1.6      NTIELIAMDLPMVSGDRIHCLDILFAFTKRVLGDSGELDILRQQMEERFVASNPSKVSYE   1884
hNav1.7      NKVQLIAMDLPMVSGDRIHCLDILFAFTKRVLGESGEMDSLRSQMEERFMSANPSKVSYE   1878
hNav1.8      NRNILIQMDLPLVPGDKIHCLDILFAFTKNVLGESGELDSLKANMEEKFMATNLSKSSYE   1840
hNav1.9      NKYQFLVMDLPMVSEDRLHCMDILFAFTARVLGGSDGLDSMKAMMEEKFMEANPLKKLYE   1722
             *   :: :***:*  *::**:*****:* .*** *. :* ::  **::*: :*  *  *:
```

```
hNav1.1      PITTTLKRKQEEVSAVIIQRAYRRHLLKRTVKQASFTYNKNKIKG--GANLLIKEDMIID   1962
hNav1.2      PITTTLKRKQEEVSAIIIQRAYRRYLLKQKVKKVSSIYKKDKGKE--CDGTPIKEDTLID   1952
hNav1.3      PITTTLKRKQEEVSAAIIQRNFRCYLLKQRLKNISSNYNKEAIKG--RIDLPIKQDMIID   1947
hNav1.4      PITTTLKRKHEEVCAIKIQRAYRRHLLQRSMKQASYMYRHSHDGS--GDDAPEKEGLLAN   1774
hNav1.5      PITTTLRRKHEEVSAMVIQRAFRRHLLQRSLKHASFLFRQQAGSGLSEEDAPEREGLIAY   1950
hNav1.6      PITTTLRRKQEEVSAVVLQRAYRGHLARRGFICKKTTSNK--------------------   1924
hNav1.7      PITTTLKRKQEDVSATVIQRAYRRYRLRQNVKNISSIYIKDGDR---DDDLLNKKDMAFD   1935
hNav1.8      PIATTLRWKQEDISATVIQKAYRSYVLHRSMALSNTPCVPRAEE---EAASLPDEGFVAF   1897
hNav1.9      PIVTTTKRKEEERGAAIIQKAFRKYMMKVTKGDQGDQNDLENGP-----HSPLQ--TLCN   1775
             **.** : *.*:  *  :*: :* :  :

hNav1.1      RIN-------ENSITEKTDLTMSTAACPPSYDRV-TKPIVEKHEQEGKDEKAKG----K-   2009
hNav1.2      KLN-------ENSTPEKTDMTPS-TTSPPSYDSV-TKPEKEKFEKDKSEKEDKG----K-   1998
hNav1.3      KLN-------GNSTPEKTDGSSS-TTSPPSYDSV-TKPDKEKFEKDKPEKESKG----K-   1993
hNav1.4      TMSKMYGHENGNSSSPSPEEKGEAGDAGPTMGLMPISPSDTAWPPAPP----PG----QT   1826
hNav1.5      VMSENFSRPLGP----PSSSSISSTSFPPSYDSVTRATSDNLQVRGSDYSHSED----LA   2002
hNav1.6      LEN-------GGTHREKKESTP-STASLPSYDSV-TKPEKEKQQRAEEGRRERA----K-   1970
hNav1.7      NVN-------ENSSPEKTDATSS-TTSPPSYDSV-TKPDKEKYEQDRTEKEDKG----K-   1981
hNav1.8      TAN-------ENCVLPDKSETASATSFPPSYESVTRGLSDRVNMRTSSSIQNEDEATSME   1950
hNav1.9      GDLSSFGVAKGKVHCD--------------------------------------------   1791


hNav1.1      --------------  2009
hNav1.2      -------DIRESKK  2005
hNav1.3      -------EVRENQK  2000
hNav1.4      VRP----GVKESLV  1836
hNav1.5      DFPPSPDRDRESIV  2016
hNav1.6      RQK----EVRESKC  1980
hNav1.7      -------DSKESKK  1988
hNav1.8      LIAPGP--------  1956
hNav1.9      --------------  1791
```

Appendix D: MSA of Nav1.7 orthologues across species

```
Nav1.7-human        ----MAMLPPPGPQSFVHFTKQSLALIEQRIAERKSKEPKEE------------------      38
Nav1.7-macaque      ----MAMLPPPGPQSFVHFTKQSLALIEQRIAERKSKEPKEE------------------      38
Nav1.7-cattle       ----MAMLPPPGPQSFVFFTKQSLALIEQRIAEGKAKEPKEE------------------      38
Nav1.7-opossum      --EKMATLPPPGPESFVFFTRQSLELIEQRISEGKSKEPKEE------------------      40
Nav1.7-chicken      --MAQAMLVPPGSDCFFYFTRESLAAIEKRIADEKSNRDKDE------------------      40
Nav1.7-rat          ----MAMLPPPGPQSFVHFTKQSLALIEQRISEEKAKEHKDE------------------      38
Nav1.7-mouse        ----MAMLPPPGPQSFVHFTKQSLALIEQRISEEKAKGHKDE------------------      38
Para-fly            MTEDSDSISEEERSLFRPFTRESLVQIEQRIAAEHEKQKELERKRAEGEVPQYGRKKKQK      60
                           :     . *  **::**  **:**:  : :  : *

Nav1.7-human        -KKDD---DEEAPKPSSDLEAGKQLPF-IYGDIPPGMVSEPLEDLDPYYADKKTFIVLNK      93
Nav1.7-macaque      -KKDD---DEEAPKPSSDLEAGKQLPF-IYGDIPPGMVSEPLEDLDPYYADKKTFIVLNK      93
Nav1.7-cattle       -KKDD---DDEGPKPSSDLEAGKQLPF-IYGDIPPGMVSEPLEDLDPYYADKKTFIVLNK      93
Nav1.7-opossum      -KTDE---EEEGPKPSSDLEAGKQLPF-IYGDIPPGMVSEPLEDMDPYYMDKNTFIVLNK      95
Nav1.7-chicken      -HKDDGGHEEVQPTPNNDLEAGKTLPF-IYGDIPPEMVSEPLEDLDPYYINKKTFIVLNK      98
Nav1.7-rat          -KKDD---EEEGPKPSSDLEAGKQLPF-IYGDIPPGMVSEPLEDLDPYYADKKTFIVLNK      93
Nav1.7-mouse        -KKDD---EEEGPKPSSDLEAGKQLPF-IYGDIPPGMVSEPLEDLDPYYADKKTFIVLNK      93
Para-fly            EIRYDDEDEDEGPQPDPTLEQGVPIPVRLQGSFPPELASTPLEDIDPYYSNVLTFVVVSK     120
                        :   ::  * *.  ** *  :*. : *.:** :.* ****:**** :  **:*:.*

Nav1.7-human        GKTIFRFNATPALYMLSPFSPLRRISIKILVHSLFSMLIMCTILTNCIFMTMNNPPDWTK     153
Nav1.7-macaque      GKTIFRFNATPALYMLSPFSPLRRISIKILVHSLFSMLIMCTILTNCIFMTMSNPPDWTK     153
Nav1.7-cattle       GKAIFRFNATPALYMLSPFSPLRRISIKILVHAAFSMLIMCTILTNCIFMTMSNPPDWTK     153
Nav1.7-opossum      GKTIFRFSATPAF----------------------MLIMCTILTNCIFMTLSSPPDWTK     132
Nav1.7-chicken      GKTIFRFSATSALYLLSPFNVIRRVAIKILVHSLFSMLIMLTILTNCVFMTWSKLPEWTK     158
Nav1.7-rat          GKAIFRFNATPALYMLSPFSPLRRISIKILVHSLFSMLIMCTILTNCIFMTLSNPPEWTK     153
Nav1.7-mouse        GKAIFRFNATPALYMLSPFSPLRRISIKILVHSLFSMLIMCTILTNCIFMTMSNPPDWTK     153
Para-fly            GKDIFRFSASKAMWMLDPFNPIRRVAIYILVHPLFSLFIITTILVNCILMIMPTTPTV-E     179
                    ** ****.*: *:                       ::*: ***.**::*   . *   :

Nav1.7-human        NVEYTFTGIYTFESLVKILARGFCVGEFTFLRDPWNWLDFVVIVFAYLTEFVNLGNVSAL     213
Nav1.7-macaque      NVEYTFTGIYTFESLVKILARGFCVGEFTFLRDPWNWLDFVVIVFAYLTEFVNLGNVSAL     213
Nav1.7-cattle       NVEYTFTGIYTFESLVKILARGFCVGEFTFLRDPWNWLDFIVIVFAYLTEFVNLGNVSAL     213
Nav1.7-opossum      NVEYTFTGIYTFESLVKILARGFCIGPFTFLRDPWNWLDFIVICFAFLTEFVNLGNVSAL     192
Nav1.7-chicken      NVEYTFTGIYTFEFLVKILARGFCIDDFTCLRDPWNWLDFVVISFAYITEFVNLGNVSAL     218
Nav1.7-rat          NVEYTFTGIYTFESLIKILARGFCVGEFTFLRDPWNWLDFVVIVFAYLTEFVNLGNVSAL     213
Nav1.7-mouse        NVEYTFTGIYTFESLIKILARGFCVGEFTFLRDPWNWLDFVVIVFAYLTEFVNLGNVSAL     213
Para-fly            STEVIFTGIYTFESAVKVMARGFILCPFTYLRDAWNWLDFVVIALAYVTMGIDLGNLAAL     239
                    ..*  ********  :*::**** :  ** *** ******:** :*::*  ::***::**

Nav1.7-human        RTFRVLRALKTISVIPGLKTIVGALIQSVKKLSDVMILTVFCLSVFALIGLQLFMGNLKH     273
Nav1.7-macaque      RTFRVLRALKTISVIPGLKTIVGALIQSVKKLSDVMILTVFCLSVFALIGLQLFMGNLKH     273
Nav1.7-cattle       RTFRVLRALKTISVIPGLKTIVGALIQSVKKLSDVMILTVFCLSVFALIGLQLFMGNLKH     273
Nav1.7-opossum      RTFRVLRALKTISVIPGLKTIVGALIQSVKKLSDVMILTLFCLSVFALIGLQLFMGNLRH     252
Nav1.7-chicken      RTFRVLRALKTISVIPGLKTIVGALIQSVKKLSDVMILTVFCLSVFALIGLQLFMGNLKN     278
Nav1.7-rat          RTFRVLRALKTISVIPGLKTIVGALIQSVKKLSDVMILTVFCLSVFALIGLQLFMGNLKH     273
Nav1.7-mouse        RTFRVLRALKTISVIPGLKTIVGALIQSVKKLSDVMILTVFCLSVFALIGLQLFMGNLKH     273
Para-fly            RTFRVLRALKTVAIVPGLKTIVGAVIESVKNLRDVIILTMFSLSVFALMGLQIYMGVLTQ     299
                    ***********:::*********:*:***:* **:***:*.******:***::** * :

Nav1.7-human        KCFRNSLENNET-LESIMNTL--------------ESEEDFRKYFYYLEGSKDALLCGFS     318
Nav1.7-macaque      KCVQNSLVNNET-LESIMNTL--------------ESEEDFRKYFYYLEGSKDALLCGFS     318
Nav1.7-cattle       KCVQSSLANNET-MENILNTL--------------DE-EEYAKYFYYLEGSKDALLCGFS     317
Nav1.7-opossum      KCVRWPLEDKNITIENIRNEILTSENKTLPISCLLSYTAQDLGYFYHLEGQKDALLCGNS     312
Nav1.7-chicken      KCLLWPSRNSTSFE-KYLAPYFNDT--VFDW----AAYIENESHFYRLEGQKDYLLCGNS     331
Nav1.7-rat          KCFRKELEENET-LESIMNTA--------------ESEEELKKYFYYLEGSKDALLCGFS     318
Nav1.7-mouse        KCFRKDLEQNET-LESIMSTA--------------ESEEELKRYFYYLEGSKDALLCGFS     318
Para-fly            KCIKKFPLDGSWG--NL-----TDE----NW----DYHNRNSSNWYSEDEGISFPLCGNI     344
                    **.     :      .                            :*  :   .  ***

Nav1.7-human        TDSGQCPEGYTCVK-IGRNPDYGYTSFDTFSWAFLALFRLMTQDYWENLYQQTLRAAGKT     377
Nav1.7-macaque      TDSGQCPEGYTCMK-IGRNPDYGYTSFDTFSWAFLALFRLMTQDYWENLYQQTLRAAGKT     377
Nav1.7-cattle       SDSGQCPEGYTCKK-IGRNPDYGYTSFDTFSWAFLALFRLMTQDYWENLYQQTLRAAGKT     376
Nav1.7-opossum      TDAGQCPEGYRCVK-ACTNPDYGYTSFDTFSWAFLALFRLMTQDFWENLYQQTLRAAGKT     371
Nav1.7-chicken      SDAGKCPEEFICVK-AGRNPNYGYTSFDTFSWAFLSLFRLMTQDYWENLYQLTLRAVGKT     390
Nav1.7-rat          TDSGQCPEGYICVK-AGRNPDYGYTSFDTFSWAFLALFRLMTQDYWENLYQQTLRAAGKT     377
Nav1.7-mouse        TDSGQCPEGYECVT-AGRNPDYGYTSFDTFGWAFLALFRLMTQDYWENLYQQTLRAAGKT     377
Para-fly            SGAGQCDDDYVCLQGFGPNPNYGYTSFDSFGWAFLSAFRLMTQDFWEDLYQLVLRAAGPW     404
                    :.:*:* : : *      **:*******:*.****: *******:**:*** .***.*
```

```
Nav1.7-human        YMIFFVVVIFLGSFYLINLILAVVAMAYEEQNQANIEEAKQKELEFQQMLDR----LKKE      433
Nav1.7-macaque      YMIFFVVVIFLGSFYLINLILAVVAMAYEEQNQANIEEAKQKELEFQQMLDR----LKKE      433
Nav1.7-cattle       YMIFFVVVIFLGSFYLINLILAVVAMAYEEQNQANIEEARQKELEFQQMLDR----LKKE      432
Nav1.7-opossum      YMIFFVVVIFLGSFYLINLILAVVAMAYEEQNQATIEEARQKELEFQQMLDR----LKKE      427
Nav1.7-chicken      YMIFFVLVIFLGSFYLINLILAVVAMAYEEQNQATMVEAEQREADLQQMLEQ----LKKQ      446
Nav1.7-rat          YMIFFVVVIFLGSFYLINLILAVVAMAYEEQNQANIEEAKQKELEFQQMLDR----LKKE      433
Nav1.7-mouse        YMIFFVVVIFLGSFYLINLILAVVAMAYEEQNQANIEEAKQKELEFQQMLDR----LKKE      433
Para-fly            HMLFFIVIIFLGSFYLVNLILAIVAMSYDELQKKAEEEEAAEEEAIREAEEAAAAKAAKL      464
                    :*:**:::********:*****:***:*:* ::    *   .*  :::  :       *

Nav1.7-human        QEEAEAIAAA-----AAEYTSIRRSRIMGLSESSSETSKLSSKSAKERRNRRKKKNQKKL      488
Nav1.7-macaque      QEEAEAIAAA-----AAEYTSIRRSRIMGLSESSSETSKLSSKSAKERRNRRKKKNQKKL      488
Nav1.7-cattle       QEEAEAIALA-----AAEYTSIGRSRIMGLSESSSETSKLSSKSAKERRNRRKKKNQKKL      487
Nav1.7-opossum      QEEAEAIIAA-----ADEYTSIGGGKVMGLSESSSETSKLSSKSAKERRNRRKKKNQKKQ      482
Nav1.7-chicken      QEEAQAIAAA-----AVEMTEFGGE--SGPSDSSSEASKFSSKSAKERRNRRKKRRQREH      499
Nav1.7-rat          QEEAEAIAAA-----AAEFTSIGRSRIMGLSESSSETSRLSSKSAKERRNRRKKK-QKM      487
Nav1.7-mouse        QEEAEAIAAA-----AAEYTSLGRSRIMGLSESSSETSRLSSKSAKERRNRRKKK-QKL      487
Para-fly            EERANAQAQAAADAAAAEEAALHPEMAKSPTYSCISYELFV---GGEKGN----------      511
                    :*.*:*   *     * * : :      . : *. . . :    . *: *

Nav1.7-human        SSGEEKGDAEKLS------KSESEDSIRRKSFHLGVEGHRRAHEKRLSTPNQSPLSIRGS      542
Nav1.7-macaque      SSGEEKGDAEKLS------KSDSEENIRRKSFHLGVEGHRRAHEKRLSTPSQSPLSIRGS      542
Nav1.7-cattle       SSGEEKGDDEKLS------KSESEESIRRKSFHLGVEGHRRAREKRLSTPNQSPLSIRGS      541
Nav1.7-opossum      SSGDEKRDNEKLS------KSESDESIRKKSFHLGVEGHKLAREKRMSSPNQSPLSIRGS      536
Nav1.7-chicken      SGEEDNMKDTKLS------KSESDGSIRRKGFRFSFDGNKLAYGTRLTSPHQSLLSIRGS      553
Nav1.7-rat          SSGEEKGDDEKLS------KSGSEESIRKKSFHLGVEGHHRTREKRLSTPNQSPLSIRGS      541
Nav1.7-mouse        SSGEEKGDDEKLS------KSGSEESIRKKSFHLGVEGHHRAREKRLSTPNQSPLSIRGS      541
Para-fly            ----DDNNKEKMSIRSVEVESESVSVIQRQPAP--TTA---HQATKVRKVSTTSLSLPGS      562
                        :. .  *:*      :* *   *:::       .      .:: .   : **: **

Nav1.7-human        LFSARRSSRTSLFSFKGRGR-DIG-------------------SETEFADDEHSIFGDNES      583
Nav1.7-macaque      LFSARRSSRTSLFSFKGRGR-DIG-------------------SETEFADDEHSIFGDNES      583
Nav1.7-cattle       LFSARRSSRTSLFSFKGRGR-DIG-------------------SETEFADDEHSIFGDNES      582
Nav1.7-opossum      LLSARRSSRTSLFSFRGRGK-DLG-------------------SETEFADDEHSIFGDNES      577
Nav1.7-chicken      LFSPRRSSRTSLFSFRDHGK-EIG-------------------SENDFADDEHSTFDDNGS      594
Nav1.7-rat          LFSARRSSRTSLFSFKGRGR-DLG-------------------SETEFADDEHSIFGDNES      582
Nav1.7-mouse        LFSARRSSRTSLFSFKGRGR-DLG-------------------SETEFADDEHSIFGDNES      582
Para-fly            PFNIRRGSRSSHKYTIRNGRGRFGIPGSDRKPLVLSTYQDAQQHLPYADDSNAVT-PMSE      621
                     :. **.**:*      .*:  :*                   ..  :***.::      .

Nav1.7-human        RRGSLFVPHRPQERR---SSNISQASRSP---PMLPVNGKMHSAVDCNGVVS--------      629
Nav1.7-macaque      RRGSLFVPHRPQERR---SSNISQASRSP---PILPVNGKMHSAVDCNGVVS--------      629
Nav1.7-cattle       RRGSLFVPHRPRERR---SSNISQASRSP---PVLPVNGKMHSAVDCNGVVS--------      628
Nav1.7-opossum      RRGSLFVPHRHRERR---SSNISQASRSP---RMLPVNGKMHSAVDCNGVVS--------      623
Nav1.7-chicken      RRGSLFVPLRHSERR---GSNISQASRPSRRLTLFPVNGKMHSTVDCNGVVS--------      643
Nav1.7-rat          RRGSLFVPHRPRERR---SSNISQASRSP---PVLPVNGKMHSAVDCNGVVS--------      628
Nav1.7-mouse        RRGSLFVPHRPRERR---SSNISQASRSP---PVLPVNGKMHSAVDCNGVVS--------      628
Para-fly            ENGAIIVPVYYGNLGSRHSSYTSHQSRIS-----YTSHGDLLGGMAVMGVSTMTKESKLR      676
                    ..*:::**    :     .*  *: **          :*.: . :   ** :

Nav1.7-human        ----------LV-DGRSALMLPNGQLLPEVIIDKATSDDSGTTNQ-----IH-KKRRC--      670
Nav1.7-macaque      ----------LV-DGRSALMLPNGQLLPE-----------GTTNQ-----IH-KKRRC--      659
Nav1.7-cattle       ----------LV-DGPSALMLPNGQLLPEVIIDKATSDDSGTTNQ-----IH-KKRRH--      669
Nav1.7-opossum      ----------LV-DGPTALMLPNGQLLPEVIIDKATSDDSGGTTK-----IDPNKRRS--      665
Nav1.7-chicken      ----------LV-DRPPCLLSPTGQLLPELIIDKPTTDDNSTTTE-----MEIKKRRS--      685
Nav1.7-rat          ----------LV-DGPSALMLPNGQLLPEVIIDKATSDDSGTTNQ-----MR-KKRLS--      669
Nav1.7-mouse        ----------LV-DGPSALMLPNGQLLPEVIIDKATSDDSGTTNQ-----MR-KKRLS--      669
Para-fly            NRNTRNQSVGATNGGTTCLDTNHKLDHRDYEIGLECTDEAGKIKHHDNPFIEPVQTQTVV      736
                              . .   .*        :           .  ..     :   :

Nav1.7-human        --SSYLLSEDMLNDPNLRQRAMSRASIL-----TN-TVEELEESRQKCPPWWYRFAHKFL      722
Nav1.7-macaque      --SSYLLSEDMLNDPNLRQRAMSRASIL-----TN-TVEELEESRQKCPPWWYRFAHKFL      711
Nav1.7-cattle       --SSYLLSEDMLNDPNLRQRAMSRASIL-----TN-TVEELEESRQKCPPWWYRFAHTFL      721
Nav1.7-opossum      --SSFQISMDMLDDPTVRQRALSIASII-----TN-TMEELEESRQKCPPWWYKFANTFL      717
Nav1.7-chicken      --SSYQIPMDLLEDPNLRQRAMSIAGII-----TN-TMEELEESRQKCPPCWYKFAHTYL      737
Nav1.7-rat          --SSYFLSEDMLNDPHLRQRAMSRASIL-----TN-TVEELEESRQKCPPWWYRFAHTFL      721
Nav1.7-mouse        --SSYFLSEDMLNDPHLRQRAMSRASIL-----TN-TVEELEESRQKCPPWWYRFAHTFL      721
Para-fly            DMKDVMVLNDIIEQAAGRHSRASDRGVSVYYFPTEDDDEDGPTFKDKALEVILKGIDVFC      796
                      ..  :  *::::   *:   *  .:      *:   *:    ::*.     :  . :
```

```
Nav1.7-human        IWNCSPYWIKFKKCIYFIVMDPFVDLAITICIVLNTLFMAMEHHPMTEEFKNVLAIGNLV      782
Nav1.7-macaque      IWNCSPYWIKFKKCIYFIVMDPFVDLAITICIVLNTLFMAMEHHPMTEEFKNVLAIGNLV      771
Nav1.7-cattle       IWNCSPYWIKFKKFIYFIVMDPFVDLAITICIVLNTLFMAMEHHPMTEEFKNVLVVGNLV      781
Nav1.7-opossum      IWNCSPRWLKFKKFIHLIVMDPFVDLAITICIVLNTLFMAMEHYPMTEGFKNMLTVGNLV      777
Nav1.7-chicken      IWNCCEVWLKVKSVVSFIVMDPLVDLAITICIILNTLFMAMEHYPMTETFNNTLKVGNQV      797
Nav1.7-rat          IWNCSPYWIKFKKLIYFIVMDPFVDLAITICIVLNTLFMAMEHHPMTEEFKNVLAVGNLI      781
Nav1.7-mouse        IWNCSPYWIKFKKFIYFIVMDPFVDLAITICIVLNTLFMAMEHHPMTDEFKNVLAVGNLV      781
Para-fly            VWDCCWVWLKFQEWVSLIVFDPFVELFITLCIVVNTMFMAMDHHDMNKEMERVLKSGNYF      856
                    :*:*.  *:*.:. : :**:**:*:* **:**::**:****:*: *.. ::. *  ** .

Nav1.7-human        FTGIFAAEMVLKLIAMDPYEYFQVGWNIFDSLIVTLSLVELFLADVEGLSVLRSFRLLRV      842
Nav1.7-macaque      FTGIFAAEMVLKLIAMDPYEYFQVGWNIFDSLIVTLSLVELFLADVEGLSVLRSFRLLRV      831
Nav1.7-cattle       FTGIFAAEMVLKLIAMDPYEYFQIGWNIFDSLIVTLSLVELFLSDVEGLSVLRSFRLLRV      841
Nav1.7-opossum      FTGIFAAEMVLKIIAMDPYEYFQVGWNIFDSVIVTLSLVELFLADVEGLSVLRSFRLLRV      837
Nav1.7-chicken      FTGIFAAEMVLKIIAMDPFYYFQVGWNIFDSFIVTLSLVELFLANVDGLSVLRSFRLLRV      857
Nav1.7-rat          FTGIFAAEMVLKLIAMDPYEYFQVGWNIFDSLIVTLSLIELFLADVEGLSVLRSFRLLRV      841
Nav1.7-mouse        FTGIFAAEMVLKLIAMDPYEYFQVGWNIFDSLIVTLSLVELFLADVEGLSVLRSFRLLRV      841
Para-fly            FTATFAIEATMKLMAMSPKYYFQEGWNIFDFIIVALSLLELGLEGVQGLSVLRSFRLLRV      916
                    **. ** * .:*::**.*  *** ****** .**:***:** * .*:**************

Nav1.7-human        FKLAKSWPTLNMLIKIIGNSVGALGNLTLVLAIIVFIFAVVGMQLFGKSYKECVCKINDD      902
Nav1.7-macaque      FKLAKSWPTLNMLIKIIGNSVGALGNLTLVLAIIVFIFAVVGMQLFGKSYKECVCKINDD      891
Nav1.7-cattle       FKLAKSWPTLNMLIKIIGNSVGALGNLTLVLAIIVFIFAVVGMQLFGKSYKECVCKINED      901
Nav1.7-opossum      FKLAKSWPTLNMLIKIIGNSVGALGNLTLVLAIIVFIFAVVGMQLFGKSYKECVCKISSD      897
Nav1.7-chicken      FKLAKSWPTLNMLIKIIGNSVGALGNLTLVLAIIVFIFAVVGMQLFGKYYKECVCKISSD      917
Nav1.7-rat          FKLAKSWPTLNMLIKIIGNSVGALGNLTLVLAIIVFIFAVVGMQLFGKSYKECVCKINVD      901
Nav1.7-mouse        FKLAKSWPTLNMLIKIIGNSVGALGNLTLVLAIIVFIFAVVGMQLFGKSYKECVCKINEN      901
Para-fly            FKLAKSWPTLNLLISIMGRTMGALGNLTFVLCIIIFIFAVMGMQLFGKNYHDHKDRF-PD      975
                    ***********:**.*:*.::*******:**.**:*****:******* *::   ::  :

Nav1.7-human        CTLPRWHMNDFFHSFLIVFRVLCGEWIETMWDCMEVAGQAMCLIVYMMVMVIGNLVVLNL      962
Nav1.7-macaque      CTLPRWHMNDFFHSFLIVFRVLCGEWIETMWDCMEVAGQAMCLIVYMMVMVIGNLVVLNL      951
Nav1.7-cattle       CTLPRWHMNDFFHSFLIVFRVLCGEWIETMWDCMEVAGQAMCLIVYMMVMVIGNLVVLNL      961
Nav1.7-opossum      CELPRWHMNDFFHSFLIVFRVLCGEWIETMWDCMEVAGQSMCLIVYMMVMVIGNLVVLNL      957
Nav1.7-chicken      CELPRWHMHDFFHSFLIVFRVLCGEWIETMWDCMEVAGQPMCLTVFMMVMVIGNLVVLNL      977
Nav1.7-rat          CKLPRWHMNDFFHSFLIVFRVLCGEWIETMWDCMEVAGQTMCLIVYMMVMVIGNLVVLNL      961
Nav1.7-mouse        CKLPRWHMNDFFHSFLIVFRVLCGEWIETMWDCMEVAGQTMCLIVYMMVMVIGNLVVLNL      961
Para-fly            GDLPRWNFTDFMHSFMIVFRVLCGEWIESMWDCMYV-GDVSCIPFFLATVVIGNLVVLNL     1034
                      ****:: **:***:************:***** * *:  *: .:: .:**********

Nav1.7-human        FLALLLSSFSSDNLTAIEEDPDANNLQIAVTRIKKGINYVKQTLREFILKAFSKKPKISR     1022
Nav1.7-macaque      FLALLLSSFSSDNLTAIEEDPDANNLQIAVTRIKKGINYVKQTLREFILKTFSKKPKISR     1011
Nav1.7-cattle       FLALLLSSFSSDNLTAIEEDTDANNLQIAVARIKKGIKYVKQTLREFVLKAFSKKPKISK     1021
Nav1.7-opossum      FLALLLSSFSSDNLTAIEEDTDANNLQIAVVRIKKGINYIKKTIRELIQKAFVNKPKISN     1017
Nav1.7-chicken      FLALLLSSFSSDSLSPTEDDNEMNNLQIAVARIQKGIDYVKEKVGEYIQKSCWRKQMAAN     1037
Nav1.7-rat          FLALLLSSFSSDNLTAIEEDTDANNLQIAVARIKRGINYVKQTLREFILKSFSKKPKGSK     1021
Nav1.7-mouse        FLALLLSSFSSDNLTAIEEDTDANNLQIAVARIKRGINYVKQTLREFILKSFSKKPKGSK     1021
Para-fly            FLALLLSNFGSSSLSAPTADNDTNKIAEAFNRIGRFKSWVKRNIADCFKLIRN---KLTN     1091
                    *******.*.*..*:    * : *::  *. ** :  .::*..: : .          :.

Nav1.7-human        EIRQAEDLNTKKENYI----------SNHTLAEMSKGHNFLKEK-----DKI--------     1059
Nav1.7-macaque      EIRQTEDLNTKKENYI----------SNYTLAEMSKGHNFLKEK-----DKI--------     1048
Nav1.7-cattle       EIRQTEDLNCKKENYI----------SNRTLAEMSKDHKFHKEK-----DKT--------     1058
Nav1.7-opossum      EIRKVDDRNIKKENYI----------SNRTLAEMSKDQHFHIDR-----DGT--------     1054
Nav1.7-chicken      ERTATDQLNDERHHCI----------SNCTVAEIKADTTYHKNE-----NGT--------     1074
Nav1.7-rat          DTKRTADPNNKKENYI----------SNRTLAEMSKDHNFLKEK-----DRI--------     1058
Nav1.7-mouse        DTKRTADPNNKRENYI----------SNRTLAEISKDHNFLKEK-----DKI--------     1058
Para-fly            QIS--DQPSGERTNQISWIWSEGKGVCRCISAEHG-DNELELGHDEILADGLIKKGIKEQ     1148
                    :     : . :: : *          ..   **   .      .     :

Nav1.7-human        ----SGFGSSVDKHLME-----DSDGQSFIHNPSLTVTVPIAPGESDLENMNAEELSSDS     1110
Nav1.7-macaque      ----SGFGSCVDKYLME-----DSDGQSFIHNPSLTVTVPIAPGESDLENMNTEELSSDS     1099
Nav1.7-cattle       ----SGFGNSMDKYLME-----ESDGQSFIHNPSLTVTVPIAPGESDLEIMNTEELSSDS     1109
Nav1.7-opossum      ----SGFGSSMERYMME-----ESDCQSYIHNPSLTVTVPIAQGESDFENVNTEEFSSES     1105
Nav1.7-chicken      ----AGVVG-------------SSDYPLFINNPSLTVTVPIAVGESDFEHLNTEEFSSDS     1117
Nav1.7-rat          ----SGYGSSLDKSFMD-----ENDYQSFIHNPSLTVTVPIAPGESDLEIMNTEELSSDS     1109
Nav1.7-mouse        ----SGFSSSLDKSFMD-----ENDYQSFIHNPSLTVTVPIAPGESDLENMNTEELSSDS     1109
Para-fly            TQLEVAIGDGMEFTIHGDMKNNKPKKSKYLNNATDDDTASINSYG----SHKNRPFKDES     1204
                         .  .            . .   :::* :   *. *          : . :..:*
```

```
Nav1.7-human        DSEYSKVRL----NRSSSSECSTVDNPLPGEGEE------------AEAEPMNSDEPEAC      1154
Nav1.7-macaque      DSEYSKVRL----NQSSSSECSTVDNPLPGEGEE------------AEAEPMNSDEPEAC      1143
Nav1.7-cattle       DSEYSKGRL----NQSSSSECSTVDNPVPGEGEE------------AEAEPVNSDEPEAC      1153
Nav1.7-opossum      DVEGSKERV----HRSSSSEGSTIDNAIPEDREE------------AVAEPENSDEPEAC      1149
Nav1.7-chicken      DLEESKEKI----NLSSSSEGSTVNLALFGE-EK------------AETEPEKAAELQTC      1160
Nav1.7-rat          DSDYSKEKR----NRSSSSECSTVDNPLPGEE-E------------AEAEPVNADEPEAC      1152
Nav1.7-mouse        DSDYSKERR----NRSSSSECSTVDNPLPGEE-E------------AEAEPINADEPEAC      1152
Para-fly            -HKGSAETMEGEEKRDASKEDLGLDEELDEEGECEEGPLDGDIIIHAHDEDILDEYPADC      1263
                      . *        : .:*.*   ::  :  :               *  *         *

Nav1.7-human        FTDGCVWRFSCCQVNIESGKGKIWWNIRKTCYKIVEHSWFESFIVLMILLSSGALAFEDI      1214
Nav1.7-macaque      FTDGCVRRFSCCQVNIESGKGKIWWNIRKTCYKIVEHSWFESFIVLMILLSSGALAFEDI      1203
Nav1.7-cattle       FTDGCVQRFPCCQVNIESGKGKIWWNIRKTCFRIVEHSWFESFIVLMILLSSGALAFEDI      1213
Nav1.7-opossum      FTDGCVRRFPCCQVSVESGNGKVWWNIRKTCYRIVEHNWFESFIVLMILLSSGALAFEDI      1209
Nav1.7-chicken      FTEGCIQKFKCCRCSIESRRGIIWWNLRKTCYRIVEHNWFETFIVFMILLSSGTLAFEDI      1220
Nav1.7-rat          FTDGCVRRFPCCQVNVDSGKGKVWWTIRKTCYRIVEHSWFESFIVLMILLSSGALAFEDI      1212
Nav1.7-mouse        FTDGCVRRFPCCQVNIDSGKGKVWWTIRKTCYRIVEHSWFESFIVLMILLSSGALAFEDI      1212
Para-fly            CPDSYYKKFPILAGDDDSPFWQGWGNLRLKTFQLIENKYFETAVITMILMSSLALALEDV      1323
                      :.   :*     . :*     * .:* . ::::*:.:**: :: ***:** :**:**:

Nav1.7-human        YIERKKTIKIILEYADKIFTYIFILEMLLKWIAYGYKTYFTNAWCWLDFLIVDVSLVTLV      1274
Nav1.7-macaque      YIERKKTIKIILEYADKIFTYIFILEMLLKWIAYGYKTYFTNAWCWLDFLIVDVSLVTLV      1263
Nav1.7-cattle       YIEKKKNIKIILEYADKIFTYIFILEMLLKWVAYGYKTYFTNAWCWLDFLIVDVSLVTLV      1273
Nav1.7-opossum      YIEQRKTIKTVLEYADKIFTYVFILEMLLKWVAYGYKVYFTNAWCWLDFLIVDVSIITLV      1269
Nav1.7-chicken      YIEQRKTIKVILDYADKIFTYIFILEMVLKWVAYGFQTYFTNAWCWLDFLIVDVSLVSLV      1280
Nav1.7-rat          YIEKKKTIKIILEYADKIFTYIFILEMLLKWVAYGYKTYFTNAWCWLDFLIVDVSLVTLV      1272
Nav1.7-mouse        YIEKKKTIKIILEYADKIFTYIFILEMLLKWVAYGYKTYFTNAWCWLDFLIVDVSLVTLV      1272
Para-fly            HLPQRPILQDILYYMDRIFTVIFFLEMLIKWLALGFKVYFTNAWCWLDFVIVMVSLINFV      1383
                    :: ::  :: :* * *:*** :*:***::**:* *::.***********:** **::.:*

Nav1.7-human        ANTLGYSDLGPIKSLRTLRALRPLRALSRFEGMRVVVNALIGAIPSIMNVLLVCLIFWLI      1334
Nav1.7-macaque      ANTLGYSDLGPIKSLRTLRALRPLRALSRFEGMRVVVNALIGAIPSIMNVLLVCLIFWLI      1323
Nav1.7-cattle       ANTLGYSDLGPIKSLRTLRALRPLRALSRFEGMRVVVNALIGAIPSIMNVLLVCLIFWLI      1333
Nav1.7-opossum      ASTLGYSDLGPIKSLRTLRALRPLRALSRFEGMRVVVNALLGAIPSIMNVLLVCLIFWLI      1329
Nav1.7-chicken      ATALGFSELGAIKSLRTLRALRPLRALSRFEGMRVVVNALTGAIPSIMNVLLVCLTFWLI      1340
Nav1.7-rat          ANTLGYSDLGPIKSLRTLRALRPLRALSRFEGMRVVVNALIGAIPSIMNVLLVCLIFWLI      1332
Nav1.7-mouse        ANTLGYSDLGPIKSLRTLRALRPLRALSRFEGMRVVVNALIGAIPSIMNVLLVCLIFWLI      1332
Para-fly            ASLVGAGGIQAFKTMRTLRALRPLRAMSRMQGMRVVVNALVQAIPSIFNVLLVCLIFWLI      1443
                    *. :* . :  :*::***********:**::*********  *****:******* ****

Nav1.7-human        FSIMGVNLFAGKFYECINTTDGSRFPASQVPNRSECFALMNVSQNVRWKNLKVNFDNVGL      1394
Nav1.7-macaque      FSIMGVNLFAGKFYECINTTDGSRFPASQVPNRSECFALMNVSQNVRWKNLKVNFDNVGL      1383
Nav1.7-cattle       FSIMGVNLFAGKFYECINTTNGLRFPTSEVENRSACLALMNVSQNVRWKNLKVNFDNVGL      1393
Nav1.7-opossum      FSIMGVNLFAGKFYECVNTTNGERFPVTVVETYEQCKQLMNSSHDVRWKNVKVNFDNVGI      1389
Nav1.7-chicken      FSIMGVNLFAGKFFYCVNTTTGVQFKPYEVDNKSMCENLGNTASDVRWKNVKVNFDNVGA      1400
Nav1.7-rat          FSIMGVNLFAGKFYECVNTTDGSRFPTSQVANRSECFALMNVSGNVRWKNLKVNFDNVGL      1392
Nav1.7-mouse        FSIMGVNLFAGKFYECVNTTDGSRFSVSQVANRSECFALMNVSGNVRWKNLKVNFDNVGL      1392
Para-fly            FAIMGVQLFAGKYFKCEDM-NGTKLSHEIIPNRNACE-----SENYTWVNSAMNFDHVGN      1497
                    *:****:*****:: * :   * ::    : . . *      : :  * *  :***:**

Nav1.7-human        GYLSLLQVATFKGWTIIMYAAVDSVNVDKQPKYEYSLYMYIYFVVFIIFGSFFTLNLFIG      1454
Nav1.7-macaque      GYLSLLQVATFKGWTIIMYAAVDSVNVDKQPKYEYSLYMYIYFVIFIIFGSFFTLNLFIG      1443
Nav1.7-cattle       GYLSLLQVATFKGWMDIMYAAVDSVNVDKQPIYEYSLYMYIYFVIFIIFGSFFTLNLFIG      1453
Nav1.7-opossum      GYLSLLQVATFKGWMIIMYAAVDSVNINFQPKYEASLYMYLYFVIFIIFGSFFTLNLFIG      1449
Nav1.7-chicken      GYLSLLQVATFKGWMEIMYAAVDSRDVGKQPMYEDNLYMYLYFVAFIIFGSFFTLNLFIG      1460
Nav1.7-rat          GYLSLLQVATFKGWMDIMYAAVDSVNVNEQPKYEYSLYMYIYFVIFIIFGSFFTLNLFIG      1452
Nav1.7-mouse        GYLSLLQVATFKGWMDIMYAAVDSVNVNAQPIYEYNLYMYIYFVIFIIFGSFFTLNLFIG      1452
Para-fly            AYLCLFQVATFKGWIQIMNDAIDSREVDKQPIRETNIYMYLYFVFFIIFGSFFTLNLFIG      1557
                    .**.*:********  **  *:** ::. **  * .:***:*** ***************

Nav1.7-human        VIIDNFNQQKKK--------LGGQDIFMTEEQKKYYNAMKKLGSKKPQKPIPRPGNKIQG      1506
Nav1.7-macaque      VIIDNFNQQKKK--------LGGQDIFMTEEQKKYYNAMKKLGSKKPQKPIPRPGNKIQG      1495
Nav1.7-cattle       VIIDNFNQQKKK--------LGGQDIFMTEEQKKYYNAMKKLGSKKPQKPIPRPGNKFQG      1505
Nav1.7-opossum      VIIDNFNQQKKKIIFILFLYLGGQDIFMTEEQKKYYNAMKKLGSKKPQKPIPRPGNKFQG      1509
Nav1.7-chicken      VIIDNFNQQKKK--------LGGQDIFMTEEQKKYYNAMKKLGSKKPQKPIPRPANKLQG      1512
Nav1.7-rat          VIIDNFNQQKKK--------LGGQDIFMTEEQKKYYNAMKKLGSKKPQKPIPRPGNKFQG      1504
Nav1.7-mouse        VIIDNFNQQKKK--------LGGQDIFMTEEQKKYYNAMKKLGSKKPQKPIPRPGNKFQG      1504
Para-fly            VIIDNFNEQKKKA-------GGSLEMFMTEDQKKYYNAMKKMGSKKPLKAIPRPRWRPQA      1610
                    *******:****         *. ::****:**********:***** * ****  : *.
```

```
Nav1.7-human        CIFDLVTNQAFDISIMVLICLNMVTMMVEKEGQSQHMTEVLYWINVVFIILFTGECVLKL      1566
Nav1.7-macaque      CIFDLVTNQAFDISIMVLICLNMVTMMVEKEGQSPYMTDVLYWINVVFIILFTGECVLKL      1555
Nav1.7-cattle       CIFDLVTNQAFDIAIMVLICLNMVTMMVEKEGQSDYVTEVLNWINVVFIILFSGECVLKL      1565
Nav1.7-opossum      CIFDIVTKQAFDITIMVLICLNMVTMMVEKDEQSETMTYVLYWINMVFIILFTGECVLKL      1569
Nav1.7-chicken      LVFDIVTKQAFDIGIMVLICLNMVTMMIETDDQSELMQNILYWINFVFVVLFTGECVLKL      1572
Nav1.7-rat          CIFDLVTNQAFDITIMVLICLNMVTMMVEKEGQTEYMDYVLHWINMVFIILFTGECVLKL      1564
Nav1.7-mouse        CIFDLVTNQAFDITIMVLICLNMVTMMVEKEGQTDYMSFVLYWINVVFIILFTGECVLKL      1564
Para-fly            IVFEIVTDKKFDIIIMLFIGLNMFTMTLDRYDASDTYNAVLDYLNAIFVVIFSSECLLKI      1670
                     :*::**.: *** **::* ***.** ::    :     :* ::* :*:::*:.**:**:

Nav1.7-human        ISLRHYYFTVGWNIFDFVVVIISIVGMFLADLIETYFVSPTLFRVIRLARIGRILRLVKG      1626
Nav1.7-macaque      ISLRYYYFTIGWNIFDFVVVIISIVGMFLADLIETYFVSPTLFRVIRLARIGRILRLVKG      1615
Nav1.7-cattle       ISLRCYYFTVGWNIFDFVVVILSIVGMFLADLIERYFVSPTLFRVIRLARIGRILRLIKG      1625
Nav1.7-opossum      ISLRHYYFTIGWNIFDFVVVILSIVGMFLADLIEKYFVSPTLFRVIRLARIGRILRLIKG      1629
Nav1.7-chicken      FSLRYYYFTVGWNIFDFVVVILSIVGMFLAKVIEKYFVSPTLFRVIRLARIGRILRLIKG      1632
Nav1.7-rat          ISLRHYYFTVGWNIFDFVVVILSIVGMFLAEMIEKYFVSPTLFRVIRLARIGRILRLIKG      1624
Nav1.7-mouse        ISLRHYYFTVGWNIFDFVVVILSIVGMFLAEMIEKYFVSPTLFRVIRLARIGRILRLIKG      1624
Para-fly            FALRYHYFIEPWNLFDVVVVILSILGLVLSDIIEKYFVSPTLLRVVRVAKVGRVLRLVKG      1730
                    ::** :**   **:**.****:**:*:.*:.:** *******:**:*:*::**:***:**

Nav1.7-human        AKGIRTLLFALMMSLPALFNIGLLLFLVMFIYAIFGMSNFAYVKKEDGINDMFNFETFGN      1686
Nav1.7-macaque      AKGIRTLLFALMMSLPALFNIGLLLFLVMFIYAIFGMSNFAYVKKEDGINDMFNFETFGN      1675
Nav1.7-cattle       AKGIRTLLFALMMSLPALFNIGLLLFLVMFIYAIFGMSNFAYVKKEAGINDMFNFETFAN      1685
Nav1.7-opossum      AKGIRTLLFALMMSLPALFNIGLLLFLVMFIYAIFGMSNFAYVKKEEGINDMFNFETFGN      1689
Nav1.7-chicken      AKGIRTLLFALMMSLPALFNIGLLLFLVMFIYAIFGMSNFAYVKREAGIDDMFNFETFGN      1692
Nav1.7-rat          AKGIRTLLFALMMSLPALFNIGLLLFLVMFIYAIFGMSNFAYVKKEAGINDMFNFETFGN      1684
Nav1.7-mouse        AKGIRTLLFALMMSLPALFNIGLLLFLVMFIYAIFGMSNFAYVKKEAGINDMFNFETFGN      1684
Para-fly            AKGIRTLLFALAMSLPALFNICLLLFLVMFIFAIFGMSFFMHVKEKSGINDVYNFKTFGQ      1790
                    *********** ********* *********:****** * :**.: **:*::**:**.:

Nav1.7-human        SMICLFQITTSAGWDGLLAPILNSKPPDCDPKKVHPGSSVEGDCGNPSVGIFYFVSYIII      1746
Nav1.7-macaque      SMICLFQITTSAGWDGLLAPILNSKPPDCDPKKVHPGSSVEGDCGNPSVGIFYFVSYIII      1735
Nav1.7-cattle       SMICLFQITTSAGWDGLLAPILNSKPPDCDPKKVHPGSSVEGDCGNPSVGIFYFVSYIII      1745
Nav1.7-opossum      SMICLFQITTSAGWDGLLAPILNSGPPDCDPEKVHPGSSVKGDCGNSSVGIFYFVSYIII      1749
Nav1.7-chicken      SMICLFQITTSAGWDGLLAPILNSGKPDCDPNKPHPGSSVKGDCGNPSVGIFFFVSYIII      1752
Nav1.7-rat          SMICLFQITTSAGWDGLLAPILNSAPPDCDPKKVHPGSSVEGDCGNPSVGIFYFVSYIII      1744
Nav1.7-mouse        SMICLFQITTSAGWDGLLAPILNSAPPDCDPKKVHPGSSVEGDCGNPSVGIFYFVSYIII      1744
Para-fly            SMILLFQMSTSAGWDGVLDAIINEE--ACDPPDND--KGYPGNCGSATVGITFLLSYLVI      1846
                    *** ***::*******:*  *:*.    *** . .  ..  *:**. :*** :::**::*

Nav1.7-human        SFLVVVNMYIAVILENFSVATEESTEPLSEDDFEMFYEVWEKFDPDATQFIEFSKLSDFA      1806
Nav1.7-macaque      SFLVVVNMYIAVILENFSVATEESTEPLSEDDFEMFYEVWEKFDPDATQFIEYNKLSDFA      1795
Nav1.7-cattle       SFLVVVNMYIAVILENFSVATEESTEPLSEDDFEMFYEVWEKFDPDATQFIEYSKLSDFA      1805
Nav1.7-opossum      SFLVVVNMYIAVILENFSVATEESTEPLSEDDFEMFYEVWEKFDPDATQFIEYSKLSDFA      1809
Nav1.7-chicken      SFLVVVNMYIAVILENFGVATEESAEPLSEDDFEMFYEVWEKYDPDATQFIEYSKLSDFA      1812
Nav1.7-rat          SFLVVVNMYIAVILENFSVATEESTEPLSEDDFEMFYEVWEKFDPDATQFIEFCKLSDFA      1804
Nav1.7-mouse        SFLVVVNMYIAVILENFSVATEESTEPLSEDDFEMFYEVWEKFDPDATQFIEFCKLSDFA      1804
Para-fly            SFLIVINMYIAVILENYSQATEDVQEGLTDDDYDMYYEIWQQFDPEGTQYIRYDQLSEFL      1906
                    ***:*:**********:. ***:  * *::**::*:**:*:::**:.**:*.: :**:*

Nav1.7-human        AALDPPLLIAKPNKVQLIAMDLPMVSGDRIHCLDILFAFTKRVLGESGEMDSLRSQMEER      1866
Nav1.7-macaque      AALDPPLLIAKPNKVQLIAMDLPMVSGDRIHCLDILFAFTKRVLGESGEMDSLRSQMEER      1855
Nav1.7-cattle       AALDPPLLIAKPNKVQLIAMDLPMVSGDRIHCLDILFAFTKRVLGEGGEMDSLRSQMEER      1865
Nav1.7-opossum      ASLDPPLHIAKPNKVQLVAMDLPMVNGDRIHCLDILFAFTKRVLGESEEMDTLRLQMEER      1869
Nav1.7-chicken      ASLDPPLNIPKPNKVQLIAMDLPMVSGDRIHCLDILFAFTKRVLGESDEMDALRVQMEDR      1872
Nav1.7-rat          AALDPPLLIAKPNKVQLIAMDLPMVSGDRIHCLDILFAFTKRVLGEGGEMDSLRSQMEER      1864
Nav1.7-mouse        AALDPPLLIAKPNKVQLIAMDLPMVSGDRIHCLDILFAFTKRVLGESGEMDSLRSQMEER      1864
Para-fly            DVLEPPLQIHKPNKYKIISMDIPICRGDLMYCVDILDALTKDFFARKGNPI--EETGEIG      1964
                      *:*** * **** ::::**:*:  ** ::*:*** *:** .:..  :    .   *

Nav1.7-human        FMSANPSKVSYEPITTTLKRKQEDVSATVIQRAYRRYRLRQNVKNISSIYIKDGDRDDDL      1926
Nav1.7-macaque      FMSANPSKVSYEPITTTLKRKQEDVSATVIQRAYRRYRLRQNVKNISSIYIKDGDRDDDL      1915
Nav1.7-cattle       FMSANPSKVSYEPITTTLKRKQEDVSATVIQRAYRRYRLRQNVKNISSIYIKDGDRDDDL      1925
Nav1.7-opossum      FVAANPSKVSFEPITTTLKRKQEEVSATIIQRAFRHYRLRQNVKHISGIYNKGGERV-DL      1928
Nav1.7-chicken      FMAANPSKVSYEPITTTLKRKQEEVSATIIQRAYRCYLLRRSIKKLSCMYRKDGV---DV      1929
Nav1.7-rat          FMSANPSKVSYEPITTTLKRKQEEVSATIIQRAYRRYRLRQHVKNISSIYIKDGDRDDDL      1924
Nav1.7-mouse        FMSANPSKVSYEPITTTLKRKQEDVSATIIQRAYRRYRLRQNVKNISSIYIKDGDRDDDL      1924
Para-fly            EIAARPDTEGYEPVSSTLWRQREEYCARLIQHAWRKHKARGEGGG---SFEPDTDHGDG-      2020
                     ::*.*.. .:**:::** *::*: .* :**:*:* :  *         :  .     .
```

```
Nav1.7-human        LNKKDMAFDNVNENSSPEKTD-ATSSTTSPPSYD-SVTKPDKEKYEQDRTEKEDKGKDSK      1984
Nav1.7-macaque      LNKKDMAFDNVNENSSPEKTD-ATSSTTSPPSYD-SVTKPDKEKYEQDRTEKEDKGKDSK      1973
Nav1.7-cattle       PNKEDMVFDNVNENSSPEKTG-ATPSTVSPPSYD-SVTKPDREKYEKDKTEKEDKGKDGK      1983
Nav1.7-opossum      TMKEDMVFGKVNGNSTPEKTDEVTPSTTSPPSYD-SVTKRDKEKYEKDKAEKEDKDKDGR      1987
Nav1.7-chicken      LSKNYMLFGKLSENSASEKTN-MTASTTYPPSYD-SVTKQEKEKYEDDKSEKEDKGKDRK      1987
Nav1.7-rat          PNKEDTVFDNVNENSSPEKTD-VTASTISPPSYD-SVTKPDQEKYETDKTEKEDKEKDES      1982
Nav1.7-mouse        PNKEDIVFDNVNENSSPEKTD-ATASTISPPSYD-SVTKPDQEKYETDKTEKEDKEKDES      1982
Para-fly            ---GDP----DAGDPAPDEA---TDG-DAPAGGDGSVNGTAEGAADADESNVNSPGEDAA      2069
                                 : : :::   * .   * . * **.   .   : *.:: :.  :*

Nav1.7-human        E-----------------------------------------SKK----------------      1988
Nav1.7-macaque      E-----------------------------------------SKK----------------      1977
Nav1.7-cattle       E-----------------------------------------GKK----------------      1987
Nav1.7-opossum      E-----------------------------------------GKK----------------      1991
Nav1.7-chicken      G-----------------------------------------NKK----------------      1991
Nav1.7-rat          R-----------------------------------------K------------------      1984
Nav1.7-mouse        R-----------------------------------------K------------------      1984
Para-fly            AAAAAAAAAAAAAGTTTAGSPGAGSAGRQTAVLVESDGFVTKNGHKVVIHSRSPSITSRTA      2129


Nav1.7-human        --      1988
Nav1.7-macaque      --      1977
Nav1.7-cattle       --      1987
Nav1.7-opossum      --      1991
Nav1.7-chicken      --      1991
Nav1.7-rat          --      1984
Nav1.7-mouse        --      1984
Para-fly            DV      2131
```

Appendix E: MSA of hNav1.7 splice isoforms and the hNav1.7 structure PDB code: 6J8G

```
Q15858-1_5N11L      -------------------------------------------MAMLPPPGPQSFVHFTK      17
FC_SCN9A_5N11S      -------------------------------------------MAMLPPPGPQSFVHFTK      17
PDB_6J8G_5N11L      MASWSHPQFEKGGGARGGSGGGSWSHPQFEKGFDYKDDDDKGTMAMLPPPGPQSFVHFTK      60
                                                              *****************

Q15858-1_5N11L      QSLALIEQRIAERKSKEPKEEKKDDDEEAPKPSSDLEAGKQLPFIYGDIPPGMVSEPLED      77
FC_SCN9A_5N11S      QSLALIEQRIAERKSKEPKEEKKDDDEEAPKPSSDLEAGKQLPFIYGDIPPGMVSEPLED      77
PDB_6J8G_5N11L      QSLALIEQRIAERKSKEPKEEKKDDDEEAPKPSSDLEAGKQLPFIYGDIPPGMVSEPLED      120
                    ************************************************************

Q15858-1_5N11L      LDPYYADKKTFIVLNKGKTIFRFNATPALYMLSPFSPLRRISIKILVHSLFSMLIMCTIL      137
FC_SCN9A_5N11S      LDPYYADKKTFIVLNKGKTIFRFNATPALYMLSPFSPLRRISIKILVHSLFSMLIMCTIL      137
PDB_6J8G_5N11L      LDPYYADKKTFIVLNKGKTIFRFNATPALYMLSPFSPLRRISIKILVHSLFSMLIMCTIL      180
                    ************************************************************

Q15858-1_5N11L      TNCIFMTMNNPPDWTKNVEYTFTGIYTFESLVKILARGFCVGEFTFLRDPWNWLDFVVIV      197
FC_SCN9A_5N11S      TNCIFMTMNNPPDWTKNVEYTFTGIYTFESLVKILARGFCVGEFTFLRDPWNWLDFVVIV      197
PDB_6J8G_5N11L      TNCIFMTMNNPPDWTKNVEYTFTGIYTFESLVKILARGFCVGEFTFLRDPWNWLDFVVIV      240
                    ************************************************************

Q15858-1_5N11L      FAYLTEFVNLGNVSALRTFRVLRALKTISVIPGLKTIVGALIQSVKKLSDVMILTVFCLS      257
FC_SCN9A_5N11S      FAYLTEFVNLGNVSALRTFRVLRALKTISVIPGLKTIVGALIQSVKKLSDVMILTVFCLS      257
PDB_6J8G_5N11L      FAYLTEFVNLGNVSALRTFRVLRALKTISVIPGLKTIVGALIQSVKKLSDVMILTVFCLS      300
                    ************************************************************

Q15858-1_5N11L      VFALIGLQLFMGNLKHKCFRNSLENNETLESIMNTLESEEDFRKYFYYLEGSKDALLCGF      317
FC_SCN9A_5N11S      VFALIGLQLFMGNLKHKCFRNSLENNETLESIMNTLESEEDFRKYFYYLEGSKDALLCGF      317
PDB_6J8G_5N11L      VFALIGLQLFMGNLKHKCFRNSLENNETLESIMNTLESEEDFRKYFYYLEGSKDALLCGF      360
                    ************************************************************

Q15858-1_5N11L      STDSGQCPEGYTCVKIGRNPDYGYTSFDTFSWAFLALFRLMTQDYWENLYQQTLRAAGKT      377
FC_SCN9A_5N11S      STDSGQCPEGYTCVKIGRNPDYGYTSFDTFSWAFLALFRLMTQDYWENLYQQTLRAAGKT      377
PDB_6J8G_5N11L      STDSGQCPEGYTCVKIGRNPDYGYTSFDTFSWAFLALFRLMTQDYWENLYQQTLRAAGKT      420
                    ************************************************************

Q15858-1_5N11L      YMIFFVVVIFLGSFYLINLILAVVAMAYEEQNQANIEEAKQKELEFQQMLDRLKKEQEEA      437
FC_SCN9A_5N11S      YMIFFVVVIFLGSFYLINLILAVVAMAYEEQNQANIEEAKQKELEFQQMLDRLKKEQEEA      437
PDB_6J8G_5N11L      YMIFFVVVIFLGSFYLINLILAVVAMAYKEQNQANIEEAKQKELEFQQMLDRLKKEQEEA      480
                    ****************************:*******************************

Q15858-1_5N11L      EAIAAAAAEYTSIRRSRIMGLSESSSETSKLSSKSAKERRNRRKKKNQKKLSSGEEKGDA      497
FC_SCN9A_5N11S      EAIAAAAAEYTSIRRSRIMGLSESSSETSKLSSKSAKERRNRRKKKNQKKLSSGEEKGDA      497
PDB_6J8G_5N11L      EAIAAAAAEYTSIRRSRIMGLSESSSETSKLSSKSAKERRNRRKKKNQKKLSSGEEKGDA      540
                    ************************************************************

Q15858-1_5N11L      EKLSKSESEDSIRRKSFHLGVEGHRRAHEKRLSTPNQSPLSIRGSLFSARRSSRTSLFSF      557
FC_SCN9A_5N11S      EKLSKSESEDSIRRKSFHLGVEGHRRAHEKRLSTPNQSPLSIRGSLFSARRSSRTSLFSF      557
PDB_6J8G_5N11L      EKLSKSESEDSIRRKSFHLGVEGHRRAHEKRLSTPNQSPLSIRGSLFSARRSSRTSLFSF      600
                    ************************************************************

Q15858-1_5N11L      KGRGRDIGSETEFADDEHSIFGDNESRRGSLFVPHRPQERRSSNISQASRSPPMLPVNGK      617
FC_SCN9A_5N11S      KGRGRDIGSETEFADDEHSIFGDNESRRGSLFVPHRPQERRSSNISQASRSPPMLPVNGK      617
PDB_6J8G_5N11L      KGRGRDIGSETEFADDEHSIFGDNESRRGSLFVPHRPQERRSSNISQASRSPPMLPVNGK      660
                    ************************************************************

Q15858-1_5N11L      MHSAVDCNGVVSLVDGRSALMLPNGQLLPEVIIDKATSDDSGTTNQIHKKRRCSSYLLSE      677
FC_SCN9A_5N11S      MHSAVDCNGVVSLVDGRSALMLPNGQLLPE-----------GTTNQIHKKRRCSSYLLSE      666
PDB_6J8G_5N11L      MHSAVDCNGVVSLVDGRSALMLPNGQLLPEVIIDKATSDDSGTTNQIHKKRRCSSYLLSE      720
                    ******************************          ******************

Q15858-1_5N11L      DMLNDPNLRQRAMSRASILTNTVEELEESRQKCPPWWYRFAHKFLIWNCSPYWIKFKKCI      737
FC_SCN9A_5N11S      DMLNDPNLRQRAMSRASILTNTVEELEESRQKCPPWWYRFAHKFLIWNCSPYWIKFKKCI      726
PDB_6J8G_5N11L      DMLNDPNLRQRAMSRASILTNTVEELEESRQKCPPWWYRFAHKFLIWNCSPYWIKFKKCI      780
                    ************************************************************

Q15858-1_5N11L      YFIVMDPFVDLAITICIVLNTLFMAMEHHPMTEEFKNVLAIGNLVFTGIFAAEMVLKLIA      797
FC_SCN9A_5N11S      YFIVMDPFVDLAITICIVLNTLFMAMEHHPMTEEFKNVLAIGNLVFTGIFAAEMVLKLIA      786
PDB_6J8G_5N11L      YFIVMDPFVDLAITICIVLNTLFMAMEHHPMTEEFKNVLAIGNLVFTGIFAAEMVLKLIA      840
                    ************************************************************

Q15858-1_5N11L      MDPYEYFQVGWNIFDSLIVTLSLVELFLADVEGLSVLRSFRLLRVFKLAKSWPTLNMLIK      857
FC_SCN9A_5N11S      MDPYEYFQVGWNIFDSLIVTLSLVELFLADVEGLSVLRSFRLLRVFKLAKSWPTLNMLIK      846
PDB_6J8G_5N11L      MDPYEYFQVGWNIFDSLIVTLSLVELFLADVEGLSVLRSFRLLRVFKLAKSWPTLNMLIK      900
                    ************************************************************
```

```
Q15858-1_5N11L      IIGNSVGALGNLTLVLAIIVFIFAVVGMQLFGKSYKECVCKINDDCTLPRWHMNDFFHSF      917
FC_SCN9A_5N11S      IIGNSVGALGNLTLVLAIIVFIFAVVGMQLFGKSYKECVCKINDDCTLPRWHMNDFFHSF      906
PDB_6J8G_5N11L      IIGNSVGALGNLTLVLAIIVFIFAVVGMQLFGKSYKECVCKINDDCTLPRWHMNDFFHSF      960
                    ************************************************************

Q15858-1_5N11L      LIVFRVLCGEWIETMWDCMEVAGQAMCLIVYMMVMVIGNLVVLNLFLALLLSSFSSDNLT      977
FC_SCN9A_5N11S      LIVFRVLCGEWIETMWDCMEVAGQAMCLIVYMMVMVIGNLVVLNLFLALLLSSFSSDNLT      966
PDB_6J8G_5N11L      LIVFRVLCGEWIETMWDCMEVAGQAMCLIVYMMVMVIGNLVVLNLFLALLLSSFSSDNLT      1020
                    ************************************************************

Q15858-1_5N11L      AIEEDPDANNLQIAVTRIKKGINYVKQTLREFILKAFSKKPKISREIRQAEDLNTKKENY      1037
FC_SCN9A_5N11S      AIEEDPDANNLQIAVTRIKKGINYVKQTLREFILKAFSKKPKISREIRQAEDLNTKKENY      1026
PDB_6J8G_5N11L      AIEEDPDANNLQIAVTRIKKGINYVKQTLREFILKAFSKKPKISREIRQAEDLNTKKENY      1080
                    ************************************************************

Q15858-1_5N11L      ISNHTLAEMSKGHNFLKEKDKISGFGSSVDKHLMEDSDGQSFIHNPSLTVTVPIAPGESD      1097
FC_SCN9A_5N11S      ISNHTLAEMSKGHNFLKEKDKISGFGSSVDKHLMEDSDGQSFIHNPSLTVTVPIAPGESD      1086
PDB_6J8G_5N11L      ISNHTLAEMSKGHNFLKEKDKISGFGSSVDKHLMEDSDGQSFIHNPSLTVTVPIAPGESD      1140
                    ************************************************************

Q15858-1_5N11L      LENMNAEELSSDSDSEYSKVRLNRSSSSECSTVDNPLPGEGEEAEAEPMNSDEPEACFTD      1157
FC_SCN9A_5N11S      LENMNAEELSSDSDSEYSKVRLNRSSSSECSTVDNPLPGEGEEAEAEPMNSDEPEACFTD      1146
PDB_6J8G_5N11L      LENMNAEELSSDSDSEYSKVRLNRSSSSECSTVDNPLPGEGEEAEAEPMNSDEPEACFTD      1200
                    ************************************************************

Q15858-1_5N11L      GCVWRFSCCQVNIESGKGKIWWNIRKTCYKIVEHSWFESFIVLMILLSSGALAFEDIYIE      1217
FC_SCN9A_5N11S      GCVRRFSCCQVNIESGKGKIWWNIRKTCYKIVEHSWFESFIVLMILLSSGALAFEDIYIE      1206
PDB_6J8G_5N11L      GCVWRFSCCQVNIESGKGKIWWNIRKTCYKIVEHSWFESFIVLMILLSSGALAFEDIYIE      1260
                    *** ********************************************************

Q15858-1_5N11L      RKKTIKIILEYADKIFTYIFILEMLLKWIAYGYKTYFTNAWCWLDFLIVDVSLVTLVANT      1277
FC_SCN9A_5N11S      RKKTIKIILEYADKIFTYIFILEMLLKWIAYGYKTYFTNAWCWLDFLIVDVSLVTLVANT      1266
PDB_6J8G_5N11L      RKKTIKIILEYADKIFTYIFILEMLLKWIAYGYKTYFTNAWCWLDFLIVDVSLVTLVANT      1320
                    ************************************************************

Q15858-1_5N11L      LGYSDLGPIKSLRTLRALRPLRALSRFEGMRVVVNALIGAIPSIMNVLLVCLIFWLIFSI      1337
FC_SCN9A_5N11S      LGYSDLGPIKSLRTLRALRPLRALSRFEGMRVVVNALIGAIPSIMNVLLVCLIFWLIFSI      1326
PDB_6J8G_5N11L      LGYSDLGPIKSLRTLRALRPLRALSRFEGMRVVVNALIGAIPSIMNVLLVCLIFWLIFSI      1380
                    ************************************************************

Q15858-1_5N11L      MGVNLFAGKFYECINTTDGSRFPASQVPNRSECFALMNVSQNVRWKNLKVNFDNVGLGYL      1397
FC_SCN9A_5N11S      MGVNLFAGKFYECINTTDGSRFPASQVPNRSECFALMNVSQNVRWKNLKVNFDNVGLGYL      1386
PDB_6J8G_5N11L      MGVNLFAGKFYECINTTDGSRFPASQVPNRSECFALMNVSQNVRWKNLKVNFDNVGLGYL      1440
                    ************************************************************

Q15858-1_5N11L      SLLQVATFKGWTIIMYAAVDSVNVDKQPKYEYSLYMYIYFVVFIIFGSFFTLNLFIGVII      1457
FC_SCN9A_5N11S      SLLQVATFKGWTIIMYAAVDSVNVDKQPKYEYSLYMYIYFVVFIIFGSFFTLNLFIGVII      1446
PDB_6J8G_5N11L      SLLQVATFKGWTIIMYAAVDSVNVDKQPKYEYSLYMYIYFVVFIIFGSFFTLNLFIGVII      1500
                    ************************************************************

Q15858-1_5N11L      DNFNQQKKKLGGQDIFMTEEQKKYYNAMKKLGSKKPQKPIPRPGNKIQGCIFDLVTNQAF      1517
FC_SCN9A_5N11S      DNFNQQKKKLGGQDIFMTEEQKKYYNAMKKLGSKKPQKPIPRPGNKIQGCIFDLVTNQAF      1506
PDB_6J8G_5N11L      DNFNQQKKKLGGQDIFMTEEQKKYYNAMKKLGSKKPQKPIPRPGNKIQGCIFDLVTNQAF      1560
                    ************************************************************

Q15858-1_5N11L      DISIMVLICLNMVTMMVEKEGQSQHMTEVLYWINVVFIILFTGECVLKLISLRHYYFTVG      1577
FC_SCN9A_5N11S      DISIMVLICLNMVTMMVEKEGQSQHMTEVLYWINVVFIILFTGECVLKLISLRHYYFTVG      1566
PDB_6J8G_5N11L      DISIMVLICLNMVTMMVEKEGQSQHMTEVLYWINVVFIILFTGECVLKLISLRHYYFTVG      1620
                    ************************************************************

Q15858-1_5N11L      WNIFDFVVVIISIVGMFLADLIETYFVSPTLFRVIRLARIGRILRLVKGAKGIRTLLFAL      1637
FC_SCN9A_5N11S      WNIFDFVVVIISIVGMFLADLIETYFVSPTLFRVIRLARIGRILRLVKGAKGIRTLLFAL      1626
PDB_6J8G_5N11L      WNIFDFVVVIISIVGMFLADLIETYFVSPTLFRVIRLARIGRILRLVKGAKGIRTLLFAL      1680
                    ************************************************************

Q15858-1_5N11L      MMSLPALFNIGLLLFLVMFIYAIFGMSNFAYVKKEDGINDMFNFETFGNSMICLFQITTS      1697
FC_SCN9A_5N11S      MMSLPALFNIGLLLFLVMFIYAIFGMSNFAYVKKEDGINDMFNFETFGNSMICLFQITTS      1686
PDB_6J8G_5N11L      MMSLPALFNIGLLLFLVMFIYAIFGMSNFAYVKKEDGINDMFNFETFGNSMICLFQITTS      1740
                    ************************************************************

Q15858-1_5N11L      AGWDGLLAPILNSKPPDCDPKKVHPGSSVEGDCGNPSVGIFYFVSYIIISFLVVVNMYIA      1757
FC_SCN9A_5N11S      AGWDGLLAPILNSKPPDCDPKKVHPGSSVEGDCGNPSVGIFYFVSYIIISFLVVVNMYIA      1746
PDB_6J8G_5N11L      AGWDGLLAPILNSKPPDCDPKKVHPGSSVEGDCGNPSVGIFYFVSYIIISFLVVVNMYIA      1800
                    ************************************************************
```

```
Q15858-1_5N11L      VILENFSVATEESTEPLSEDDFEMFYEVWEKFDPDATQFIEFSKLSDFAAALDPPLLIAK      1817
FC_SCN9A_5N11S      VILENFSVATEESTEPLSEDDFEMFYEVWEKFDPDATQFIEFSKLSDFAAALDPPLLIAK      1806
PDB_6J8G_5N11L      VILENFSVATEESTEPLSEDDFEMFYEVWEKFDPDATQFIEFSKLSDFAAALDPPLLIAK      1860
                    ************************************************************

Q15858-1_5N11L      PNKVQLIAMDLPMVSGDRIHCLDILFAFTKRVLGESGEMDSLRSQMEERFMSANPSKVSY      1877
FC_SCN9A_5N11S      PNKVQLIAMDLPMVSGDRIHCLDILFAFTKRVLGESGEMDSLRSQMEERFMSANPSKVSY      1866
PDB_6J8G_5N11L      PNKVQLIAMDLPMVSGDRIHCLDILFAFTKRVLGESGEMDSLRSQMEERFMSANPSKVSY      1920
                    ************************************************************

Q15858-1_5N11L      EPITTTLKRKQEDVSATVIQRAYRRYRLRQNVKNISSIYIKDGDRDDDLLNKKDMAFDNV      1937
FC_SCN9A_5N11S      EPITTTLKRKQEDVSATVIQRAYRRYRLRQNVKNISSIYIKDGDRDDDLLNKKDMAFDNV      1926
PDB_6J8G_5N11L      EPITTTLKRKQEDVSATVIQRAYRRYRLRQNVKNISSIYIKDGDRDDDLLNKKDMAFDNV      1980
                    ************************************************************

Q15858-1_5N11L      NENSSPEKTDATSSTTSPPSYDSVTKPDKEKYEQDRTEKEDKGKDSKESKK      1988
FC_SCN9A_5N11S      NENSSPEKTDATSSTTSPPSYDSVTKPDKEKYEQDRTEKEDKGKDSKESKK      1977
PDB_6J8G_5N11L      NENSSPEKTDATSSTTSPPSYDSVTKPDKEKYEQDRTEKEDKGKDSKESKK      2031
                    ************************************************
```